Experimental study of two counter rotating axial flow fans

Juan Wang

2014-ENAM-0024

École doctorale n° 432 : Sciences des Métiers de l'Ingénieur

Doctorat ParisTech

T H È S E

pour obtenir le grade de docteur délivré par

l'École Nationale Supérieure d'Arts et Métiers

Spécialité " Mécanique "

présentée et soutenue publiquement par

Juan WANG

Le 22 Septembre 2014

Experimental study of two counter rotating axial flow fans

Directeur de thèse : **Farid BAKIR**
Co-encadrement de la thèse : **Florent RAVELET**

Jury

M. Gérard BOIS, Professeur**,** Arts et Métiers ParisTech - Lille	Président
M. Carlos SANTOLARIA MORROS, Professeur, Universidad de Oviedo	Rapporteur
M. Xavier Carbonneau, Professeur, ISAE-Toulouse	Rapporteur
M. Farid BAKIR, Professeur, DynFluid, Arts et Métiers ParisTech - Paris	Examinateur
M. Florent RAVELET, Maître de conférence, DynFluid, Arts et Métiers ParisTech - Paris	Examinateur
Mme. Amélie Danlos, Maître de conférence, CNAM	Examinateur
M. Manuel HENNER, Docteur, Manager R&D Valeo	Invité

T H È S E

Arts et Métiers ParisTech - Centre de Paris
DynFluid

Abstract The counter rotating subsonic axial flow fans could be a good solution for applications where the highly improved static pressure and efficiency are required without the increase of rotational speed and fan diameter. However, the mechanism of high performance CRS and the influence of parameters are not well understood nowadays. This thesis is an experimental investigation of the performance and parameter studies of two counter rotating axial flow ducted fans. The design and measurement methods are based on the previous research work in Laboratory Dynfluid (Arts et Métiers ParisTech). Three Counter Rotating Stages (CRS) (named JW1, JW2 and JW3) are developed and tested on a normalized test bench (AERO2FANS). These systems have the same design point and differ by the distribution of loading as well as the ratio of angular velocity between the Front Rotor (FR) and Rear Rotor (RR). The first part of results focuses on the JW1. The overall performance is obtained by the experimental results of the static pressure rise and static efficiency, as well as the wall pressure fluctuations recorded by a microphone on the casing wall. The parameter study is conducted to investigate the effects of the axial distance and the ratio of angular velocity between the FR and RR on the global performance and flow fields measured by Laser Doppler Velocimetry (LDV). The last part of the work is devoted to analyzing the differences of the three CRS with different distribution of work, in terms of the global performance and flow features.

Keywords: Counter rotating fans, performance, parameters influences,Wall pressure fluctuations, LDV

Résumé Les machines axiales à rotors contrarotatifs subsoniques sont une bonne solution pour les industries où de fortes élévations de pressions et d'efficacités sont nécessaires sans augmenter le diamètre ou la vitesse de rotation des rotors. Néanmoins, le comportement des CRS et les paramètres impactant ses performances ne sont pas encore totalement compris. Cette thèse mène une investigation expérimentale sur la performance et les paramètres influents sur un étage contrarotatif. La technique de design et les méthodes de mesure sont repris sur une thèse précédente réalisée au laboratoire Dynfluid (Arts et métiers ParisTech). Trois étages contrarotatifs ont été fabriqués (JW1, JW2 et JW3) et testés sur le banc d'essai normalisé AERO2FANS. Ces machines ont été conçues pour avoir le même point de fonctionnement mais avec une répartition de charge différente. Les résultats expérimentaux se concentrent dans un premier temps sur JW1. Les grandeurs physiques regardées sont l'efficacité globale et l'élévation de pression statique pour juger de la performance globale de la machine. La fluctuation de pression pariétale et le champ de vitesse sont aussi mesurés. L'impact du changement de rapport de vitesse ou la distance entre les deux rotors sur la machine JW1 a été étudiée grâce aux grandeurs physiques décrits précédemment. Enfin dans une dernière partie, les trois machines sont comparées toujours grâce aux grandeurs physiques définies précédemment.

Mots clés : Rotors contrarotatifs, Ventilateur axial , Turbomachine, Performance, Influence des paramètres, Interaction rotors, Mesure de fluctuations pression pariétale, LDV

Remerciements

Je tiens tout d'abord à remercier mes deux directeurs, Monsieur Farid Bakir, professeur et Monsieur Florent Ravelet, maître de conférence, pour m'avoir aider pendant ces trois années.

Mes remerciements s'adressent ensuite aux membres du jury: Monsieur Gérard BOIS, professeur, d'avoir présidé ma soutenance et examiné mon rapport, Messieurs Xavier Carbonneau et Carlos SANTOLARIA MORROS , pour avoir accepté de rapporter mon manuscrit de thèse et enfin, le examinateur, Mme. Amélie Danlos, Maître de conférence au CNAM et l'invité, Monsieur Manuel Henner, responsable R&D à Valeo, qui s'est intéressé à mes travaux.

Je pense également à tous ceux avec qui j'ai partagé des moments agréables : M Noguera et Rey, Sofiane, Richard, Michael, Christophe ... et à tous les docteurs et doctorants du laboratoire : Moisés, mon collègue de bureau Salah, Amrid, Petar, Joseph, Fatiha, Takfarinas, Charles, Mohamed, Ewen, Sylvain...

Je voulais aussi remercier grandement le jeune docteur Hussain Nouri, qui m'a laissé une très bonne base pour pouvoir travailler et qui m'a permis par son aide de continuer efficacement sa thèse.

Je remercie ma famille pour m'avoir soutenu et ... Hervé : On va pouvoir acheter notre cuisine !

Juan

“*To my parents and Hervé*”

Contents

Abstract **iii**

Remerciements **v**

1 Theoretical Background **3**
1.1 Basics of turbomachinery . . . 3
1.1.1 Classification of turbomachines . . . 3
1.1.2 Functioning of subsonic axial fans . . . 4
1.1.3 Performance of subsonic axial fan . . . 5
1.2 Main aerodynamics structures in subsonic axial fans . . . 7
1.2.1 wakes . . . 8
1.2.2 potential effects . . . 9
1.2.3 Tip clearance flow . . . 9
1.2.4 Loss due to unsteady flow . . . 9
1.3 Influence factors related to loss in subsonic axial fans . . . 10
1.3.1 Incidence and deviation in the rotor of an axial fan . . . 10
1.3.2 Flow Deviation . . . 11
1.3.3 Reynolds number . . . 11
1.4 Counter Rotating Stage(CRS) . . . 12
1.4.1 working principle of Counter Rotating Stage(CRS) . . . 12
1.4.2 Main research on CRS machines . . . 12
1.5 Conclusion . . . 20

Introduction **3**

2 Experimental facilities and methods **23**
2.1 Test rig . . . 23
2.2 Quantities of interest . . . 23
2.3 Design of the counter rotating Stages (CRS) . . . 26
2.3.1 Methodology . . . 26
2.3.2 Characteristics of the three different CRS . . . 26
2.3.3 Limitations of the Conception Method . . . 30
2.4 Experimental method and uncertainties . . . 30
2.4.1 global performance . . . 31
2.4.2 LDV . . . 37
2.4.3 Microphone . . . 40
2.5 Conclusion . . . 43

3 Results JW1 **45**
3.1 Validation of the design method 45
3.1.1 Overall performance of JW1 working on the design parameters . . . 45
3.1.2 Validation of the design assumptions at design flow rate Q_v = 1 m^3.s^{-1} 47
3.1.3 Euler power at design flow rate Q_v = 1 m^3.s^{-1} 55
3.1.4 Deviation angle and loss 57
3.1.5 Conclusion 58
3.2 The characteristics of JW1 working at different flow rates 60
3.2.1 Comparison of Velocity fields for JW1 at Zp = 5 mm at different flow rates 60
3.2.2 Comparison of Velocity fields between JW1FR and JW1 at Z_p = 5 mm at different flow rates 62
3.2.3 Velocity fields of JW1 at Z_p = 5 mm and Z_p = 50 mm at different flow rates 62
3.2.4 Conclusion 64
3.3 Analysis of the wall pressure fluctuations 66
3.4 Influence of the axial distance S on the performances of JW1 at $\theta = \theta_C$ and Q_v = 1 m^3.s^{-1} 68
3.4.1 Influence of S on the global performance of JW1 68
3.4.2 Influence of S on the velocity fields between FR and RR 71
3.4.3 Influence of S on the flow angles between FR and RR 74
3.4.4 Influence of S on the velocity field at different axial positions when S is fixed 75
3.4.5 Conclusion 75
3.5 Influence of speed ratio θ on the performances of CRS 78
3.5.1 Influence of θ on the global performance at N_{FR} = 2300 rpm 78
3.5.2 Influence of θ on the velocity field at N_{FR} = 2300 rpm 78
3.5.3 Influence of θ on the flow angles at N_{FR} = 2300 rpm 82
3.5.4 Influence of θ at different rotating speeds of FR 84
3.5.5 Conclusion 86
3.6 Influence of both the axial distance S and θ on the performances of JW1 . 86

4 Results of all CRS **93**
4.1 Characteristics of the three CRS working on design parameters 93
4.1.1 Overall performance 93
4.1.2 Flow fields at design point by MFT and LDV 98
4.1.3 Conclusion 100
4.2 Velocity fields for all CRS at different volume flow rates 101
4.2.1 Velocity profiles downstream of FR in CRS at different flow rates . 102
4.2.2 Velocity profiles downstream FR in FR only and CRS 102
4.2.3 Velocity profiles downstream the RR in CRS at different flow rates 105
4.2.4 Conclusion 108
4.3 Analysis of the wall pressure fluctuations 108
4.4 Influence of the axial distance S on the performances of CRS at $\theta = \theta_C$ and Q_v = 1 m^3.s^{-1} 112
4.5 Influence of speed ratio θ on the performances of CRS 115

4.6 Mix match of CRS 116

5 Conclusions ans perspective **119**
5.1 Summary 119
5.1.1 Uncertainty evaluation of experimental methods 119
5.1.2 Design of three new CRS 119
5.1.3 Validation of design methods 120
5.1.4 Flow features at different flow rates 121
5.1.5 Wall pressure fluctuation in CRS 122
5.1.6 Parameter study 122
5.2 Recommendations for Future Work 124

Appendix **133**

A Experimental comparison between HSN and RSS **137**

B Flow fields comparison between CRS and RSS by LDV **149**
B.1 Velocity field downstream FR measured by LDA at crosspoint1 149
B.2 Velocity field downstream FR measured by LDA at $Q_v = 1$ m^3.s^{-1} 153

C Résumé de Thèse **155**
C.1 Introduction 157
C.2 Théorie des ventilateur et étude Bibliographique 157
C.3 Configuration Expérimentale et incertitude de mesure 159
C.3.1 Banc d'essai 159
C.3.2 Grandeurs Pertinentes 159
C.3.3 Design des CRS 160
C.3.4 Incertitude expérimentales 162
C.4 Résultat du JW1 163
C.4.1 Validation de la méthode de design 163
C.4.2 Champ de vitesse du JW1 pour des débits différents 164
C.4.3 Fluctuations de pressions pariétale 166
C.4.4 L'influence de distance axiale S 168
C.4.5 L'influence de rapport de vitesse θ 170
C.5 Résultat des trois systèmes 173
C.5.1 Performance global pour les CRS 173
C.5.2 Champs de vitesse au débit du conception pour les CRS 173
C.5.3 Champs de vitesse au débits différents pour les CRS 176
C.5.4 Comparaison des fluctuations de pressions pariétale 176
C.5.5 L'influence de S sur les CRS 177
C.5.6 L'influence de θ sur les CRS 177
C.6 Conclusion 179

Nomenclature

Abbreviations

CRS	Counter Rotating Stage
FR	Front Rotor
LDV	Laser Doppler Velocimetry
PSD	Power Spectral Density
RR	Rear Rotor
RSS	Rotor Stator Stage
Std	Standard deviation

Greek Letters

α	absolute angle, [°]
β	relative angle, [°]
β'	blade angle, [°]
γ	stagger angle, [°]
δ	deviation angle, [°]
ϵ	relative uncertainty
η_s	static efficiency
θ	rotational speed ratio
ρ_a	density of air, [Kg.m^{-3}]
σ	cascade solidity
τ	torque, [N.m]
ϕ	flow coefficient
ψ	head coefficient
ω	angular velocity of the blade, [rad.s^{-1}]

Roman Letters

C_x	drag coefficient
C_z	lift coefficient
D	ducting piper diameter, [mm]
$\mathcal{D}$	diffusion factor
e	absolute uncertainty
$\vec{F}$	force exerted on the fluid by the blade, [N]
i	incidence angle, [°]
L	distribution of load
L_{chord}	chord of the blade, [mm]
Ma	Mach number
$\dot{m}$	mass flow rate, [Kg.s^{-1}]
P_a	atmospheric pressure, [Pa]
P_{dyn}	dynamic pressure, [Pa]
$\mathcal{P}_{Euler}$	Euler power, [W]

$\mathcal{P}_w$	power consumption, [W]
ΔP_{Euler}	Euler pressure rise, [Pa]
ΔP_s	static pressure rise, [Pa]
ΔP_q	pressure drop through orifice plat, [Pa]
ΔP_v	static pressure rise without correction, [Pa]
Q_v	volume flow rate, [$m^3.s^{-1}$]
r	arbitrary radial position, [m]
R	radius, [mm]
Re	Reynold's number
S	axial spacing, [mm]
T_{ad}	wet temperature, [°]
T_{seche}	dry temperature, [°]
U	blade speed, [$m.s^{-1}$]
$\vec{V}$	absolute velocity, [$m.s^{-1}$]
V_z	axial velocity , [$m.s^{-1}$]
V_θ	tangential velocity, [$m.s^{-1}$]
V_r	radial velocity , [$m.s^{-1}$]
$\vec{W}$	relative velocity, [$m.s^{-1}$]
Z_p	axial position, [mm]
Z	number of blades

Subscripts

1	fan inlet
2	fan outlet
bpf	blade passing frequency
C	conception
s	static
t	total
z	axial
θ	tangential
r	radial

Introduction

To achieve higher performances with more compact turbomachines, the counter rotating machines have become one of the most promising solutions. For these machines, the traditional downstream stator is replaced by a second rotor (Rear Rotor) which turns in the opposite direction with respect to the upstream rotor (Front Rotor). This Rear Rotor (RR) has two main contributions for the whole machine: recovering static pressure from the outflow of front rotor, and also transferring energy to the working fluid directly. However, the characteristics and unsteady flow of a Counter Rotating Stage (CRS) are still not clear, especially for the influence of parameters and rotor-rotor interaction mechanisms.

Therefore, some experimental test-rigs have been studied experimentally and numerically in different countries to understand the physical behavior of the unsteady flow in counter rotating compressor/fan. The early exploration of a low speed counter rotating axial compressor in the early 1990s [1] gave a first glimpse of the influence of parameters on the aerodynamic performance. Then other recent studies [2][3][4] provide the global performance and flow fields in their applications. However, there are few configurations with a relatively comprehensive investigation of both global performance and influence of parameters through the rotor-rotor interactions.

In the Dynfluid Laboratory (Arts et Métiers ParisTech), a low speed counter rotating ducted fan has been designed using an original method with an in-house code named MFT. A prototype (named "HSN") has been manufactured and tested in a normalized test bench (AERO2FANS), built according to the ISO-5801 standard [5][6]. The experimental results show that HSN has remarkably high maximum static efficiency and large stable working range in a wide range of operating conditions regardless of the various axial distance between the two rotors and the ratio of the angular velocities. But an important design parameter, the distribution of the load is chosen randomly. Nevertheless, the previous research provides a platform for developing high performance counter rotating stage fans and for measuring the performance and flow fields with various methods of instrumentation. It is a good opportunity to conduct a complex analysis of the influence of various design parameters on the physics of low speed counter rotating ducted fans.

The following work is composed of three main parts. Firstly, after a review of the theoretical background and bibliography, the experimental facilities are depicted. The design of three CRS (JW1, JW2,JW3) which can achieve the same design point on varying the distribution of load is given in detail. The measuring techniques are kept the same as those in Ref. [5]; thus, they are presented briefly. Moreover, a detailed analysis of the uncertainty of experiments is given, which is important for the evaluations of results.

Then, the detailed analysis of one of the CRS (JW1) is presented, concerning the validation of the design method, flow characteristics on the design and off design flow rates, wall pressure fluctuations at different conditions, as well as the influence of axial

spacing and speed ratio.

Finally, the flow characteristics of three CRS (JW1,JW2,JW3) having the same design point but with different design distribution of load are depicted in detail with the same method used for JW1.

Chapter 1

Theoretical Background

To explore the mechanism of counter rotating fan stage, what is first required is a global understanding of the basic working principle and complex flow structures inside a conventional Rotor Stator fan Stage. This chapter introduces an overview of the necessary physical aspects of this work. It contains an introduction to the basics of a conventional subsonic axial fan. Then, an overview of the unsteady flow structures in subsonic axial fans is presented. Later, the working principle of counter rotating fan stage and a short review of state of the art for counter rotating machines are given.

1.1 Basics of turbomachinery

1.1.1 Classification of turbomachines

A turbomachine is a device which exchanges mechanical work with continuous working fluid, by the rotating of the blade rows [7][8]. There are two main categories:

- firstly, the work-absorbing turbomachines which absorb the mechanical work (in the form of shaft work) and transfer to fluid pressure or head rise, such as compressors, ducted or unducted fans and pumps;
- secondary, the work-producing turbomachines which produce mechanical work by expanding fluid, generally known as turbines.

They are further categorised by the type of meridional flow path. If the flow path is mainly or exactly parallel to the axis of rotation, the device is termed axial-flow type. However, if the meridional flow path changes its direction from parallel to perpendicular to the rotation axis, the stage is referred to as centrifugal or radial type. Otherwise, the stage is termed mixed turbomachines in which the meridional flow at outlet of rotor has significant amounts in both axial and radial components.

Additionally, turbomachines can be classified as incompressible or compressible machines. For compressible machines, the fluid has significant changes in density. This is the case when the fluid (for example air) Mach number is greater than about 0.3. On the contrary, for the incompressible machines, the density of the fluid is constant. The working medium could be either liquid or low speed gas(highest Mach number is below 0.3).

The present manuscript deals with an axial, incompressible subsonic ducted fan.

1.1.2 Functioning of subsonic axial fans

Subsonic axial flow fans normally use air as working fluid, operate at low speeds and provide moderate pressures [9]. They are mainly applied for ventilating and air conditioning of the vehicles, underground transportation systems, and IT devices. A conventional fan stage is composed of two blade rows: a rotating part called rotor and a fixed part called stator. The rotor provides energy to the fluid trough increasing its kinetic and pressure energy. The augmentation of kinetic energy is then partly transformed into pressure energy by the stator. To understand the detailed energy conversion process, the basic Euler Work Equation and a rotor stator velocity triangle are shortly presented.

Work done by an axial rotor

In an axial rotor [7][10], the fluid enters the control volume with relative velocity $\vec{W}_1$ and leaves it with a relative velocity $\vec{W}_2$. According to the law of moment of momentum, the vector sum of the moments of all external forces is equal to the time rate change of angular momentum of the system about that axis. At an arbitrary radial position r, we obtain:

$$\sum \vec{r} \times \vec{F} = \dot{m}\vec{r} \times (\vec{W}_2 - \vec{W}_1) \tag{1.1}$$

$\vec{F}$ is the force exerted on the fluid by the blade. Subscripts 1 and 2 represent respectively the inlet and outlet of the blade row.

We obtain:

$$\tau = rF_\theta = \dot{m}r(W_{\theta 2} - W_{\theta 1}) = \dot{m}(V_{\theta 2} - V_{\theta 1})r \tag{1.2}$$

W_θ is the relative velocity projected on the circumferential direction. According to the triangle of velocity, we could clearly see that: $W_{\theta 2} - W_{\theta 1} = V_{\theta 2} - V_{\theta 1}$. V_θ is the tangential component of the absolute velocity of the fluid.

For an axial rotor, the work done by the blade row on the control volume per unit time is

$$\mathcal{P}_{Euler} = \tau\omega = \dot{m}(V_{\theta 2} - V_{\theta 1})r\omega = \dot{m}U\Delta V_\theta \tag{1.3}$$

With the blade speed $U = r\omega$. This is known as the Euler Work Equation. And $\mathcal{P}_{Euler}$ is termed as Euler power for the present research.

Additionally, in this thesis, the Euler pressure rise is defined as $\Delta P_{Euler} = \rho U \Delta V_\theta$, which represents the work done on the fluid by the rotor blade per unit volume flow rate. Thus,

$$\mathcal{P}_{Euler} = \rho U \Delta V_\theta \times Q_v = \Delta P_{Euler} \times Q_v \tag{1.4}$$

Q_v denotes for the volume flow rate.

Further, since turbomachinery is usually adiabatic, the best possible process in a turbomachine is an isentropic process. It is defined as that the flow undergoes a process which is both adiabatic and reversible (entropy unchanged) [7]. Therefore, the work done by the rotor in an isentropic process in an incompressible flow is transferred to the total pressure rise of the fluid. The total pressure rise is composed of two parts: static

pressure rise (ΔP_s) and dynamic pressure rise $\frac{\rho \Delta V^2}{2}$. The absolute velocity consists of three components: axial (V_z), tangential (V_θ) and radial (V_r). Usually, the radial velocity component (V_r) is assumed to be 0 according to the simple radial equilibrium, which will be depicted in the following part. The axial velocity V_z is constant at each section of a duct or passage, based on the equation of continuity. But the tangential velocity is largely increased. This part of energy is not directly useful for fans and is then usually transferred to static pressure by a stator. The detailed velocity changes of the fluid in a fan stage are illustrated in the following velocity triangle.

Velocity triangles of a Rotor-Stator Stage (RSS)

Figure 1.1 shows typical velocity triangles in a Rotor Stator Stage (RSS). For the purpose of simplicity, the fluid enters the rotor axially with an absolute inlet velocity $\vec{V}_{1,R}$. Subtracting vectorially the blade speed $\vec{U}$ gives the inlet relative velocity $\vec{W}_{1,R}$ at angle $\beta_{1,R}$, which is almost parallel to the rotor blade angle at their leading edge at design condition. When traversing the rotor, the flow is turned to the direction $\beta_{2,R}$ at outlet with a relative velocity $\vec{W}_{2,R}$, which is obviously lower than $\vec{W}_{1,R}$. This turning $\Delta\beta$ can be reflected by the increase of the tangential velocity of the fluid ΔV_θ, which relates to the work transfer from the rotor to the fluid. In this process, the total pressure of the fluid increases.

In this process, the flow turning, referred to as the amount of diffusion achieved by a blade row, is limited by the process of boundary layer growth and stall in a blade passage. A useful diffusion parameter is the diffusion factor expressed as [11]:

$$\mathcal{D} = 1 - \frac{W_2}{W_1} + \frac{W_{\theta 2} - W_{\theta 1}}{2\sigma W_1} \tag{1.5}$$

With σ the cascade solidity. The suggested maximum values of $\mathcal{D}$ for a subsonic flow are 0.45 at the rotor tip and 0.55 at the rotor mean and hub region [11].

On the other hand, the fluid approaches the stator with an absolute velocity $\vec{V}_{1,S} = \vec{V}_{2,R}$, by adding vectorially the blade speed $\vec{U}$ to $\vec{W}_{2,R}$ at outlet of the rotor. When passing through the stator, the flow is diffused and deflected towards the axis and gets an outlet velocity $\vec{V}_{2,S}$. In this process, the work input is 0 and static pressure is recovered by diminishing the dynamic pressure.

1.1.3 Performance of subsonic axial fan

Figure 1.2 shows a typical performance curve of a fan including static pressure rise and static efficiency as a function of volume flow rate. As the flow rate decreases from the free delivery (maximum flow rate), the angle of attack increases and static pressure rises up. When the limit value of angle of attack is passed, the flow separates from the blade surface. Eddies appear at downstream hub and even upstream tip. This causes a diminution of the flow turning angle and of the work done by the blade, consequently a pressure drop (at point c in Fig. 1.2). Then the fan works in an unstable condition with low efficiency and high noise and non uniform flow goes through the fan blades. As flow rate continues to decrease, the size of eddies grows larger and reaches its maximum size at zero flow rate. The air goes through the blade with large radial component, thus the pressure almost reaches its maximum for zero volume flow [12].

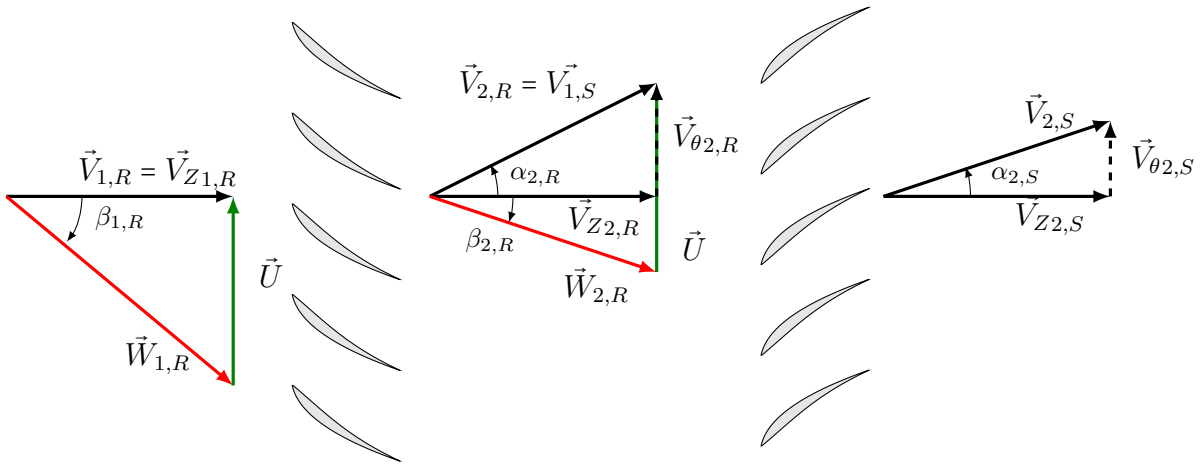

Figure 1.1: Velocity triangles in a compressor/fan: Rotor-Stator Stage [5].

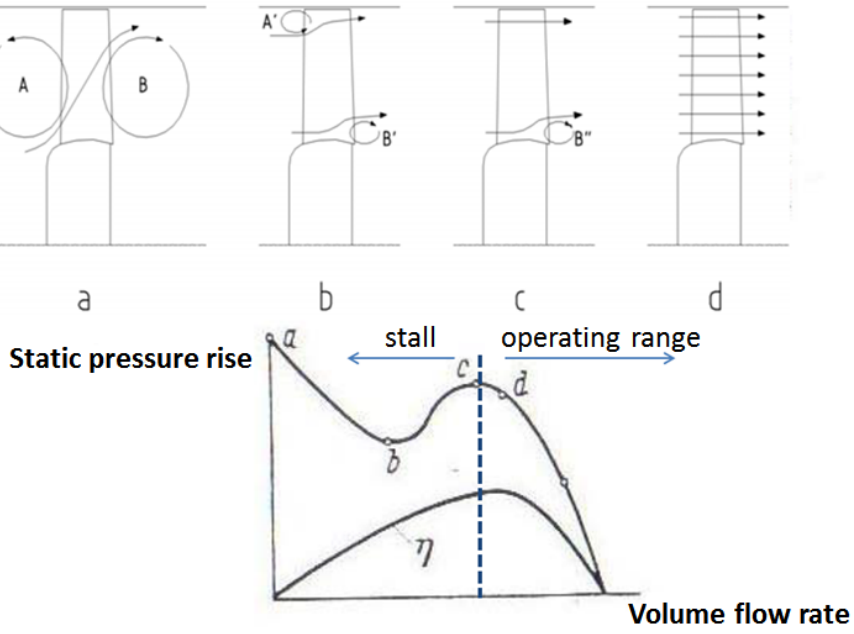

Figure 1.2: Performance of an axial fans [9][12][13]

Stall

One should pay attention to the part of the characteristics between point a and point c in Fig. 1.2. The fan is working in an unstable operating condition named Stall. Stall also refers to the result of boundary layer separation. When the fluid velocity near the blade wall is reduced to zero by the viscous shear effect and adverse pressure gradient, the streamlines adjacent to the wall will leave the wall and a reverse flow will develop on the wall surface. This could appear when the fan works at a given speed and the flow rate is continuously reduced. At partial flow rate, the loading of the the fan/compressor increases, additional diffusion is required. When the required loading is beyond the loading limit, large scale separation and blockage occur and the efficiency falls [11]. Probably a highly unstable flow will result and stall is triggered at blade passage. Further, Japikse et Baines [11] report that stall occurs as a result of increased blockage on the passage end walls instead of directly a blade loading limit. The loading limit is also influenced by the flow Reynolds number, the tip clearance and the axial spacing of the blade rows. These parameters control the growth and development of the end wall boundary layers.

Further, when the fan stage has strong stall in one of its elements and the flow characteristic of the whole stage is no longer stable (negatively sloped), the stage stall happens. In stage stall, the flow characteristic becomes positive and is no longer stable. Japikse et Baines [11] mention that one possible criterion for stage stall is the slope of the pressure ratio curve *vs.* flow rate at a constant rotating speed of stage: negative slope means stable operation while positive slope means unstable operation. In other words, when the pressure ratio versus flow rate is horizontal, the stage reaches the limit of stable operation.

1.2 Main aerodynamics structures in subsonic axial fans

Usually, in the design process, the flow of axial turbomachines is assumed to be axisymmetric and is confined to concentric streamtubes. It means that the flow through the blade rows is assumed to be two-dimensional, which means that the radial velocity is zero. This is known as the simple radial-equilibrium condition. This condition also mentions a radial pressure gradient is necessary to provide the centrifugal force to maintain a curved flow path through the machine [14]. And the simple radial equilibrium theory excludes streamline curvature effects [15].

In reality, with relative low hub to tip ratios, the flow in a subsonic axial fan is three-dimensional. The balance between the strong centrifugal forces on the fluid and radial pressure gradient is temporarily broken and the fluid is transported radially to change the pressure distribution until the equilibrium is re-achieved. This three dimensional flow is referred to as the secondary flow which is not organised as axisymmetric streamtubes, such as the blade migration, end wall boundary layers and wakes resulting from viscosity effects, as well as tip-clearance leakage flow which has an inviscid nature [15]. These unsteady flows generate additional loss and degrade the performance of the subsonic axial fans. Therefore, it is difficult to improve the performance without accounting for the three dimensional unsteadiness of the flow fields. Therefore, it is worthwhile to give a detailed description of the mainly unsteady three dimensional flow in a subsonic axial fan stage.

1.2.1 wakes

Wakes are formed by the pressure and suction-side flow streams mixing together and only affect the downstream rows. They arise from viscous effects on the blade boundary layer and involve a velocity deficit in the exit flow field. It is an important loss source for turbomachines. The wakes decay when passing downstream, mainly in three forms [16]:

- viscous mixing, the mixing of wake with the main stream flow.
- wake stretching: Viscous mixing reduces velocity deficit. Then wakes are chopped into segments and stretched as they transport through the downstream blade rows. As the velocity deficit is proportional to the width, the wake decay is aggravated(See Fig. 1.3). This phenomenon is called "wake recovery" [17]. Sanders *et al.* [17] indicate the inviscid stretching is the dominant wake decay mechanism.
- negative jet. It arises from the difference of the relative velocity between the wake and free stream. As shown in Fig. 1.3, this difference drifts the accumulation of low momentum fluid on the pressure sides of the blades. This accumulation thickens the boundary layer near the pressure side and thins it on the suctions side. Further, the flow is replaced at the suction side of blade by the high-momentum free stream fluid. While the chopped segments of rotor wake pass through the successive blade rows, counter-rotating vortices are also generated on each side of the segment and act as an additional source of unsteadiness [17].

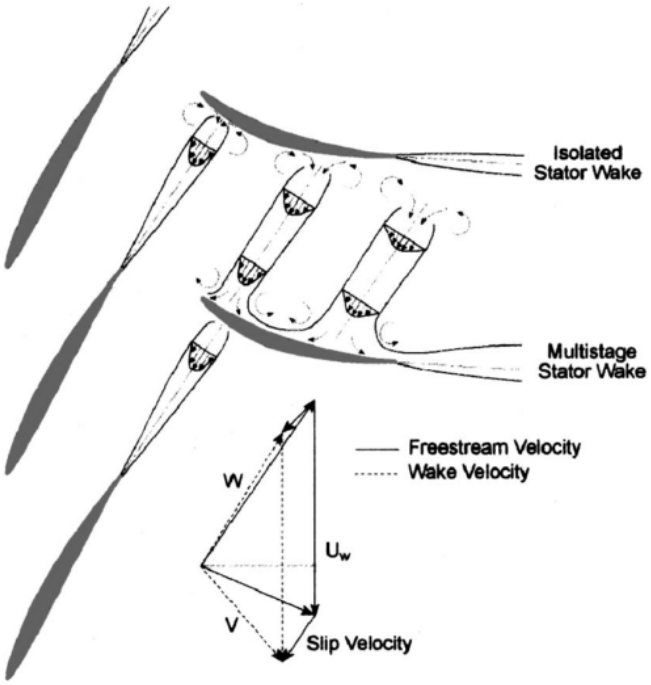

Figure 1.3: Wake in a rotor stator stage [17]

1.2.2 potential effects

The relative motion of two adjacent blade rows results in the interactions of their potential fields, consequently this will have an influence on their flow fields where the loss is generated. Precisely, the potential effects are related to the adaptation of the downstream and upstream pressure fields to the presence of the blades [16]. Behr [18] indicates that the potential fields propagate in the upstream and downstream direction as pressure waves and their magnitudes vary approximately as $\exp(-2\pi\sqrt{1-Ma^2}x/s)$, with x the distance from the blade row and s blade pitch. He also notes that the potential field interactions are insignificant for axial spacing greater than 30% of the blade pitch in low speed flows.

1.2.3 Tip clearance flow

Due to the clearance between the tips of the rotating blade and the casing of the machine, the flow leaks through this clearance from the pressure side to the suction side of blade tip. This leakage flow reduces blade work and affects the efficiency, due to the fact that the leakage flow is not turned like the main flow. It is an inviscid nature flow. At the outlet of the tip clearance region, a tip vortex is generated and interacts with the main stream flow (See Fig. 1.4). This tip vortex can still be detected far downstream the blade rows. The complex flow in blade tip region and vortex mixing with main stream deteriorates the stage performance [19]. Therefore,it is considered to be an important loss source.

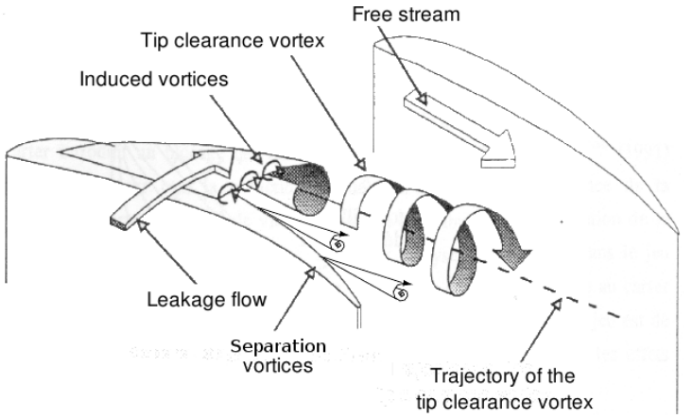

Figure 1.4: Tip clearance flow and tip vortex [16]

1.2.4 Loss due to unsteady flow

A common division of loss in low speed axial turbomachines is listed as [7][20]:

- profile loss, the loss based on the two dimensional cascade tests which arises from the growth of the boundary layer, the surface friction and blockage effects, usually well away from the end walls. The loss caused by a trailing edge and the wake shed from it is usually included as profile loss.
- secondary flow loss, is referred to as endwall loss arising from the distortion of fluid during the turning process in the blade passage including the hub and shroud

boundary layers, and annulus loss associated with the hub and shroud wall boundary layers between blade rows.

- tip clearance loss, caused by the leakage flow through the gap between the blade tip and shroud.

1.3 Influence factors related to loss in subsonic axial fans

It is commonly recognized that the flow in a turbomachine is 3D and unsteady. Therefore, in order to improve the efficiency, it is necessary to understand the factors which could cause the loss in the turbomachines.

1.3.1 Incidence and deviation in the rotor of an axial fan

Two angles can reflect the loss in the rotor blades : the incidence i and deviation δ angles. In general, the angles are defined in a cascade. In this thesis, all the definitions are applied directly in the rotor coordinate. In an ideal case, the flow in the rotor of an axial fan is entirely congruent with the blade profile. This means the relative inlet flow angle β_1 and relative outlet flow angle β_2 are coherent with the blade angles at the leading edge β_1' and trailing edge β_2'. The blade angles β_1' and β_2' are defined as the angles between the tangent of camber line at the leading edge and trailing edge to the axial directions. However, in reality there are differences between the camber line and the flow angles. The difference between the β_1 and β_1' is defined as the incidence angle i and at exit, the difference $\beta_2 - \beta_2'$ is termed deviation angle δ [21][22][7]. This term should be distinguished from the air deflection angle, defined as $\Delta\beta = \Delta\beta_1 - \beta_2$.

Incidence effects

At the design point of a rotor blade, the relative inlet flow angle is nearly parallel to the blade inlet angle, which means the incidence angle is close to zero. In this case, the air deflection is achieved by the camber of the blade. As the incidence angle increases, the flow suffers from higher diffusion on the suction surface of the blade, which could induce higher blade loss. Hence, the positive incidence angle may cause higher blade loading and increased flow deflection. Once the positive incidence is beyond a limit value, the flow will separate on the suction surface. At negative incidence, the diffusion is increased on the pressure surface. In this situation, the flow deflection and load are diminished. When the negative incidence is lower than a limit value, the flow can separate on the pressure surface [7]. The experimental data of NACA 65-27-10 in Fig. 1.5 show the trends for the performance varying with the incidence angle. The drag coefficient C_x is marked as i increases beyond a particular value and same situation as i decreases below another value. The two limits are defined as: i_A (stall on the pressure surface) and i_B (stall on the suction surface), corresponding to a loss coefficient C_x equals to twice the minimum loss [10]. In Fig. 1.5, the difference between i_A and i_B is around 14°.

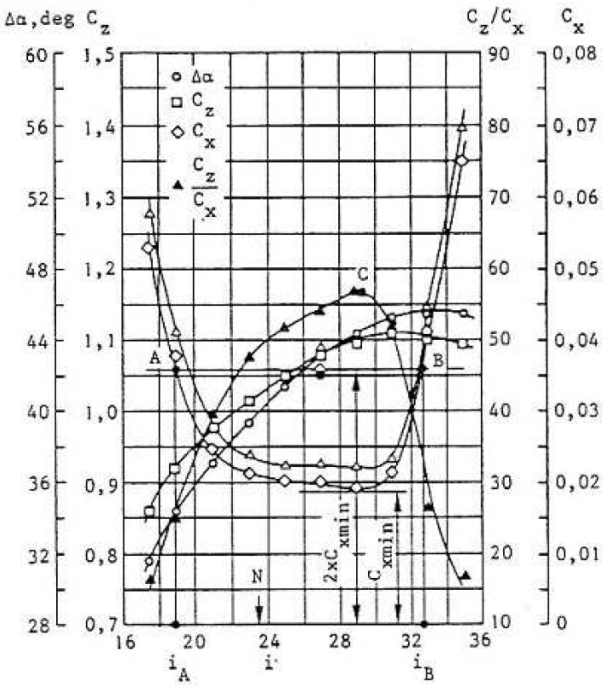

Figure 1.5: Variation of performance with incidence angle for cascade of NACA 65-27-10 with absolute inlet angle $\alpha_1 = 45°$ and solidity $\sigma = 1$. $\Delta\alpha$ is the deflection angle in the cascade, C_z and C_x are the lift and drag coefficient respectively [10]

1.3.2 Flow Deviation

This deviation angle δ reflects how well the flow leaves a rotor, following the blade chamber line at the trailing edge. Hence, δ is a measure of the departure of flow deflecting from the blade curvature. This flow deviation arises from the deterioration effects, such as boundary layer growth due to viscous effects, flow separation and recirculation, secondary flow, etc. Consequently, the flow does not follow the blade angle exactly and thus leaves the trailing edge with an angle that is different from the blade exit angle. Additionally, this flow deviation could be influenced by the blade spacing which determines how the flow is guided. Generally, due to the adverse (unfavourable) static pressure gradient in compressors or fans, δ could be very high [8].

In the book by Wennerstrom [15], the magnitude of the deviation angle will typically vary from a low value of 1 to 2 degree at the fan tip to a high value of possibly 12 to 13 degrees for a highly cambered hub section. If δ is still larger, it will be related to lower efficiency and lower stall margin. Usually, the level of work at a rotor tip is most strongly influenced by errors in deviation angle.

In conclusion, the incidence angle and deviation angle influence the design flow defection. When the fan works at off-design condition, the velocity triangle changes. The blade is subject to incidence variation and the flow deflection changes. This results in the modification in blade geometry. Consequently, the performance is affected.

1.3.3 Reynolds number

Japikse et Baines [11] note that the losses and deviation angle increase when the Reynolds

number is low. The limit Reynolds number (based on blade chord) varies between 0.7×10^5 and 2.5×10^5 depending on different cascade tests. Below the limit value, losses and deviation increase rapidity. The deterioration in performance at low Reynolds number is related to large laminar boundary layers and its separation in the adverse pressure gradient on the blade surface. These are cascade experimental results. In compressor stages, this limit could be as low as 4×10^4.

1.4 Counter Rotating Stage(CRS)

1.4.1 working principle of Counter Rotating Stage(CRS)

The Counter Rotating Stage (CRS) consists of two rotors located on their shafts successively without a stator between them and rotating in opposite directions. It means that instead of placing a stator at the outlet of the Front Rotor(FR), a Rear Rotor (RR) is adopted which turns oppositely to the FR. It can be seen in Fig. 1.6 that the relative velocity at inlet of the RR ($W_{1,RR}$) is largely improved owing to its contra-rotation. Then as in the FR, the fluid with enhanced $W_{1,RR}$ is diffused and deflected through the RR and provides a significant improvement in the CRS pressure rise. Compared with RSS, the RR not only recovers the static pressure but also supplies energy to the fluid.

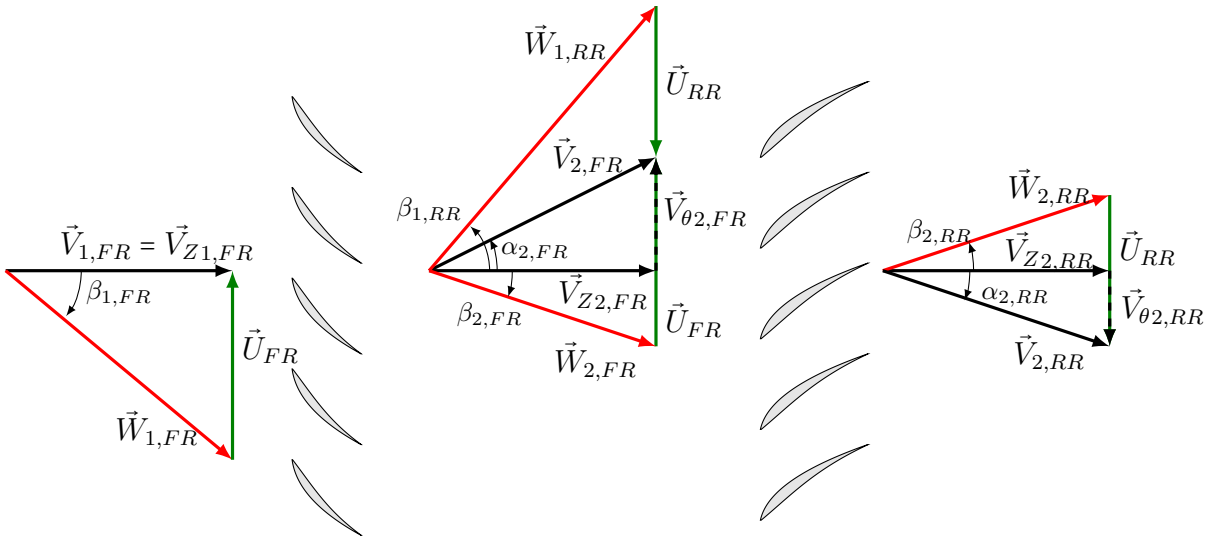

Figure 1.6: Velocity triangles in a Counter Rotating compressor/fan [5], $\alpha_{2,RR} \neq 0°$.

1.4.2 Main research on CRS machines

Research about the counter rotating method applied to turbomachines dates back to as early as the 19th century [5] for boat propellers. Then in the beginning of the 20th century, Lesley [23] carried out a series of experiments on the counter rotating propellers. For the propellers, as we know, the maximum thrust is the target. Firstly, he investigated the U.S. Navy type model which was combined with a counter rotating propeller. He found that the rear propeller blades set at from +2 to −2° to the propeller axis should obtain nearly

the maximum thrust. After further tests, he suggested that at the same rotational speed, with a smaller diameter, lower tip speed, greater efficiency and considerably less noise could possibly be attained with counter rotating propellers. This suggestion was proved in the following tests conducted on tandem air propellers with the forward propeller being a tractor and rear propeller a pusher, with the interference between them [24]. The purpose was to get the characteristics of the tandem propellers at a close spacing. Three kinds of spacing were investigated: 8.5%, 15% and 30% of propeller diameter. He found that the spacing had little effect on the characteristics of tandem propellers but the noise could be noticeably decreased with increased spacing. Later, Lesley [25] increased the blade numbers of tandem propellers from two to three. And he pointed out that the tandem propellers had 2 to 15% greater maximum efficiency than the single six blade propeller and also had higher efficiency gain than the single three blade propeller. The blade angle of the forward propeller was a key parameter to determine the value of maximum efficiency gain.

Then further application has arisen in civil aviation. In civil aviation, counter-rotating rotors have several application forms: the Contra-Rotating Open Rotors (CRORs), counter rotating shrouded Propfan and counter-rotating Turbo Fan (CRTF). Up to 30 to 40 % of fuel saving and a much greater flow capacity compared to a rotor-stator stage are considered attainable through the use of counter-rotating fans with an unducted or ducted arrangement. Additionally, these kinds of machines are known to provide much better off-design performance, specifically for rotating stall, which could possibly improve the operating range of fans [1]. But in the early 1990s, CRORs was rejected due to high levels of noise emission, which was one of the main challenges of the introduction of CRORs in civil aviation. On the other hand, Schimming [26] conducted experiments on the counter-rotating shrouded fan. The investigation results show that counter rotating fans do have a potential to be an alternative propulsor for high bypass engines. These engines have a remarkable improvement in efficiency because of the swirl-free exit flow compared with a single rotating propfan. Further, the measurements on the contra rotating fan were conducted by a laser-two-focus method, which was developed for double periodic flow in turbomachinery. They could observe the interaction of the vortices of both rotors through a movie. Additionally, it showed that the wakes of both rotors could be observed behind the second rotor. They concluded that counter rotating fans are an efficient alternative to traditional turbofans in terms of less fuel consumption and therefore less emissions. Until recently, SNECMA is developing architectures of CRORs and CRTF to achieve the ACARE 2020 goals that are a reduction of fuel consumption and CO_2 emissions by 20% and of perceived external noise by 6 dB [27].

More recently, counter rotating method have been increasingly familiar in the subsonic domain, such as low-speed counter rotating fans, pumps, turbines. Extensive research focused on the counter rotating subsonic machines has been reported, from both theoretical and experimental points of view. These studies usually focused on global performance, flow characteristics of CRS at design and off-design conditions as well as the influence of parameters, which are listed in the following part of this section.

Overall performance

Many researchers have pointed out that the counter rotating machines could improve the performance compared with a conventional turbomachine.

Pundhir et Sharma [1] pointed out that the contra-rotating axial flow compressor/fan had raised a considerable interest as a feasible application in future generation aircraft engines. This contra stage provided a much greater flow capacity than a rotor stator stage and offers a significantly improved off-design performance, especially in terms of its rotating stall behavior. Thus, it improves the stability of the operation of a fan stage.

In a contra rotating pump, the rear rotor not only recovered the static pressure like a stator, but also transferred energy to the working fluid. Therefore, to reach the required performance, the rotational speed could be reduced, as well as the pump size. And these could compensate the disadvantage of complex mechanical structures including two driving shafts [28]. Shigemitsu *et al.* [29] compared the performance characteristics of conventional and counter rotating axial flow pumps. Stable head characteristic curve with large negative slope and higher efficiency at partial flow rate were observed in counter rotating stage compared with the conventional stage. However, at very low flow rate, the head slope became gradual. They attributed this to the positive slope of the front rotor which had lower rotational speed and lower stagger angle.

Further, Shigemitsu *et al.* [30] started to apply the contra-rotating method to small-size fans as air coolers for electric equipments. They depicted that there is strong demand for higher efficiency and higher power of fans for the cooling of electrical requirements, such as laptops, desktop computers and servers. To achieve this, the traditional design would not be sufficient due to the restriction of fan diameters in space and deterioration of efficiency with the higher rotational speed design. Therefore, contra-rotating rotors of small-sized fans are introduced to improve the performance. Contra rotating fans were designed by assigning the same rotational speed and same pressure rise for the FR and RR. The advantages of contra rotating fans were confirmed by the numerical analysis of the performance curve.

Fukutomi *et al.* [31] studied contra-rotating rotors used in a sirocco centrifugal fan. The contra rotating rotors showed a total pressure coefficient 2.5 times greater than a single rotor, mainly owing to a considerably increase in circumferential component of velocities at outlet of outer rotor. Additionally, the blade row interaction is considered to be small when comparing two contra rotating fans with different diameters of inner rotors.

Moroz *et al.* [32] introduced another application form of the counter rotating method. They have designed multi stage counter-rotating turbines. They emphasized that special attention should be paid to the selection of optimal rotation speed and flow radial equilibrium conditions. They concluded that for the same performance level, the counter rotating prototype could reduce the axial length and total mass of vanes and blades by 30% and 40% respectively, compared with the initial traditional turbines. They considered this could balance all disadvantages in terms of complication of design in counter-rotating turbine. Additionally, the calculation results showed that the counter- rotating turbine had a higher efficiency in wider ranges of rotation speeds and could create more advantages in terms of aerodynamic quality and overall cost-efficiency than traditional configurations.

In Korea, Cho *et al.* [33] presented the design procedures of counter rotating axial fan (CRF), by applying the simplified meridional flow method with free vortex design condition. The same degree of reaction was assigned to the FR and RR. The performance estimation showed the hub to tip ratio was more important on fan efficiency compared with the other design parameters studied. The experimental results of non-dimensional performance is shown in Fig.1.7. They showed the peak efficiency point was lower than the design flow rate due to the fact that the real flow field was different from the radial equilibrium axisymmetric flow of design assumption. And the stall point was found at the position where the slopes of pressure coefficient and shaft power coefficient began to be positive in Fig. 1.7.

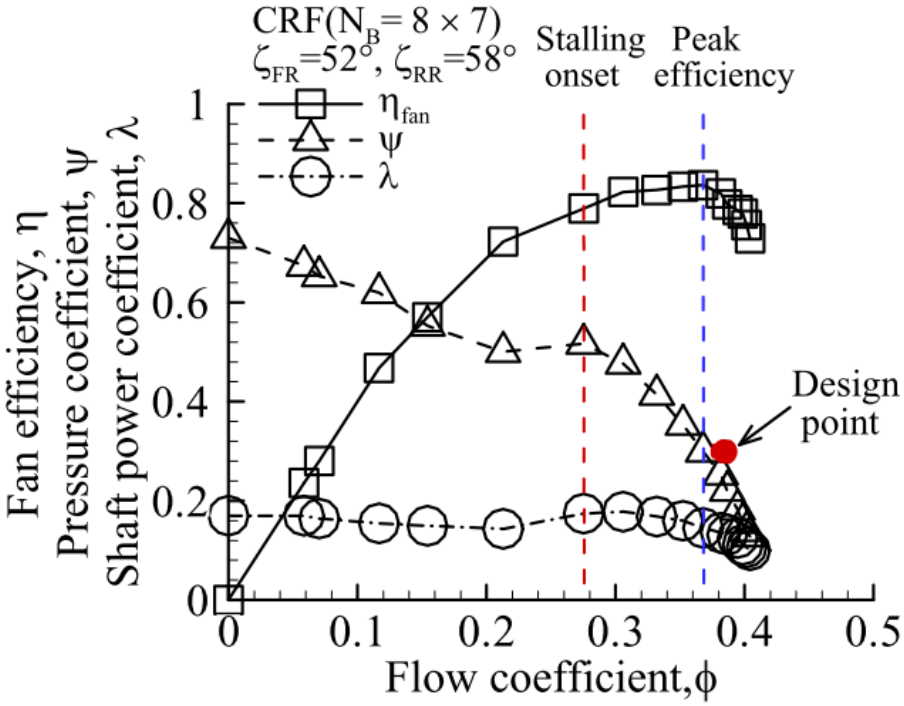

Figure 1.7: Performance curves of counter rotating axial fans [33]

Flow characteristics

Flow fields investigations are mainly focused on instantaneous pressure fields and velocity fields.

Shigemitsu *et al.* [28] designed two kinds of rear rotor to investigate the blade row interactions. One is named RR1, which has 3 blades designed by conventional empirical method. Another is RR2, redesigned which has 5 blades, smaller stagger angle, thinner blades and lower solidity. They argued that in a contra rotating axial pump the unsteady outlet flow from the Front Rotor would result in the blade loading fluctuation, unsteady blade forces and shaft vibrations. To investigate further rotor-rotor interactions, they measured the instantaneous pressures on the casing wall of the two contra rotating axial pumps, at different axial positions in accordance with the position changes of the blades. Then the radial distributions of flow velocities were measured by a 5-hole yaw-meter. They concluded that the large loss at the partial flow rate is due to the large tangential

velocity component between the FR and RR, and reverse flow at the hub of front rotor outlet. The amplitude for blade passing frequency (BPF) for measured head fluctuation indicated the blade loading was mainly located around the leading edge of both rotors at design flow rate. They also observed that amplitude of BPF decreases rapidly in downstream direction and decays gradually in upstream direction. This can entail that the pressure field of front rotor is strongly influenced by the rear rotor. And the maximum amplitude of BPF of rear rotor is much higher than that of the front rotor. Consequently, they found that the unsteady pressure fluctuations were more apparent in the front rotor than in the rear rotor due to the influence of rear rotor pressure field.

Later, Shigemitsu *et al.* [29] measured the velocity fields between the FR and RR in the contra-rotating axial pump (with RR1), at low partial flow rate by Laser Doppler Velocimetry (LDV). They observed the reversed flow at inlet tip and out low hub of the front rotor as well as the inlet tip of the rear rotor at low flow rate, as shown in Fig.1.8. The blade to blade relative velocities showed that the back flow region only occurred near the tip region. Moreover, they noted that the flow inclined to blade tip at outlet of the FR suppressed the back flow region at tip of the RR. Additionally, they suggested that the decreased rotational speed of rear rotor would be beneficial for the stable operation of the pump, by suppressing the back flow region at the inlet tip region of the RR.

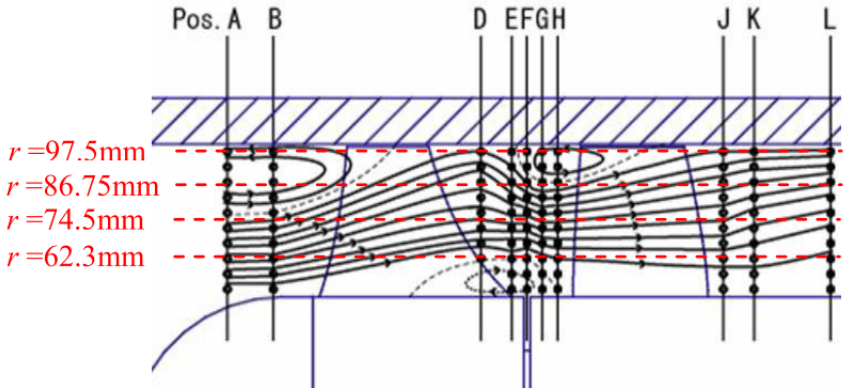

Figure 1.8: Meridional streamlines at partial flow rate in an axial pump, calculated from circumferentially averaged axial velocities obtained by LDV [29]

Further, similar measurement methods have been used to investigate the same contra rotating pump (with RR1) at design flow rate [34]. The blade to blade flow field between front rotor and rear rotor is presented at design flow rate by LDV. At blade tip, back flow component of the leakage vortex was observed in front rotor but not in rear rotor. And it disappeared at lower span, which indicated that the back flow at the tip resulted from the tip leakage vortex. Moreover, they ascribed the dissatisfaction of the performance of the RR to the mismatching of the stagger angle with incoming flow from the FR. They observed that the wake from the FR decayed and flow became uniform by the mid position of the axial spacing between the FR and RR. Therefore, the normalized uniform flow would be applied for the RR design. However, the rear rotor effect on the flow field seemed stronger than the FR wake effects as the blockage effect of the RR can reach upstream to near the trailing edge of the FR. Additionally, the pump performance of the tip region of the FR could be deteriorated by the leakage flow from the tip and frictional

loss on the casing wall.

Later, Momosaki *et al.* [35] investigated the contra-rotating pump (RR2) performance and velocity fields by experiment(using a 5-hole yaw-meter and LDV) and simulation. They found that the numerical results agreed well with that of the experiments at design flow rates. They observed a positive slope of head curve at partial flow rate and they thought it comes from the rear rotor which also has a positive slope at the same flow rate. From time averaged velocity in r-z plane at different chord positions, at design flow rate, no significant vortex structure could be found in the rear rotor. But at partial flow rate, strong tip leakage vortex initiated from the leading edge of rear rotor then became larger along main flow direction and induced back flow near the shroud. Besides, a flow separation was observed at trailing edge of rear rotor from hub till midspan. This flow separation, combined with the tip leakage vortex, caused the blockage effect which reduced the flow turning in rear rotor. This might be a possible reason for the positive slope of pressure curve. Streamline pictures by experimental (oil film) and CFD showed that there was radial flow near the hub of suction surface of rear rotor at both design and partial flow rate. Additionally, instantaneous disturbance fields showed there was large velocity disturbance at pressure surface of front rotor blades, and they thought it results from the tip leakage vortex of the rear rotor.

Recently, Shigemitsu *et al.* [2] turned research interest to contra-rotating small-sized fans. Numerical results were presented on the internal flow fields in a contra-rotating small-sized fan with a 40 mm square casing. The configuration was set at a fixed distance and high rotating speed of 15000-14000 rpm. Meridional velocities showed that a vortex occurred at the inlet corner of the front rotor and passed through downstream. Then the flow condition at outlet of front rotor was not uniform but inlet of the rear rotor was uniform. Additionally, the leakage flow was observed at both front rotor and rear rotor tip. They pointed out the back flow near the shroud of the rear rotor was larger than that of the front rotor. This research showed that the numerical calculation could be a convenient way to look into the complex flow field in contra rotating fans.

Cho *et al.* [33] measured circumferential-averaged flow fields of the contra-rotating fan by five-hole probe at peak efficiency point, which is located at lower flow coefficient compared with the design point. The five-hole probe measurement results showed that the static pressure was decreased before front rotor resulting from the suction effect of the FR rotation. Moreover, the axial velocity increased at the mean radius as a result of the contraction effects and decreased at the hub region due to the flow separation and hub vortex from upstream of FR to downstream of RR. Further, Cho *et al.* [36] presented a more detailed phase-locked averaged and circumferential averaged velocities fields analysis at peak efficiency point, based on the measurements of hot-wire probe upstream, in between and downstream the rotors of the same CRF. The circumferential averaged axial and radial velocities showed that the inlet flow before the front rotor is quite uniform except for the hub and tip region(see Fig. 1.9). They reasoned the axial velocities decreased at the inlet tip region of both rotors due to tip vortex not tip leakage flow and decreased at inlet hub region due to the flow separation and the hub vortex. Between the rotors, the axial velocities increased at mean radius by the flow contraction effect due to boundary layer of the fan casing and hub vortex. At downstream of the rear rotor, the axial velocity is higher at the mean radius as a result of flow contraction effect and largely decreased at the hub region by the flow separation and hub vortex of both

rotors. They also showed the incidence angles for both rotors are higher at the hub region owing to the flow separation at the driving motor which caused the increased pressure loss.

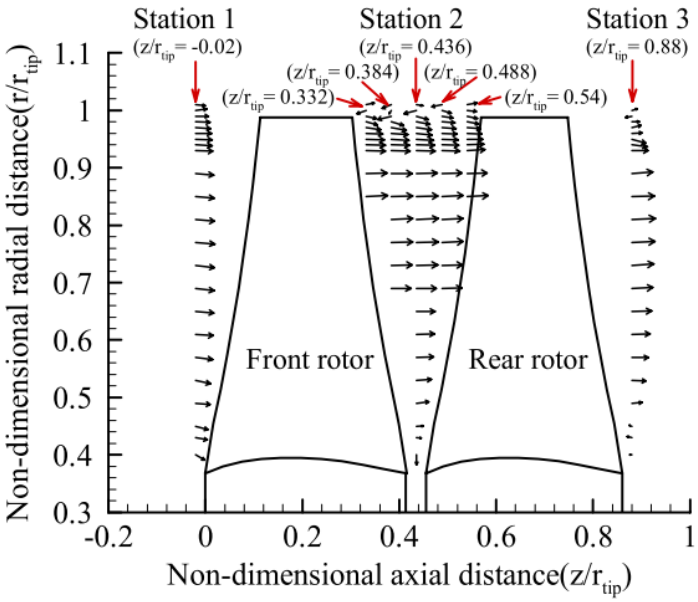

Figure 1.9: Circumferential Averaged axial and radial velocities in contra-rotating axial fans[36]

Parameter influence of CRS

Research about parameter influence of counter rotating parameters is mainly focused on two categories:

- rotating speed ratio θ;
- axial spacing S between the Front Rotor and Rear rotor

After exploring the performance and flow features of CRS pumps and fans at a fixed axial spacing and equal rotating speed, Shigemitsu *et al.* [37] investigated the influence of blade row distance on the static pressure and velocity field of small-size contra rotating axial fans, by both experiments and numerical simulation. They observed from static pressure rise curves that the static pressure had almost no changes as $S < 30$ mm, but decreased with higher S. Moreover, S had a larger influence on static pressure rise at partial flow rate than at design flow rate. S had a slight influence on the static pressure rise of front rotor, but gradually decreased the static pressure of rear rotor as S was larger than 30 mm. It could be concluded that there is a limit axial distance, beyond which the performance deteriorates. On the other hand, they used a one-hole cylindrical pitot tube to measure the axial and circumferential velocity at inlet, 5 mm upstream of the RR, and outlet of the same CRS fans, as axial distance increased from 10 to 100 mm at design flow rate. They found that S had little influence on the inlet flow of CRS by experimental results at design flow rate. Between the FR and RR, the drop in dynamic pressure at

different S was calculated then compared to its decrease of static pressure, to see the portion of this loss in total loss. It was found that the frictional loss could be the main reason for the loss in stage static pressure at large axial distance, by the decrements of circumferential velocity between the FR and RR. After the RR, small difference of axial and tangential velocities were obtained at S changed. Additionally, numerical results showed that when S varied from 10 to 30 mm, influence of Rear Rotor on the pressure distribution of the Front Rotor decreased. Therefore, they concluded that the blade row distance of 30 mm (1.27 chord length of front rotor at the tip) was an appropriate distance in terms of the performance and pressure interaction.

In the early 1990s, Pundhir et Sharma [1] presented the experimental investigation on the effect of speed ratio and axial spacing on the aerodynamic performance of an axial contra-rotating compressor. They investigated the performance of contra stage at three speed ratios and two settings of axial gaps. Then concluded that:

- An increase in speed ratio could bring in an improvement in the stage pressure rise and stage through flow capacity.
- The increased speed ratio could make the stall point shift towards a lower flow rate. However, an increased axial spacing would make the stall point shift towards a higher flow rate.
- The increased speed ratio improved the flow structure at lower portion of blade downstream of the first rotor, by decreasing both the absolute and relative outlet flow angles and increasing axial velocity at this region. While an increased axial gap resulted in the deterioration of blade element efficiency in the lower half span of the first rotor and all blade span of the second rotor.

Mistry et Pradeep [3] found that a higher rotational speed in rear rotor could improve the operating range and efficiency, according to the former studies in literature. But very limited published literature could be found on the effects of axial spacing in counter rotating fans/compressors. Several researchers have found that lower axial distance helped in suppressing the stall on the first rotor and was beneficial for performance improvement. They summed up writing that for earlier published literature an axial spacing of 50% chord is optimum for the low aspect ratio blades (of order of 1.0). For high aspect ratio blade (3.0), the optimal axial spacing was different. They measured the total pressure ratio, velocities and flow angles by total pressure probe rake, 4-hole probe and a kiel probe rake, at upstream, between and downstream the rotors of counter rotating axial fans. They found that the higher rotational speed of the second rotor could generate a strong suction effect and improve the performance of the stage. At design speed combination, the axial spacing had slight influence on the performance. The optimum axial spacing changed with the speed combinations of the two rotors, which was 0.9 chord for design speed combination of two rotors but 0.7 chord at off design speed combinations of rotors. Additionally, two stall zones are detected: partial stall (second rotor on stall) and full stall (both rotors on stall), while the first rotor is considered to be stall free.

Following the research work on the performance and flow fields on contra rotating axial pumps by Shigemitsu *et al.* [34] and Momosaki *et al.* [35], Cao *et al.* [4] proposed a way to improve the hydraulic and cavitation performance in contra-rotating pumps by designing

the lower speed of rear rotor. Three CRS were designed and simulated by CFX. Then only one of them was constructed and investigated experimentally. This article firstly presented the axial (V_z) and tangential (V_θ) velocity fields at outlet of the front rotor. It indicated that V_z at tip region decreased instead of being constant and the incidence angle was negative at inlet of the rear rotor. So they proposed to consider a forced vortex at the tip region and a positive incidence angle at all blade span for the design of near rear rotor. Besides, they found in literature that the secondary flow could be controlled if they loaded the leading edge at the tip and loaded trailing edge at the hub. So they took into account of the variation the maximum camber location in the new rear rotor. Additionally, considering the cavitation, all the new rotors turned more slowly than the old rear rotor (mentioned in Ref. [35]), and the front rotor remained the same but turned faster than that of an old CRS pump. The simulation results showed that the new CRS named RR3-Z both considering the forced vortex at the tip and various maximum cambers had the best hydraulic and cavitation performance. Then they constructed RR3-Z and measured them experimentally. The new CRS pump showed higher head and efficiency at higher flow rates.

Further, Cao *et al.* [38] conducted detailed investigation of the effect of rotating speed of the rear rotor on the pressure field of the front rotor on the new contra rotating axial pump (RR3-Z), by comparing the static pressure fluctuation obtained by experiments and simulation. The results in both experiments and simulation showed a good agreement in tendency, which indicated the CFD could be an available method to estimate the blade row interaction. They concluded that the new rear rotor which turned more slowly could reduce the static pressure drop from the front rotor outlet to rear rotor inlet at partial flow rate. In addition, the amplitude of Blade passing frequency in static pressure fluctuation decreased rapidly downstream but reduced gently upstream for all the front and rear rotors. Therefore, the blade row interaction was mainly characterised by the BPF of the rear rotor. The slower new rear rotor showed a much lower amplitude at the pressure field between the rotors and in front rotor. Hence, the reduced rotating speed of the rear rotor could weaken the blade row interaction, mainly due to the rear rotor influence on the front rotor.

1.5 Conclusion

The chapter shows the complex flow structures due to tip clearance flow, rotor stator interactions which are closely related to loss in the conventional subsonic axial turbomachines. In counter rotating stage, these three-dimensional effects are exacerbated by the rotor-rotor interactions. The bibliography studies prove the low speed counter rotating machines (compressors, pumps, turbines, small fans) do have a higher performance, as well as providing a much greater through flow capacity than a rotor stator stage. The parameter influences are mainly focused on the axial distance (S) and speed ratio (θ) between the two rotors.

However, for different configurations, the results of parameter influences are not the same. For the CRS pump, a slower Rear Rotor (RR) is suggested in terms of the cavitation in RR [29][4]. However, the larger speed ratio could improve the stage pressure rise and flow structures, owing to the increased suction effects of Rear Rotor (RR) [1][3].

On the other hand, the increased axial distance deteriorates the efficiency for a compressor stage [1]. On the contrary, an appropriate axial distance is suggested by observing in a small-sized CRS fans in terms of the performance and pressure interaction [37].

The studies on CRS "HSN" in Dynfluid laboratory [5] shows the performance does not significantly vary with S when S is below twice the FR chords. And an optimal θ could be found.

To sum up, only a few studies have investigated the parameter influence in sufficient variations to provide a comprehensive understanding of their basic characteristics. Quite surprisingly, very few have considered the outlet flow characteristics of the FR in the design of the RR. Moreover, none of them have investigated the work distribution between the FR and RR, which is one of the important parameters for the design of the CRS. Therefore, the following work will focus on the study of three counter rotating axial fans intended to achieve the same design point with different distributions of load.

Chapter 2

Experimental facilities and methods

This chapter is dedicated to the experimental facilities and methods, as well as the uncertainty of measurements. It is divided into four sections. Firstly, the test bench is introduced briefly, followed by the measurement methods. Then the design process for counter rotating rotors is presented. Last, the experimental uncertainty analysis is given in detail.

2.1 Test rig

The experimental investigations are performed in a test rig, named AERO2FANS, built according to the ISO-5801 standard. A considerable amount of research about this test rig has been conducted in the previous work in DynFluid laboratory [5]. Therefore, only a summary is given here. For easy understanding, the schematic diagram of test rig is shown in Fig. 2.1. First, the air comes into the test pipe of diameter D = 380 mm through a bell mouth, then passes through the driving motor of the Front Rotor, and is homogenized by a honeycomb. Next, energy is transferred to the fluid by the Counter Rotating Stage (CRS). The axial distance S between Front rotor (FR) and Rear Rotor (RR) can be modified by a series of blocks (Fig. 2.2). Then, the flow passes the driving motor of the Rear Rotor and an anti-gyration device to remove the rotational component of the flow, before the measurement of the static pressure by 4 pressure taps. After that, the fluid goes through an ISO-5167 orifice plate in order to measure the volume flow rate (Q_v). Finally, the fluid is regulated by an axial blower and an iris damper before being discharged into the ambient atmosphere.

2.2 Quantities of interest

The present research focuses on three types of measurements: global performance, velocity field and wall pressure fluctuations. The global performance consists of the static pressure rise ΔP_s and the static efficiency η_s as a function of the volume flow rate Q_v.

Volume flow rate measurement. In the present research, the volume flow rates are measured by an ISO-5167 orifice plate, 15D downstream the CRS. The detailed calculation methods will be presented later in this chapter.

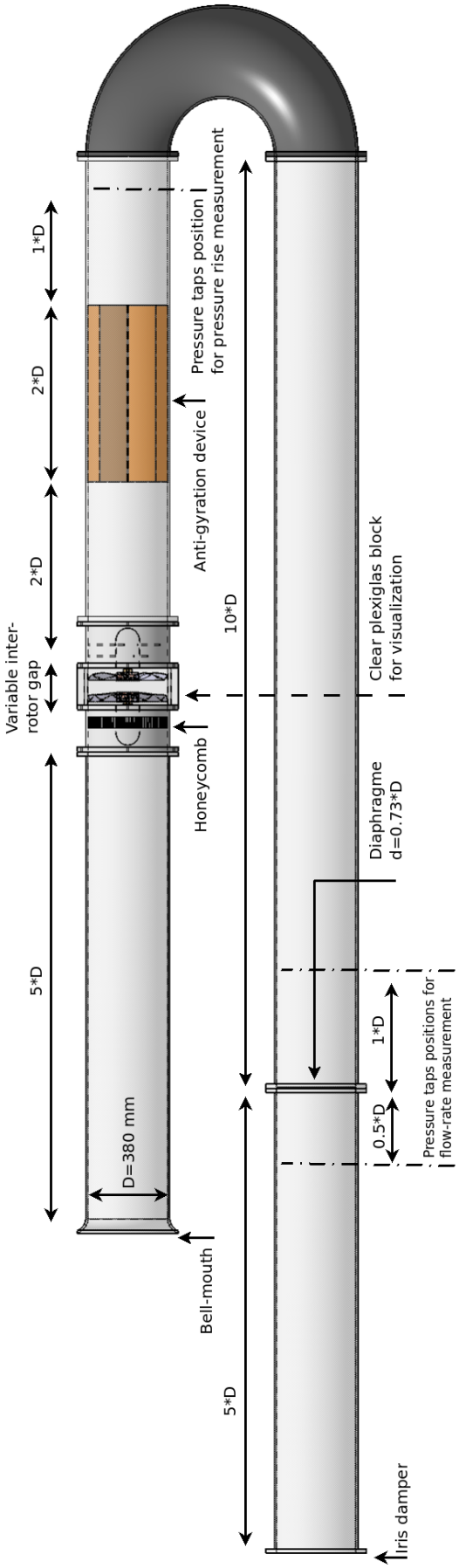

Figure 2.1: Schematics of test rig : AERO2FANS [5]

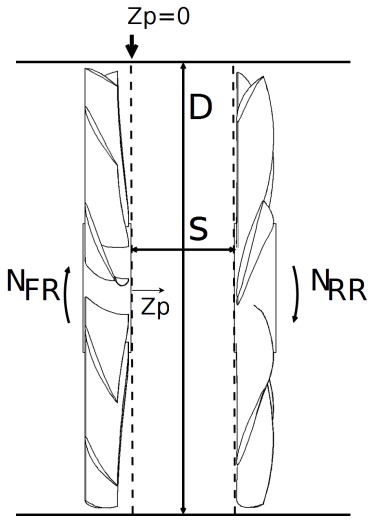

Figure 2.2: Sketch of the CRS arrangement that is considered in the present paper, showing the coordinate system and the main dimensions. The front rotor (FR) is on the left, and the rear rotor (RR) is on the right. The bold arrow stands for the microphone (position $Z_p = 0$ mm).

Static pressure rise ΔP_s. According to standard ISO-5801, the static pressure rise is defined as the difference between the static pressure downstream of studied machine and total pressure at the inlet (atmospheric pressure):

$$\Delta P_s = P_{s,CRS} - P_a \tag{2.1}$$

Static efficiency η_s. Static efficiency is defined as :

$$\eta_s = \frac{\Delta P_s Q_v}{(\tau_{FR}\omega_{FR}) + (\tau_{RR}\omega_{RR})} \tag{2.2}$$

The torque τ is measured by the drivers of motors and has been calibrated against a rotating torquemeter [5].

Velocity measurement: V_z and V_θ. Instantaneous velocities are measured at a fixed point by Laser Doppler Velocimetry (LDV), in the axial and tangential directions. Then the circumferential averaged velocities could be obtained at this point, denoted as V_z (axial) and V_θ (tangential). In the present research, a series of points along radial directions are measured in different axial positions of the configurations.

Wall pressure fluctuations. The casing wall pressure fluctuations are recorded by a 40BP pressure microphone, which has been calibrated by an acoustic calibrator. Then the power spectral density and total average power of the pressure fluctuations are calculated and compared.

2.3 Design of the counter rotating Stages (CRS)

Aside from the test rig, another important experimental facility is the Counter Rotating Stage (CRS). Most studies in the conception of axial flow fans have focused on single or traditional rotor-stator stage. However, to the best of our knowledge, no mature conception method exists for the design of subsonic ducted CRS. The previous work experience on design of CRS in DynFluid Laboratory [5], provides an essential platform to the present research. In view of the preceding research in Ref. [5], an original method to design the CRS has been developed and validated on a first prototype. The influences of the axial distance S and of the rotational speed ratio $\theta = \frac{N_{FR}}{N_{RR}}$ have been investigated on this configuration. For this prototype, named HSN, the distribution of load between FR and RR is chosen randomly. Nevertheless, this is an important parameter for the design of a CRS. Therefore, more configurations with different distributions of load need to be developed. Besides, the results show that the slope of global performance curves of initial CRS HSN is quite flat and similar to that of the Front Rotor only. But the relationship of slope of stage and front rotor only is not sure with just one configuration. So the slopes of front rotor of new configurations need to be varied as well.

2.3.1 Methodology

The objective is to design three CRS which can achieve the same design point for various distributions of the total load between the front and rear rotors. The design point is presented in Tab. 2.1. In this table, the total pressure rise is the difference of *total pressure* between the inlet and the outlet of the CRS. One of the design constraint is to have a pure axial flow downstream of the CRS. Therefore, the corresponding expected *static* pressure rise is calculated as $\Delta P_{sC} = \Delta P_{tC} - \frac{1}{2}\rho_a(\frac{Q_{vC}}{\pi D^2/4})^2 \approx 373$ Pa.

D (mm)	R_{tip} (mm)	R_{hub} (mm)	ΔP_{tC} (Pa)	Q_{vC} ($m^3.s^{-1}$)
380	187.5	65	420	1

Table 2.1: Design point for air at $\rho_a = 1.21$ $kg.m^{-3}$.

The details of the conception method can be found in Ref. [6]. The outlines could be depicted as follows. In the first place, the front rotor was designed to achieve a part of the total pressure rise at design flow rate, by the in-house code MFT [39]. The geometrical parameters of the FR are given by MFT with the inverse method. In the second place, the axial and tangential velocities at the outlet of the FR are analyzed and taken as the input conditions for the conception of the RR. Therefore, the RR is adapted to the outflow of the FR predicted by MFT. Moreover, RR is designed such that the absolute tangential velocity at the outlet of the system vanishes. Based on this, the angular velocity of RR is estimated to match the rest part of the total pressure rise.

2.3.2 Characteristics of the three different CRS

The main parameters can be found in Tab. 2.2 and Fig. 2.3. The distribution of load is defined as the ratio of the total pressure rise due to the Rear Rotor to that of the Counter-

Rotating System at the design flow rate: $L_C = \frac{\Delta P_{t,RR}}{\Delta P_t}$. All the three CRS have different L_C at the same design point. The Front Rotors of the three systems are designed with the same blade loading repartition, with a "Constant Vortex" Design (see Refs. [40, 41]). The peculiar features of each system are the following:

JW1. The Front Rotor of JW1 is designed to have large stagger angles, in order to obtain a steep curve of static pressure rise ΔP_s as a function of the volume flow rate Q_v (see Fig. 2.3). Aside from this, the other parameters (rotation rates and ratio θ) are very similar to those of the configuration that was studied in Ref. [6].

JW2. Among the three CRS, JW2 has the highest L_C = 52%, that is to say, in this Counter-Rotating System, the Rear Rotor transfers more energy to the fluid than the Front Rotor. Consequently, the Front Rotor of JW2 possess the lowest ΔP_s among the three Front Rotors. It is furthermore designed with low stagger angles and has a slowly decaying characteristics (see Fig. 2.3). The Rear Rotor rotates 1.44 times faster than the Front Rotor in that configuration.

JW3. This is an extreme case where the Front Rotor of JW3 leads to the highest and steepest characteristics, as shown in Fig. 2.3. As a result, JW3 has the lowest L_C = 23% among the three configurations, and the Rear Rotor rotates much more slowly than the Front Fotor.

	N_{FR}/N_{RR} (rpm)	θ_C	L_C %	Z_{FR}/Z_{RR}	γ_{FR}
JW1	2300/2200	0.96	41	10/7	large
JW2	1800/2600	1.44	52	13/7	small
JW3	2600/1100	0.42	23	10/7	large
HSN	2000/1800	0.9	38	11/7	small

Table 2.2: Design parameters of the three CRS JW1, JW2 JW3 and Initial CRS HSN.

Additionally, please note that since the Rear Rotors are designed to rectify the outflow of the Front Rotors toward the axial direction, the shape of the Rear Rotors that are obtained is not usual, with non-monotonic stagger angle and blade camber profiles (see Fig. 2.4 for an example on the Rear Rotor of JW1).

Finally, the main parameters of three spanwise sections for JW1, JW2 and JW3 are presented in Tab. 2.3. An example of the CRS prototype (JW1) is shown in Fig. 2.5.

It could be seen from Tab. 2.3 that for the RRs, the stagger angles at the hub are as high as at the tip but relatively smaller at midspan, which is different to the conventional design. Furthermore, the Reynolds numbers in RRs are much higher than those of their FR except at midspan of JW3. Then for FRs, the Re of JW1 and JW3 are in the order of 1.3×10^5, which are much higher than that of RR in JW2 by 8.0×10^4. And for RRs, the Re of JW1 and JW2 are 1.7×10^5 and 2.0×10^5, which is relatively higher than that of JW3 by 1.2×10^5. Moreover, the Re is decreased significantly at the hub of all the rotors, mainly in the order of 10^4. As we know, this low Re could induce loss in the hub region.

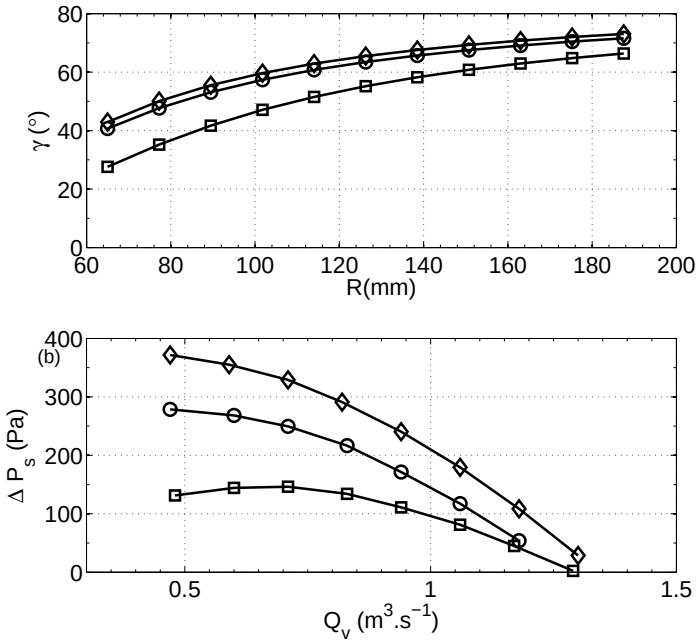

Figure 2.3: Conception by MFT [39], Front Rotor of JW1 (∘); JW2 (□) and JW3(◇). (a): radial profile of the stagger angle and (b): static pressure rise calculated by a semi-empirical model [39].

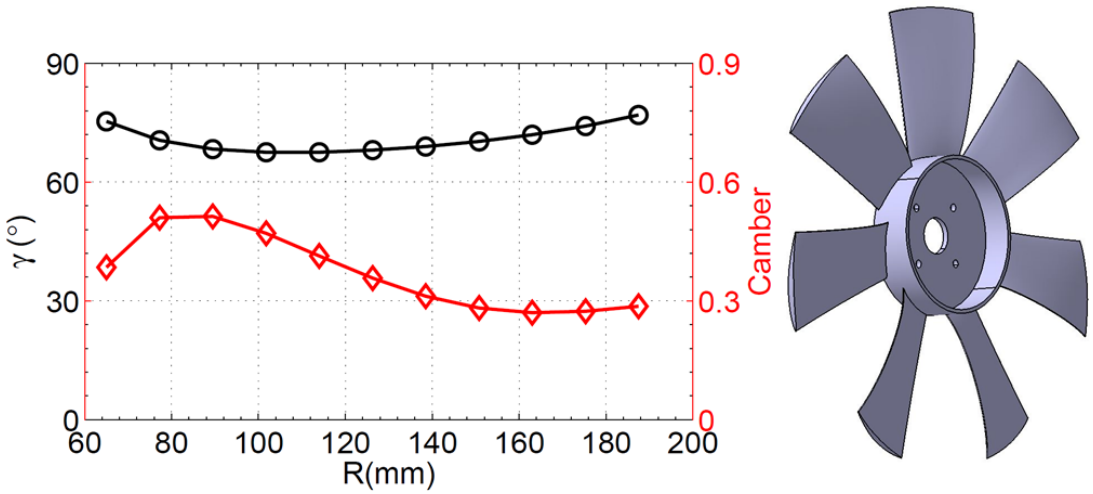

Figure 2.4: Radial profiles of the stagger angle (∘) and of the aerodynamic camber (◇, see Ref. [41] for a definition) for the Rear Rotor of JW1.

		R (mm)	γ (°)	L_{chord} (mm)	σ	$\mathcal{D}$	Profile	Re
FR of JW1	hub	65	40.7	47.2	1.2	0.55	NACA 65(15)11	5.9×10^4
	midspan	126.5	63.5	54.6	0.7		NACA 65(08)09	1.3×10^5
	tip	187.5	71.6	62.0	0.5	0.37	NACA 65(06)08	1.7×10^5
FR of JW2	hub	65	27.6	42.5	1.4	0.57	NACA 65(21)12	4.6×10^4
	midspan	126.5	55.2	44.3	0.7		NACA 65(14)11	8.0×10^4
	tip	187.5	66.4	46.1	0.5	0.52	NACA 65(10)11	1.1×10^5
FR of JW3	hub	65	42.9	43.0	1.1	0.62	NACA 65(17)12	5.9×10^4
	midspan	126.5	65.5	51.1	0.6		NACA 65(09)10	1.4×10^5
	tip	187.5	73.1	59.2	0.5	0.39	NACA 65(07)08	1.8×10^5
RR of JW1	hub	65	75.3	49.2	0.8	0.68	NACA 65(04)12	9.0×10^4
	midspan	126.5	68.1	67.3	0.6		NACA 65(04)09	1.7×10^5
	tip	187.5	76.9	85.4	0.5	0.37	NACA 65(03)07	3.1×10^5
RR of JW2	hub	65	74.9	48.6	0.8	0.52	NACA 65(03)12	8.9×10^4
	midspan	126.5	70.8	67.1	0.6		NACA 65(03)09	2.0×10^5
	tip	187.5	78.3	85.6	0.5	0.31	NACA 65(02)07	3.5×10^5
RR of JW3	hub	65	66.9	53.6	0.9	0.44	NACA 65(04)11	7.9×10^4
	midspan	126.5	55.3	70.1	0.6		NACA 65(10)09	1.2×10^5
	tip	187.5	68.6	86.6	0.5	0.63	NACA 65(07)07	2.0×10^5

Table 2.3: Design parameters of the three CRS. R radius; γ stagger angle; L_{chord} chord length; σ solidity; $\mathcal{D}$ diffusion factor ; NACA65(xx)yy with xx standing for the relative camber and yy representing the relative thickness(Ref.[6]); Re is calculated by relative velocity, chord length on each radius at the design flow rate $Q_v = 1m^3.s^{-1}$.

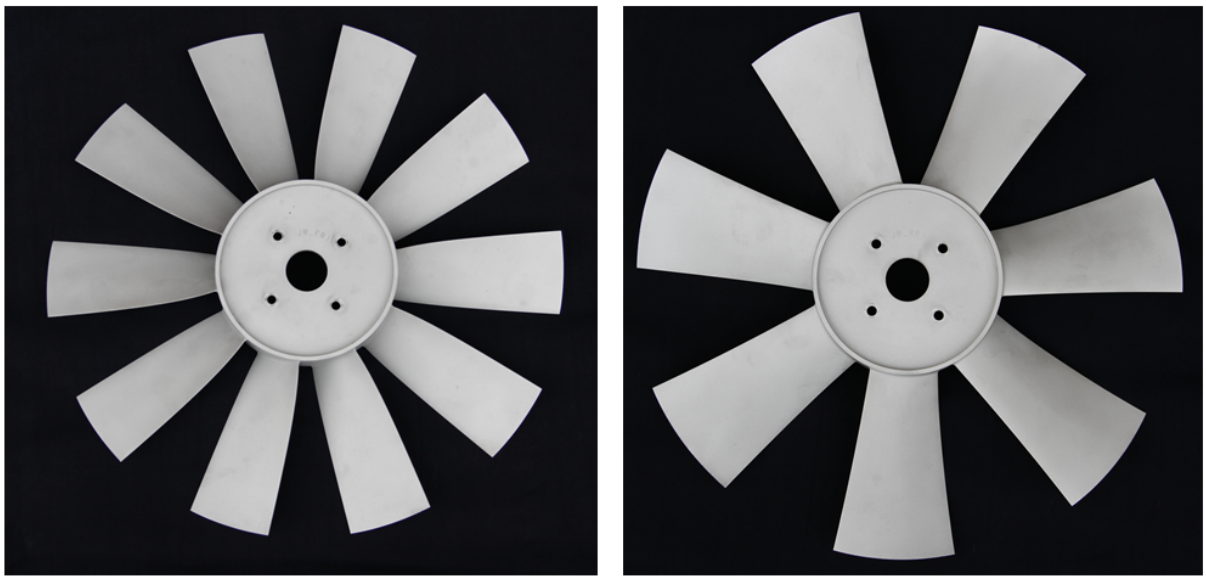

Figure 2.5: Prototype of JW1.

2.3.3 Limitations of the Conception Method

This part of the thesis will present the limitations of the conception method for CRS.

The first limitation is the absence of an analysis of performance of the entire stage. For the FR, the total pressure is calculated by MFT. In MFT, the total pressure is determined by global efficiency, which is related to the form loss and wall loss. But for the RR, total pressure is estimated by Euler equation for a perfect fluid then multiplied by an empirical factor. This is a coarse estimation. Therefore, it would be useful for designer to add an analysis of performance of RR in MFT.

The second limitation is that no rotor-rotor interaction is considered. In the conception process, it is supposed that the flow in both FR and RR are not modified, for the purpose of simplification. In fact, numerous studies have attempted to explain the interactions between two blade rows and its relation to loss. On one hand, it is known that the wake was an important loss source for turbomachine. In CRS, with a normal axial spacing, downstream of the trailing edge of first blade row, the wake may be modified by RR. On the other hand, the RR could influence the flow field of the FR through potential effects.

No influence of axial distance between rotors are taken accounted. As we known, axial distance is an important parameter for traditional rotor stator stage [42][43]. For the conception of CRS, the velocity flow fields at inlet of the Rear Rotor(RR) are considered the same as those of outlet of Front Rotor(FR). In reality, the velocity field would change with distance due to the mixing of wake. Then this assumption could be less appropriate as the distance increases.

2.4 Experimental method and uncertainties

To interpret the experimental results correctly, it is essential to indicate the uncertainty. Generally, uncertainty is a measurement range of possible true values. In this section, all the variables are expressed on two parts: estimated true value and its uncertainty. For a quantity x which is measured directly, the estimated true value is represented by the mean value of N repeated measurements:

$$\bar{x} = \frac{1}{N}\sum_{i=1}^{N} x_i \tag{2.3}$$

The uncertainty is represented by the standard deviation of the repeated values :

$$\sigma_x = \sqrt{\frac{1}{N-1}\sum_{i=1}^{N}(x_i - \bar{x})^2} \tag{2.4}$$

When a measurement is repeated several times, normally, it can be noticed that the measured values are likely to fall near the average. This is a normal or Gaussian distribution. In this case, 68% of the measured values are falling within $\pm\sigma_x$ from the mean, and 95% are within $2\sigma_x$ from the mean. The uncertainty given here is also named as absolute uncertainty e. It means that for the quantity measured directly, $e = \sigma_x$.

Another way to express uncertainty is relative uncertainty(ϵ), defined as the absolute uncertainty divided by the estimated true value. Usually, ϵ is given in percentage form.

For the repeated measurements:

$$\epsilon_x = \frac{\sigma_x}{\bar{x}} \tag{2.5}$$

Likewise, for the quantity which is determined by several variables, the first part is calculated by the mean values of these variables. And the second part is computed by the combination of uncertainties, according to the simplified error propagation functions. In the present research, the simplified error propagation rules are listed in Tab. 2.4.

Functions	e	ϵ
$f = x \pm y$	$e_f = e_x + e_y$	$\epsilon_f = \frac{e_x + e_y}{\lvert f \rvert}$
$f = xy$ or $f = x/y$	$\frac{e_f}{\lvert f \rvert} = \frac{e_x}{\lvert x \rvert} + \frac{e_y}{\lvert y \rvert}$	$\epsilon_f = \epsilon_x + \epsilon_y$
$f = kx$	$e_f = \lvert k \rvert e_x$	$\epsilon_f = \epsilon_x$
$f = x^k$	$\frac{e_f}{\lvert f \rvert} = \lvert k \rvert \frac{e_x}{\lvert x \rvert}$	$\epsilon_f = \lvert k \rvert \epsilon_x$

Table 2.4: Simple error propagation rules: f, x, y are variables, k is constant, e is absolute uncertainty and ϵ is relative uncertainty

The following part of this section is divided into three parts. First part discusses uncertainties related to global performance. It is based on the repeated measurements of JW2 at the design point. The second part presents the uncertainties analysis of the measured quantities in LDV. It is founded on repeated measurements at 7 different radial positions. And the third part focus on the measurements of the wall pressure fluctuation by a microphone.

2.4.1 global performance

Estimation of uncertainty for global performance is based on the repetition of measurements of JW2 at the design point. Specifically, ten measurements have been performed at the same rotation rates and for a fixed diameter of the iris damper. For simplicity, the mean value is denoted as the quantity itself, $\bar{x} = x$.

The repeated results for the measured quantities are presented in Fig. 2.6. It can be noticed that the dry temperature increased monotonically with the time. Aside from this, the torques are distributed almost randomly. In the following part, uncertainty analysis are conducted on these repeated measurements.

Measured quantities

Atmospheric pressure P_a. The values of P_a is given by meteociel [44]. As the repeated experiments are performed in a short time, the values could be noted as: $P_a = 100880 \pm 100$ Pa.

Dry temperature T_{seche}. The dry temperature is measured at the inlet of test rig, by Fluke 51 Series II thermometers, with accuracy 0.05%+0.3° C. According to the repeated measurement, the dry temperature is $T_{seche} = 290.0 \pm 0.4$ K.

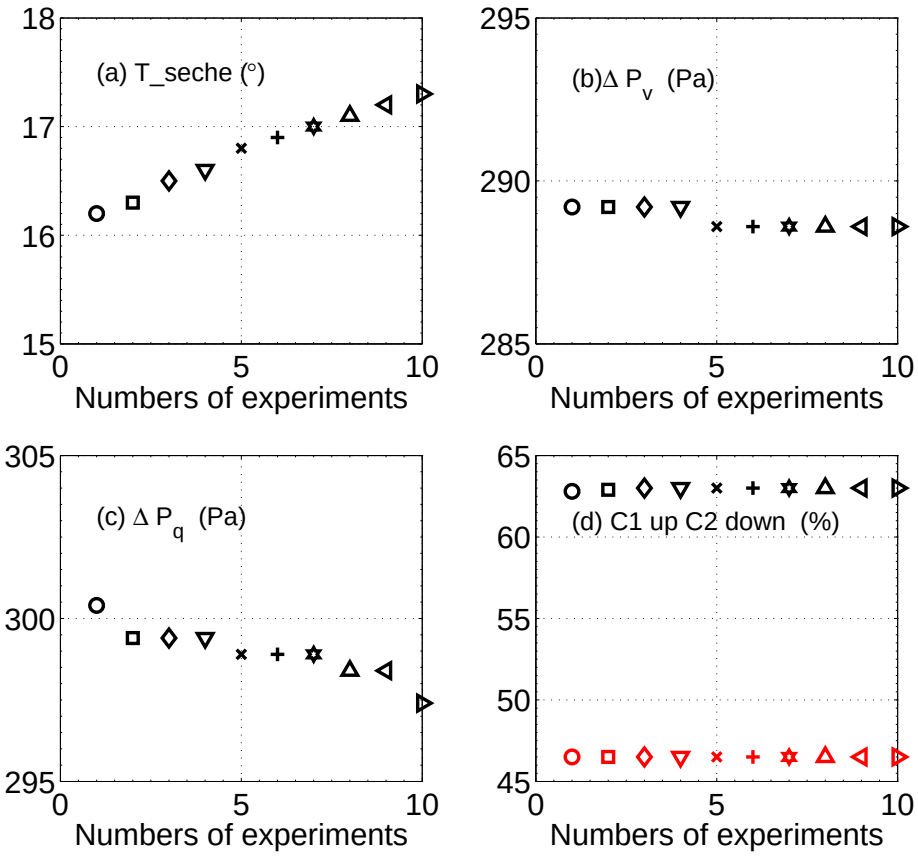

Figure 2.6: The repeated results of JW2 for the variables measured directly (a) T_{sech} vs. *Sequence number of tests; (b) ΔP_v* vs. *Sequence number of tests; (c) ΔP_q* vs. *Sequence number of tests; (d) $C1$ and $C2$* vs. *Sequence number of tests.*

Pressure drop through orifice plat ΔP_q. The pressure drop is measured by the difference of pressure taps between upstream and downstream an ISO-5167 orifice plat. These pressure taps are connected to a differential pressure transmitter FCO318, scaled at ±2.5 kPa. The accuracy of transmitter is not constant, by $< 0.25\%$ of reading. At the design flow rate, ΔP_q is around 300 Pa, which means 0.7 Pa of uncertainty. According to the repeated measurements, $\Delta P_q = 299.0 \pm 1.2$ Pa.

Static pressure rise without correction: ΔP_v The static pressure rise without correction, is also measured by the same FCO318, which is linked with 4 pressure taps at 1D downstream the anti-gyration device. This anti-gyration device permits to remove the tangential part of energy in the flow. Therefore downstream the anti-gyration device, the fluid could be considered as axial and uniform. Hence, the averaged pressure measured at casing wall could represent the averaged static pressure in this cross section. [5]. The value given by the transmitter, is the difference between the average static pressure downstream of stage and the atmospheric pressure. The pressure difference contains the static pressure rise generated by CRS and loss in the test bench. Based on the repeated measurements, $\Delta P_v = 288.8 \pm 0.7$ Pa. On considering about the accuracy of transmitter at all range of measurement, the absolute uncertainty could increase to 1.0 Pa. This means $\Delta P_v = 288.8 \pm 1.0$ Pa.

Torque for motors of FR $C1$ and RR $C2$ The torques of motor are measured by the servo-controllers of the two brush-less AC motors and have been calibrated against a rotating torquemeter. According to the repeated results, $C1 = 63.0 \pm 0.2$ and $C1 = 46.5 \pm 0.2$. These values are expressed as a percentage of the nominal torque, which is 2.4 N.m.

All the measured quantities and their absolute and relative uncertainties are listed in Tab. 2.5.

Quantities	mean value	absolute uncertainty e	relative uncertainty ϵ (%)
Pa (Pa)	100880	100	0.1
T_{Seche} (K)	290	0.4	0.1
ΔP_q (Pa)	299.0	1.2	0.4
ΔP_v (Pa)	288.8	1.0	0.3
$C1$ (%)	63.0	0.2	0.3
$C2$ (%)	46.5	0.2	0.4

Table 2.5: Mean values and uncertainties for quantities measured directly, according to the 10 *repeated experiments in Fig. 2.6.*

Derived quantities

Density of air ρ_a. The static pressure rise and the power consumption vary with the density of air ρ_a. To compare and interpret result correctly, it is important to take account of the density of air for each experiment. The actual density is evaluated according to the ISO-5801 standard, by measuring the atmospheric pressure P_a, the dry temperature

T_{ad} and the wet temperature T_{aw}, from which the partial pressure of the water vapor P_{av} is computed.

$$\rho_a = \frac{P_a - 0.378P_{av}}{287T_{ad}} \tag{2.6}$$

According to the repetition of measurements and simple propagation of uncertainty rules, the relative uncertainty of ρ_a is computed as:

$$\begin{aligned}\epsilon_{\rho_a} &= \epsilon_{(P_a - 0.378P_{av})} + \epsilon_{T_{ad}} \\ &= \frac{100 + 0.378 \times 37}{100880 - 0.378 \times 1130} + \frac{0.4}{290} \\ &\approx 0.0011 + 0.0014 = 0.0025 = 0.25\% \approx 0.3\%\end{aligned}$$

then $\rho_a = \frac{100880 - 0.378 \times 1130}{287 \times 290} = 1.21 \pm 0.3\%$.

Volume flow rate Q_v. The volume flow rate is measured by an ISO-5167 orifice plat situated at more than $15D$ downstream of the CRS. According to the standard:

$$Q_v = \frac{\alpha \epsilon \pi d^2}{4} \sqrt{2 \frac{\Delta P_q}{\rho_a}} \tag{2.7}$$

For the repeated experiments, the uncertainty of α and ϵ are $\alpha = 0.727 \pm 0.000018$ and $\epsilon = 0.999 \pm 0.000005$. It is obvious that α and ϵ could be considered as constants: $\epsilon_\alpha = \epsilon_\epsilon = 0$.

Based on the Eqn. 2.7, near the design point, the uncertainty of Q_v is $\epsilon_{Q_v} = 0.5 \times (\epsilon_{\Delta P_q} + \epsilon_{\rho_a}) = (0.5 \times (0.4 + 0.3))\% \approx 0.4\%$. And $Q_v = \frac{0.727 \times 0.999 \times 3.14 \times 0.28^2}{4} \sqrt{2 \frac{299.0}{1.21}} = 0.994$, so $Q_v = 0.994 \pm 0.4\%$.

Correction for the losses $Corr$. In order to eliminate the influence of the experimental facilities such as the honeycomb, the driving motor housing and the anti-gyration device, the static pressure drop is measured with both the Front and Rear Rotors removed. Meanwhile, the axial blower at the outlet of the test rig was used to create a flow. Then the correction $Corr$ is modeled as a function of the orifice plate pressure drop ΔP_q. At the design point, considering about the accuracy of transmitter, the absolute uncertainty of $Corr$ is about ± 1.0 Pa and the mean value is 116.2 Pa, which means the relative uncertainty is $\epsilon_{Corr} = \pm 0.9\%$.

Static pressure rise ΔP_s. The static pressure rise ΔP_s is the difference between the static pressure downstream of the CRS and the inlet total pressure:

$$\Delta P_s = \Delta P_v + Corr - \frac{1}{2}\rho_a \left(\frac{Q_v}{\pi D^2/4}\right)^2, \tag{2.8}$$

at design point:

$$\begin{aligned}\epsilon_{\Delta P_s} &= \frac{e_{\Delta P_v} + e_{corr} + e_{\frac{\rho_a Q_v^2}{2A_2^2}}}{\Delta P_v + corr - \frac{\rho_a Q_v^2}{2A_2^2}} \\ &= \frac{1.0 + 1.0 + (0.003 + 2 * 0.004) * 1.21 * 0.994^2 * 38.91}{288.8 + 116.2 - 38.91 * 1.21 * 0.994^2} \\ &= 0.007 = 0.7\%\end{aligned}$$

To eliminate the influence of density of air, the static pressure rise is rescaled to the reference density. $\Delta P_s' = \frac{\Delta P_s}{\rho_a} \times \rho_{ref}$, so $\epsilon_{\Delta P_s'} = \epsilon_{\Delta P_s} + \epsilon_{\rho_a} = (0.7 + 0.3)\% = 1\%$. Then the absolute uncertainty of rescaled ΔP_s is about ±4 Pa near the design flow rate.

Power consumption $\mathcal{P}_{w,t}$. The total power consumed by the CRS is defined as:

$$\mathcal{P}_{w,t} = \mathcal{P}_{w,FR} + \mathcal{P}_{w,RR} = \tau_{FR}\omega_{FR} + \tau_{RR}\omega_{RR} \tag{2.9}$$

The torque τ is measured by torque meter integrated in the motor, then corrected by the value measured when the rotor is removed from the shaft.

$$\tau = (C_R - C_{vide}) * 2.4/100 \tag{2.10}$$

Front rotor:

$$\begin{aligned}\epsilon_{\tau_{FR}} &= \frac{e_\tau}{\tau} \\ &= \frac{e_{C_R} + e_{C_{vide}}}{C_R - C_{vide}} \\ &= \frac{0.2 + 0.1}{63.0 - 3.5} = \frac{0.3}{59.5} = 0.005 = 0.5\%\end{aligned}$$

The torque for FR is $\tau_{FR} = 59.5 * 2.4/100 = 1.428 \pm 0.5\%$ N.m. The rotational speed is $N_{FR} = 1800 \pm 2$ rpm $= 1800 \pm 0.1\%$ rpm. Hence, the angular rotational speed is $\omega_{FR} = 188.5 \pm 0.1\%$ rad.s^{-1}. Therefore, the power consumed by FR is $\mathcal{P}_{w,FR} = \tau_{FR} * \omega_{FR} = 1.428 * 188.5 = 269.2$ W. The relative uncertainty is $\epsilon_{\mathcal{P}_{w,FR}} = \epsilon_{\tau_{FR}} + \epsilon_{\omega_{FR}} = (0.5 + 0.1)\% = 0.6\%$.

Rear rotor:

$$\begin{aligned}\epsilon_{\tau_{RR}} &= \frac{0.2 + 0.1}{46.5 - 4.7} \\ &= \frac{0.3}{41.8} = 0.0072 = 0.7\%\end{aligned}$$

The torque for RR is $\tau_{RR} = 41.8 * 2.4/100 = 1.003 \pm 0.7\%$ N.m. The rotational speed is $N_{RR} = 2600 \pm 2$ rpm$= 2600 \pm 0.1\%$ rpm, $\omega_{RR} = 272.3 \pm 0.1\%$ rad.s^{-1}. The power consumed by RR is $\mathcal{P}_{w,RR} = \tau_{RR} * \omega_{RR} = 273.1$ W. The relative uncertainty is $\epsilon_{\mathcal{P}_{w,RR}} = (0.7+0.1)\% = 0.8\%$

For the stage, the total power consumption is

$$\begin{aligned}\mathcal{P}_{w,t} &= \mathcal{P}_{w,FR} + \mathcal{P}_{w,RR} \\ &= 269.2 + 273.1 = 542.3\ W\end{aligned}$$

And the relative uncertainty is

$$\begin{aligned}\epsilon_{\mathcal{P}_{w,t}} &= \frac{e(\mathcal{P}_{w,FR}) + e(\mathcal{P}_{w,RR})}{\mathcal{P}_{w,FR} + \mathcal{P}_{w,RR}} \\ &= \frac{0.006 \times 269.2 + 0.008 \times 273.1}{542.3} \\ &= 0.007 = 0.7\%\end{aligned}$$

The uncertainties of the total power consumption is ±3.8 W that is 0.7% of the power at the design point. Similarly, to eliminate the influence of density, the power consumption is also rescaled to the reference density $\mathcal{P}_w = \frac{\mathcal{P}_w}{\rho_a} \times \rho_{ref}$. Then the absolute uncertainties for FR, RR and CRS are ±2.4 W, ±3.0 W and ±5.4 W respectively.

Static efficiency η_s. The static efficiency is calculated as:

$$\eta_s = \frac{\Delta P_s \times Q_v}{\mathcal{P}_{w,t}} \tag{2.11}$$

Finally, the relative uncertainty of η_s could be calculated as:

$$\begin{aligned}\epsilon_{\eta_s} &= \epsilon_{\Delta P_s} + \epsilon_{Q_v} + \epsilon_{\mathcal{P}_{w,t}} \\ &= (0.7 + 0.4 + 0.7)\% = 1.8\% \approx 2\%\end{aligned}$$

It should be pointed out that the static pressure rise and power consumption in Eqn.2.11 are the values without the correction of ρ_{ref}. Therefore, the relative uncertainties are slightly smaller than those of the values with the correction.

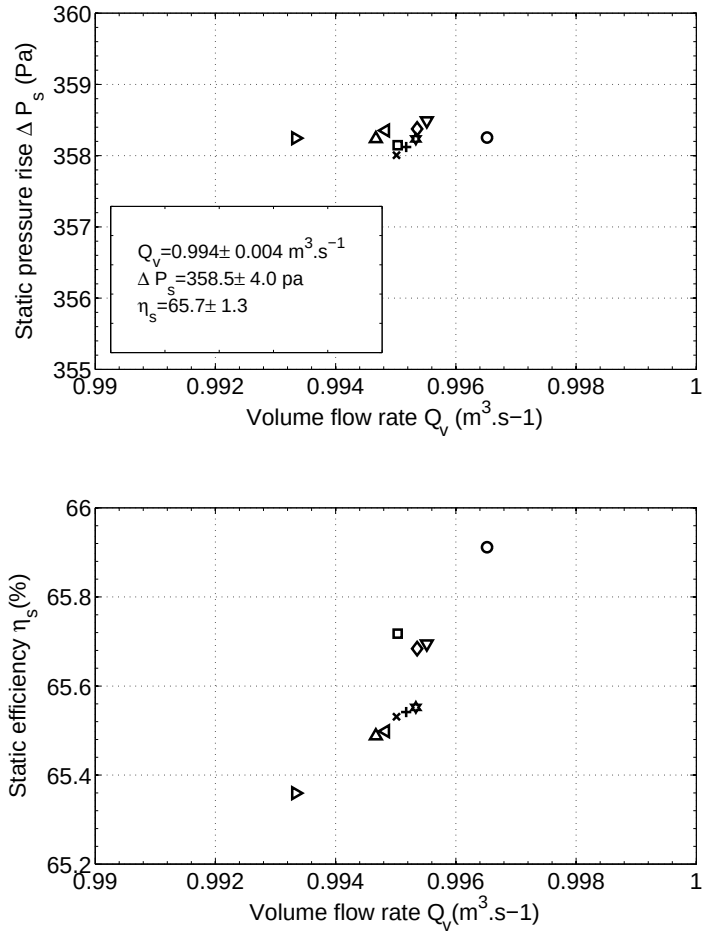

Figure 2.7: The repeated results of JW2 for the derived variables (a)Static pressure rise ΔP_s vs. Volume flow rate Q_v, ΔP_s presented here is rescaled by ρ_{ref}; (b)Static efficiency η_s vs. Volume flow rate Q_v.

The relative uncertainty of η_s is ±2% (around ±1.3 percentage-points at the nominal flow rate). For the repeated experiments, derived ΔP_s and η_s are presented in Fig.2.7 as

a function of the derived volume flow rates Q_v. Similarly, these two variables were also changed randomly with time.

The main derived variables and their relative uncertainties are listed in Tab. 2.6.

Quantities	mean value	absolute uncertainty e	relative uncertainty ϵ (%)
ρ_a (kg.m^{-3})	1.21	0.004	0.3
Q_v (m^3.s^{-1})	0.994	0.004	0.4
ΔP_s (Pa)	358.5	4.0	1.0
$\mathcal{P}_{w,FR}$ (W)	269.2	2.4	0.9
$\mathcal{P}_{w,RR}$ (W)	273.1	3	1.1
$\mathcal{P}_{w,t}$ (W)	542.3	5.4	1.0
η_s (%)	65.7	1.3	2

Table 2.6: Mean values and uncertainties for derived quantities, the values of ΔP_s and $\mathcal{P}_w$ are after correcting by ρ_{ref}

It should be award that all the uncertainty values are estimated value. Due to the simplified propagation rules, the uncertainty of derived variables are slightly overestimated.

2.4.2 LDV

Working principle

The Laser Doppler Velocimetry(LDV) is a technique to measure the velocity in a flow by using the Doppler shift in a laser beam. The working principle of LDV is: two laser beams which has the same frequency, come out from the head of laser and form a interference area. When the particle pass through this area, it will generate a scatted beam, which has different frequency to the incident beams. This scatted beam is received by the head of laser again. The frequency difference is detected by a photo-multiplier and calculated by the computer. At last, the velocity is obtained as this frequency difference are corresponded to the velocity of particle. The detailed description could be found in Ref. [5].

In the present research, the heart of the system is a Coherent Innova Argon Ion Laser. Particles are added into the flow by a smoke machine. Laser beams coming out of the head of laser, traverse a thin and flat window and formed a interference area. Particles which passed through this area are measured and counted. When number of particles equals to the critical value (eg. $50,000$), laser moves to next fixed point. In some region, there are few particles, laser will stay a time given by the interval value (eg. 60 s) then move to next point.

Measurement methods of LDV

LDV measurements have been conducted on three axial positions in CRS: upstream of the FR, between the FR and RR and downstream the RR, which is $Z_p = -46,5$ and 50 mm respectively. At each axial position, velocities are measured on 25 radial positions from $R = 65$ to 185 mm, as shown in Fig.2.8(the dots). One should notice that the measurement area in radial direction does not continue to last position $R = 190$ mm. Because this

position is the casing wall, it is impossible to measure with LDV. The detailed measurement process is presented as follows. Laser beams are fixed on an axial positions, then firstly focus on a radial position and measure the instantaneous velocities of the particles passing trough this measurement volume. Next, when the required number of particles or the interval time are reached, laser beams move to next radial positions. Therefore each radial positions contain about 30,000 to 50,000 instantaneous velocities. By averaging these instantaneous velocities, we get the circumferential averaged velocity at the given axial positions. And the Standard deviation based on the instantaneous velocities represent the fluctuation of the velocity at this radial position. In our case, the averaged axial and tangential velocities are denoted as V_z and V_θ respectively. The averaged value is taken as the velocity at this position. Additionally, it should be pointed out that all the instantaneous velocities are not triggered, which means that the relationship between the velocities and rotor positions is unknown.

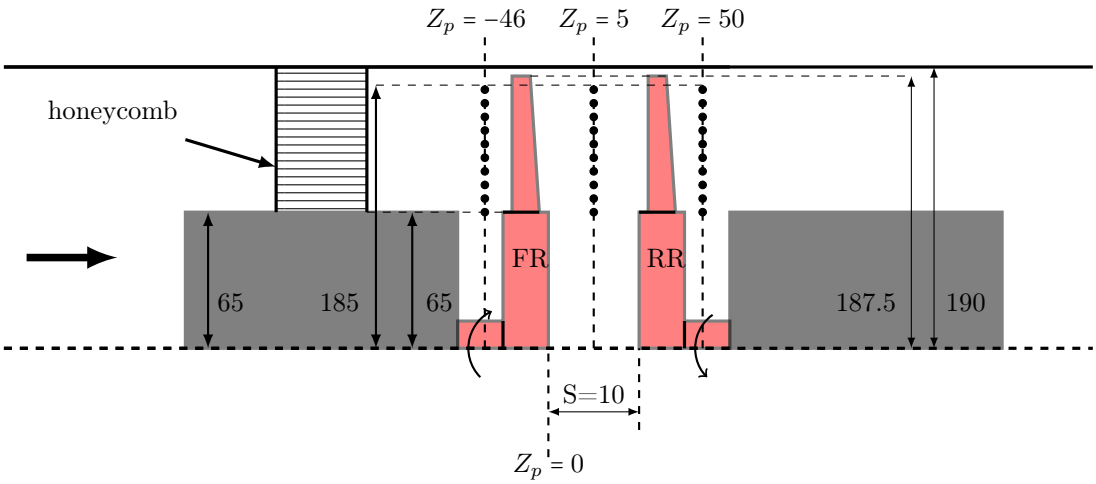

Figure 2.8: The axial and radial positions of LDV measurement points for CRS (in mm). S is the axial distance between the rotors, the default value is 10 *mm. The dots represent the radial measurement points from* $R = 65$ *to* 185 *mm, with a step of* 5 *mm.*

variability: an important parameter to estimate uncertainty

As presented above, the average value is taken as an estimator for the true value. For the LDV, the mean value could be denoted as:

$$\bar{u} = \frac{1}{N}\sum_{i=1}^{N} u_i \tag{2.12}$$

But the only way to get a true average is to have an infinite number of identified experiments: $N \to \infty$. The problem is in a real experiment, we can never have a true mean $\bar{u}$. For a definite number, the average is denoted as u_N. To investigate the convergence of u_N towards $\bar{u}$, variability is introduced[45].

$$\epsilon_N^2 = \frac{(u_N - \bar{u})^2}{\bar{u}^2} \tag{2.13}$$

Inserted by Eqn. 2.13, we can get:

$$\begin{aligned}\epsilon_N^2 &= \frac{(\frac{1}{N}\sum_{i=1}^{N} u_i - \bar{u})^2}{\bar{u}^2} \\ &= \frac{\frac{1}{N^2}\sum_{i=1}^{N}(u_i - \bar{u})^2}{\bar{u}^2} \\ &= \frac{1}{N}\frac{var(u)}{\bar{u}^2} \\ &\approx \frac{1}{N}\frac{\sigma_u^2}{\bar{u}^2}\end{aligned}$$

Where variance is estimated as:

$$var(u) = \frac{1}{N}\sum_{i=1}^{N}(u_i - \bar{u})^2 \approx \sigma_u^2 \tag{2.14}$$

For error analysis, if the N samples are uncorrelated, ϵ_N is a measure of uncertainty caused by the limited number of samples [45]. From Eqn. 2.14, $\epsilon_N \sim 1/\sqrt{N}$. Theoretically, $\epsilon_N \to 0$ as $N \to \infty$. Therefore, ϵ_N is an important parameter to investigate the uncertainty of an experiment.

To estimate ϵ_N, tangential velocities at different radial positions are measured, at design condition for JW1. The critical values of measurement are set to : number of bursts $50,000$ and interval 60 s. It permits to measure sufficient number of particles at a fixed point.

Near the hub region, $R = 95$ mm(50% of radius of tube):

$$\begin{aligned}\epsilon_N &= \frac{1}{\sqrt{N}}\frac{\sigma_u}{\bar{u}} \\ &= \frac{1}{\sqrt{50000}}\frac{2.5774}{0.7068} \\ &= 0.0163 = 1.6\%\end{aligned}$$

So the variability is remain reasonable near the hub, if the number of particles is sufficient. Nevertheless, this can not be granted at a real experiment. The reason is: near the region of hub, velocity is naturally quite low. Additionally, with the turbulence even reversed flow, few particles could be detected. In this case, only solution is to add more particles. With this effort, the normal measured numbers of particles are in $[10000, 30000]$. In this case, $\epsilon_N \approx 3.7\%$, Still in accepted range.

However, in most part of blade, $50,000$ are available. For $R = 170$ mm(89% of radius of tube), $\epsilon_N = \frac{1}{\sqrt{50000}}\frac{3.2794}{3.7566} \approx 0.4\%$.

Uncertainty: estimated from repeated measurements

Apart from influence of numbers of samples, uncertainty of averaged velocity is also affected by the environment conditions. For this reason, 10 repeated measurements are performed at 7 radial positions $R \in [85, 170]$ mm for JW1, at design condition. The axial position of all measured points are downstream of RR ($Z_p = 50$mm). The results can be found in Tab. 2.7.

Position R (mm)	mean of averaged V_θ ($m.s^{-1}$)	absolute uncertainty e ($m.s^{-1}$)	relative uncertainty ϵ (%)
85	−1.52	0.03	2.0
90	−0.58	0.04	6.9
95	0.64	0.05	7.8
120	1.94	0.01	0.5
125	2.17	0.01	0.5
165	3.61	0.02	0.6
170	3.83	0.03	0.8

Table 2.7: Repeated measurement of average tangential velocity V_θ at 7 radial position downstream RR (Z_p = 50 mm), for JW1 at design condition: R=[85 ~ 170] mm.

It can be noticed that over the mid-span(R = 126 mm) the relative uncertainties remain lower than 1%. Nonetheless, below the mid-span where the average tangential velocities are relatively lower, the relative uncertainties grows up rapidly. Especially, at the region $R \in [90, 95]$ mm, the averaged velocities are really close to 0 and changing from negative to positive, which have the highest relative uncertainty by around 7%. Hereafter, near the hub region, uncertainty decreases as a result of growth of average V_θ in reverse direction. This study demonstrated that uncertainty of average velocity was sensible to its magnitude. Near the region where velocity is quite low, the uncertainty could rise up significantly.

2.4.3 Microphone

The wall pressure fluctuations are measured by a pressure microphone calibrated by an acoustic calibrator. The details about the microphone and its calibrations could be found in Ref. [5]. This microphone is placed at the top of the block of CRS (seen in Fig. 2.9). And the axial position of the microphone is denoted as Z_p, shown in Fig. 2.2. The sampling frequency for the signal is 6 kHz. Then the signal is transformed to frequency domain by the Fourier transform. Thus, the Power Spectral Densities (PSD) are calculated, based on the measurements.

Before analysing the uncertainty of wall pressure fluctuations, one thing should be noticed that the test results could be different when the microphone is placed on the tip or on the side of the block, due to the influence of the structures of rod rows supporting the drive motors. Therefore, the influence of positions on the block is given, then followed by the analysis of repeating measurements by the microphone.

Influence of the positions of Microphone

Two measurements have been conducted at the 'top' and 'side' of JW1 by replacing the microphone and recalibrating it each time, at Z_p = 45mm (downstream of RR) on the design flow rate of JW1, $\theta = \theta_C$, S = 10mm. The measured wall pressure fluctuation is transformed in the frequency domain, as shown in Fig. 2.10. The PSD at the 'top' and 'side' has the similar characteristics, composed of three types of peaks. These peaks are at the frequencies which correspond to the blade passing frequencies of FR ($f_{bpf,FR}$ =

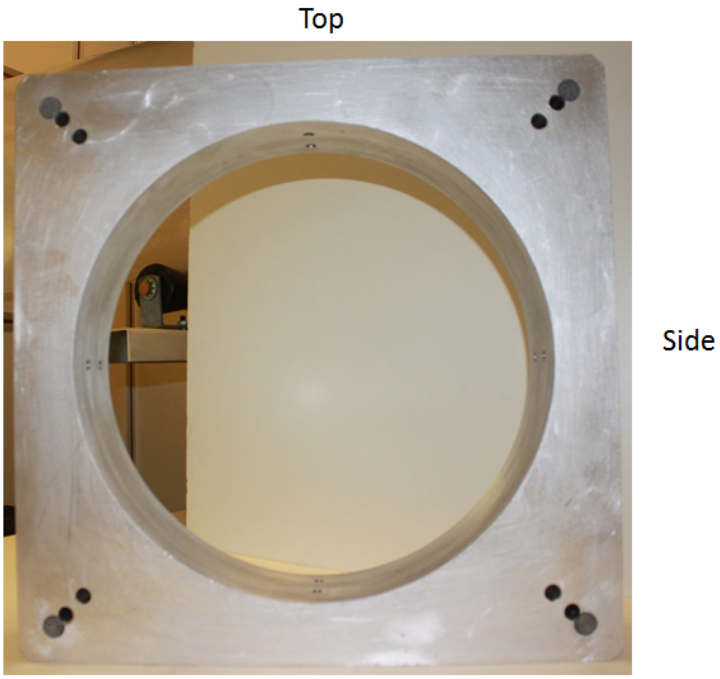

Figure 2.9: Positions of micro on the block

383.3 Hz), RR ($f_{bpf,RR}$ = 256.7 Hz) and their harmonics, as well as their interactions. The detailed analyse of the features of peaks are presented in Chapter 3 and 4. Here, only the amplitudes corresponding to $f_{bpf,FR}$ and $f_{bpf,RR}$, their main harmonics and interactions are listed in Tab. 2.8. Apparent discrepancy could be noticed for the amplitudes of the frequencies corresponding to each blade passing frequency and their main harmonics. This could be caused by the influence of the rods for supporting the drive motor of rear rotor. The detailed structures of the rods could be found in Ref. [5]. Another reason could be the influence of the depth of the microphone related to the block. To verity this effect, 5 repeated measurements are carried out by placing the microphone at the 'top' of the block at the same working conditions.

Uncertainty analysis of the microphone from repeated tests

The repeated tests are performed at the 'top' of the block, by replacing the microphone and recalibrating it each time at different days, for JW1 working at design flow rate, $\theta = \theta_C$, S = 10mm. The mains amplitudes variation are presented in Tab. 2.9. It can be seen that the amplitudes of the main peaks exhibit good repeatability. According to the data in Tab. 2.9, the maximum standard deviation are 1 dB/Hz, observed at the harmonics of $f_{bpf,RR}$. Then the power of the total signal (Std(p')) is also calculated by calculating the Standard Deviation(Std) of wall pressure fluctuations. For the 5 repeated measurements, the power of total signal is Std(p')=28.9 ± 0.1 dB.

Therefore, the wall pressure fluctuation has satisfying repeatability, with ±1 dB/Hz absolute uncertainty for the amplitudes in PSD of main peaks and 0.1 dB for the power of total signal. Since the effects of microphone positions on the block, in the following analysis of this thesis, the microphone is fixed on the tip of the block for all the wall

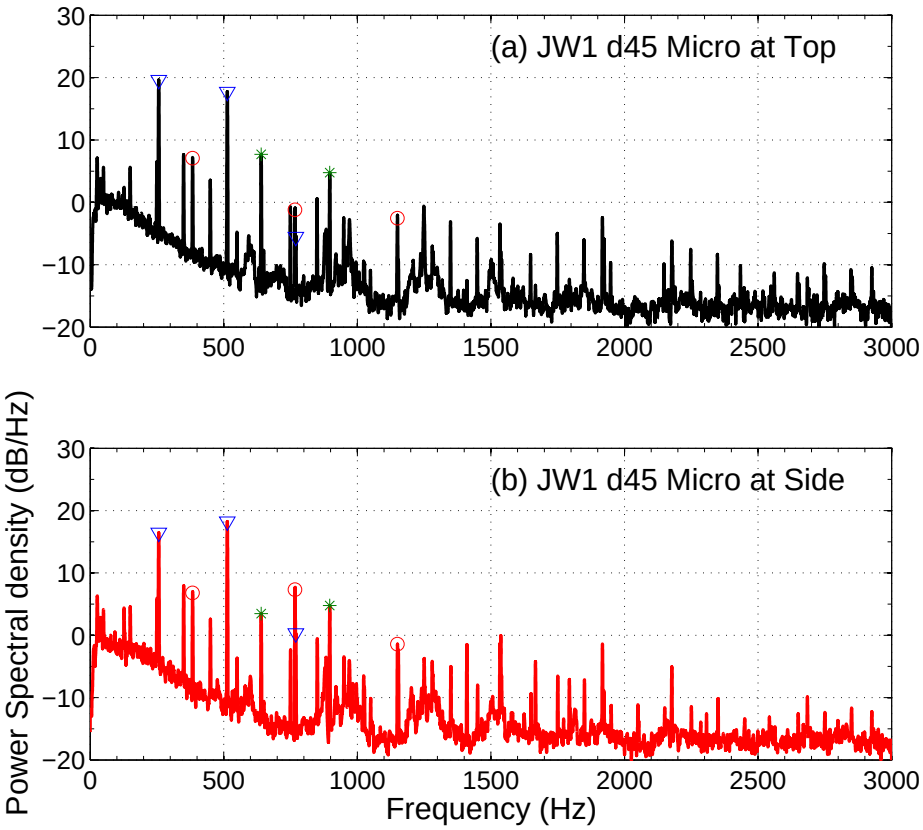

Figure 2.10: PSD of the wall pressure fluctuations measured at Z_p = 45 mm, for JW1 at N = 2300 – 2200 rpm and S = 10mm, Q_v = 1 $m^3.s^{-1}$; (∘): $mf_{bpf,FR}$; (▽): $nf_{bpf,RR}$; and (∗): $mf_{bpf,FR} + nf_{bpf,RR}$ with $m \neq 0$ and $n \neq 0$. (a) Microphone at position 'Top';(b) Microphone at position 'Side'

	Frequency	Amplitudes (dB/Hz)	
		Top	side
FR	$f_{bpf,FR}$	7.1	6.8
	$2f_{bpf,FR}$	-1.2	7.3
	$3f_{bpf,FR}$	-2.5	-1.4
RR	$f_{bpf,RR}$	19.6	16.4
	$2f_{bpf,RR}$	17.7	18.2
	$3f_{bpf,RR}$	-5.5	0.3
Interactions	$f_{bpf,FR}+f_{bpf,FR}$	7.7	3.5
	$f_{bpf,FR}+2f_{bpf,FR}$	4.8	4.8
Std(p') (dB)		28.9	28.0

Table 2.8: Comparison of amplitudes of the frequencies corresponding to $f_{bpf,FR}$, $f_{bpf,RR}$ and main harmonics , as well as the interactions $mf_{bpf,FR} + nf_{bpf,RR}$, by placing the microphone at the 'top' and 'side' of the block, for JW1 at N = 2300 – 2200 rpm and S = 10mm, Q_v = 1 $m^3.s^{-1}$. Std(p') represents the power of the total signal

	Frequency	Amplitudes (dB/Hz)				
		No.1	No.2	No.3	No.4	No.5
FR	$f_{bpf,FR}$	7.3	7.1	7.7	7.1	7.7
	$2f_{bpf,FR}$	0.4	-1.2	-1.0	0.2	-1.1
	$3f_{bpf,FR}$	0.2	-2.5	-1.9	-1.7	-1.9
RR	$f_{bpf,RR}$	19.5	19.6	19.9	19.6	19.6
	$2f_{bpf,RR}$	17.7	17.7	17.8	17.8	17.8
	$3f_{bpf,RR}$	-4.7	-5.5	-4.3	-4.1	-4.9
Interactions	$f_{bpf,FR}+f_{bpf,FR}$	7.5	7.7	7.6	7.8	7.5
	$f_{bpf,FR}+2f_{bpf,FR}$	4.4	4.8	4.4	4.7	4.2
Std(p') (dB)		28.8	28.8	29.0	29.0	28.9

Table 2.9: Comparison of amplitudes of the frequencies corresponding to $f_{bpf,FR}$, $f_{bpf,RR}$ and main harmonics , as well as the interactions $mf_{bpf,FR} + nf_{bpf,RR}$ from 5 repeated experiments, with the microphone at the 'top' of the block, for JW1 at $N = 2300-2200$ rpm and $S = 10mm$, $Q_v = 1\ m^3.s^{-1}$. Std(p') represents the power of the total signal

pressure fluctuation measurements.

2.5 Conclusion

This chapter presents the experimental facilities, consisting of the test rig, the design of counter rotating fans and the measurement methods as well as their uncertainties. Three CRS have been designed to achieve the same design point but with different distribution of load between the FR and RR. They are tested on the normalized test rig and the main measurement quantities could be listed as follows:

- the volume flow rate by an ISO-5167 orifice plat situated far downstream the CRS;
- the static pressure downstream the anti-gyration device by the averaging of pressure taps;
- the instantaneous axial and tangential velocities by Laser Doppler Velocimety (LDV);
- the wall pressure fluctuations by a microphone;

Based on the above measurements, the global performance, flow fields and wall fluctuations can be obtained. Moreover, a detailed analysis of uncertainties for each measured and derived quantities, which is necessary for the evaluation of experiments results in the following parts.

Chapter 3

Results JW1

The aim of this study is to seek for a physical understanding of the mechanisms involved in the operation of a counter-rotating stage. This chapter is devoted to the analysis of experimental results for JW1. The following issues are addressed:

- the validation of the design method
- The exploration of the features of JW1 working at different volume flow rates.
- A study of the wall pressure fluctuations at different axial positions.
- An investigation of the influence of parameters S and θ on the characteristics of CRS.

3.1 Validation of the design method

To evaluate the design method, first of all, the overall performance of the first Counter-Rotating System (CRS) JW1 is presented to check the characteristics at the design point Q_v = 1 $m^3.s^{-1}$. Next, the design assumptions are verified specifically. Then the radial distribution of the Euler work between the Front Rotor (FR) and Rear Rotor (RR) is explored.

3.1.1 Overall performance of JW1 working on the design parameters

The static pressure rise and the static efficiency as a function of the volume flow rate are presented in Fig. 3.1, for an isolated Front Rotor (named JW1FR) and for the CRS (JW1). Closed symbols stand for the JW1FR working at $N_{FR,C}$ and open symbols stand for JW1 at their θ_C and with S = 10 mm. The experimental data and the expected value at the design flow rate (Q_v = 1 $m^3.s^{-1}$) are given in Tab. 3.1. Overall, the isolated FR achieves the predicted values quite well. When coupled to the Rear Rotor to form the Counter-Rotating Systems, the ΔP_s of JW1 is close to the design point, with a discrepancy of −2.7%.

Furthermore, it can be observed from Fig. 3.1(a) that the characteristics can be divided into 4 regions where the slopes are different:

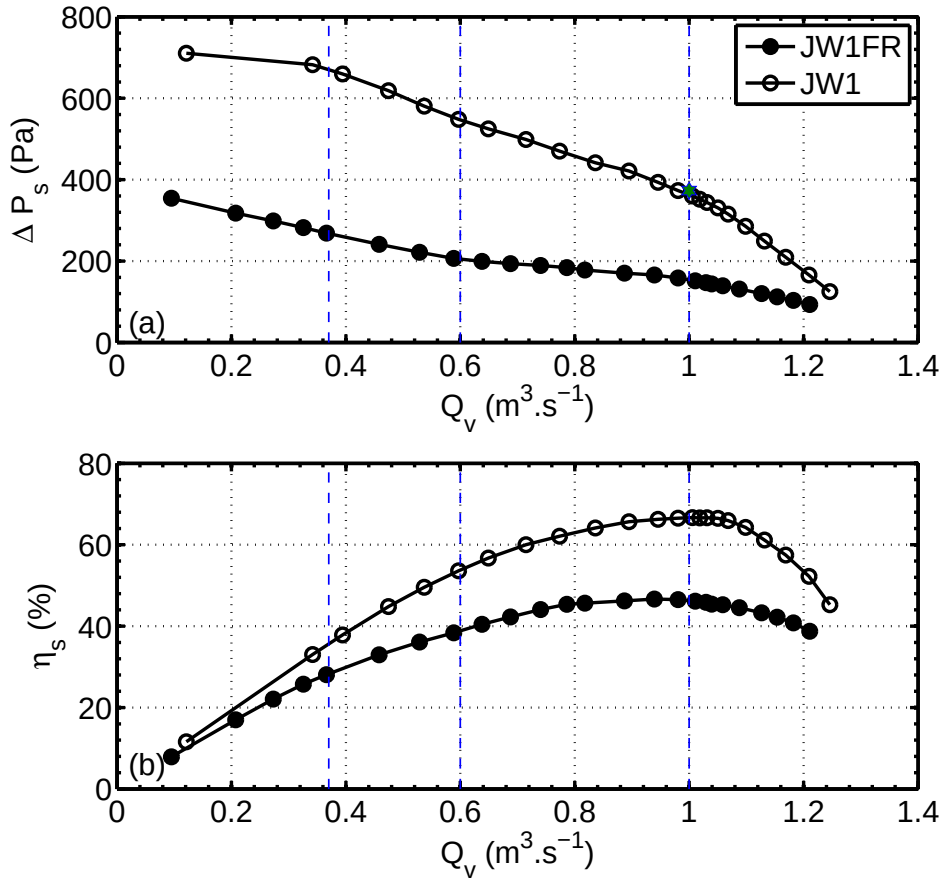

Figure 3.1: Overall performance of the JW1FR (•), JW1 (∘) and the design point (✶) (a): Static pressure rise ΔP_s vs. volumetric flow rate Q_v (ΔP_s is corrected by ρ_{ref}). (b): Static efficiency η_s vs. volumetric flow rate Q_v, at $S = 10$ mm.

	Isolated FR			CRS		
	Exp (Pa)	*MFT* (Pa)	δ %	*Exp* (Pa)	*C* (Pa)	δ %
JW1	154±2	144	7.0	363 ±4	373	−2.7

Table 3.1: Comparison of ΔP_s for the isolated FR and CRS ($S = 10mm$) at $Q_v = 1\ m^3.s^{-1}$. Exp: experimental value(corrected by ρ_{ref}), MFT: value predicted for the Front Rotor alone, and C: design point. The relative difference between the actual and the predicted value is δ.

Region I, $Q_v \in [0, 0.38]$ $\mathbf{m^3.s^{-1}}$**.** In this region, the volume flow rates are very low. For the curve of the JW1FR, the slope in this region is around −302 Pa.m^{-3}.s. For the JW1, the slope is quite flat. As Q_v is lower than the smallest controlled value of the iris damper in the case of JW1, it is difficult to vary the Q_v gradually.

Region II, $Q_v \in [0.38, 0.6]$ $\mathbf{m^3.s^{-1}}$**.** In this region, the slope of the curve for the JW1FR is flatter, approximately −277 Pa.m^{-3}.s. However, the curve has relatively high slope for JW1, around −600 Pa.m^{-3}.s. Please note that these values could change rather strongly according to the chosen points. They nevertheless illustrate the trend.

Region III, $Q_v \in [0.6, 1]$ $\mathbf{m^3.s^{-1}}$**.** In this region of moderate partial flow rates, the curves of ΔP_s have the smallest slopes. The values are roughly −110 Pa.m^{-3}.s for JW1FR and −458 Pa.m^{-3}.s for JW1.

Region IV, $Q_v \in [1, 1.3]$ $\mathbf{m^3.s^{-1}}$**.** In this region of overflow, the curves of ΔP_s have the biggest slopes. The values are roughly −282 Pa.m^{-3}.s for JW1FR and −951 Pa.m^{-3}.s for JW1.

To better understand the different slopes of the ΔP_s curves, the power consumption of the FR in both configurations are presented in Fig.3.2. It can be noticed that the slopes of power consumption change at $Q_v = 0.6$ and 1 m^3.s^{-1}. Hence, the different slopes regions in the curves of ΔP_s may be mainly due to the FR, reflecting in the two inflection points in power consumption curves.

In short, the characteristics of the CRS are steeper than that of the isolated Front Rotor and are always negative on a wide range of partial and over flow rates. It indicates that CRS has good operating stability. Similar features have been observed by Shigemitsu [29] in a contra-rotating axial pump.

Isolated FR	η_{sFR} %	CRS	η_{sCRS} %
JW1FR	46.3 ± 1.0	JW1	66.6 ± 1.4

Table 3.2: Comparison of η_s at design point $Q_v = 1$ $m^3.s^{-1}$

The values of the static efficiencies η_s at the design flow rate are reported in Tab. 3.2. The CRS is very efficient, the typical peak efficiency of a traditional rotor-stator stage being of the order of 55% according to Ref. [46], and up to 60% for exceptional stages. For a single rotor stage, the typical static efficiency is 50%, up to 55% (see also Refs. [41, 46, 47]). In view of this, the Counter-Rotating System is a promising solution for the designers who seek for high static efficiency turbomachines.

3.1.2 Validation of the design assumptions at design flow rate $Q_v = 1$ $\mathbf{m^3.s^{-1}}$

During the conception process, four main assumptions have been made. In order to verify these hypothesis, LDV measurements are conducted near the inlet of FR ($Z_p = -46$ mm),

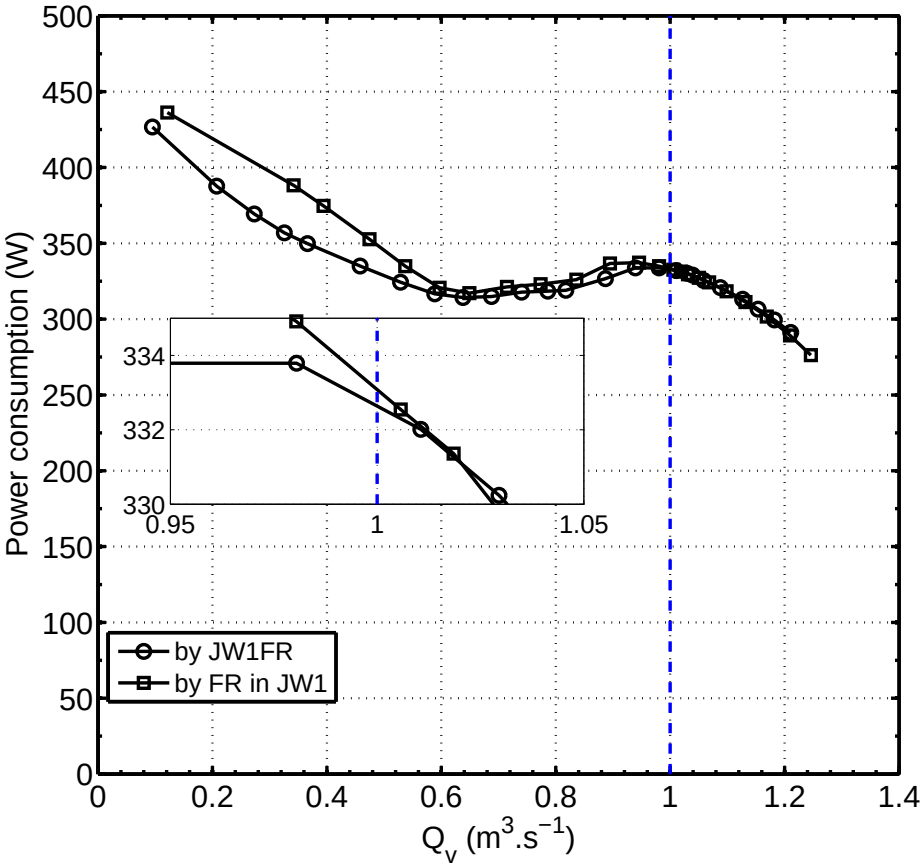

Figure 3.2: Shaft power (rescaled by ρ_{ref}) consumed by JW1FR (∘), consumed by FR in JW1(□). JW1 worked at $\theta = \theta_C$, $S = 10$ mm

between the FR and RR (Z_p = 5 mm) and near the outlet of the RR (Z_p = 50 mm), as shown in Fig. 2.8. It should be pointed out that the velocity given at each radial position is circumferential averaged value.

Assumption 1: axial inlet.

It is assumed that the flow at inlet of CRS is purely axial. Nevertheless, as observed by Sturm et Carolus [48], the streamlines of real inlet flow for an axial fan are helical which indicates vortex type structures. Hence, for the present research, a honeycomb is placed upstream of the front rotor to homogenize the inlet flow. As we known, the inlet conditions are important to the loss and noise [48] in the fans. It is necessary to confirm this assumption.

Figure 3.3 shows the averaged tangential velocity V_θ and the Standard Deviation(STD) measured 5 mm upstream of JW1 at different radial positions, obtained by LDV at the design flow rate. The vertical axis is non-dimensional radius (%) scaled as percentage of blade height. Therefore, 0 and 100 correspond to the hub and the tip of the blade respectively. The averaged V_θ are almost zero in the most part of the blade height (nearly $10 \sim 80\%$). On the other hand, positive averaged V_θ are observed close to the hub (below 10%) and tip (beyond 90%) of the blades. This could be possibly caused by the aspiration effects, as well as the influence of tip clearance and hub corner. Hence, the flow direction at inlet of the front rotor could be considered as only in axial direction.

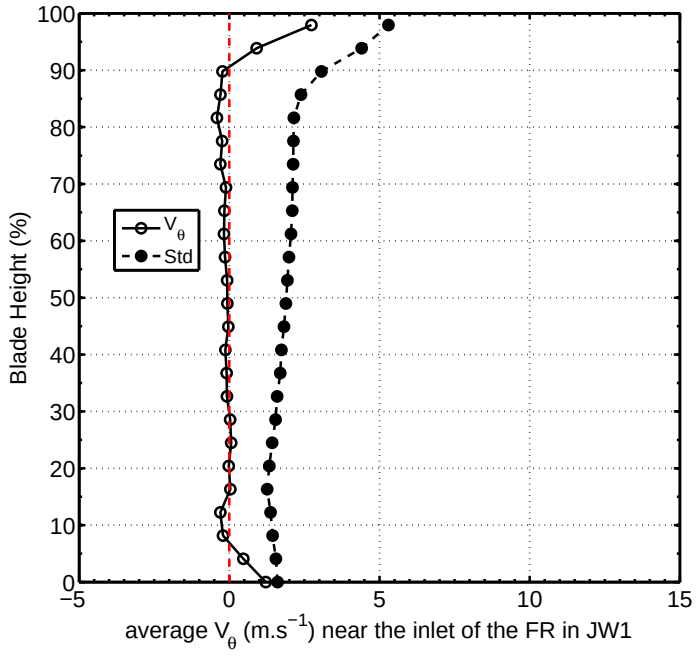

Figure 3.3: Averaged tangential velocity V_θ (∘) by LDV and the their Standard Deviation (•) at the inlet of JW1 (Position $Z_p = -46mm$) at design point $Q_v = 1\ m^3.s^{-1}$, $\theta = \theta_C$

Additionally, the fluctuations of V_θ are in the order of 2 m.s^{-1} (Fig.3.3) except near the tip region. To explain this, Power Spectrum Density (PSD) of the fluctuations of tangential velocities are calculated at a certain radial position. Figure 3.4 indicates the presence of a dominant frequency f = 383 Hz near the mid-span, which is the Blade

Passing Frequency (BPF) of the Front Rotor in JW1. It implies that the fluctuations are caused by the effect of the rotating FR in JW1 which propagates upstream.

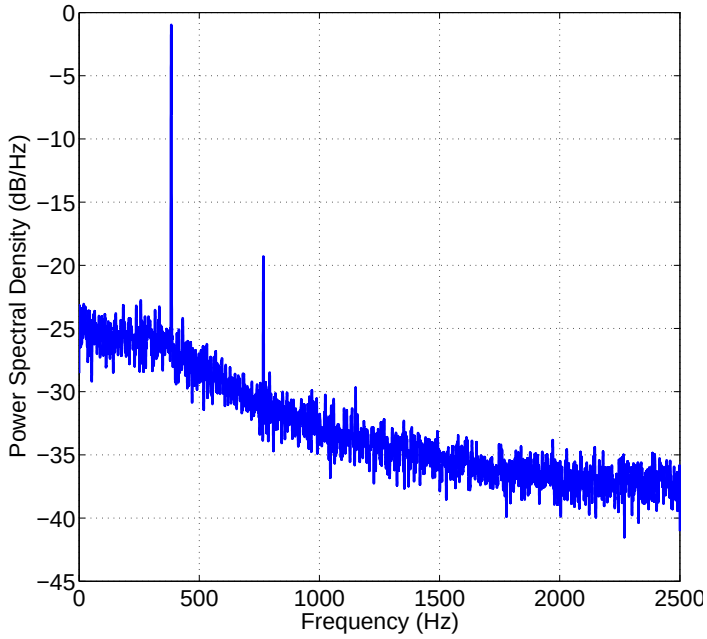

Figure 3.4: Power Spectrum Density of the fluctuations in tangential velocity V_θ at R = 125 mm (49% of blade height) near the inlet of JW1 (Position Z_p = −46mm), at design point $Q_v = 1m^3.s^{-1}$, $\theta = \theta_C$

Assumption 2: velocity at outlet of the FR= velocity at inlet of the RR.

For the conception of the Rear Rotor, an important hypothesis is that the inlet velocity field of the RR is taken from the outlet of the FR. This assumption ignores the interaction between the FR and RR, as well as the loss in the axial gap S between FR and RR. Actually, downstream of the FR, the velocities mix out and decay continually with the distance [20]. Therefore, this assumption should be verified as well.

The averaged velocities 5 mm downstream the FR are presented in Figures 3.5 and 3.6, for both configurations: JW1FR and JW1 at the design flow rate. At the same time, MFT also gives the predicted velocity profiles at outlet of the JW1FR, which are presented as well. Overall, the averaged velocities predicted by MFT have the same tendency as those measured by LDV in both axial and tangential directions. Additionally, as mentioned previously, the FR is designed by the vortex constant method. It means that theoretically tangential velocity at outlet of the FR should be constant along the radial direction and the axial velocity should vary linearly with radius for a perfect fluid. One can notice that neither the predicted value by MFT nor the results of LDV satisfy this feature. In fact, for both configurations, averaged axial velocities by LDV seems to have the expected form below 80% of blade height. But for higher blade span, the averaged V_z are relatively lower than in the middle. This is due to the casing boundary layers and may be enhanced by the tip clearance effects, which is also confirmed by Cho *et al.* [36]. On the other hand, the averaged tangential velocity profile is obviously not

constant, even for the predicted value by MFT. This is possibly due to the fact that the design process in MFT took into account the empirical correlations for cascade losses and effects of small Reynolds numbers. For both configurations, the averaged V_θ decreases approximately from 10 to 6m.s^{-1} with R from 20 to 80% of blade height.

Specifically, for the averaged velocities V_z (Fig. 3.5), the presence of the RR affects the distribution of the profile by diminishing V_z near the hub and tip region, as well as increasing the V_z at $10 \sim 80\%$ of the blade height. As the averaged axial velocity stands for the volume flow rate, it means that the Rear Rotor increased the air flow around the middle blade height. This indicates the contraction effect which may be related to the aspiration effect of RR interacting with the boundary layer of fan casing and hub vortex.

For the averaged tangential velocities V_θ (Fig. 3.6), the Rear Rotor decreases the V_θ almost along all the blade height, compared to the isolated JW1FR. This implies that the RR can reduce the blade loading of the FR. It is reasonable that the RR can slow down the outlet flow of the FR in tangential direction through a potential effect. Especially, this diminution is significant below 15% of the blade height, where V_θ decreases from 10 to near 0 by the presence of the RR. This indicates a substantial reduction of loading near the hub region. Additionally, the fluctuations of velocities in JW1 is much higher than in JW1FR alone due to the influence of the Rear Rotor.

Despite these modifications, this assumption is surprisingly robust and could be used for the preliminary design of CRS, working at small axial distance between FR and RR.

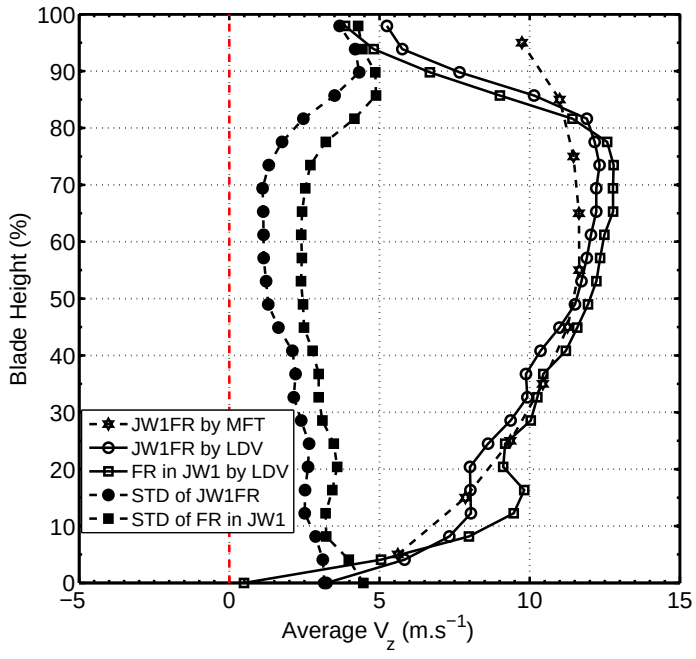

Figure 3.5: Averaged axial velocity V_z near the outlet of the FR (Position $Z_p = 5mm$) at design point $Q_v = 1m^3.s^{-1}$, $\theta = \theta_C$, in: JW1FR analyzed by MFT(☆); JW1FR measured by LDV(∘) and their STD(•); JW1 measured by LDV(□) and their STD(■)

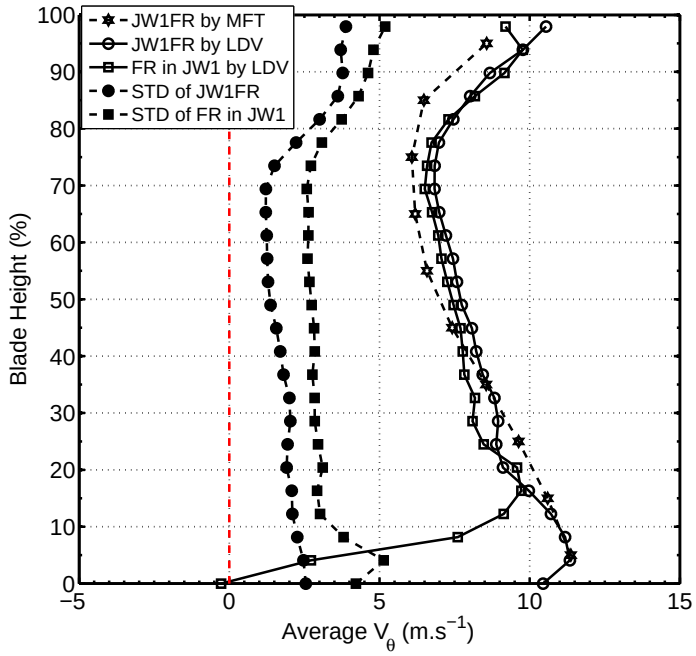

Figure 3.6: Averaged axial velocity V_θ near the outlet of the Front Rotor (Position Z_p = 5mm) at the design point $Q_v = 1m^3.s^{-1}$, $\theta = \theta_C$, In: JW1FR analyzed by MFT(☆); JW1FR measured by LDV (∘) and their STD(•); JW1 measured by LDV(□) and their STD(■)

Assumption 3: Axial outlet of RR.

The design purpose for CRS is to recover all the tangential energy by RR. Hence, in the design process of RR, the tangential velocity is considered to vanish. This assumption is directly related to the work output by RR.

In figure 3.7, the LDV results show the profile of the averaged tangential velocities V_θ and their STD 5 mm downstream of the RR in JW1. Above 20% of the blade height, the tangential velocities are still around $2 \sim 4$ m.s^{-1} instead of 0. On the contrary, on the rest of the blade height, negative V_θ appear and could reach nearly -1.5 m.s^{-1}. This indicates that RR does not completely recover the tangential part of energy at most part of the blade height, but over corrects the swirled flow near the hub region. This assumption of pure axial outlet is not properly met. The work done by CRS is not completely transferred to static pressure rise. Therefore, it is reasonable that the experimental static pressure rise is slightly lower than the target value. Additionally, the outlet flow of this CRS consists of a counter-vortex pair: the flow at large part of blade span turning in the rotational direction of FR and at low blade span turning in the rotational direction of the RR.

Assumption 4: Axial velocity is constant at a fixed radius when the fluid passes through the Rear Rotor.

In the design process, axial velocity V_z is assumed to be constant for a given radius R, during the flow passing through the Rear Rotor.

In fact, the LDV results show that the averaged axial velocities V_z in JW1 varies in a certain level among upstream of FR (Z_p = −46mm), between the FR and RR (Z_p = 5mm)

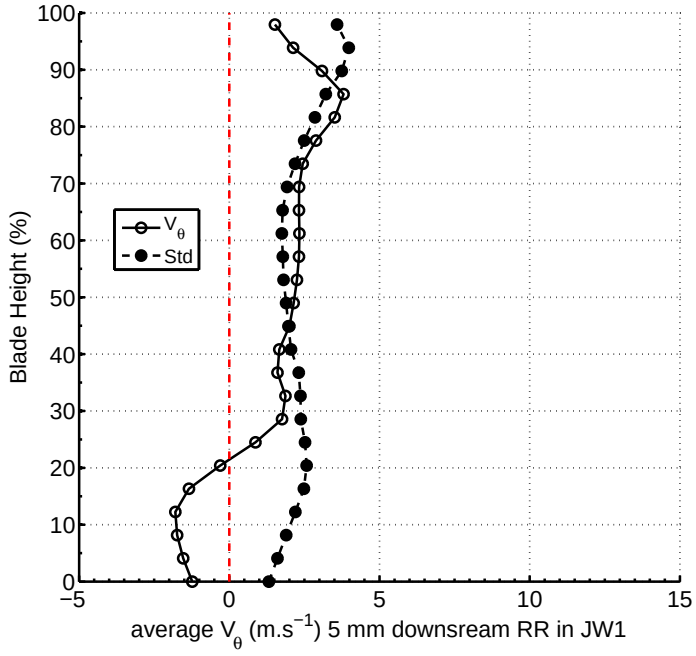

Figure 3.7: Averaged tangential velocity V_θ (∘) by LDV and its STD (•) at the outlet of stage JW1 (Position $Z_p = 50mm$) at design point $Q_v = 1m^3.s^{-1}$, $\theta = \theta_C$

and downstream of RR in JW1 (Z_p = 50mm)(Fig. 3.8). Near the tip region (beyond 80% blade height),the axial velocities are relatively much lower between FR and RR than upstream of the FR and downstream of RR. This could be caused by the interaction of tip vortex of FR and RR, which has been observed in Ref. [36]. Between 50 – 80% blade height, the axial velocities upstream of the FR are slightly lower than downstream positions. Between 20 – 50% blade height, V_z upstream of the FR are contrarily higher. Near the hub region, the axial velocities are significantly lower at downstream of RR than the other axial positions. This highly decrements in V_z in hub region result from the flow separation and hub vortex reflected in Fig. 3.7. Overall, the RR has obvious effects of transferring the air from hub to tip region. It could be concluded that when the fluid passes through the FR, the axial velocities decreases moderately near the tip region and increase near the hub also at 50 – 80% blade span. When the fluid passes through the RR, axial velocities decrease significantly below 30% of the blade span and increase considerably above 70% of the blade span. The whole changes in averaged axial velocities between inlet of FR and outlet of RR is that V_z decrease below 50% of the blade height and increases at 50 – 90% of the blade height.

Besides, negative axial velocities appear downstream of the RR, which indicates a back flow close to the hub region. It means that the flow structures near outlet of the RR are very complex, in the shape of a counter vortex propagating downstream RR (mainly turning in the rotational direction of the FR and near the hub turning in the rotational direction of the RR), and reversed flow close to the hub region.

Additionally, it can be observed that the standard deviation of averaged V_z between the FR and RR is significantly higher than that of in the other axial position due to the interaction of the FR and RR.

Further, the circumferential averaged axial velocities V_z is considered as the mean

velocity at the cross area between the measured radial positions. Therefore, the volume flow rate could be estimated as the integral of averaged axial velocities in radial direction.

$$Q_{LDV} = \int_R 2\pi R V_z dR \tag{3.1}$$

Then the calculated volume flow rate are compared with the measurements of the manometer Q_v = 1 m^3.s^{-1}. It should be pointed out that all the LDV measurements are conducted from the hub (R = 65 mm) to near the tip(R = 185 mm). But the real tip of the blade is at R = 187.5 mm. And the pipe outer radius is 190 mm. Therefore, the velocities at 5 mm near the blade tip (between 185 and 190 mm) are missing. To solve this problem, an estimation is made during the integration of the velocities, by adding the amounts $\frac{3}{4} \times V_{z,R=185} \times \Delta R$, considering the velocities extremely close to the casing are nearly 0. After this, we get Q_{LDV} = 0.99, 0.96, 0.96 m^3.s^{-1} for upstream the FR, between the rotors and downstream the RR, respectively. It reveals that the computed volume flow rate upstream of the FR is really close to the real value, with −1% of discrepancy. While for the position between the rotors and downstream the RR, the discrepancy increased to 4%. The reason could be that between the rotors and downstream of the RR, the flow is more fluctuating than upstream of the FR. Therefore, the circumferential averaged V_z deviates more from the expected value. Another reason could be due to the hub vortex and reversed flow at hub region. As a result, the integrated value is less than 1 m^3.s^{-1}.

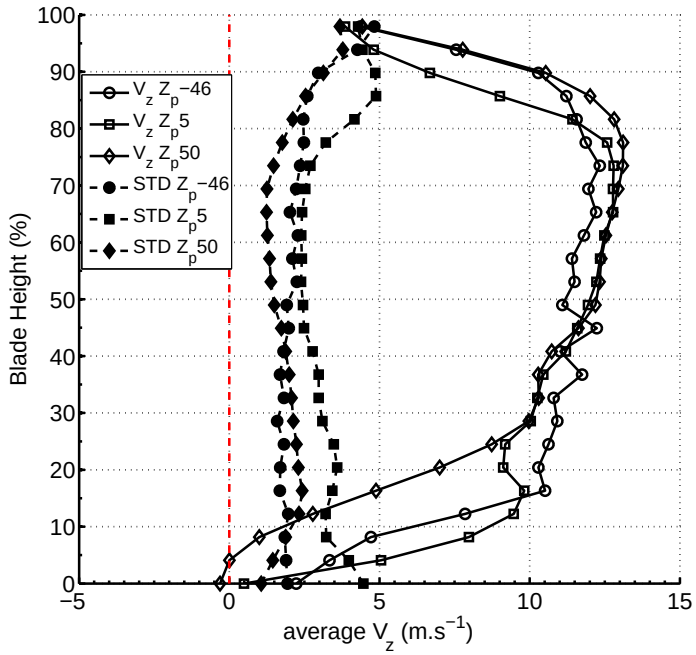

Figure 3.8: Averaged axial velocity V_z at: inlet of stage JW1(Position Z_p = −46mm)(∘); between the FR and RR in JW1 (Position Z_p = 5mm)(□); at outlet of stage JW1 (Position Z_p = 50mm)(◇) and their STD (Filled symbols) at design point Q_v = 1$m^3.s^{-1}$, $\theta = \theta_C$

3.1.3 Euler power at design flow rate $Q_v = 1$ m^3.s^{-1}

As presented in Chapter 1, the physical means of Euler power $\mathcal{P}_{Euler}$ is the amount of energy transferred from the axial rotor blades to fluid per unit time. At a given mass flow rate, the Euler power $\mathcal{P}_{Euler}$ represents the power consumption of the rotor, equals to the shaft power minus mechanical loss of the shaft. In the following part, the Euler power is estimated based on the LDV experimental results.

Firstly, the Euler pressure rise is computed based on the LDV measurements at radial points for each rotor. As presented previously : $\Delta P_{Euler} = \rho U \Delta V_\theta$. Then Euler power is calculated as:

$$\mathcal{P}_{Euler} = \Delta P_{Euler} \times Q_v = \int_R \rho U \Delta V_\theta 2\pi R V_z dR \tag{3.2}$$

All the axial V_z and tangential V_θ are obtained by the circumferential averaged values measured by LDV at each radial points.

To figure out the effect of Rear Rotor and the work done in CRS, the radial profiles of the calculated Euler pressure rise ΔP_{Euler} by the FR are analyzed in the isolated rotor JW1FR and in CRS JW1 firstly. Then the calculated Euler power $\mathcal{P}_{Euler}$ by FR and RR in the stage JW1 are compared.

The effects of Rear Rotor : work done by the FR in the isolated rotor and in CRS

Figure 3.9 shows the Euler pressure rise ΔP_{Euler} by the FR in JW1FR and in JW1, calculated from the LDV measurements and analyzed by MFT as well (For JW1FR). The averaged V_θ at the inlet of the FR for both configurations is considered to be the same. First of all, MFT could well predict the tendency of Euler pressure rise distribution at radial direction. Further, it can be seen that with the influence of the RR, the Euler pressure rise of the FR diminishes at all blade span, especially large reduction occurs below 20% of blade height. According to the simple equilibrium conditions, it is supposed that the streamlines are parallel when the fluid passes through FR. Then the Euler power $\mathcal{P}_{Euler}$ is estimated as the integration of Euler pressure rise multiplied by the volume flow rate based on the measurements of LDV at $Z_p = 5$ mm in radial direction. Thus, the Euler power of FR in JW1FR and in JW1 are: 300 and 286 W, respectively. It infers that with the presence of the rear Rotor the work done of the FR is reduced by about 5%. As presented previously, the relative uncertainty of averaged tangential velocities depends significantly on the radial position, from about 0.5% to 7.8% (Chapter 2). Not mentioning the uncertainty of the averaged axial velocities, this decrements in the Euler power is in the uncertainty range. But the radial profile of the Euler pressure rise in Fig. 3.9 could reflect the tendency of a slightly work reduction in FR by the influence of the RR. Additionally, according to the constant vortex condition $V_\theta = const.$, the curve of Euler pressure rise should be linear with radius. It is clear that the predicted radial profile of P_{Euler} by MFT is not linear with radius. The reason is that MFT took into accounts the loss from the end wall, the blade cascade and friction.

However, according to the measurement of torque meter, the shaft power consumption of FR approximately equals to 333 W for both JW1FR and CRS, at design flow rate ($Q_v = 1$ m^3.s^{-1}) (Fig. 3.2). This result indicates that at design flow rate the presence

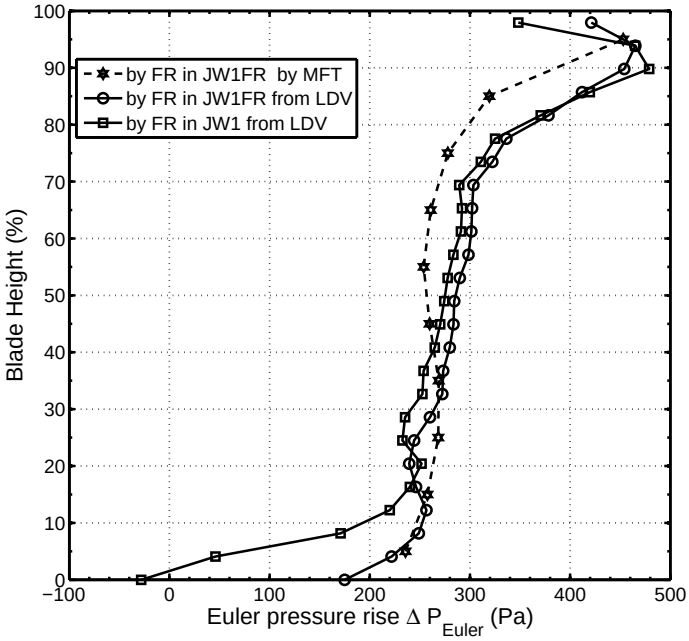

Figure 3.9: Radial profiles of the Euler pressure rise of the FR in JW1FR analyzed by MFT (☆); in JW1FR calculated from LDV measurements (∘), and in JW1 calculated from LDV measurements (□), at design point $Q_v = 1m^3.s^{-1}$, $\theta = \theta_C$, $S = 10$ mm

of the RR has no influence on the power consumption of FR. As we know, this power consumption is also named as shaft power, which represents the work done on the fluid by the rotor (Euler power). At design flow rate, the differences between the shaft power and the value measured by LDV is about 33 W (10%) and 47W (14%) in JW1FR and in CRS separately. Generally, the discrepancy between the shaft power and the calculated work done is owing to the mechanical efficiency of the shaft. In our case, the uncertainty of the velocity measurements also contributes to this discrepancy.

To summarize, at the design flow rate, the power consumption of the FR does not change with or without the RR. But the calculated Euler power of the FR has 5% decline with the presence of the RR. This could ascribe to the increased fluctuations of the velocities downstream FR by the influence of FR. Then the circumferential averaged value deviate more from the value with less fluctuations.

The distribution of work in JW1

Based on the LDV measurements, the calculated Euler pressure rise ΔP_{Euler} by FR and RR is presented in Fig. 3.10. Since the Euler pressure rise represents the work done per unit volume flow rate by the rotor, which would be transferred to the total pressure rise of the fluid for an isotropic compression. Hence, the Euler pressure rise relates to the ΔP_t of the fluid plus the loss.

Therefore, the calculated distribution of work between the FR and RR could be obtained by $\frac{\Delta P_{Euler,RR}}{\Delta P_{Euler,FR}+\Delta P_{Euler,RR}} = 0.40$. This value is close to the designed distribution of load of JW1 $L_C = 0.41$. It indicates that the estimation of total pressure rise in the design process is acceptable. The discrepancy could be due to the loss in the blades and

fluctuations of the measured velocities.

According to the data in Fig. 3.10, the Euler power is calculated for FR and RR in JW1 at the design volume flow rate. The results are 286 and 192 W for FR and RR respectively. Additionally, the shaft power measured by torque meter for the stage JW1 at design point Q_v = 1 m^3.s^{-1} is 333 W for the FR and 211 W for the RR (L = 0.39). Therefore, the values of work done calculated by the LDV measurements are 14% and 9% lower than the measured power consumption, for the FR and RR respectively.

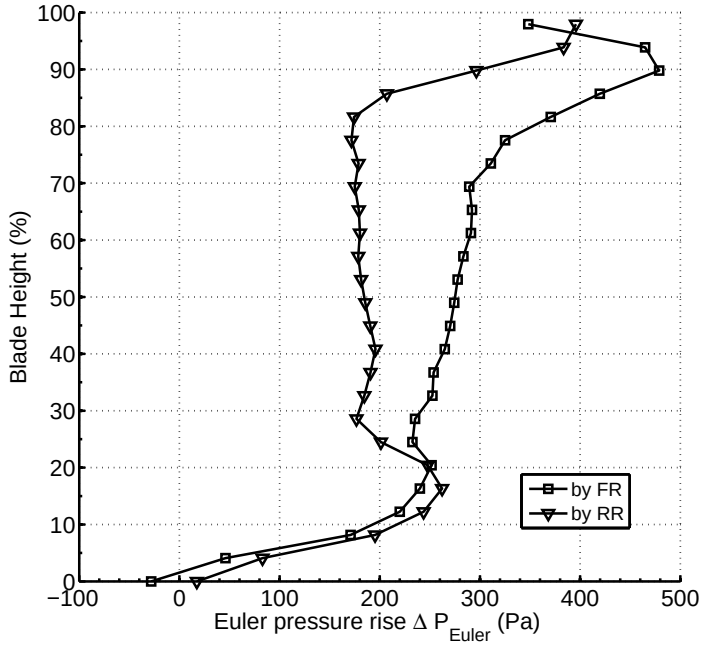

Figure 3.10: Radial profiles of the calculated Euler pressure rise by FR(□) and RR(▽), in stage JW1 at design point $Q_v = 1m^3.s^{-1}$, $\theta = \theta_C$. ΔP_{FR}.

3.1.4 Deviation angle and loss

As we know, the deviation angle δ is defined as the difference between the relative outlet flow direction and the tangent of camber line at the trailing edge in a rotor [7]. Thus, δ indicates how the flow actually follows the blade profile. The value can reflect the loss during the flow passing through the blades. Figure 3.11 shows the modification of δ downstream of FR by the presence of RR. It can be seen that δ changes slightly in most part of blade height. Additionally, at low blade height(around 20%), δ decreases by about 5 degrees with the presence of RR. Contrarily, 10 – 20 degrees of increase can be found close to hub region, below 10% of blade height. This significant increase indicates loss in FR at this region of blade. The reason for this large deviation could be that the RR significantly slows down the velocities close to the hub of the FR outlet(Figs. 3.5 and 3.6). This could induce the growth of boundary layer close to the hub region which could generates a blockage that modifies the flow direction.

Further, the deviation angles of the FR predicted by MFT and calculated from LDV measurements have the same tendency at most part of the blade span except near the

hub and tip region. Specifically, near the tip region, MFT underestimated the δ by about 5 degrees. This indicates that the empirical loss correlations in MFT analysis is not sufficient to predict the loss in tip region, possibly due to the complex tip clearance flow and casing boundary layer interaction. According to Wennerstrom [15], these errors in the prediction of deviation angles strongly influence the level of work at the rotor tip, as shown in Fig.3.9.

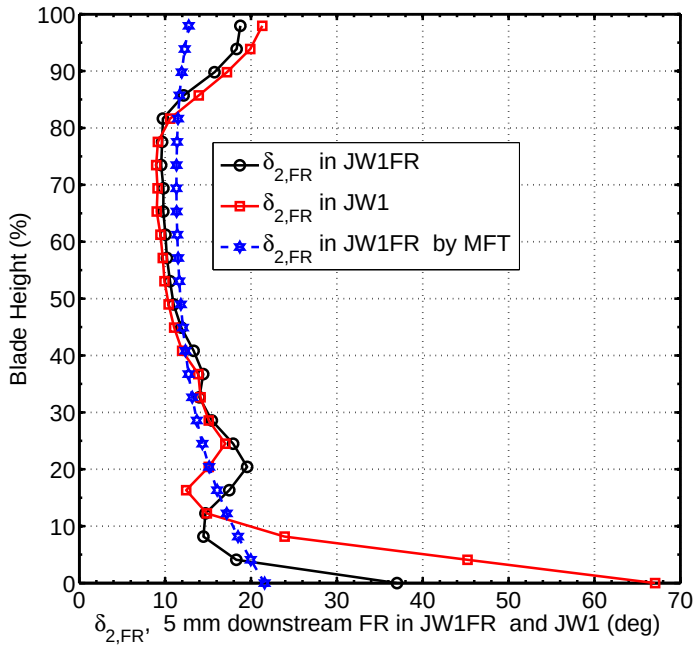

Figure 3.11: Deviation angle $\delta_{2,FR}$ at the outlet of the Front Rotor (Position Z_p = 5mm) at design point $Q_v = 1m^3.s^{-1}$, $\theta = \theta_C$, in : Isolated JW1FR analyzed by MFT(☆); Isolated JW1FR measured by LDV (∘); JW1 measured by LDV (□)

3.1.5 Conclusion

This section permits to verify the conception methods and the results are as follows:

- At design flow rate, JW1FR can achieve the predicted values very well and static pressure rise of JW1 is 2.7% below the design point.
- LDV measurements provide the circumferential averaged axial and tangential velocities distribution along the blade span at inlet, between and outlet of CRS at design flow rate. The inlet flow of CRS could be confirmed as almost only in axial direction, excepted the slightly positive tangential velocities close to the hub and tip region due to the aspiration effects as well as the tip clearance and hub corner effects. Between the FR and RR, MFT could well predict the overall tendency of velocity profiles for JW1FR, except an over-prediction of the axial velocities near the tip region. With the presence of RR, the velocity profiles change slightly in most of blade span, besides the tangential velocities reduces largely near the hub region. For the preliminary design of CRS, the outlet velocities of a FR only could be taken

as the inlet condition of RR for a small axial distance between FR and RR. At outlet of RR, the tangential velocity is not completely recovered as static pressure rise which is considered as loss. The flow is swirling in the rotational direction of FR in most part of blade span and in the rotational direction of RR near the hub region. Additionally, when the fluid passes through the RR, the fluid is transferred from the hub region to the tip region, even a back flow appears close to hub region at outlet of RR.

- The Euler power calculated based on LDV measurements of the FR in JW1FR is 5% lower than in JW1. However, the power consumption measured by torque meter shows there is no difference of shaft power of FR with or without the presence of RR. This is because the increased fluctuations of the velocities by the influence of RR derive the circumferential averaged velocities from the value without the RR.

- The Euler pressure rise calculated based on LDV measurements proves that the estimation of total pressure rise for both FR and RR are in acceptable range.

- MFT can well predict the deviation angle at outlet of FR in JW1FR, apart from the tip region where MFT is under-estimating the deviation flow angle mainly due to the over-estimated axial velocities in this region. This reveals the empirical loss correlation in MFT analysis is quite good but not sufficient to predicted the loss in the tip region where exits the complex interaction between tip clearance and casing boundary layer. In addition, the deviation angle increases significantly close to hub region of FR outlet with the presence of RR. The reason could be the potential effects of RR largely decreases the velocities close to the hub region and induce growth of boundary layer, which acts as a blockage and change the flow path of the fluid.

3.2 The characteristics of JW1 working at different flow rates

As well as determining the design performance, it is important to explore the characteristics at different inlet flow conditions to have the off-design behavior. Theoretically, at partial volume flow rate, axial velocities V_z diminish at the inlet region. According to the velocity triangle (Fig. 3.12), at the inlet of the rotor, relative velocities W decrease but relative angle β increase at the same radial position. Consequently, the incidence angle i increase. Supposing the flow still follows the blade curvature at the outlet, the air deflection angle $\Delta\beta$ increases. Consequently, the ΔV_θ enlarges and the Euler pressure rise ΔP_{Euler} as well. Thus, the pressure rise is higher. Moreover, as depicted in Ref. [22], when i is increased beyond a particular value, the loss owing to the increase in deflection angle is significant. In other words, beyond the critical incidence angle, the deflection angle and static pressure rise decrease due to suction surface separation. The fan enters into stall, which is indicated by a pressure rise peak and a positive slope (Fig. 1.2). In our case, both the JW1FR and JW1 show a continuous negative static pressure slope (Fig. 3.1). Only the degree of slopes varies at $Q_v = 0.6, 0.37$ m^3.s^{-1}. To understand the flow characteristics at partial flow rates, it is interesting to investigate the velocity fields. Therefore, in the present research LDV measurements have been conducted on $Q_v = 0.6, 0.37$ m^3.s^{-1}, at two axial positions: between the FR and RR (Z_p = 5 mm) and downstream of JW1 (Z_p = 50 mm). And the velocity fields at design flow rate Q_v = 1 m^3.s^{-1} are plotted as well to compare the changes.

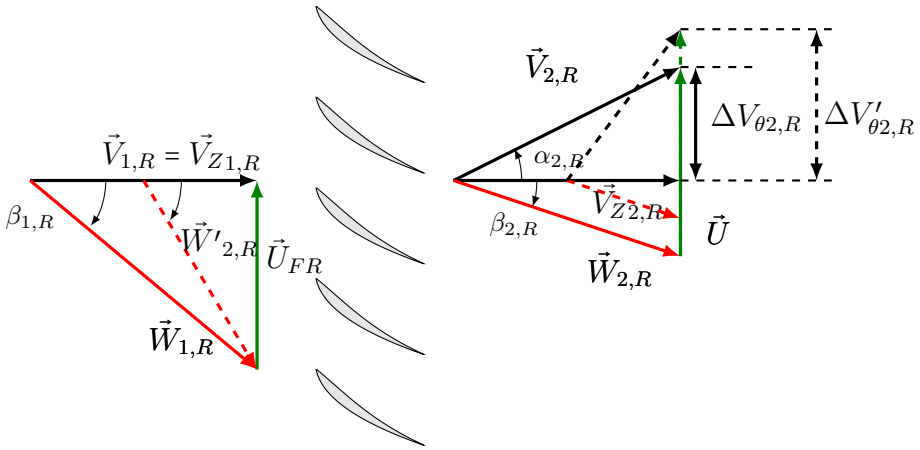

Figure 3.12: Velocity triangles at partial flow rate for an axial rotor.

3.2.1 Comparison of Velocity fields for JW1 at Zp = 5 mm at different flow rates

Figure 3.13 illustrates the difference in averaged velocity fields at different volume flow rates $Q_v = 1, 0.6, 0.37$ m^3.s^{-1}, downstream the FR in JW1. When Q_v decreases from 1 to 0.6 m^3.s^{-1}, axial velocities reduce significantly and negative V_z appear close to the hub region (below 10% blade height). Meantime the tangential velocities V_θ increase

significantly at most part of blade span (above 30% of the blade span) and decrease until negative at the low blade span. This indicates that at Q_v = 0.6 $m^3.s^{-1}$ the increased incidence angle at FR inlet is still below the limit and consequently the flow turning angle increase above 30% blade span. On the contrary, near the hub region, the flow turning angle decreases and reversed flow appears. The effects increase the loss of FR.

When Q_v decreases to 0.37 $m^3.s^{-1}$, it is interesting to notice that the axial and tangential velocity near the hub region increased to positive compared with that of Q_v = 0.6 $m^3.s^{-1}$. However, at most part of blade height, both axial and and tangential velocities decrease. In addition, compared with velocities of Q_v = 1 $m^3.s^{-1}$, V_θ increases only between 50 – 85% blade span. A possible explication for this is that the incidence angle is increased to more close to the limit value and large separation occurs at the blade wall near the tip and below mid-span. This boundary separation derives the flow from the blade wall and the flow turning angle decreased largely. In this point, the Front Rotor works at an unstable state.

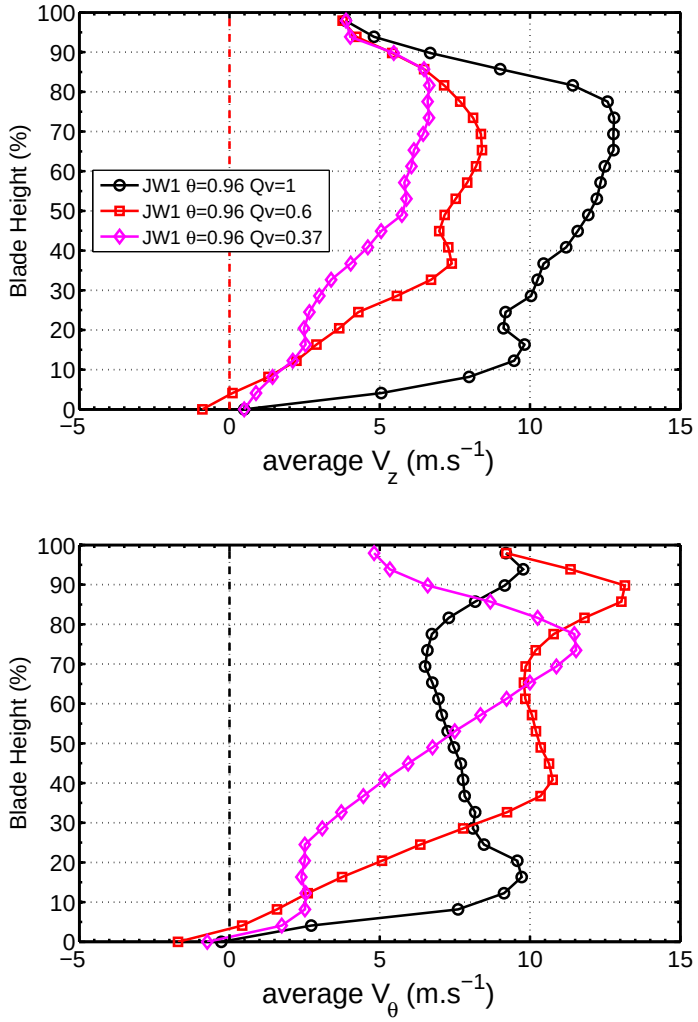

Figure 3.13: Averaged velocity fields at Z_p = 5 mm for JW1 on Q_v = 1 (∘), 0.6(□), 0.37 $m^3.s^{-1}$ (◇) in JW1, at $\theta = \theta_C$, S = 10 mm

3.2.2 Comparison of Velocity fields between JW1FR and JW1 at $Z_p = 5$ mm at different flow rates

In order to understand the influence of RR on the FR at partial flow rates, the axial and tangential velocities are measured at $Z_p = 5$ mm in both JW1FR and JW1.

Figure 3.14 shows that the radial profiles of velocities 5 mm downstream the FR in both JW1FR and JW1, at partial flow rates $Q_v = 0.6, 0.37$ m^3.s^{-1}. Closed symbols stand for JW1FR and open symbols for JW1. The velocities at $Q_v = 1$ m^3.s^{-1} are also plotted for comparison. At design flow rate, the Rear Rotor does not have obvious influence on the velocity profiles at most part of blade span near outlet of FR.

Figure 3.14a illustrate that for FR alone obvious negative axial velocities V_z appear at low blade region as Q_v decreases. Overall, with the presence of RR, V_z could be corrected to be positive except at very close to hub region. Specifically, when Q_v diminishes to 0.37 m^3.s^{-1}, negative V_z occur almost below 50% of blade height for FR only. Surprisingly, the RR could eliminate negative axial velocities of all the blade height. As we know, negative axial velocity indicates the reverse flow near the hub region, which could be caused by the interaction of secondary flow and boundary layer. The presence of RR seems to have an suction(aspiration) effect on the fluid and correct it to positive axial direction.

On the other hand, Fig. 3.14b displays that for FR only averaged tangential velocity increase almost most part of blade span except decreasing below 20% span, as Q_v reduces from the design point. When Q_v decreases from 1 to 0.37 m^3.s^{-1}, the averaged tangential velocities increase more than that of at 0.6 m^3.s^{-1} above 50% span. Below 50% blade span, the averaged tangential velocities still augment but lower that that of at 0.6 m^3.s^{-1}. Same decrease of averaged tangential velocities exit but slightly more than that of at 0.6 m^3.s^{-1}. It indicates that the loss increases below midspan as Q_v decreases to very low flow rate. Then the presence of RR diminishes the averaged tangential velocities V_θ compared with FR alone at partial flow rates. This diminution appears from the hub region and tip region, then both spread towards the middle span of blade as flow rate reduced.

In brief, the Rear Rotor could eliminate the reverse flow downstream of the FR and diminishes the load of the Front Rotor at the partial flow rates. This effects are more obvious at lower partial flow rates.

3.2.3 Velocity fields of JW1 at $Z_p = 5$ mm and $Z_p = 50$ mm at different flow rates

Figure 3.15 shows that the velocity fields downstream of FR and downstream of RR in JW1, at different volume flow rates.

At the design flow rate $Q_v = 1$ m^3.s^{-1}, when fluid pass through RR, averaged axial velocity increase near tip region and consequently decrease near hub. Meantime averaged tangential velocity are reduced to almost 0.

At partial flow rates, downstream RR, large area of negative V_z arise below 30% of blade height(Fig. 3.15a). It refers to the large reverse flow at outlet of RR in JW1. Moreover, averaged tangential velocities V_θ become negative at most part of the blade height, until completely all blade span (Fig. 3.15b). It means that RR over corrects the

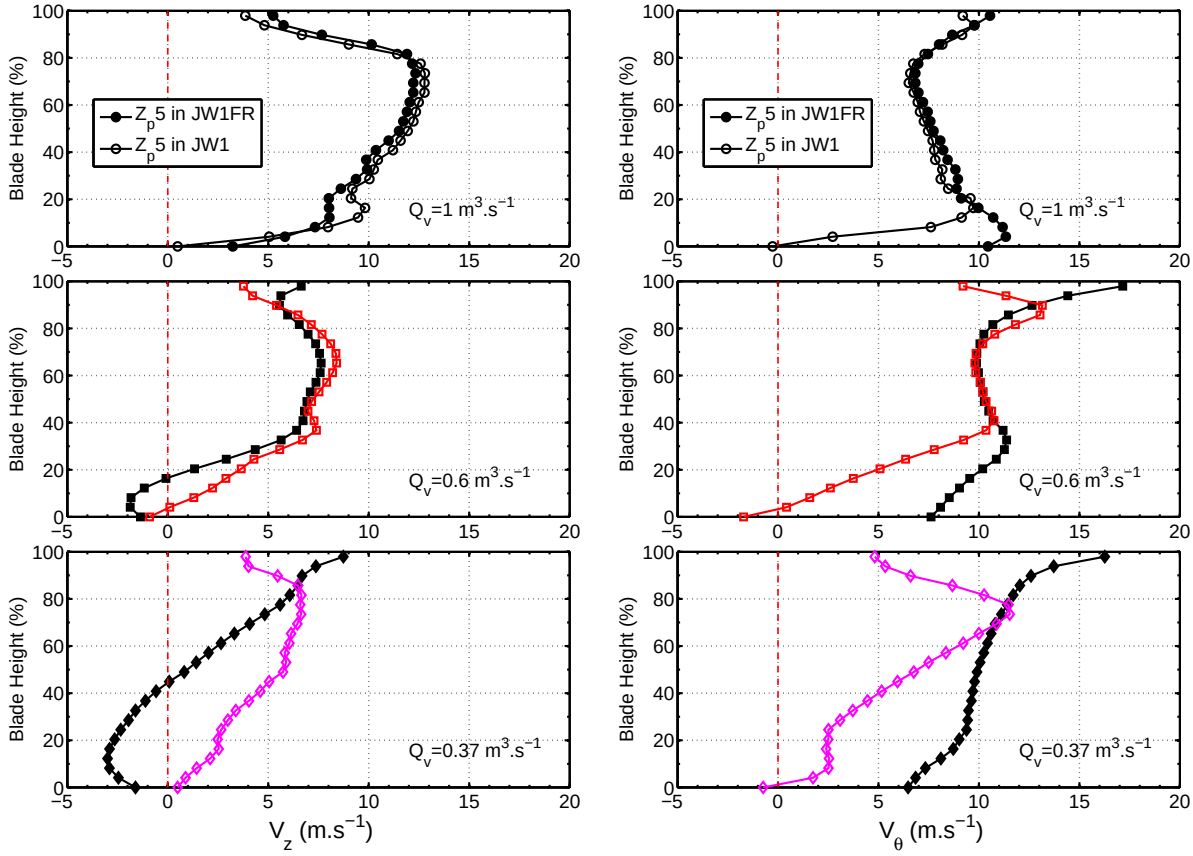

(a) Averaged axial velocities V_z *(b) Averaged tangential V_θ*

Figure 3.14: Radial distributions of circumferential averaged axial (V_z) and circumferential (V_θ) velocities at Z_p = 5 mm, for JW1FR(closed symbols) and JW1(open symbols) at Q_v = 1, 0.6, 0.37 $m^3.s^{-1}$, S = 10 mm

tangential velocities at partial flow rates which induces the loss and less static pressure rise of the fluid.

It can be concluded that the Rear Rotor works as expected at design flow rate. However, at partial flow rate, large reverse flow exists at outlet hub of the RR. Moreover, the RR significantly overturns the flow in tangential direction, which could induces large loss and lower static pressure rise.

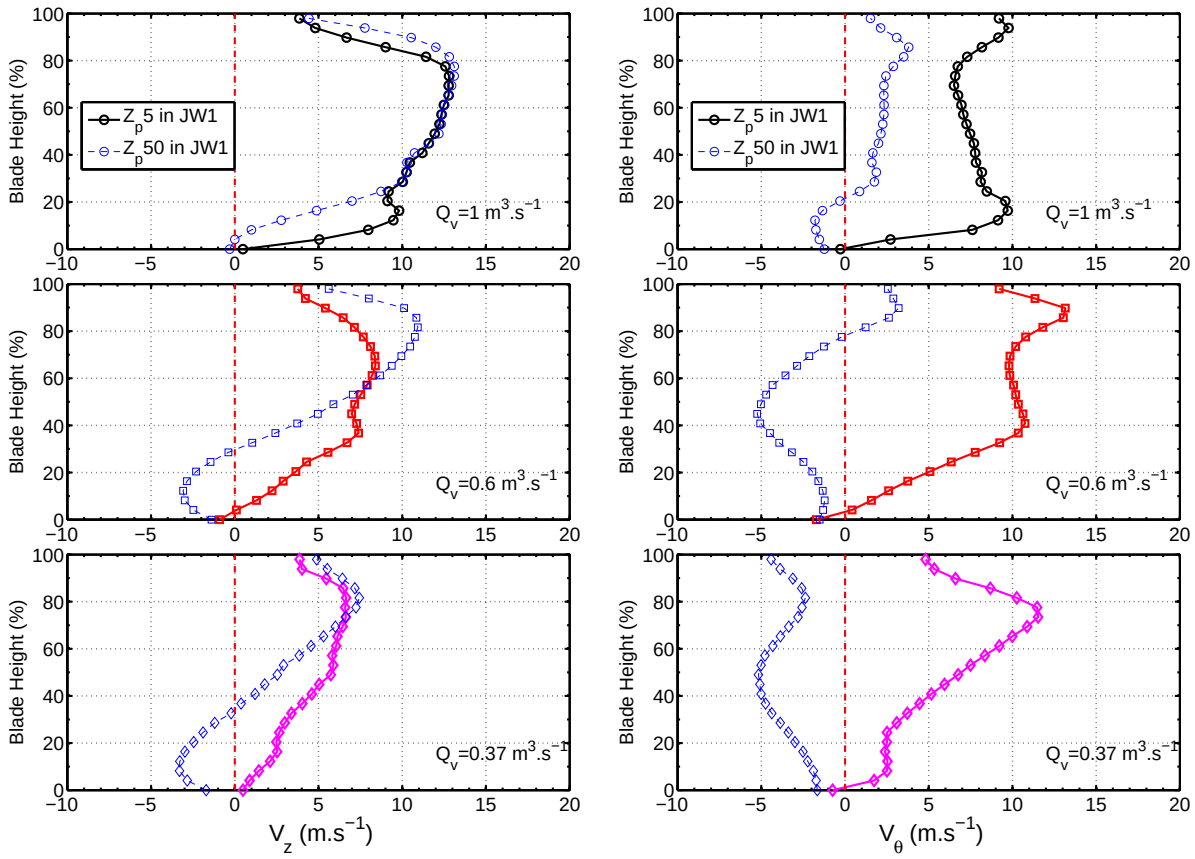

(a) Averaged axial velocities V_z *(b) Averaged tangential velocities V_θ*

Figure 3.15: Radial distributions of circumferential averaged axial (V_z) and circumferential (V_θ) velocities at Z_p = 5 mm, and Z_p = 50 mm(blue and thinner lines) for JW1 at Q_v = 1, 0.6, 0.37 $m^3.s^{-1}$, S = 10 mm

3.2.4 Conclusion

This section concentrates on the performance and flow structures of JW1FR and JW1 at partial flow rates, where the static pressure curves changes its slope in the overall performance maps of the both configurations. The results could be summarised as follows:

- When Q_v decreases from 1 to 0.6 $m^3.s^{-1}$, for outlet of FR in JW1FR, axial velocities decrease significantly and reverse flow appears near the hub. But the tangential velocities increase dramatically at almost all the blade span besides decreasing moderately near the hub region. It indicates higher load for most part of FR blade span

compared with that of design flow rate, which is reasonable in view of the velocity of triangle, aside from the near hub region due to the hub boundary layer effects. With the presence of RR, the reversed flow is suppressed near the hub region. However, the load is diminished below 40% blade span and near the tip region, owing to the potential effects of RR interacting with the hub and casing boundary layer.

- When Q_v decreases to 0.37 $m^3.s^{-1}$, for outlet of FR in JW1FR, the reversed flow extends to higher blade span and load increases at most part of span compared with that of design flow rate. But the loss increases below midspan as Q_v decreases to very low flow rate. When coupled with RR, the reversed flow almost disappears resulting from the suction effects of RR. Nevertheless, the load diminishes significantly below 50% span as well as near the tip compared with that of design flow rate. Only at the high blade span (between $50 - 90\%$) the load is increased considerably. Compared with $Q_v = 0.6$ $m^3.s^{-1}$, the load at $Q_v = 0.37$ $m^3.s^{-1}$ decreases significantly at almost all the blade span. It could be explained that as Q_v decreases to very low flow rate the loss due to increase of incidence angle augments rapidly which reduces load in both low blade span and near the tip region.

- when the flow passes through the RR, at partial flow rate, large reverse flow exists at outlet hub of the RR and RR over-corrected the flow in tangential direction which is considered to be loss.

3.3 Analysis of the wall pressure fluctuations

The wall pressure fluctuations are measured by a microphone situated at a distance Z_p = 5 mm downstream of the Front Rotor (see Fig. 2.2) and Z_p = 45 mm (at outlet of the Rear Rotor). The power spectral density (PSD) of these fluctuations for JW1 working at the design conditions and S = 10 mm are plotted in the Fig. 3.16. At each axial position, three flow rates have been studied: the design flow rate Q_v = 1 m^3.s^{-1}, a moderate partial flow rate Q_v = 0.6 m^3.s^{-1} and very low partial flow rate Q_v = 0.37 m^3.s^{-1}.

In Figure 3.16, one can notice the presence of several peaks in the spectra. These peaks can be divided into three types: those that correspond to the blade passing frequency of the Front Rotor ($f_{bpf,FR}$) and its harmonics are marked with $\circ$, while the peaks corresponding to the Rear Rotor blade passing frequency ($f_{bpf,RR}$) are marked with $\triangledown$ and finally, the interactions frequencies corresponding to combinations of the Front and Rear Rotor blade passing frequencies are marked with $*$. As a reference, the amplitudes of the symbols in the plots corresponding to partial flow rates are kept the same as in the design flow rates Z_p = 5 mm, in order to highlight the differences in the amplitudes between Q_v = 1 m^3.s^{-1}, 0.6 and 0.37 m^3.s^{-1}, and in the axial positions.

Several common features can be noticed from Fig. 3.16. Firstly, the amplitudes of the peaks corresponding to $f_{bpf,RR}$ and its harmonics are always significantly higher than that of $f_{bpf,FR}$. For the intermediate position(Fig. 3.16(a)), the influence of the Rear Rotor propagates upstream (potential effect) and is stronger than that of the Front Rotor (usually attributed to the wakes of the blades). Moreover, downstream of RR(Fig. 3.16(b)), on can notice that the peaks of the FR are still visible.

Further, it can be seen that the two rotors are in strong non-linear interaction at the design volume flow rate (Fig. 3.16(a)(b) Q_v = 1 m^3.s^{-1}). However, for partial flow rates, the peaks corresponding to the interactions are dramatically attenuated. At Z_p = 5 mm, the amplitudes corresponding to both $f_{bpf,FR}$ and $f_{bpf,RR}$ are increased (Fig. 3.16(a)Q_v = 0.6, 0.37 m^3.s^{-1}). Contrarily, for Z_p = 45 mm, the amplitudes corresponding to both $f_{bpf,FR}$ and $f_{bpf,RR}$ attenuates entirely (Fig. 3.16b(b)Q_v = 0.6,0.37 m^3.s^{-1}).

Additionally, it is obvious that the amplitudes of wall fluctuations at outlet of RR (Fig. 3.16(b)) are much lower than that of downstream the FR (Fig. 3.16(a)). It implies that the fluctuations could propagated to far upstream but attenuate quickly downstream for both the FR and RR. Therefore, at outlet of the FR, the fluctuations are reinforced by the RR and its interaction with the FR. While, at outlet of CRS, the flow is less influenced by the stage.

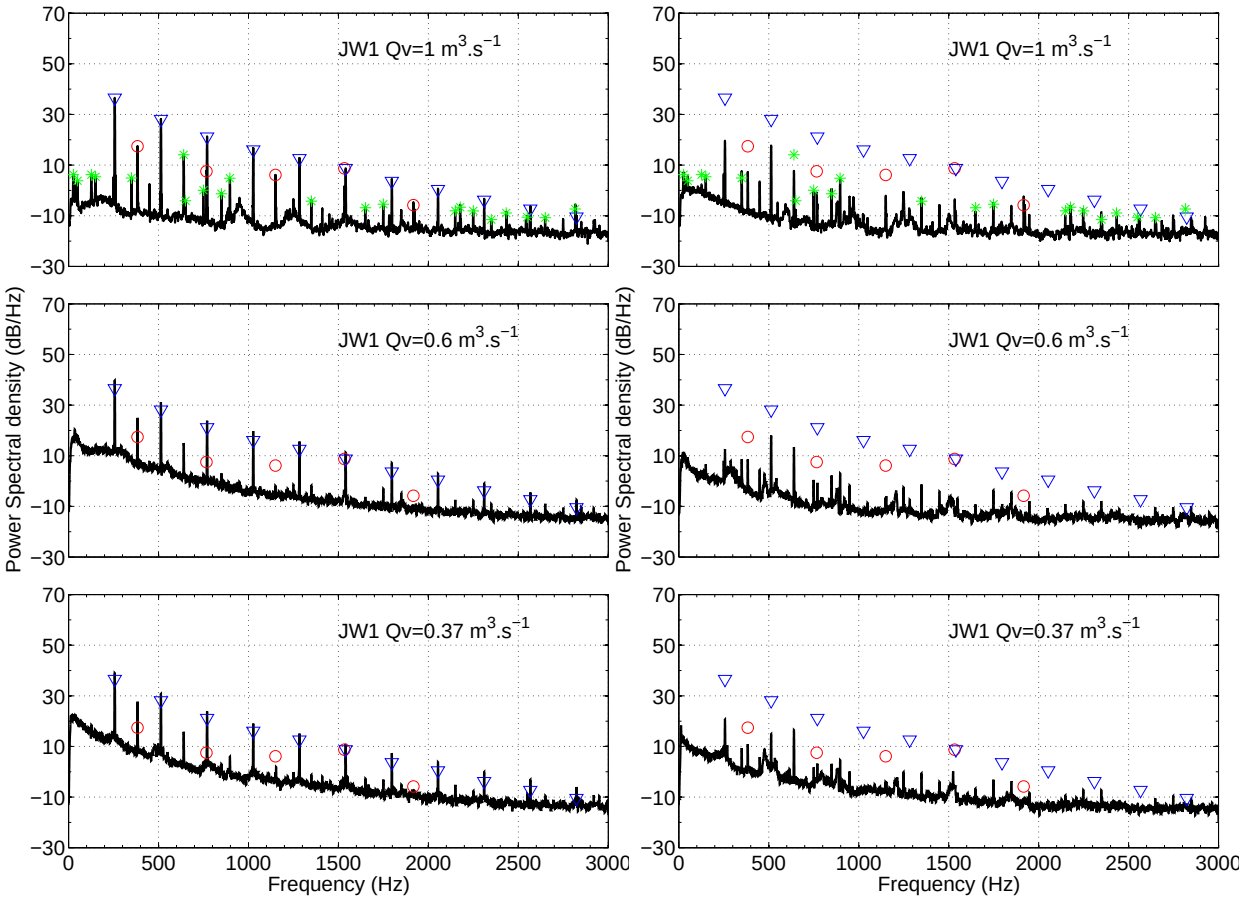

(a) at $Z_p = 5$ mm *(b) at $Z_p = 45$ mm*

Figure 3.16: PSD of the wall pressure fluctuations measured at $Z_p = 5$ and 45 mm, for JW1 at $N = 2300 - 2200$ rpm and $S = 10$mm, $Q_v = 1$, 0.6 and 0.37 $m^3.s^{-1}$. (○): $mf_{bpf,FR}$; (▽): $nf_{bpf,RR}$; and (∗): $mf_{bpf,FR} + nf_{bpf,RR}$ with $m \neq 0$ and $n \neq 0$.

3.4 Influence of the axial distance S on the performances of JW1 at $\theta = \theta_C$ and $Q_v = 1$ m^3.s^{-1}

As presented above, the effects of the axial distance S are not taken into account in the design process. Consequently, the optimal S is unknown. This section is focused on the influence of S on the global performance and velocity fields at different axial positions.

3.4.1 Influence of S on the global performance of JW1

A series of experiments varying S have been performed on JW1, with the help of the PMMA blocks [5] between the FR and RR. The global performances are plotted in Fig. 3.17 as a function of the volume flow rates Q_v, at $\theta = \theta_C$. The S varies in $[10, 300]$mm, which are $[0.2, 5.5]L_{chord}$ at midspan of FR of JW1. It can be seen that the ΔP_s and η_s decrease as the S enlarge in the whole operating range. Additionally, the amplitude of variations are relatively much smaller in $S \in [10, 100]$ mm, compared with the bigger distance.

Figure 3.18 shows the power consumption $\mathcal{P}_w$ by the stage JW1, measured by the torque meters and corrected by ρ_{ref}. According to the uncertainty analysis mentioned in Chapter 2, the uncertainties of corrected $\mathcal{P}_w$ are ±2.4, ±3.0 and ±5.4 W for the FR, RR and stage, respectively. As a reference, the power consumed by FR alone is also plotted in Fig. 3.18 (a) and (c). Overall, the presence of RR increases the power consumption of the FR compared with FR alone, as shown in Fig. 3.18 (a). Then it can be noticed that the power $\mathcal{P}_w$ consumed by the whole stage JW1 has the same trends as those by RR: it decreases monotonically while S increases. The reason is that the maximum absolute changes in $\mathcal{P}_w$ for FR are around 5 W (Fig.3.18(a)), which is relatively much smaller than that of RR (about 20 W in Fig.3.18(b)) at different S. Obviously, the axial distance has much more influence on the Rear Rotor than on the Front Rotor in JW1. It could be inferred that on one hand, as S increases, the RR has less influence on the FR, hence $\mathcal{P}_{w,FR}$ varies slightly; on the other hand, as S enlarges, the loss increases due to the mixing process downstream FR. Consequently, the RR is affected more than the FR.

Based on the experiments above, the features of performance at $Q_v = 1$ m^3.s^{-1} are picked out and plotted in Fig. 3.19 at different S. Obviously, ΔP_s and η_s decrease monotonically as S increases. Specifically, when $S \in [10, 100]$ mm, ΔP_s declines considerably by 12 Pa with slight fluctuations. At the same time, $\mathcal{P}_{w,FR}$ almost levels off and $\mathcal{P}_{w,RR}$ goes down gradually by 10.7 W. Consequently, the η_s remains almost constant. It decreases about 0.5 percentage point, which remains in the range of uncertainty. As $S \in [100, 200]$ mm, ΔP_s drops down significantly by 17 Pa. However, $\mathcal{P}_{w,FR}$ increase moderately by 1 W and $\mathcal{P}_{w,RR}$ decrease continually by 11.5 W. Hence, η_s decay by 2.0 percentage points, mainly due to rapid drop of ΔP_s.

Based on the performance analysis, it can be concluded that:

- Firstly, as axial distance increases the relative drop in static pressure is greater than the relative decrease in power consumption, which leads to a monotonic decrease in the efficiency.

- Secondly, it seems to exist a limit axial distance S around 100 mm. When S is above this value, $\mathcal{P}_{w,FR}$ increases slightly and $\mathcal{P}_{w,RR}$ decrease monotonically. Therefore,

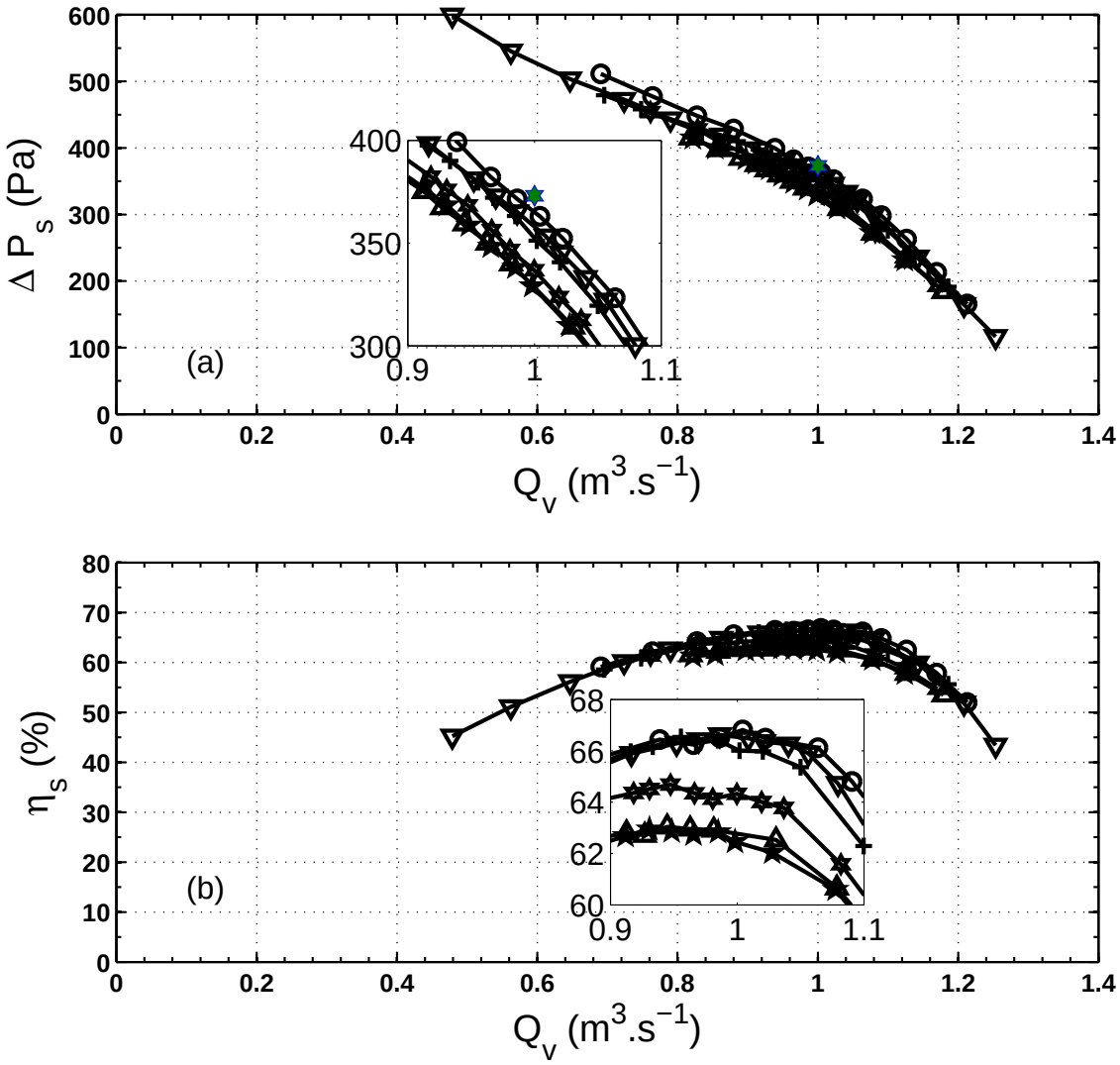

Figure 3.17: Performance $S = 10 - 300$ mm: $s = 10(\circ), 50(\triangledown)$, $100(+), 200$ $(\hexagram)$, $250(\triangle)$, 300 mm$(\bigstar)$; the design point $(\bigstar)$, ΔP_s rescaled by ρ_{ref}.

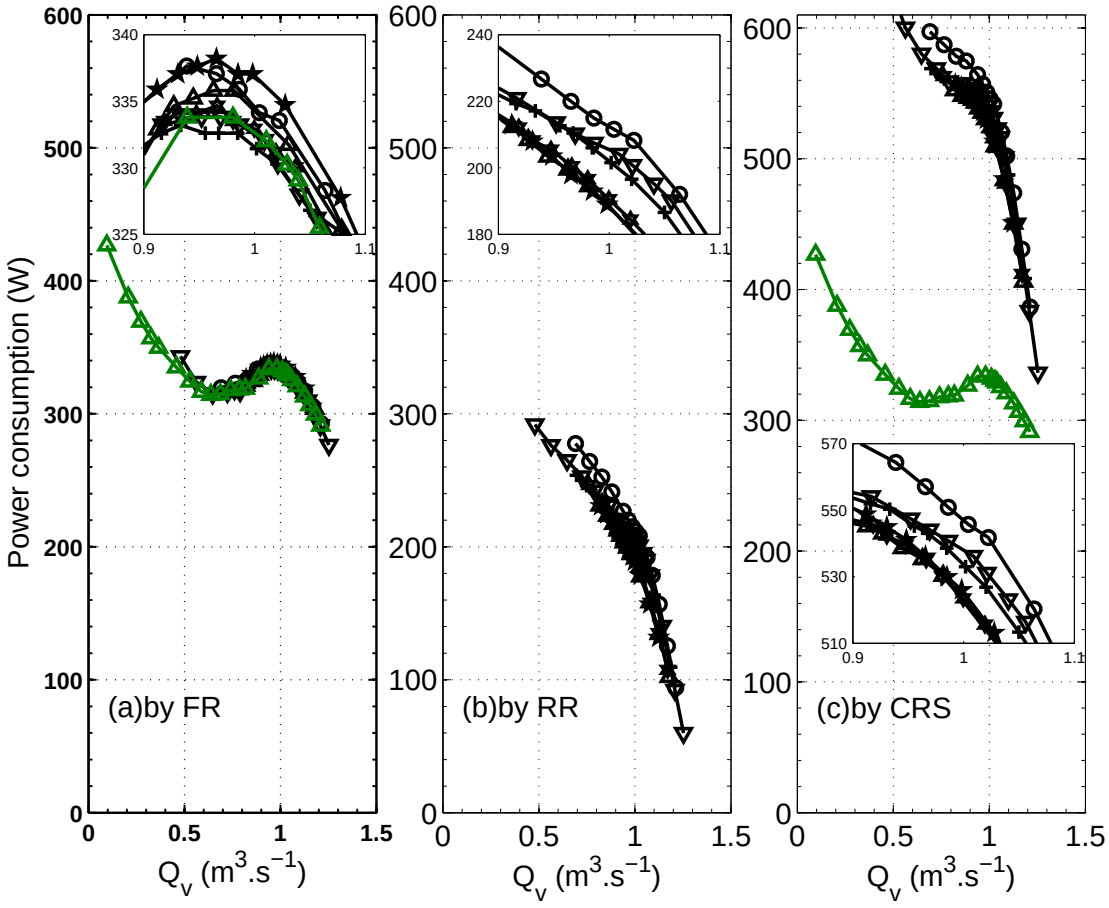

Figure 3.18: Power consumption of JW1(rescaled by ρ_{ref}) at S = 10 – 300 mm:s = 10(∘),50(▽), 100(+),200 (✡), 250(△), 300 mm(★); the power consumed by FR alone(△)

$\mathcal{P}_{w,t}$ decreases considerably. This decrease in power consumption could not cancel out the significant decline in static pressure rise. Thus, the static efficiency deteriorates dramatically. While as S is below this limit, the reduction in static pressure rise is relatively slight and could be balanced by the considerable decrease in power consumption caused by the Rear Rotor. Consequently, the static efficiency fluctuates and decays in a acceptable level by 0.5 percentage point.

- Finally, whatever S in $[10, 300]$ mm, η_s always stay beyond 62% at the design flow rate $Q_v = 1$ m^3.s^{-1}. It indicates that CRS has a stable high efficiency features on design flow rate at various axial distance.

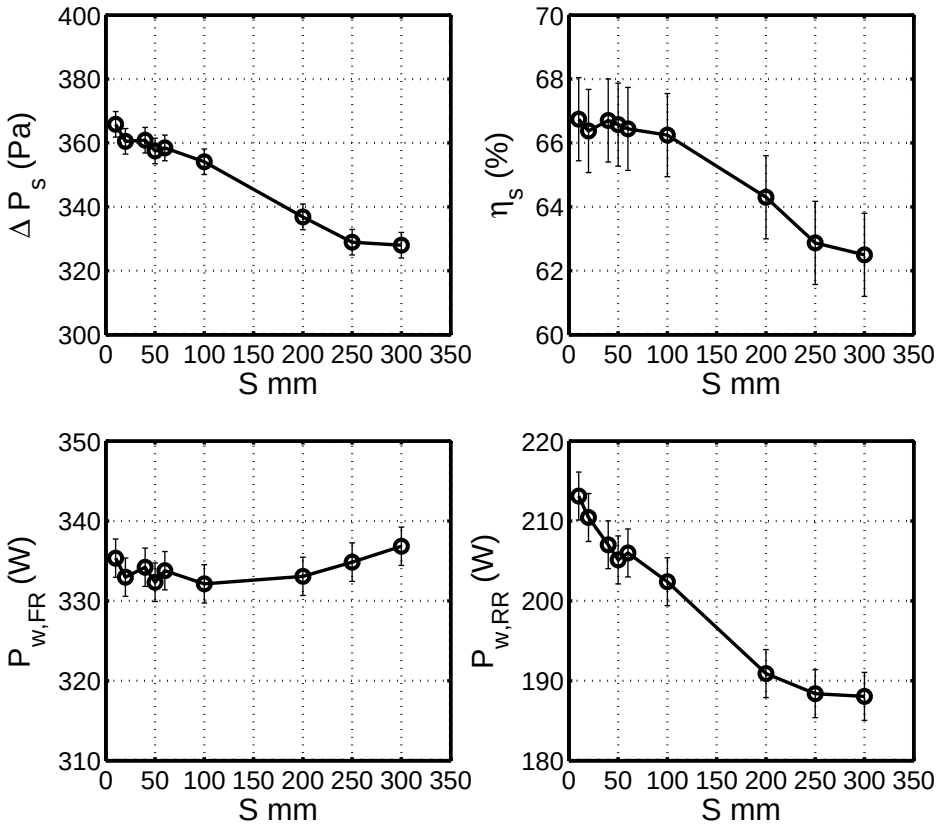

Figure 3.19: Performance of JW1 (∘)at $S = 10$, 20, 40, 50,60, 100, 200, 250, 300 mm at design point $Q_v = 1m^3.s^{-1}$, $\theta = \theta_C$, ΔP_s, $\mathcal{P}_{w,FR}$ and $\mathcal{P}_{w,RR}$ are rescaled by ρ_{MFT}

In order to understand the details of the deterioration in static pressure rise as S changes, LDV measurements have been conducted at $Q_v = 1$ m^3.s^{-1} between FR and RR at different S.

3.4.2 Influence of S on the velocity fields between FR and RR

Firstly, velocity fields 5 mm downstream of FR and 5 mm upstream of RR are analyzed to verify the influence of axial distance on the FR and RR.

Radial profiles of averaged V_z and V_θ downstream FR at various S.

Figure 3.20(a) shows the radial profiles of circumferential averaged velocity fields at Z_p = 5 mm downstream of FR, for $S = 10, 20, 40, 200$ mm. It can be seen that at S = 200 mm, V_z decreases slightly below midspan but greatly declines near the hub region. In contrary, V_θ has relatively large increase near the hub region, compared to the smaller distances. It indicates that with the RR far away, the aspiration effect from RR is attenuated at low blade span. And the blade loading increases at low blade span.

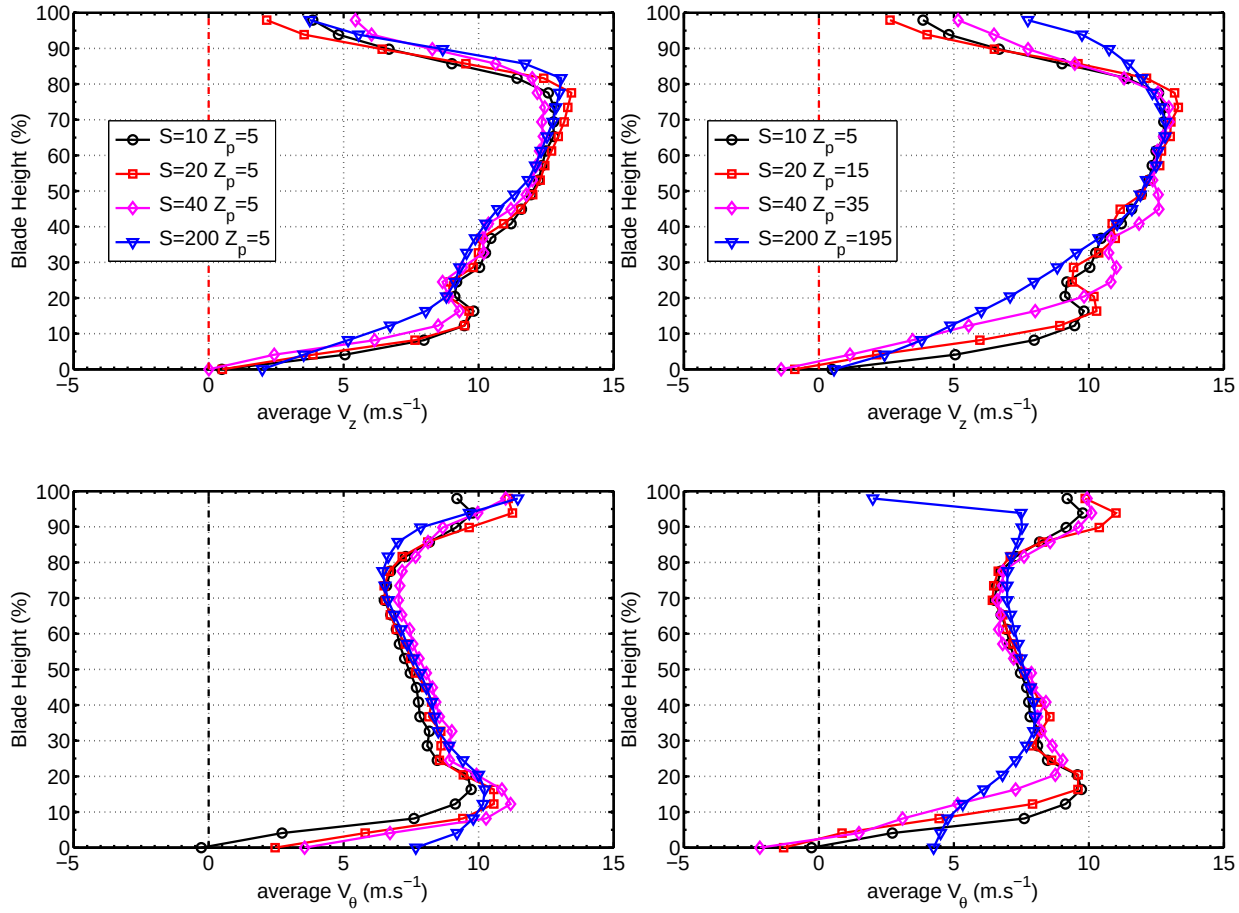

(a) Downstream FR in JW1 *(b) Upstream of RR in JW1*

Figure 3.20: Circumferential averaged velocity fields between FR and RR in JW1 at various S at design point $Q_v = 1m^3.s^{-1}$, $\theta = \theta_C$. (a) downstream of FR Z_p = 5 mm, S = 10, 20, 40, 200 mm; (b) upstream of RR at $Z_p = 5(S = 10)$, $Z_p = 15(S = 20)$,$Z_p = 35(S = 40)$ and $Z_p = 195(S = 200)$ mm

Radial profiles of averaged V_z and V_θ upstream of RR at various S.

Figure 3.20(b) shows the radial profiles of circumferential averaged velocity fields at 5 mm upstream of RR for S = 10, 20, 40, 200 mm. It means that velocities are measured at $Z_p = 5(S = 10)$, $Z_p = 15(S = 20)$,$Z_p = 35(S = 40)$ and $Z_p = 195(S = 200)$ mm. It could be

noticed that the averaged velocity fields change dramatically upstream of RR at large axial distance $S = 200$ mm. First of all, the axial velocities upstream RR increase considerably near the hub region and decrease significantly at low span at $S = 200$ mm, compared with those of smaller distances. Then the tangential velocities attenuate dramatically near both tip and hub region as S enlarges to 200 mm. Therefore, upstream of RR, the aspiration effects of RR is quite obvious at $S = 200$ mm owing to the rotation of RR. However, the tangential velocities attenuate significantly both near the tip and near the hub region but increase closed to hub region, compared with those downstream of FR. The reason could be the friction loss and the wake decay from downstream FR to upstream of RR. Near the the tip region, V_θ diminishes due to the friction loss near the casing wall. And near the hub region, the high V_θ ($10-20\%$ blade span) seems to energize the low V_θ close to hub($0-10\%$ blade span). This process could be related to the wake mixing and wake recovery as mentioned in Ref. [17][49].

Diminution of dynamic pressure between downstream of FR and upstream of RR

The tangential velocities deficit (in Fig. 3.20(b)) will introduce the decrease in the tangential part of dynamic pressure $P_{dyn,\theta}$ between FR and RR. The tangential part of dynamic pressure could be calculated based on the volume flow rate weighted of averaged tangential velocities:

$$P_{dyn,\theta} = \frac{\int_R \frac{1}{2}\rho V_\theta^2 \times 2\pi R V_z dR}{\int_R 2\pi R V_z dR} \tag{3.3}$$

This diminution of dynamic pressure could not be transformed to static pressure rise by RR and is considered as loss. To evaluate the influence of this loss on the static pressure rise drop in CRS, the volume flow weighted dynamic pressures in tangential direction are calculated at 5 mm downstream FR and 5 mm upstream RR based on the circumferential averaged velocities at each S at design flow rate, listed in Tab. 3.3. One can notice that at $S = 10$ mm the position 5 mm downstream FR is the same as 5 mm upstream RR. Therefore, tangential part of dynamic pressure $P_{dyn,\theta}$ is the same. Then as S increases from 10 to 40 mm, the tangential part of dynamic pressure drop increases about 5 Pa, and the static pressure rise ΔP_s for JW1 deceases about 5 Pa (taken from Fig.3.19). Therefore, as S enlarges moderately, the static pressure rise drop is of the same order of the tangential part of dynamic pressure drop between FR and RR. Then as S increases to 200 mm, the tangential part of dynamic pressure drop increase to 6 Pa but the static pressure rise for JW1 drops by 29 Pa. It indicates that when S increases moderately the static pressure rise drop is mainly due to the tangential part of dynamic pressure decay between the FR and RR. However, as S is large enough, the static pressure drop is much big than the tangential part of dynamic pressure drop between the FR and RR. The possible reason could be the loss in the rotors.

In order to verify the loss in both FR and RR, the deviation angle of FR and incidence angle of RR are calculated based on the circumferential averaged velocities 5 mm downstream FR and 5 mm upstream RR.

S (mm)	$P_{dyn,\theta}$ (Pa)		$\Delta P_{dyn,\theta}$ (Pa)	ΔP_s (Pa)
	5 mm downstream FR	5 mm upstream RR		
10	35.7	35.7	0	365.8 ±4
20	38.2	36.6	1.6	360.5 ±4
40	41.9	36.6	5.3	360.9 ±4
200	37.3	31.3	6	336.8 ±4

Table 3.3: Comparison between volume flow rate weighted tangential part of dynamic pressure drop $\Delta P_{dyn,\theta}$ (from 5 mm downstream FR to 5 mm upstream RR) and static pressure rise ΔP_s for JW1 at each axial distance $S = 10, 20, 40, 200$ mm, at $Q_v = 1\ m^3.s^{-1}$, $\theta = \theta_C$.

3.4.3 Influence of S on the flow angles between FR and RR

The flow angles are calculated based on the LDV results at outlet of FR and inlet of RR.

Radial distribution of $\delta_{2,FR}$ downstream FR.

Figure 3.21(a) shows the flow deviation angle $\delta_{2,FR}$ of FR, which is defined as the difference between the relative outlet flow angle $\beta_{2,FR}$ and blade outlet angle of FR $\beta'_{2,FR}$. The $\beta'_{2,FR}$ are the angle between the tangent of the camber line at the trailing edge and axial direction. In most part of the blade span, $\delta_{2,FR}$ fluctuates by maximum 3 degrees, except below 20% blade span where $\delta_{2,FR}$ for $S = 200$mm increases by $6 - 10$ degrees compared with smaller S. This implies that the flow deviate significantly from the curvature of the blade at the trailing edge, which indicates a large loss in this region. This could mainly results from the decreased axial velocities near the hub region due to weakened aspiration effects of RR as S is large. Overall, the axial distance has slightly influence on the flow in FR at most of the blade span.

Radial distribution of $i_{1,RR}$ upstream RR.

Figure 3.21(b) presents the incidence angles $i_{1,RR}$ 5 mm upstream of the RR at $S = [10, 20, 40, 200]$ mm. Overall, the incidence angle decrease from 5 degrees to near 0 at high blade span(over 80% of blade height), as S increases to 200 mm. Then S seems has no influence on the $i_{1,RR}$ at $50 - 80\%$ of blade height. After, at $30 - 50\%$ of blade height, $i_{1,RR}$ changes slightly by $1 - 2$ degrees as S varies. Lastly, near the hub, the incidence angle increase monotonically from about -5 to positive values. Briefly, as S increases to 200 mm, the incidence angle of RR decreases considerably near the tip region(beyond 80% blade span). This would decrease the blade loading and flow deflection at the tip region, thus less work will be done at this region. And this could be one of the main reason for the large static pressure drop of JW1 as S increases to 200 mm. Then the incidence angle increase moderately near the hub region, which could slightly increase the load but still not enough to compensate the diminution of work done at the tip.

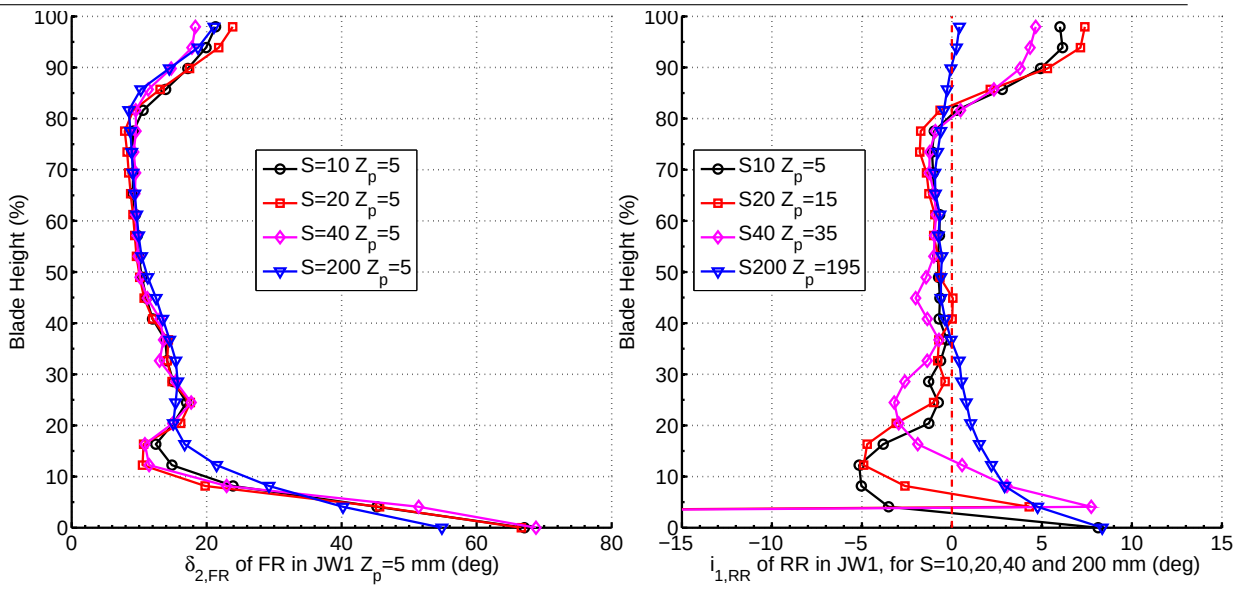

(a) Downstream FR in JW1 *(b) Upstream of RR in JW1*

Figure 3.21: Flow angles between FR and RR in JW1 at various S at design point $Q_v = 1m^3.s^{-1}$, $\theta = \theta_C$. (a) downstream of FR $Z_p = 5$ mm, $S = 10$, 20, 40, 200 mm; (b) upstream of RR at $Z_p = 5(S = 10)$, $Z_p = 15(S = 20)$,$Z_p = 35(S = 40)$ and $Z_p = 195(S = 200)$ mm

3.4.4 Influence of S on the velocity field at different axial positions when S is fixed

On the above flow structure analysis, the velocity fields are only given at the axial position near the FR and near the RR. In this part, the circumferential averaged velocity profiles are give at different axial positions at a fixed S to investigate the evolution of velocities fields between FR and RR.

Figure 3.22 shows the averaged velocity profiles downstream the FR at different axial positions $Z_p = 5, 10, 15, 20, 35$ mm at a fixed $S = 40$ mm. The axial velocities V_z increases at most of blade span $(20 - 80\%)$ and consequently decreases near the hub and tip region as axial position Z_p increases. It indicates that the fluid is transferred towards the middle span of blade from the hub and tip region as Z_p is away from outlet of the Front Rotor. And averaged tangential velocities display a dramatically deterioration near the hub region(below 20% of blade height) away from the outlet of the FR. Briefly, at a fixed axial distance $S = 40$ mm, as axial position Z_p increases, the tangential velocity decays gradually near the hub region and the aspiration effects of RR strengthens progressively .

3.4.5 Conclusion

To conclude, for our case, the small axial distance S is beneficial for the performance of JW1. Additionally, the static efficiency η_s could remain as high as 66% at design flow rate when the S varies from 10 to 100 mm. During this process, the static pressure rise decays moderately, but does not cause strong deterioration in static efficiency. This is owing to the simultaneously decrease in the total power consumption of the stage, mainly

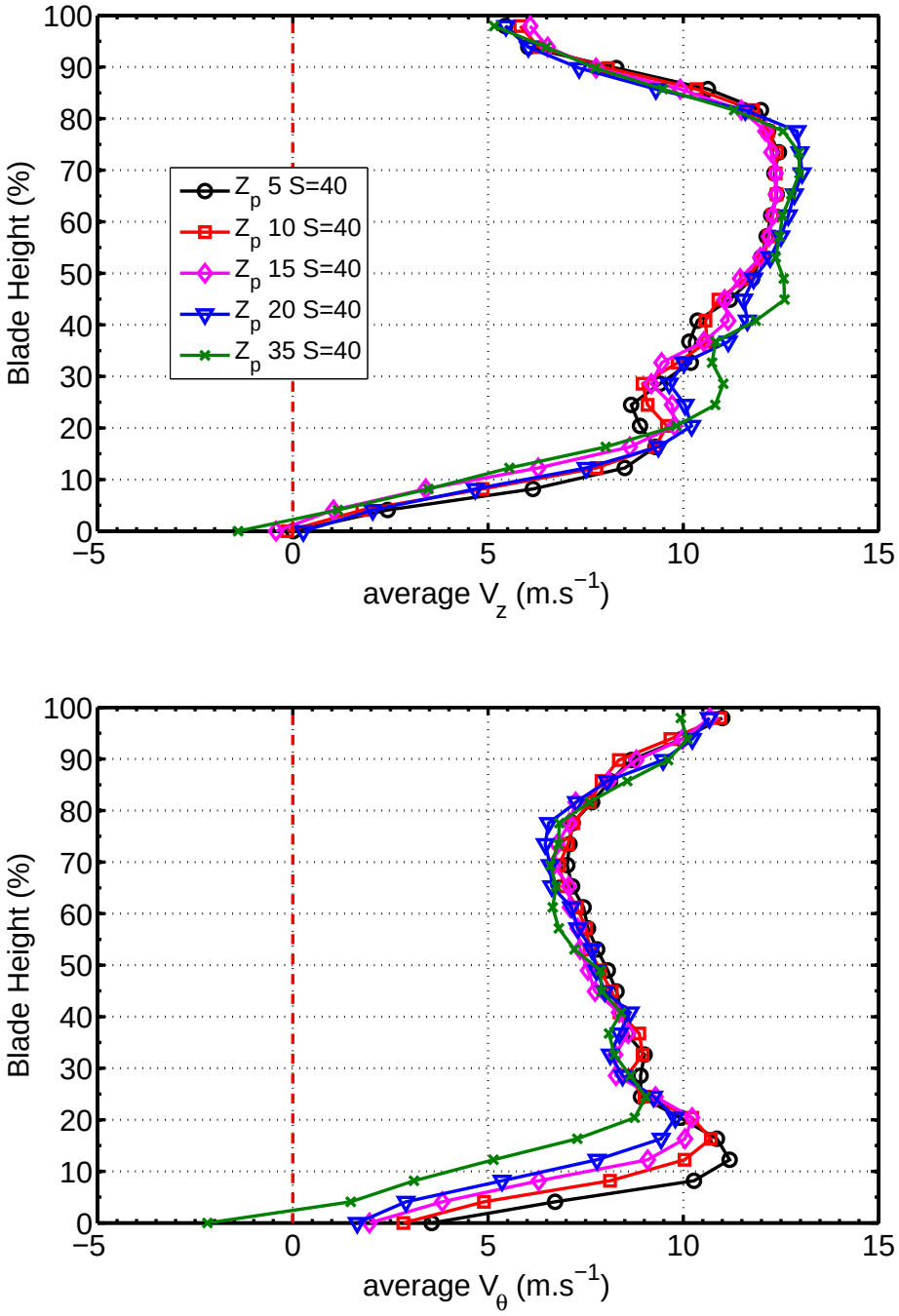

Figure 3.22: Averaged velocity fields downstream of FR Z_p = 5,10, 15, 20, 35 *mm,* S = 40 *mm, in JW1 at various* S *at design point* $Q_v = 1m^3.s^{-1}$, $\theta = \theta_C$.

resulted from the reduction in the Rear Rotor. While as S increases beyond 100 mm, the influence of significant drop in ΔP_s are more than offset by continuously decrease in total power consumption. Consequently, the static efficiency drops substantially to 62.5% at $S = 300$mm.

Looking inside the velocity fields at different S, it is found that three effects are responsible for this relatively high drop in ΔP_s at large distance. The first effect is due to the Front Rotor. When the RR is relatively far from the FR, increased load and decreased air flow near the hub region lead to the increase in deviation angle of FR. It means that the flow is less following the blade, which could probably cause the increase of loss. The second effect is due to the significant velocity deficit both near the hub and tip region between the FR and RR due to the wall friction loss and wake decay. This could induce tangential part of dynamic pressure drop which could not be transformed to stage static pressure rise. The last effect is the diminution of the work done by Rear Rotor near tip region. As S increases, the fluid tends to concentrate near the high span of the blade while tangential velocities significantly deteriorate near the hub and tip region. Thus the incidence angle of RR decreases to 0 at high blade span and increases to positive at low blade span. According to the Euler Work Equation $\mathcal{P}_{Euler} = \dot{m}U\Delta V_\theta$, the tip region has more work change between the blade and fluid than lower blade span. Thus the diminution of V_θ and $i_{1,RR}$ could induce largely static pressure drop of stage. In another word, the moderate pressure drop is mainly due to the friction loss and wake decay between the FR and RR as S is small but the largely pressure drop is mainly due to the diminution of work done near the tip region of RR.

3.5 Influence of speed ratio θ on the performances of CRS

The second important parameter for CRS is the speed ratio θ. Therefore this section is devoted to the analysis of the influence of θ on the CRS. The JW1 is designed for a design speed ratio $\theta_C = 0.96$ and rotation speed of the FR: $N_{FR} = 2300$ rpm. Firstly, experiments are conducted on JW1 at keeping the N_{FR} constant and varying $\theta \in [0.86, 1.2]($ $[0.9, 1.25]\theta_C)$, with S fixed at $S = 10$ mm. The global performance are presented as well as the velocity fields and related flow angles at different axial positions. Then, in order to get higher θ, the rotation speed of the FR is diminished to 1400 rpm.

3.5.1 Influence of θ on the global performance at $N_{FR} = 2300$ rpm

The performance curves of JW1 at a constant $N_{FR} = 2300$ rpm with various θ are illustrated in Fig. 3.23. It can be noticed that the nominal flow rate is shifted progressively towards higher flow rates as θ increases. In this section, the maximum static efficiency $\eta_{s,max}$ is presented and analyzed instead of η_s at $Q_v = 1$ m^3.s^{-1}.

Further, in Fig. 3.23(b), the performances are improved up to a maximum static efficiency of 68% when θ is increased from $0.9\theta_C$ to $1.25\theta_C$. This feature has also been observed for the prototype named "HSN" used in Ref. [6]. In addition, the maximum efficiency of the JW1 is slightly higher that that of HSN (66.5%) for various θ. There are two possible reason for this: on one hand, JW1 has ameliorated the circulation at inlet of the FR compared with that of HSN; on the other hand, the JW1 has higher Reynolds number than HSN, which could possibly lowers the loss. Then at $Q_v < 1$ m^3.s^{-1}, JW1 working at θ_C has the best static efficiency compared with that of off-design θ. In order to understand these characteristics, it is necessary to look into the velocity field at different θ.

Then the power consumption by FR and RR is plotted in Fig. 3.24 at $N_{FR} = 2300$ rpm, $\theta \in [0.86, 1.2]($ $[0.9, 1.25]\theta_C)$. It is clear that the θ has no influence on the power consumption of FR, but largely increases those of RR as θ increases. Consequently, the total power consumption by the stage JW1 increase. However, the increase in static pressure rise is faster than the increase of power consumption. Therefore, the static efficiency is improved as θ increases, as can be seen in Fig. 3.23(b).

3.5.2 Influence of θ on the velocity field at $N_{FR} = 2300$ rpm

Velocities are measured at $\theta = 0.86(0.9\theta_C), 0.96(1.0\theta_C), 1.1(1.15\theta_C)$, downstream the FR ($Z_p = 5$ mm) and downstream the RR ($Z_p = 50$ mm) in JW1 , at $Q_v = 1$m^3.s^{-1}and $S = 10$ mm.

Downstream the FR ($Z_p = 5$ mm). Figure 3.25(a) shows the averaged axial (V_z) and tangential (V_θ) velocity profiles downstream of FR of JW1 (mid position between FR and RR). As θ increases, the averaged axial velocities V_z increase at $50-80$% of blade height and consequently diminish considerably below 20% of blade height (near the hub). This is typically increased aspiration effect of RR as θ augments. At the same time, averaged tangential velocities V_θ decrease dramatically by nearly 10 m.s^{-1} near the hub and 5 m.s^{-1}

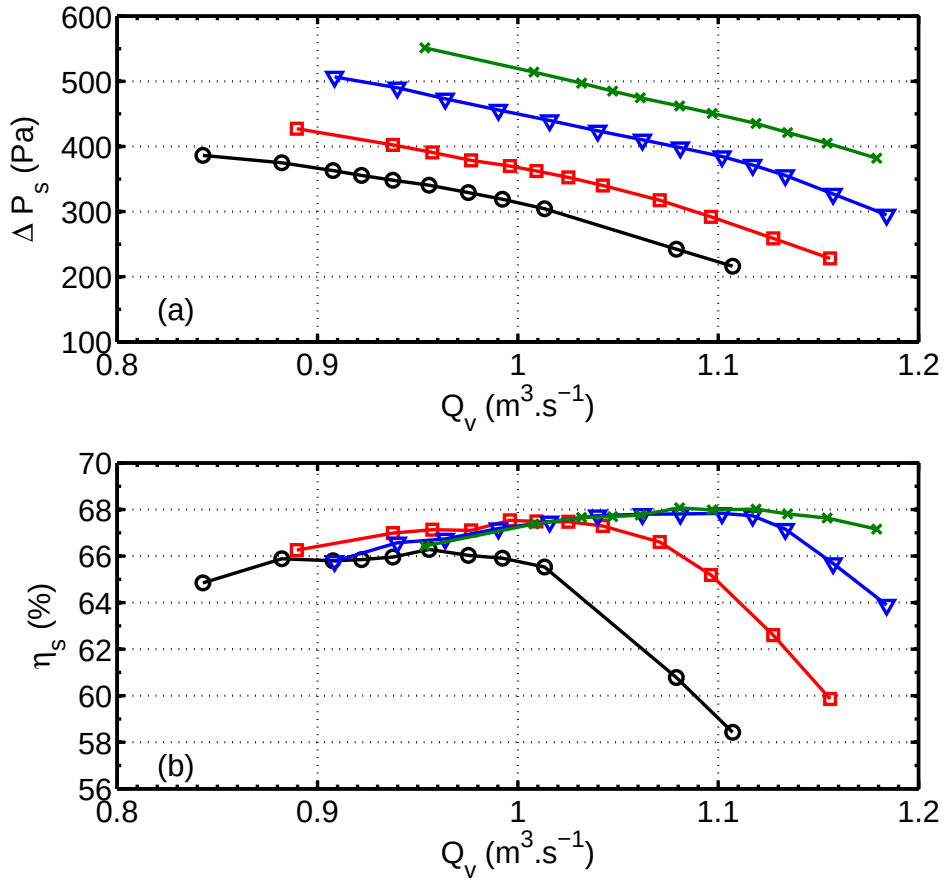

Figure 3.23: Overall performance of stage JW1 at Q_v = 1 $m^3.s^{-1}$, S = 10 mm, N_{FR} = 2300 rpm, θ = [0.86 $(0.9\theta_C$ ∘$)$, 0.96 $(1.0\theta_C$ □$)$, 1.1 $(1.15\theta_C$ ▽$)$, 1.2 $(1.25\theta_C$ ×$)$], θ_C = 0.96.

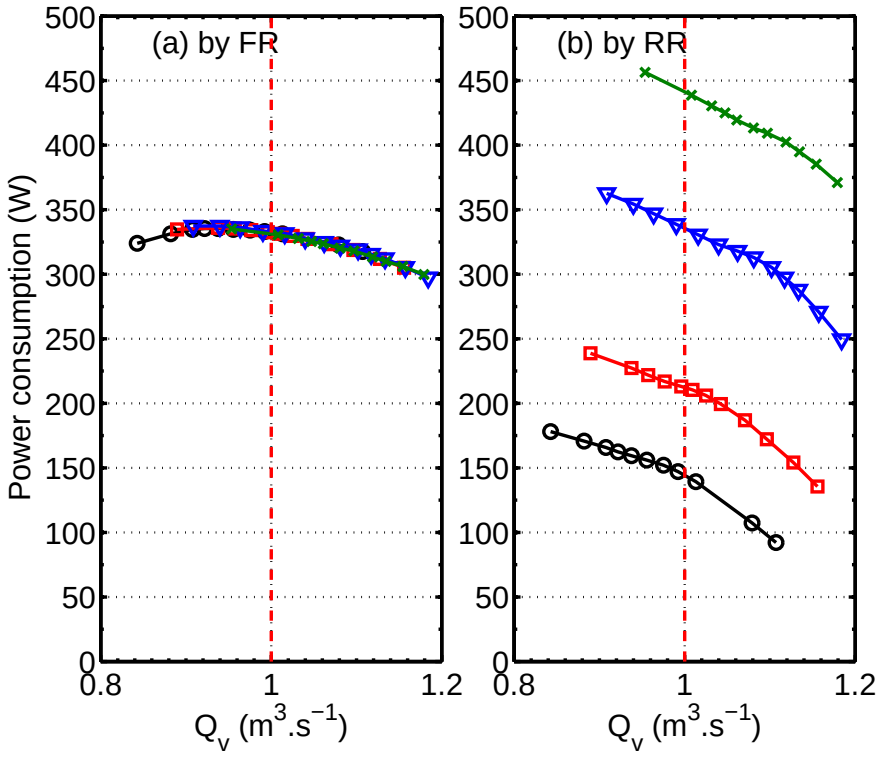

Figure 3.24: Power consumption of FR and RR in stage JW1(Rescaled by ρ_{ref}) at Q_v = 1 $m^3.s^{-1}$, S = 10 mm, N_{FR} = 2300 rpm, θ = [0.86 ($0.9\theta_C$ ∘), 0.96 ($1.0\theta_C$ □), 1.1 ($1.15\theta_C$ ▽), 1.2 ($1.25\theta_C$ ×)], θ_C = 0.96.

near the tip, with the rest part of blade almost remains constant. The declines in V_θ infers the lower blade load of the FR at these regions while θ increases.

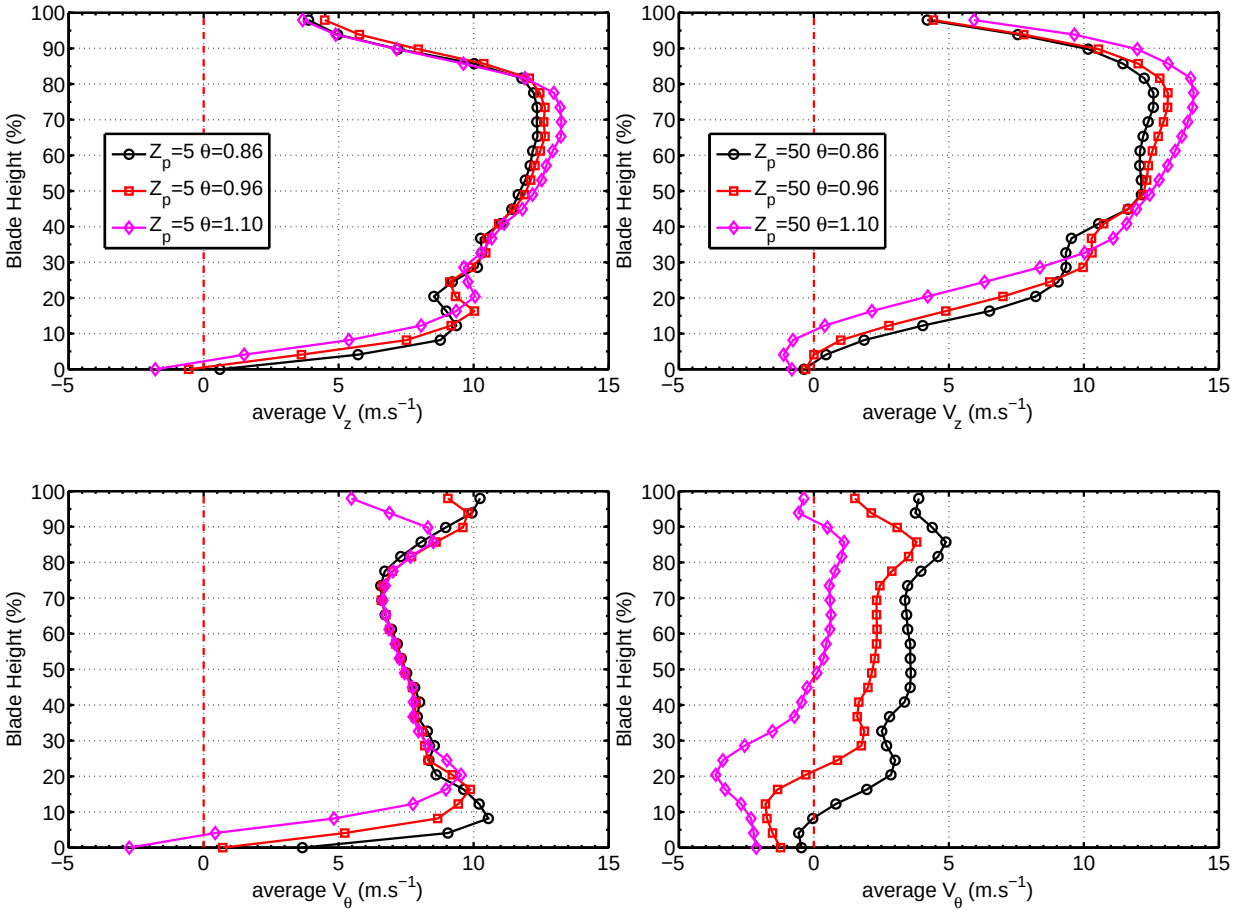

(a) Downstream FR in JW1 *(b) Downstream of RR in JW1*

Figure 3.25: Circumferential averaged velocities profiles in JW1 , for θ = 0.86$(0.9\theta_C)$,0.96(θ_C), 1.1$(1.15\theta_C)$ at design point $Q_v = 1m^3.s^{-1}$, S = 10 mm (a) downstream of the FR at Z_p = 5 mm; (a) downstream of the RR at Z_p = 50 mm

Downstream of CRS Z_p = 50 mm. Figure 3.25(b) displays a clear modification of the profile of averaged V_z and V_θ 5 mm downstream RR in JW1. One one hand, as θ enlarges, V_z decreases at low blade span, even to negative near the hub at θ = 1.1 $(1.15\theta_C)$. And V_z increases at high blade span (above 50% blade height). Therefore, the higher rotational speed of the rear rotor seems to enhance the effect of transmitting the air towards higher blade span, moreover, reversed flow appears close to the hub region at high θ. On the other hand, V_θ diminishes significantly along all the blade span. Additionally, RR with high rotational speed redresses the V_θ towards 0 above middle span, but over-corrects below the middle span, as θ increases. The decreased tangential velocity downstream RR causes the higher ΔV_θ for RR as V_θ are almost constant at most blade span at inlet of RR(downstream of FR) in Fig. 3.25(a). Additionally, the increased rotation speed of RR also contributes to the work done by the RR $W_{work,RR} = \rho U \Delta V_\theta$ per unit volume flow

rate. Therefore, the higher ΔP_s in Fig. 3.23(a) is mainly owing to the increased work done by the RR.

3.5.3 Influence of θ on the flow angles at N_{FR} = 2300 rpm

The variations in axial and tangential velocities of different θ presented above induce the modifications flow angles of the FR and RR in JW1.

Between FR and RR Figure 3.26a(a) illustrates a huge increase of deviation angle $\delta_{FR,2}$ by $10-27$ degrees near the hub region of FR (below 20% of blade span). This indicates a diminution in ΔV_θ for FR which reflects a reduction in work done of FR near the hub region. This induces the increase of loss near the hub of FR at a higher θ. On the other hand, since the axial distance is fixed at S = 10 mm, Z_p = 5 mm can also be considered as the inlet of the RR. Therefore, the incidence angle of the RR can be calculated and shown in Fig. 3.26a(b). As θ increases, the $i_{1,RR}$ increases considerably at all the blade span. Then the incidence angle of RR becomes positive above 20% blade span and with a relatively smaller negative incidence near the hub at inlet of RR as $\theta = 1.1(1.15\theta_C)$. This increased incidence angles lead to higher load and flow deflection, thus, higher work done by RR.

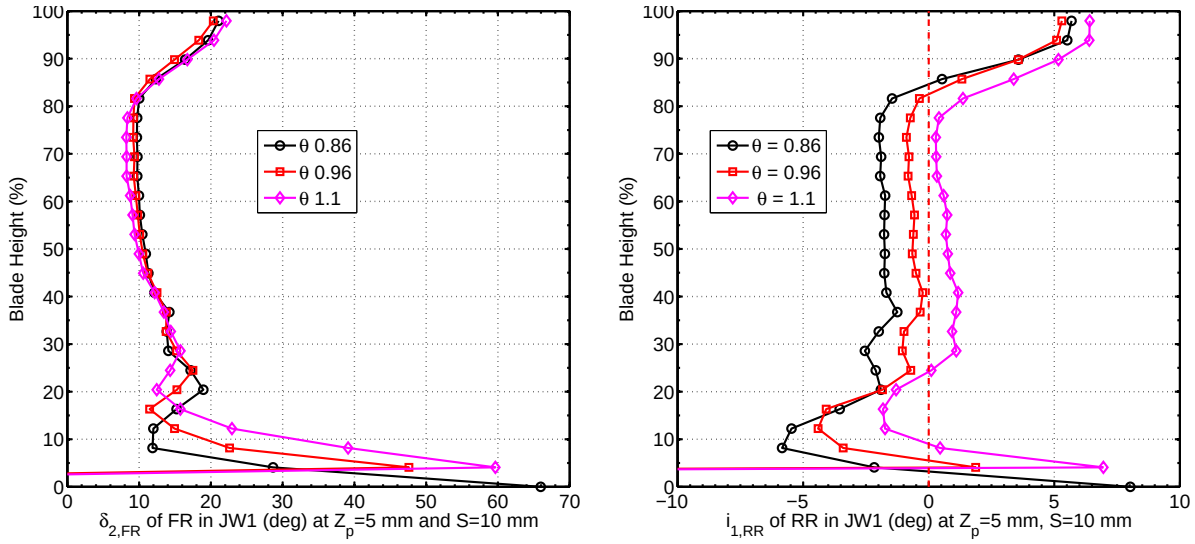

(a) Deviation angle of FR $\delta_{2,FR}$ *(b) Incidence angle of the RR $i_{1,RR}$*

Figure 3.26: Calculated flow angles downstream FR (between FR and RR) in JW1 at Z_p = 5 mm, for $\theta = 0.86(0.9\theta_C)$,$0.96(\theta_C)$, $1.1(1.15\theta_C)$, at design point $Q_v = 1m^3.s^{-1}$, S = 10 mm. (a)deviation angle of FR; (b) incidence angle of RR

downstream of RR Figure 3.27 shows the deviation angle 5 mm downstream of RR at $\theta = 0.86(0.9\theta_C)$,$0.96(\theta_C)$ and $1.1(1.15\theta_C)$, at design point $Q_v = 1\text{m}^3.\text{s}^{-1}$, S = 10 mm. The deviation angle of RR $\delta_{RR,2}$ is calculated from the averaged V_z and V_θ. It can be seen that $\delta_{RR,2}$ increases at almost all the blade span as θ augments, especially below 30%

blade span. This increased deviation angle for RR reveals the increases of loss in RR due to boundary layer separation at high diffusion.

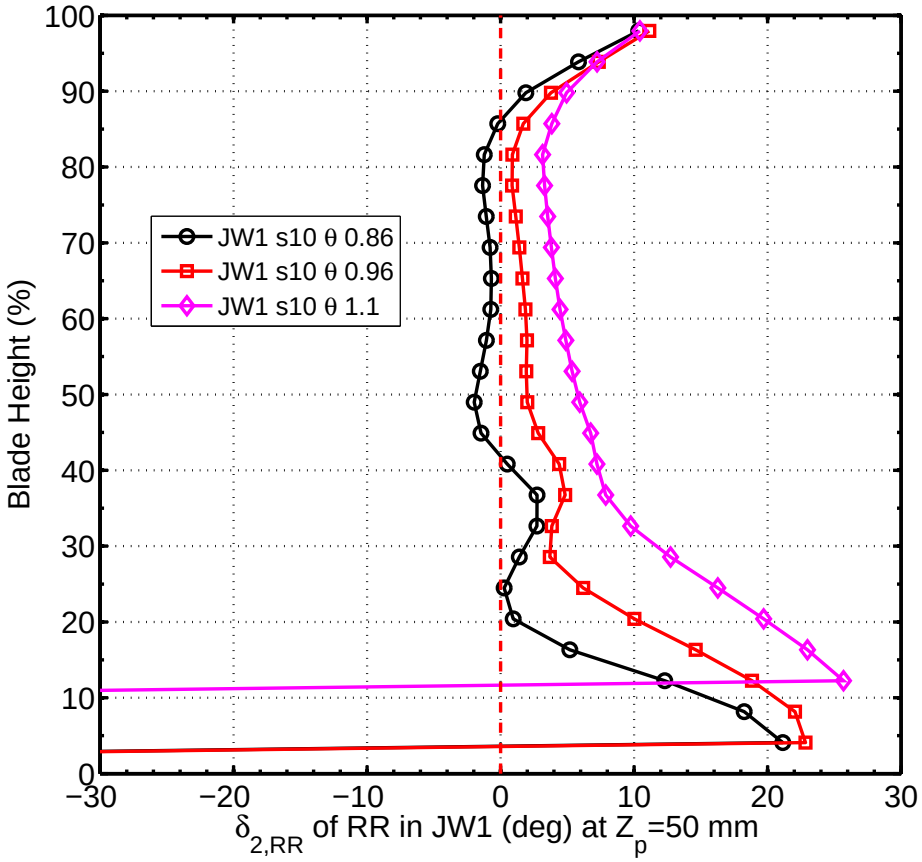

Figure 3.27: The difference between the relative outlet angle and blade outlet angle for RR in JW1 at Z_p = 50 mm, for θ = 0.86$(0.9\theta_C)$,0.96(θ_C), 1.1$(1.15\theta_C)$at design point $Q_v = 1m^3.s^{-1}$, S = 10 mm

In summary, when the RR turns faster, at outlet of FR fluid are transferred from the low blade span to high blade span. Additionally, increased θ has slightly influence on the load of FR at most of blade span, except decreasing the load of FR near the tip and hub region. Consequently the deviation angles is increased at the hub region, which induces large loss in FR. At inlet of RR, the higher rotational speed of RR increases the incidence angle from negative to positive almost at all blade span which increases load of RR. At outlet of RR, the fluid continue to be transferred from the hub to the tip region, even cause a reversed flow near the hub at $\theta = 1.15\theta_C$. And the higher rotational speed of RR recovers more tangential energy above the middle span, but over turns the flow in the opposite tangential position. Moreover, a significant increase of deviation angle of RR is observed at low blade span by 15 degrees. This is mainly caused by the increased diffusion in RR which induces large boundary layer separation. Despite this great deviation angle at outlet of RR for higher θ, more work has been done by the RR both by increasing blade speed U and flow turning ΔV_θ through RR at higher θ. Thus, the static pressure rise increased significantly at higher θ. The increases in static pressure rise is faster than

the augmentation of power consumption of stage, thus, the static efficient is improved as well.

3.5.4 Influence of θ at different rotating speeds of FR

As can be seen from Fig. 3.23, as θ increases from $0.9\theta_C$ to $1.25\theta_C$, the maximum efficiency raises monotonically. As a result, it is necessary to continue to increase the θ to find the limit of the maximum efficiency. However, due to the limitation of the rotational speed of the motors at maximum 3000 rpm, it is difficult to get higher θ and keep $N_{FR} = 2300$ rpm at the same time. One solution to get higher speed ratios is to decrease the N_{FR}.

Nevertheless, the reduced N_{FR} has a risk to introduce a deterioration on the efficiency due to lower Reynolds number effects. Hence, in the following part, the behaviour of JW1 at the same θ but different N_{FR} is compared in non-dimensional form. The non-dimensional parameters are volume flow coefficient ϕ and head coefficient ψ, which are defined as follows:

$$\phi = \frac{Q_v}{\pi\omega R_{tip}^3} \tag{3.4}$$

$$\psi = \frac{\Delta P_s}{\rho(R_{tip}\omega)^2} \tag{3.5}$$

within $R_{tip} = 0.1875$ m and $\omega = \sqrt{\omega_{FR}\omega_{RR}}$, the volume flow coefficient $\phi \propto \frac{V_z}{U}$ and $\psi \propto \frac{V_\theta}{U}$. This means that the head coefficient reflects the load of the CRS.

Then, the maximum efficiency $\eta_{s,max}$ as a function of θ/θ_C are outlined for JW1 at the design N_{FR} and reduced N_{FR}.

Global Performance at $N_{FR} = 2300$ and 1400 at $\theta = \theta_C$

A reduced $N_{FR} = 1400$ rpm is chosen considering about the desired high θ. Fig. 3.28 shows the non-dimensional performance for $N_{FR} = 2300$ and $N_{FR} = 1400$, at $\theta = \theta_C$. The two performance curves almost overlap as $\phi < 0.206$ corresponding to the design volume flow rate for JW1 working at design N_{FR}. However, considerably deterioration occurs at high over flow rates. This decrease in efficiency cause a discrepancy for $\eta_{s,max}$ by about 1 percentage point. This discrepancy could be explained as an effect of the Reynold's number Re. Lower Re induces larger losses in the flow which deteriorates the efficiency.

The Reynold's number based on the inlet relative velocity W and on the chord length L_{chord} at mid-span, $Re = \frac{\rho_a W L_{chord}}{\mu}$ is of the order of $Re \approx 1.2 \times 10^5$ for JW1 at $N_{FR} = 2300$ rpm, and $Re \approx 7.3 \times 10^4$ at $N_{FR} = 1400$ rpm.

Global performance at $N_{FR} = 1400$ rpm with $\theta/\theta_C \in [0.6, 2]$

The global performance of JW1 at a reduced $N_{FR} = 1400$ rpm with $\theta/\theta_C \in [0.6, 2]$ is plotted in Fig. 3.29. It can be seen that the static pressure rise increases monotonically as θ enlarges(Fig. 3.29(a)). However, the maximum static pressure increases firstly as θ enlarges but then drops significantly as θ beyond a limit. Moreover, the nominal flow rate(at maximum η_s) increases monotonically as θ augments. According to the flow features presented above, it could infer that as θ increases moderately the large augmentation

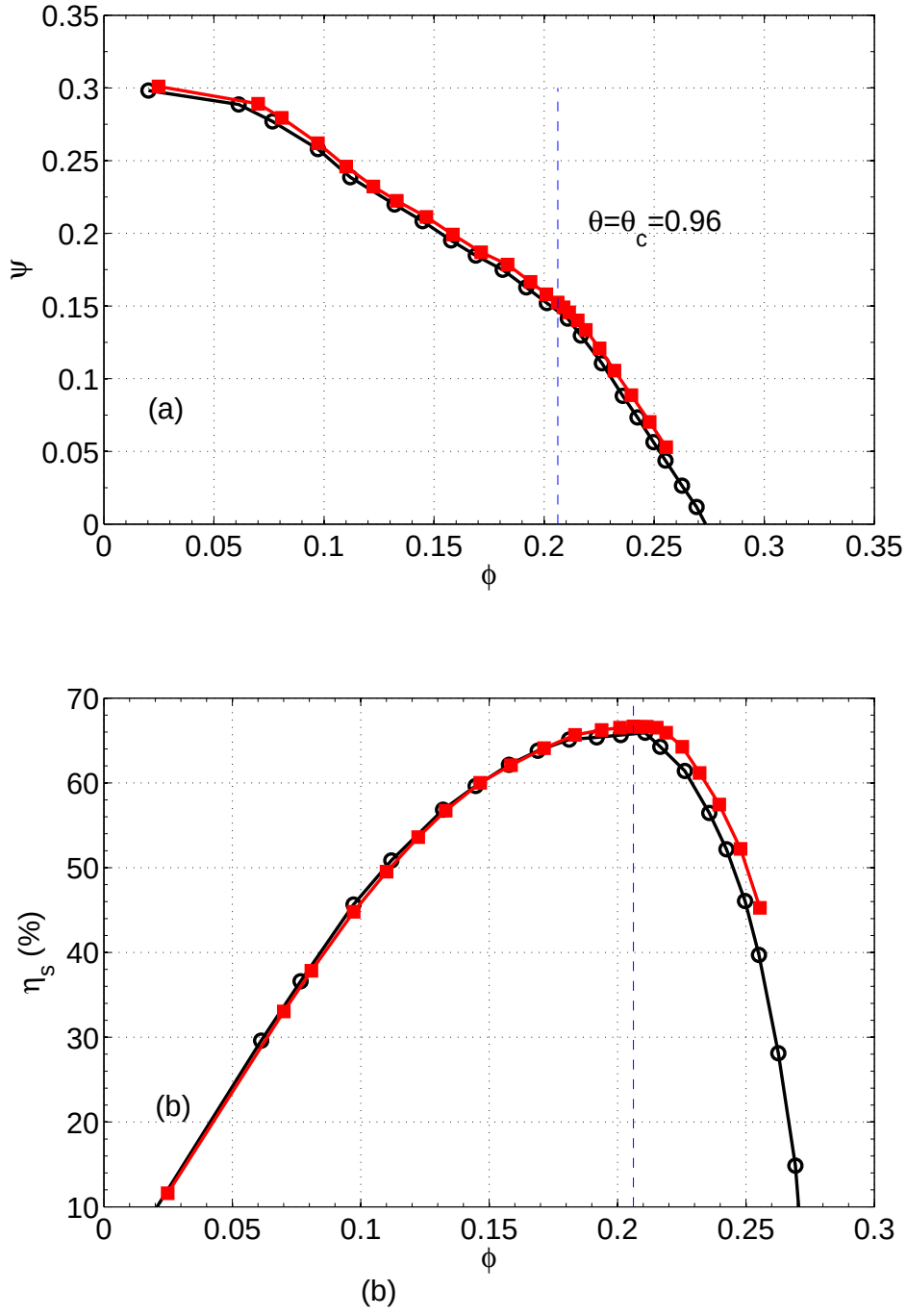

Figure 3.28: Global performance of Stage JW1, at N_{FR} = 1400 rpm (∘), N_{FR} = 2300 rpm (□), S = 10 mm.

of static pressure rise is obtained by higher work done by RR. As θ increases, incidence angles at inlet of RR are increased to positive values which augment the load and flow deflection. Thus, the higher work done results from both the augmentation of blade loading and increased blade speed by faster RR. This increment in static pressure is relatively faster than increase of power consumption of RR. Thus, the static pressure is improved. However, as θ is beyond a limit, the incidence angles is too big which induces large separation in RR, thus, loss increases rapidly. Additionally, the increased tangential velocity in the direction of rotation speed of RR below midspan could increase significantly. And this part of energy is considered to be loss. Therefore, the increase in power consumption is relatively much higher than the increase of static pressure due to the loss. Finally, the static efficiency deteriorates rapidly. For the purpose of clarity, the maximum efficiency is plotted at N_{FR} = 1400 and 2300 rpm.

Influence of θ on the maximum static pressure at N_{FR} = 1400 and 2300 rpm

Figure. 3.30 presents the $\eta_{s,max}$ as a function of θ/θ_C at N_{FR} = 2300 rpm and N_{FR} = 1400 rpm. Overall, the two curves have the same trend but are shifted by about 2 percentage points. This is due to the Reynolds effects presented above. Aside from the influence of Re, it can be seen in Fig. 3.30 that the peak value of $\eta_{s,max}$ falls into $\theta \sim [1.1\theta_C, 1.2\theta_C]$.

3.5.5 Conclusion

To conclude, at N_{FR} = $N_{FR,C}$,S=10 mm and θ increases not beyond $1.2\theta_C$, the higher θ could increase the static efficiency to 68%. During this process, the static pressures are largely increased in RR, mainly owing to the increased blade speed itself and its influence on the increased incidence angle which induces higher ΔV_θ. Thus the increase work done by RR improve significantly the static pressure rise, but also generates loss. As θ increases approximately beyond $1.2\theta_C$, the high incidence angle at inlet of RR induces large separation in RR and increases the tangential velocities in the direction of rotational speed of RR below midspan which is not interested. Hence, the increased blade work done is much rapid than the static pressures rise and static pressure rise drop rapidly.

Then the influence of θ on maximum static efficiency is investigated by reducing the rotational speed of the Front Rotor N_{FR} due to the limitation of rotating speed of the drive motor. However, the reduced N_{FR} also introduces the static efficiency loss by nearly 2 percentage points due to the Low Reynolds effects. Therefore, only the tendency of the maximum static efficiency is analyzed. The results proves that η_{smax} increases first at θ but drop rapidly as θ beyond around $1.2\theta_C$.

3.6 Influence of both the axial distance S and θ on the performances of JW1

In the previous analysis, the influence of S and θ on the performances have been investigated separately. The figure. 3.31 demonstrates that the identified trend of the maximum static efficiency increase as θ increases is similar for all the axial distance in $[10, 200]$ mm.

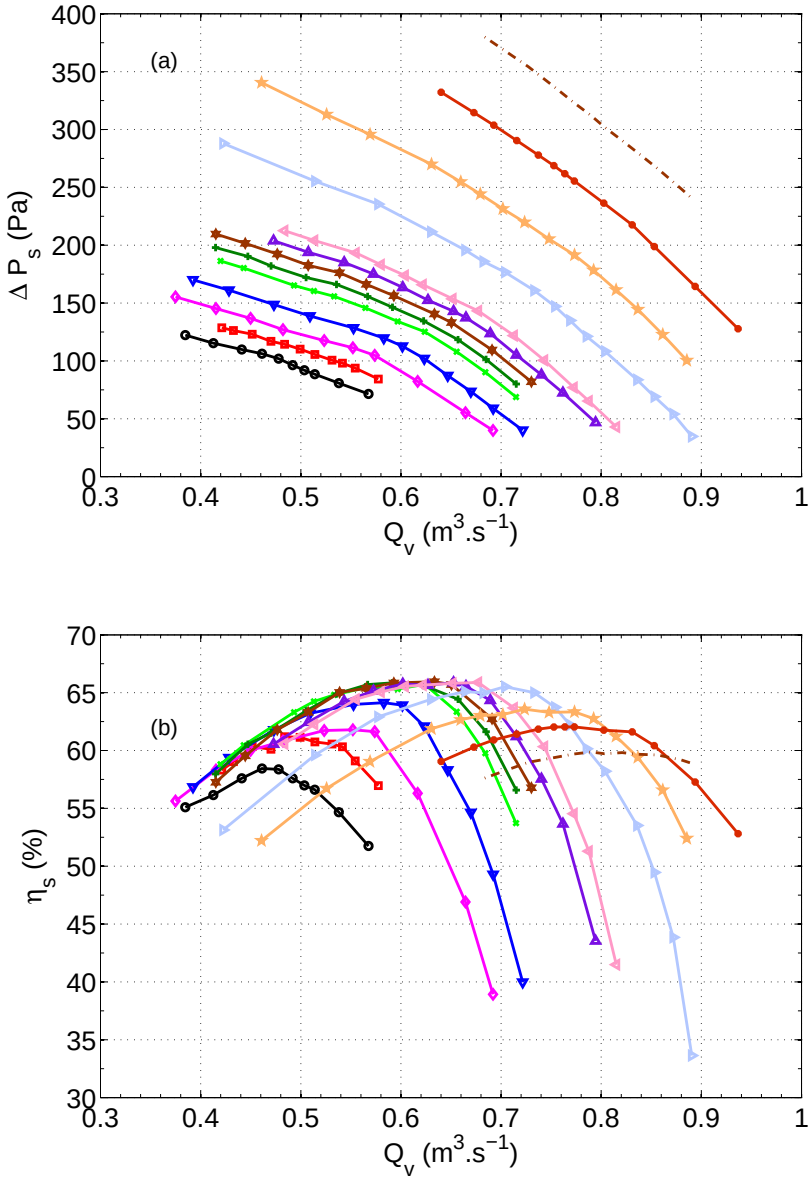

Figure 3.29: Global performance of Stage JW1, at N_{FR} = 1400 *rpm* θ/θ_C = 0.6(∘), 0.7(□), 0.8(◇), 0.9(▽),1(×),1.05(+),1.1(✡),1.15(△),1.2(◁), 1.4(▷),1.6(☆), 1.8(∗) *and* 2(.), S = 10 *mm.*

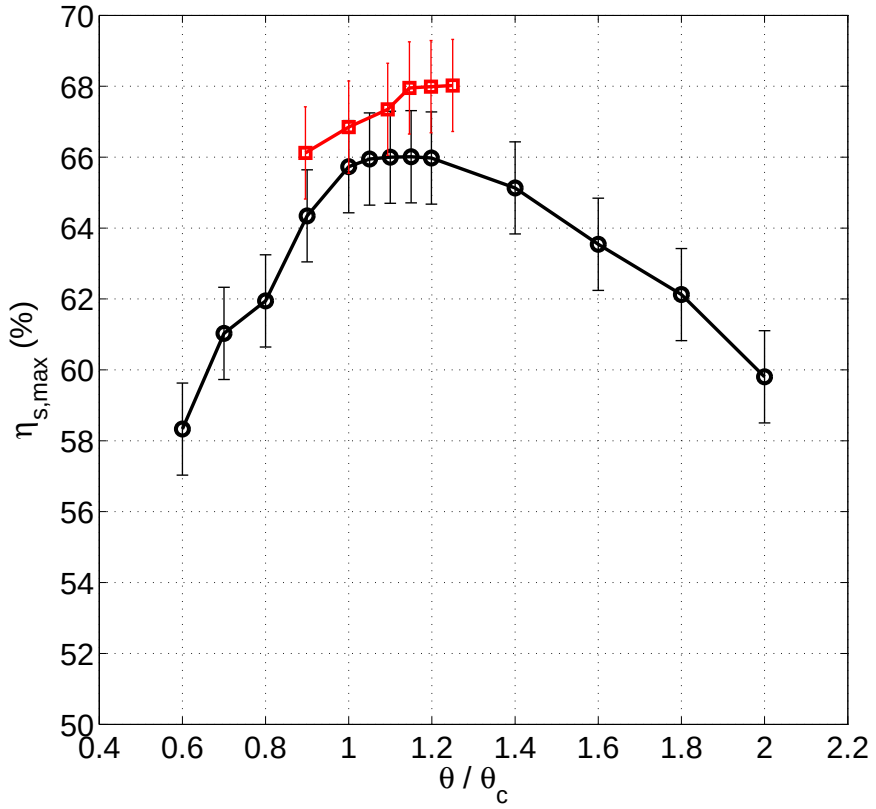

Figure 3.30: Maximum static efficiency vs. θ. *Stage JW1, at* N_{FR} = 1400 *rpm* (∘), N_{FR} = 2300 *rpm* (□), S = 10 *mm.*

The higher rotational speeds of the RR appears to be beneficial for higher static efficiency at all the axial spacing studied. Additionally, at a fixed θ, η_{smax} varies in the uncertainty range when $S < 100$ mm$(1.8L_{chord})$. Then with further increase in S, η_{smax} begins to decline about 2 percentage points.

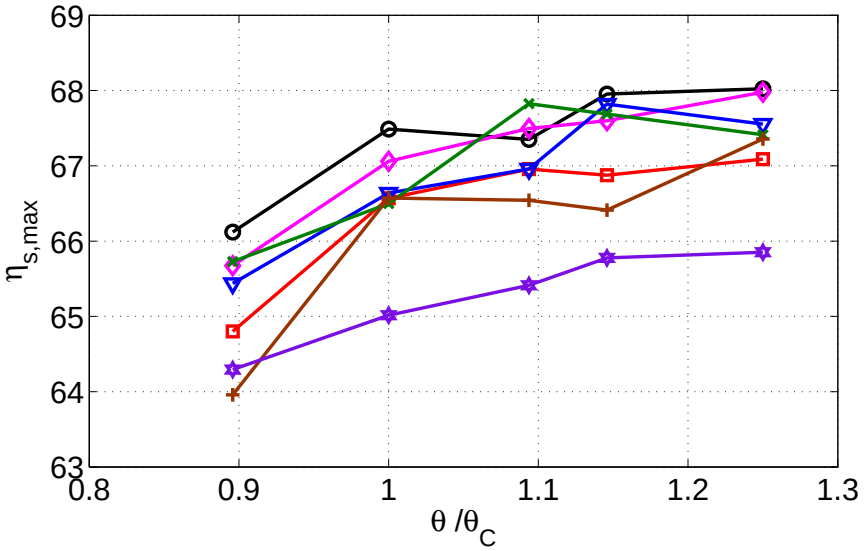

Figure 3.31: Maximum Static efficiency of the stage JW1 at N_{FR} = 2300 rpm, vs. θ/θ_C *for S = 10 mm (∘), S = 20 mm (□), S = 40 mm (◇), S = 50 mm (▽), S = 60 mm (×),S = 100 mm (+) and S = 200 mm (✡).*

In addition, as θ increases, the power consumption of the FR $\mathcal{P}_{w,FR}$ seems at constant at all the distances and all θ. Furthermore, the power consumption of the RR $\mathcal{P}_{w,RR}$ raise significantly as the RR turns faster. And at each θ, the $\mathcal{P}_{w,RR}$ decreases as S increases. The reason could be that at a fixed θ the work done near the tip region of RR is decreased due to the reduced incidence angle as S increases, based on the previous analysis.

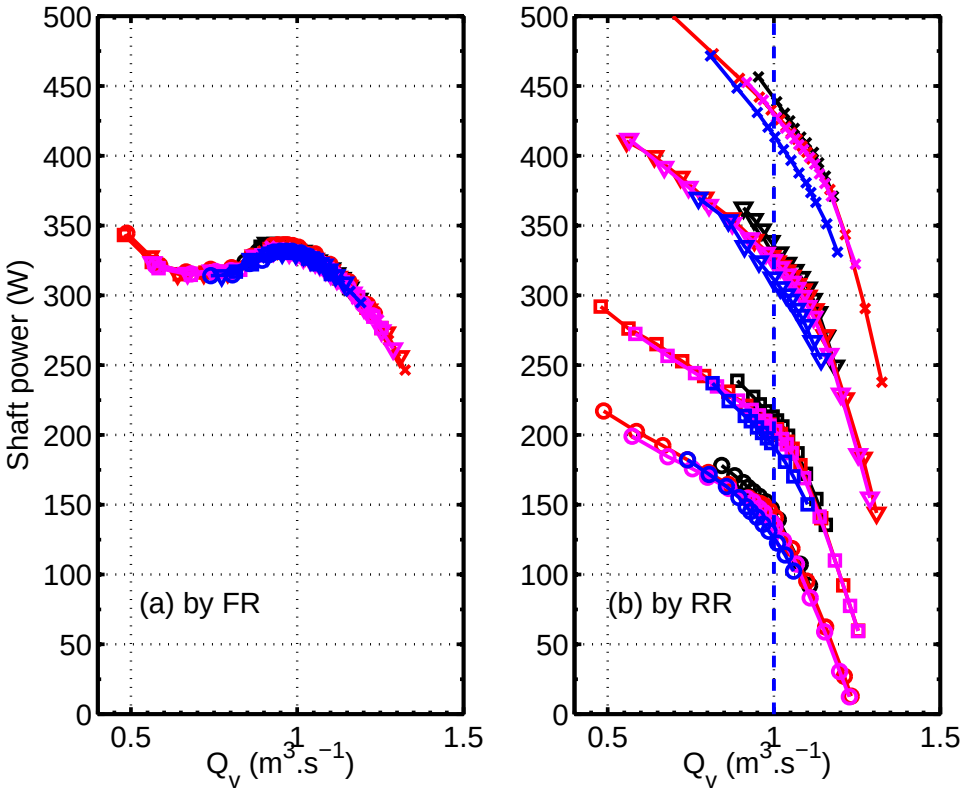

Figure 3.32: Power consumption of the stage JW1(Rescaled by ρ_{ref}) at N_{FR} = 2300 rpm, vs. θ/θ_C for S = 10 mm (black symbols), S = 50 mm (red symbols), S = 100 mm (magenta symbols) and S = 200 mm (blue symbols).

Chapter 4

Results of all CRS

In this Chapter, all the experimental results of the three CRS (JW1, JW2 and JW3) are presented. According to the design target in Chapter 2, the three CRS have been designed to achieve the same design point with three distributions of total load between the FR and RR:

L_C = 41%, 52% and 23% for JW1, JW2 and JW3 respectively.

Moreover, the main design characteristics of the three CRS are:

- FR of JW1 has large stagger angles;
- FR of JW2 possess the lowest static pressure rise;
- FR of JW3 has the highest and steepest characteristics.

Additionally, it should be indicated that JW1FR, JW2FR and JW3FR denote for the configurations of isolated rotor.

Firstly, the overall performance of the three CRS are presented and compared at the design point. Then the velocity fields and wall pressure fluctuations are shown at different flow rates. Finally, the influence of axial distance and speed ratio are analyzed and compared for the three systems.

4.1 Characteristics of the three CRS working on design parameters

4.1.1 Overall performance

Figure 4.1 shows the static pressure rise and static efficiency as a function of volume flow rate, for the three systems (open symbols) at their θ_C and with S = 10 mm, and the isolated rotors as well (Closed symbols). It could be observed that the JW2FR has the lowest and flattest static pressure curves and worst static efficiency at the whole operating range among all the Isolated rotors. But JW3FR shows opposite features. These results are consistent with those predicted by MFT (See Fig. 2.3). However, when combined with their rear rotors, JW2 provides high performance and is similar to JW1, in spite of the poor characteristics of JW2FR. This results from the contribution of large distribution of load L_C. On the contrary, JW3 has the lowest performance at design and all the partial

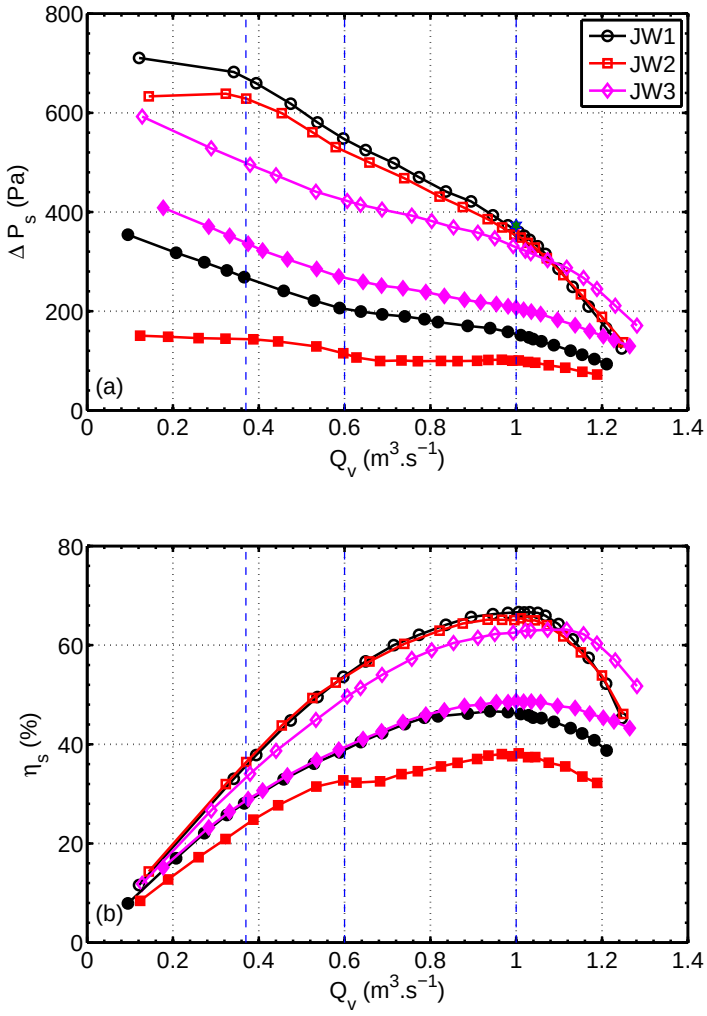

Figure 4.1: Overall performance of three systems: JW1(∘), JW2 (□) and JW3 (◇); JW1FR (•), JW2FR (■) and JW3FR (⧫), design point,(✡) (a): Static pressure rise ΔP_s (Rescaled by ρ_{ref}) vs. *volume flow rate Q_v. (b): Static efficiency η_s* vs. *volume flow rate Qv, at $S = 10$ mm.*

flow rates despite the highest performance of JW3FR. This could be owing to the smallest L_C which induces the insufficient tangential energy recovering by the RR of JW3.

Additionally, the experimental data and the expected values at the design flow rate (Q_v = 1 m^3.s^{-1}) are given in Tab. 4.1. It can be seen that the isolated Front Rotors of each system achieves the predicted values quite well, which validates the analysis of MFT at design point. When coupled to their Rear Rotors to form the Counter-Rotating Systems, the ΔP_s of the three are close to the design point, with at maximum a discrepancy of −11.0% for JW3.

	FR			CRS		
	Exp (Pa)	*MFT* (Pa)	δ %	*Exp* (Pa)	*C* (Pa)	δ %
JW1	154 ± 2	144	7.0	363 ± 4	373	−2.7
JW2	100 ± 2	96	4.2	353 ± 4	373	−5.4
JW3	207 ± 2	210	−1.4	332 ± 4	373	−11.0
HSN	152 ± 2	152	0	335 ± 4	373	−10.2

Table 4.1: Comparison of ΔP_s for the three CRS Q_v = 1 $m^3.s^{-1}$, at S = 10mm. Exp: experimental value, MFT: value predicted for the Front Rotor alone, and C: design point. The relative difference between the actual and the predicted value is δ.

Finally, the values of the static efficiency η_s at the design flow rate are reported in Tab. 4.2. The three CRS are very efficient, with minimum η_s at around 62%. Please note that the typical peak efficiency of a traditional rotor-stator stage are of the order of 55% (up to 60% for exceptional stages) and a single rotor stage of the order 50% (up to 55%) (see Refs. [46][41][47]). It could confirm that the Counter-Rotating System is a promising solution for the designers who seek for high static efficiency turbomachines.

FR	η_{sFR} %	CRS	η_{sCRS} %
JW1FR	46.3 ± 1.0	JW1	66.6 ± 1.3
JW2FR	38.0 ± 1.0	JW2	65.2 ± 1.3
JW3FR	48.7 ± 1.0	JW3	62.6 ± 1.3
HSNFR	45.7 ± 1.0	HSN	65.4 ± 1.3

Table 4.2: Comparison of η_s at design point Q_v = 1 $m^3.s^{-1}$

Furthermore, it can be observed from Fig. 4.1(a) that the characteristics of all the configurations can be divided into 4 regions where the slopes are different:

Region I, $Q_v \in [0, 0.38]$ m^3.s^{-1}. In this region, the volume flow rates are very low. For each configuration, the characteristic curves of the Front Rotors alone and of the Counter-Rotating Systems show similar trend (*i.e.*, flat curves for JW2 and JW2FR, significantly negative slopes for JW3 and JW3FR).

Region II, $Q_v \in [0.38, 0.6]$ $\mathbf{m^3.s^{-1}}$. In this region, the curves of ΔP_s have relatively high slopes for all the configurations. The slopes for the Front Rotors alone are approximately −277, −113 and −294 Pa.m^{-3}.s for JW1FR, JW2FR and JW3FR, respectively. The slopes for the CRS are steeper (−606, −537 and −357 Pa.m^{-3}.s for JW1, JW2 and JW3). Please note that these values could change rather strongly according to the chosen points. They nevertheless illustrate the trend.

Region III, $Q_v \in [0.6, 1]$ $\mathbf{m^3.s^{-1}}$. In this region, of moderate partial flow rates, the curves of ΔP_s have the smallest slopes. The values are roughly −110, +9 and −139 Pa.m^{-3}.s for JW1FR, JW2FR and JW3FR, respectively. Please note the almost zero or even slightly positive slope of JW2FR, that would lead to poor working stability for this fan if it were used alone in an air-loop. For the three CRS, the slopes are increased to −458, −435 and −208 Pa.m^{-3}.s for JW1, JW2 and JW3.

Region IV, $Q_v \in [1, 1.3]$ $\mathbf{m^3.s^{-1}}$. In this region of overflow, curves of ΔP_s have the biggest slopes. The values are roughly −282, −133 and −288 Pa.m^{-3}.s for JW1FR, JW2FR and JW3FR, respectively. Whereas the slopes are increased to −951, −836 and −468 Pa.m^{-3}.s for JW1, JW2 and JW3.

In short, regardless of the characteristics of the FR at partial flow rate, the characteristics of the three CRS are steeper than that of the Front Rotors alone and are always negative on a wide range of partial and over flow rates. This is particularly impressive for the Counter-Rotating System JW2 for which the curve of JW2FR is quite flat. The presence of the Rear Rotors thus contributes to maintain the system stability even at extremely low flow rates in this type of machines. One can finally notice that the best system in terms of static pressure rise is JW1, with an intermediate distribution of the work between the two rotors (60% for FR, 40% for RR).

Further, in order to explore the reason of the different slopes in ΔP_s curves, the power consumption of the FR, RR and whole stage for each configurations are presented in Fig. 4.2. For the FR both in isolated rotors and in CRS (Fig. 4.2(a)), positive slopes of the power consumption appear at about $Q_v \in [0.6, 1]$ m^3.s^{-1}. It reveals the working instabilities of the FR at partial flow rates. And this could be the main reason that the slopes of ΔP_s curves changes at the two volume flow rates 0.6 and 1 m^3.s^{-1}. Furthermore, the presence of RR increases the power consumption of FR compared with FR alone, at the partial flow rates $Q_v < 0.6$ m^3.s^{-1}. But only very small variations of the power consumption of FR are observed for $Q_v > 0.6$ m^3.s^{-1}. On the other hand, the power consumption by RR in JW1 and JW2 present stable negative slope in the operation range, but a positive slope in very low flow rate ($Q_v < 0.37$ m^3.s^{-1}) could be seen in Fig. 4.2(b). One can still notice that the power consumption of the RR in JW3 maintain a flat even slightly positive slopes at partial flow rate. This indicated the unstable characteristics of RR of JW3. Furthermore, at the design flow rate, the power consumption for the stages are 544.5 ± 3.8, 541.5 ± 3.8 and 525.5 ± 3.8 W by JW1, JW2 and JW3 respectively. It indicates a slight reduction in power consumption as distribution of load L_C decreases from around 50% to 23% at design flow rate.

Based on the results in Fig. 4.2, the distribution of power consumption $L_{power} = \frac{\mathcal{P}_{w,RR}}{\mathcal{P}_{w,FR}+\mathcal{P}_{w,RR}}$ is calculated, shown in Fig. 4.3. As the L_{power} is related to the distribution of load L in an isentropic process without consideration of mechanical loss, it reflects the

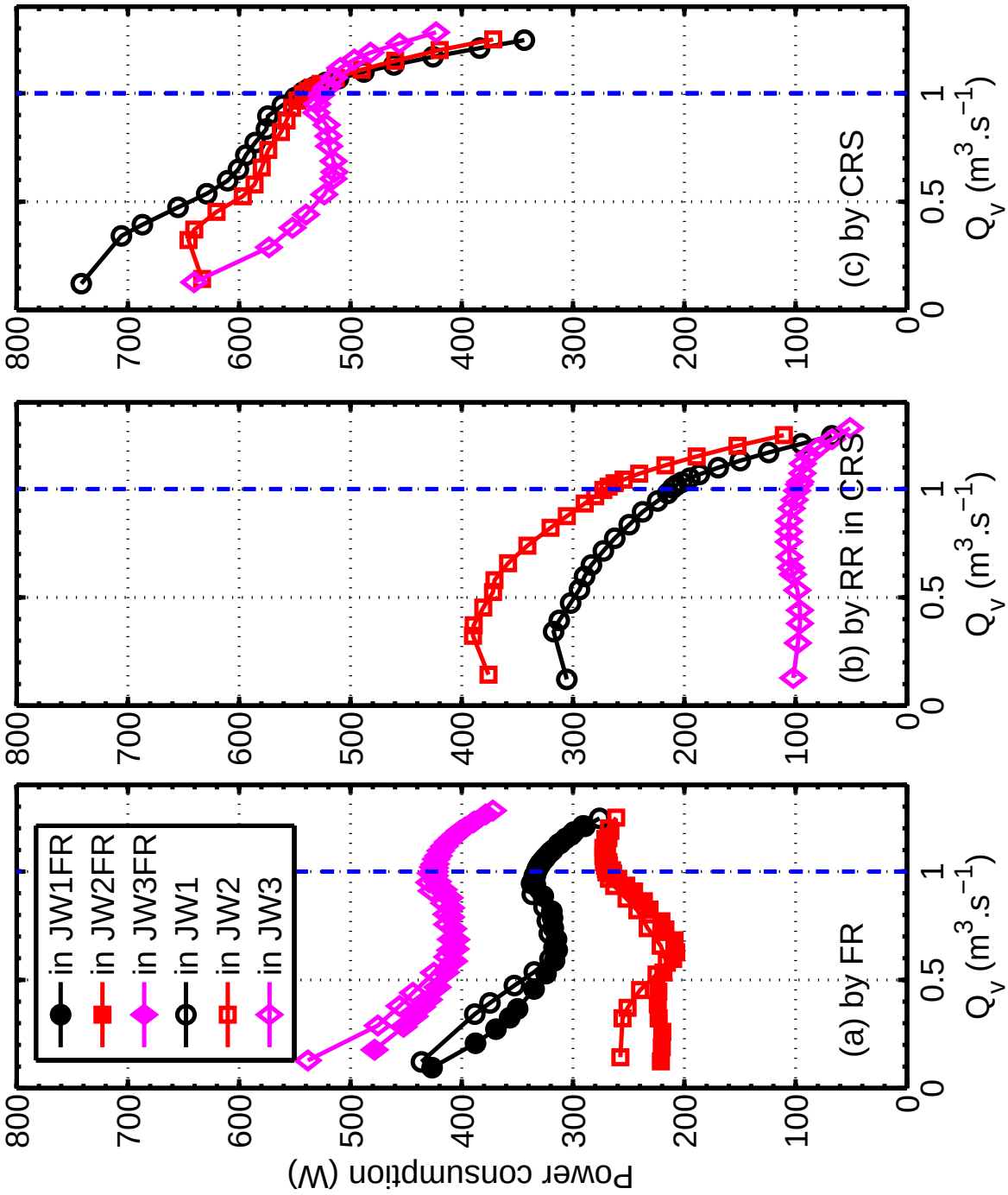

Figure 4.2: Power consumption (Rescaled by ρ_{ref}) of (a) the FR in isolated Rotors (closed symbols) and CRS (open symbols); (b) power consumption of the RR in CRS; (c) power consumption of CRS for : JW1 (○), JW2 (□) and JW3 (◇). All the results are rescaled by ρ_{ref}. CRS worked at $\theta = \theta_C$, $S = 10$ mm

tendency of L changes with volume flow rates. The distribution of power consumption at design flow rate are 39%,50%, 19% for JW1, JW2 and JW3 specifically. These values are close to those of design distribution of load L_C = 41%, 52%, 23%. Additionally, as Q_v decreases to partial flow rate, the L_{power} increases rapidly. Until around Q_v = 0.6 $m^3.s^{-1}$, the distribution of power consumption reaches a peak value for three CRS by 47%, 63% and 20% then they declines gradually. When Q_v increases from design flow rate to overflow rate, L_{power} drops dramatically for JW1 and JW2. For JW3, the L_{power} varies in a small range near 20%, except declines rapidly as $Q_v > 1.2$ $m^3.s^{-1}$.

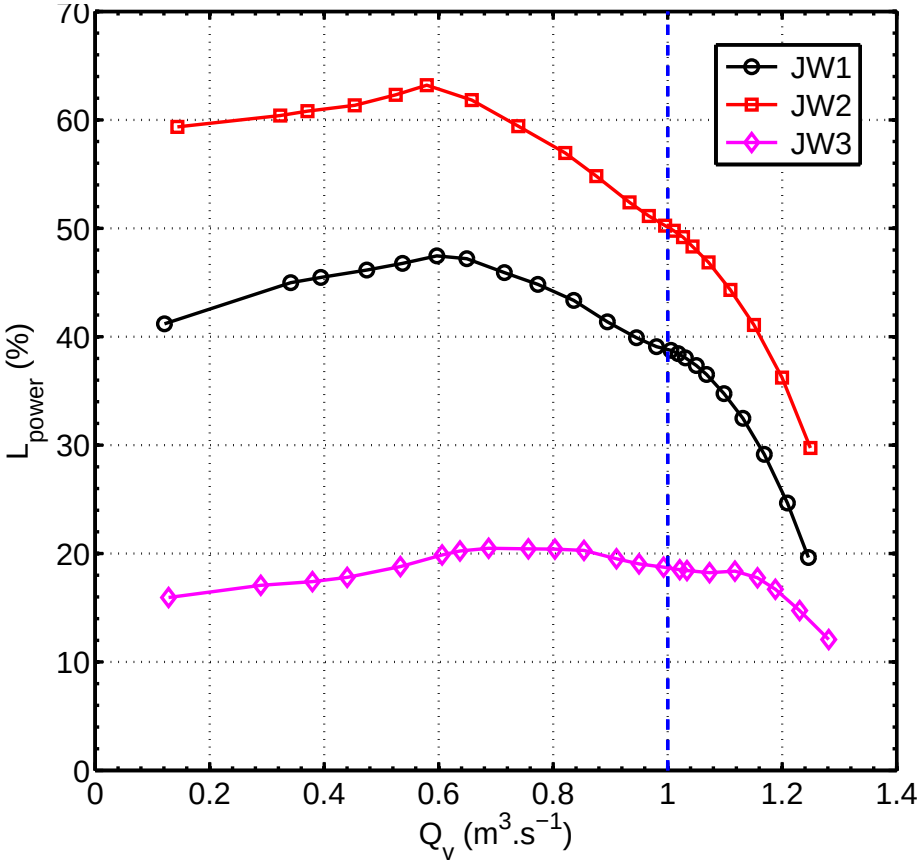

Figure 4.3: Distribution of power consumption in CRS $L_{power} = \frac{\mathcal{P}_{w,RR}}{\mathcal{P}_{w,FR}+\mathcal{P}_{w,RR}}$*: JW1 (∘), JW2 (□) and JW3 (◇). CRS worked at* $\theta = \theta_C$, S = 10 *mm*

4.1.2 Flow fields at design point by MFT and LDV

Averaged V_z and V_θ at Z_p = 5mm

Figure 4.4 shows the averaged axial (V_z) and tangential velocity (V_θ) downstream FR in FR alone and CRS for all systems. The values predicted by MFT are also plotted(✡). Overall, the profiles predicted by MFT have the same tendency as that of LDV, thus, it could be taken as an initial estimation for velocity fields downstream of FR. For averaged axial velocity V_z, Fig. 4.4a shows MFT underestimates the V_z for all the FR and overestimates at high blade span. As we know, near the tip region, there exists the tip leakage

flow which interacts with casing boundary layer. The loss model in MFT is not sufficient for predicting the flow structures at tip region. For the averaged tangential velocity V_θ, the discrepancy between the MFT and LDV is much smaller without the influence of the RR. It could be observed that the presence of RR diminish the V_θ moderately near the tip region and significantly near the hub region. Therefore, the outlet velocity fields of FR alone is different with the inlet condition of the RR near the hub and tip region, with the potential effects of RR. The large discrepancy near the hub region could induce unsuitable incidence angle at the hub of RR and then generates loss.

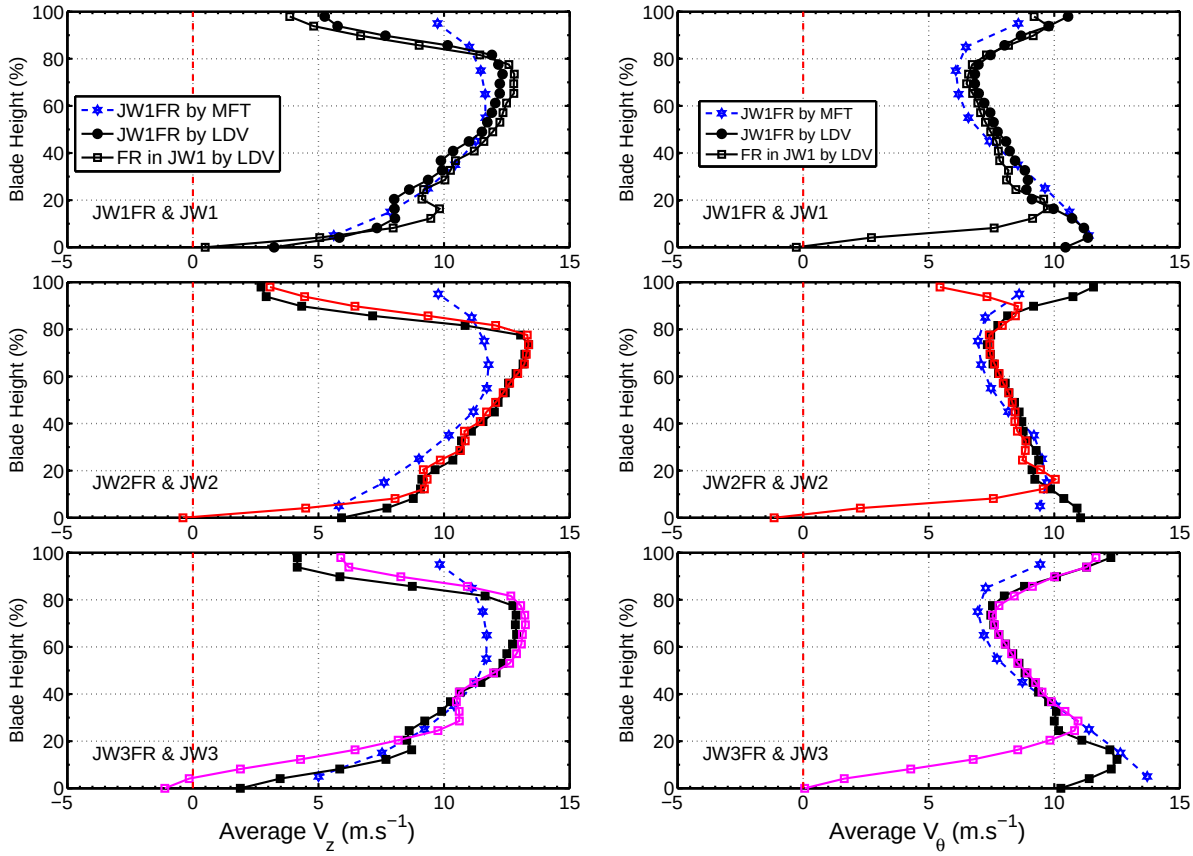

(a) Axial velocities V_z *(b) Tangential velocities V_θ*

Figure 4.4: Averaged axial V_z and tangential V_θ velocities near the outlet of the FR (Position Z_p = 5mm) at design point $Q_v = 1m^3.s^{-1}$, $\theta = \theta_C$, in: FR alone analyzed by MFT(☆); FR alone measured by LDV(closed symbols); in CRS measured by LDV(open symbols)

Incidence angle and deviation angle for the RRs in CRS

The incidence angles and deviation angles of RR in CRS are plotted in Fig. 4.5. For JW1 and JW2, first of all, the incidence angles of RR are near 0 at most part of blade span (20 – 80%) in Fig. 4.5a. This is good working condition for RR. It means the surface pressure distribution for the blade should be continuous at this part of blade and the required turning of flow can be achieved through the camber of the blades [7].

However, near the tip region (above 80% span), the incidence angle is positive (maximum about 6 degrees), still in acceptable condition. In this case, the blade loading is higher and more work is done by blade. Near the hub region, the negative incidence is found (maximum about 5 degrees in magnitude). In this region the flow deflection and loading are decreased. Dixon [7] pointed out that a typical compressor blade needs to tolerate at least ±5° changes of incidence without stalling. And this variation limit could reduce as the inlet Mach number increases. In the present research, the Mach number is quite low, we suppose the normal tolerance could be achieved. In addition, it can be found in the Ref. [10] that the loss is almost constant for an incidence approximately in the range ±7° for a cascade. As observed above, though the design assumption about the velocity is unsuitable near the hub and tip region of RR inlet, this discrepancy in incidence angle could still be reasonable.

Furthermore, for JW1 and JW2, the deviation angles of RR are always positive except at the hub in Fig. 4.5b. At high blade span($50-80\%$), deviation angle is quite low at about $1-2$ degrees. It proves that the flow is derived as expected owing to a near zero incidence angle. Then at low blade span($20-50\%$), the deviation angle increases with maximum 6°. Near the tip region (beyond 80%), the deviation angle are also increased in the order of 6°. It infers that the benefit of considerably positive incidence angle could possibly be canceled by the increased deviation angle. Then near the hub region (below 20% blade span), the deviation angle increases significantly. This could be caused by negative incidence angle interacting with the hub boundary layer at inlet of RR, which possibly induces a severe flow separation on the pressure surface of blade. And this may induce large loss in the hub region.

On the other hand, the RR of JW3 is quite different to that of JW1 and JW2. Large negative incidence angles appear at most blade span which induced considerably deviation angle. This indicates high loss in RR of JW3. This situation should be avoided in the design.

In a word, near the hub region of all RRs, the blade does not work efficiently as the other parts, due to the relatively higher negative incidence angle. The reason could be that the stagger angle is too high near the hub region of RR (Seen in Tab. 2.3). Reduced stagger angle could be beneficial for the design of RR. Thus, for CRS with very low distribution of load, it is recommended to decrease the stagger angles at all the blade span except near the tip region.

4.1.3 Conclusion

The three CRS which are designed to achieve the same design point with different distribution of load can well approach the required static pressure rise, except for JW3 which has −11.0% discrepancy. The static pressure curves for all CRS have much steeper negative slopes than that of the FR alone on a wide range of operation conditions, regardless the characteristics of their FR. It reveals that the presence of RR could maintain the system stability even at low volume flow rates. Furthermore, all CRS work with high static efficiency, with minimum 62% for JW3 which has lowest design load distribution L_C. Then the distribution of power conception $L_{power} = \frac{\mathcal{P}_{w,RR}}{\mathcal{P}_{w,FR}+\mathcal{P}_{w,RR}}$ are calculated as a function of volume flow rates. At design flow rate, L_{power} has similar values to the design load distribution L_C. For JW1 and JW2, as Q_v diminishes to partial flow rate, the L_{power}

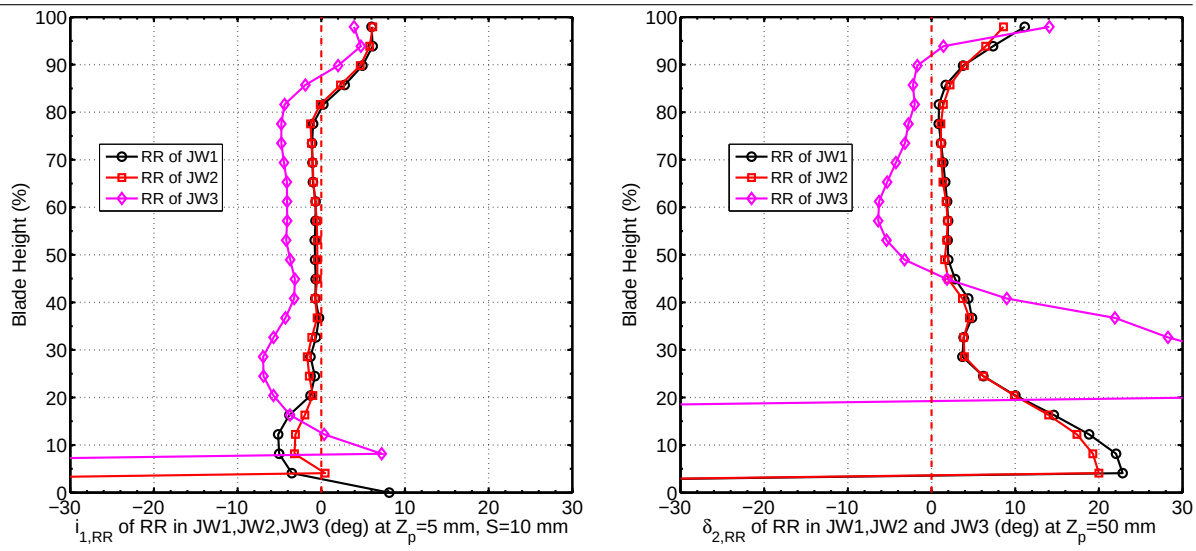

(a) Incidence angle i for RR in CRS *(b) Deviation angle δ for RR in CRS*

Figure 4.5: Incidence angle i and devation angle of RR in JW1, JW2 and JW3 at design point $Q_v = 1m^3.s^{-1}$, $\theta = \theta_C$, $S = 10$ mm

raises to a peak value around Q_v = 0.6 m^3.s^{-1} then goes down. As Q_v increases to over flow rates, the L_{power} drops quickly. For JW3, the L_{power} varies in a small range around 20% at most operating range and then falls off at $Q_v > 1.2$ m^3.s^{-1}. These tendency could be taken as a reference for the changes of distribution of load $L = \frac{\Delta P_{t,RR}}{\Delta P_t}$, because the power consumption is related to the total pressure rise for an isentropic process without consideration of mechanical loss.

The LDV results show that most part of blade span can deflect the flow as required. The unsuitable velocity fields estimation near the hub and tip region at inlet of RR introduce separation thus loss at hub and tip area. The incidence is positive at tip and negative at hub. And the blade of RR seems more sensitive to the negative incidence angle at the hub which may induce large separation at outlet hub of RR. The RR in JW3 with low distribution of load has moderate negative incidence at most blade span and introduces large loss at most of blade span. Therefore, one solution is to decrease the stagger angles near the hub of RRs in JW1 and JW2 and diminish the stagger angle below 90% of the blade span of RR in JW3.

4.2 Velocity fields for all CRS at different volume flow rates

Axial and tangential velocities have been measured downstream FR and RR in CRS for all configurations. Firstly, radial profiles of circumferential averaged velocities are presented downstream the FR at Q_v = 1 (design), 0.6 (moderate), 0.37 m^3.s^{-1} (very low) for the three CRS to see the influence of distribution of load on the flow field between the FR and RR. Secondly, the radial profiles of circumferential averaged velocities are plotted downstream the FR with and without the presence of RR to reveal the influence

of the RR at different L_C. Lastly, radial profiles of circumferential averaged velocities are compared downstream of FR and RR to investigate the changes of flow structures in each RR with various L.

4.2.1 Velocity profiles downstream of FR in CRS at different flow rates

Figures 4.6 shows the velocity profiles after FR (Z_p = 5 mm) in: JW1(L_C = 41%), JW2 (L_C = 52%) and JW3(L_C = 23%) at different flow rates.

Downstream the FR of JW2 (Fig.4.6b), which has been designed with the highest distribution of load L_C among all the CRS, the negative axial velocities V_z appear first near the hub region then near the tip region as well, as flow rate diminishes. The tangential velocity V_θ has the similar features as the FR of JW1, with larger ΔV_θ at Q_v = 0.6 and lower at Q_v = 0.37 as can be seen in Fig. 4.6b and Fig. 4.6a. Besides, the V_θ deteriorate significantly near the tip region at partial flow rate, compared with that of JW1. It could be depicted that for the FR of JW2 reverse flow occurs near hub and tip region of FR in JW2 at low partial flow rate. Work done increases first owing to the increased incidence angle then decreases largely near hub and tip region due to the flow separation induced by high incidence angle, as Q_v reduces to very low flow rate.

Downstream the FR of JW3 (Fig.4.6c), which has been designed with lowest distribution of load L_C, the profiles of axial velocities V_z totally change their forms compared with that of design flow rate (large V_z at blade tip) and always keep positive at partial flow rates. The tangential velocity V_θ increase only beyond the midspan and decrease largely below midspan as Q_v decreased to 0.6 $m^3.s^{-1}$. At Q_v = 0.37 $m^3.s^{-1}$, the V_θ diminish significantly below 70% blade span compared with that of Q_v = 1 $m^3.s^{-1}$. Near the tip region, V_θ keeps same as that of Q_v = 0.6 $m^3.s^{-1}$.

Therefore, the FR of JW3 has less reverse flow compared with FRs of JW1 and JW2 at partial flow rate, especially better at hub region. But the V_θ diminished dramatically even a large swirled flow in the opposite direction of the FR rotation occurs below midspan at very low volume flow rate. In order to identify the reason for these changes, the velocity fields downstream of FR with and without the influence of RR are plotted.

4.2.2 Velocity profiles downstream FR in FR only and CRS

Figures 4.7 and 4.8 present the circumferential averaged velocity profiles downstream FR (Z_p = 5) in FR only (JW1FR,JW2FR and JW3FR) and CRS (JW1,JW2 and JW3) at different volume flow rates.

Figure 4.7 shows that for all isolated FR, as Q_v reduces, the axial velocities decrease rapidly almost all the blade span except the tip ration. Near the hub region, V_z are diminished to negative as Q_v diminishes. It can be noticed that JW2FR has smallest negative velocities among all the isolated FRs. It represents the reverse flow downstream of the isolated FRs at partial flow rates. With the influence of their RR, V_z increases in high blade span (except near the tip region) at Q_v = 0.6 $m^3.s^{-1}$, and almost in all blade span at at Q_v = 0.37 $m^3.s^{-1}$. This mainly results from the suction effects of RR.

Figure 4.8 shows the tangential velocities V_θ downstream FR. For isolated FRs, as Q_v decreases, V_θ increases beyond midspan, but deteriorates near the hub region. With

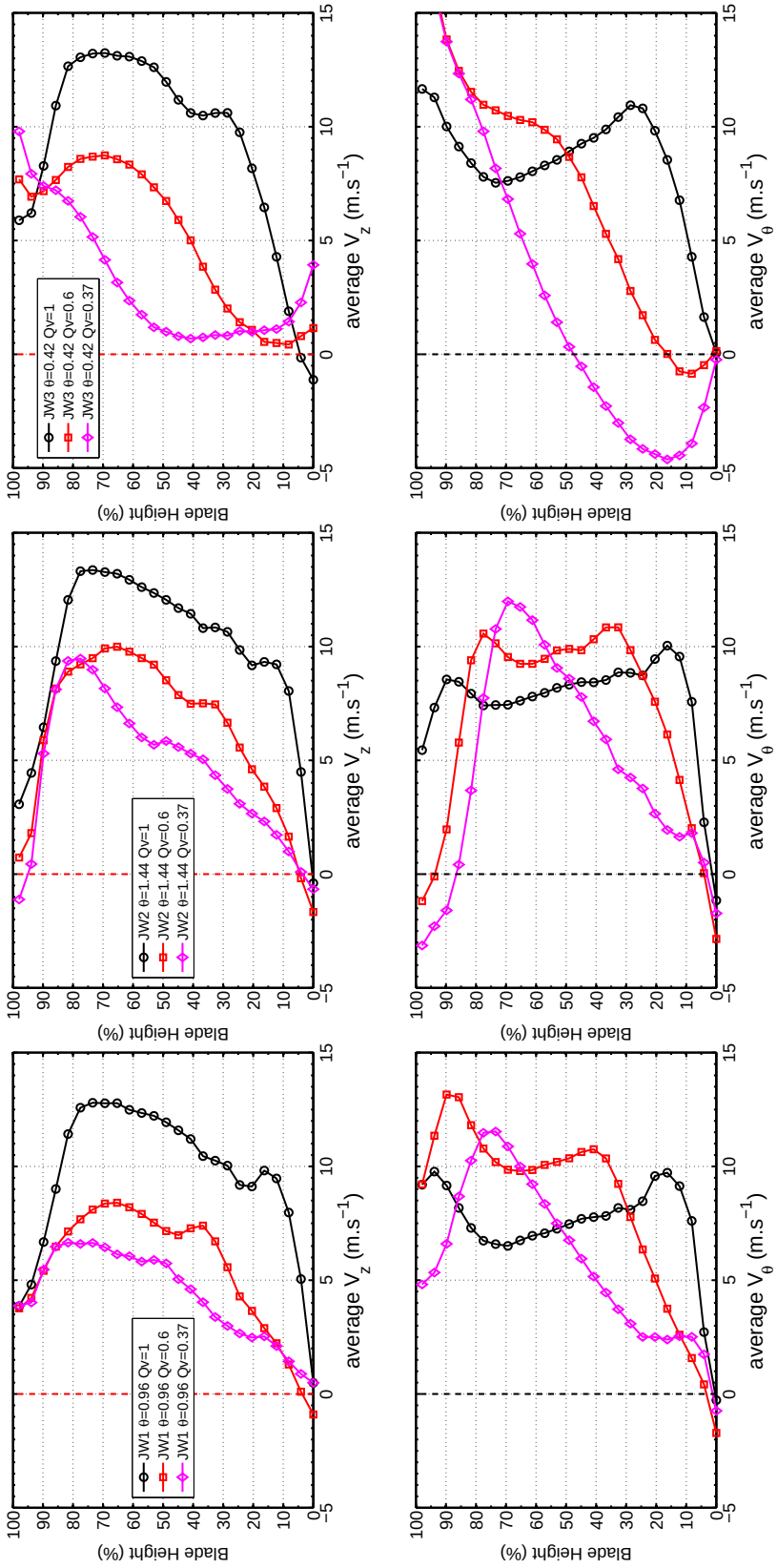

(a) JW1 *(b) JW2* *(c) JW3*

Figure 4.6: Radial distributions of circumferential averaged axial (V_z) and tangential (V_θ) velocities at $Z_p = 5\ mm$, in JW1, JW2 and JW3 at design condition $\theta = \theta_C$, for $Q_v = 1(\circ)$, $0.6(\square)$, $0.37(\diamond)$ $m^3.s^{-1}$, $S = 10\ mm$

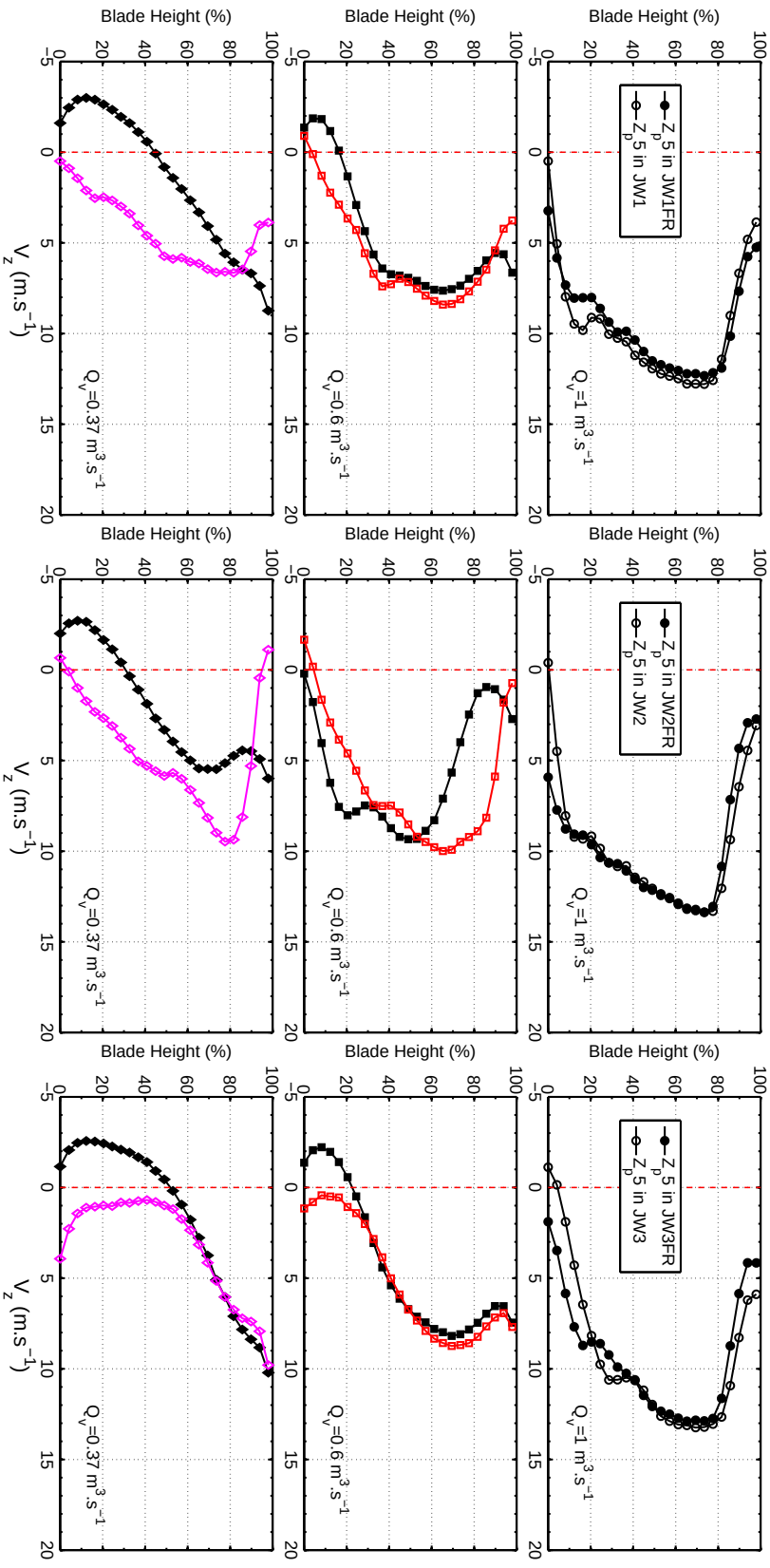

(a) JW1FR & JW1 *(b) JW2FR & JW2* *(c) JW3FR & JW3*

Figure 4.7: Radial distributions of circumferential averaged axial velocities (V_z) at Z_p = 5 mm, for JW1FR,JW2FR,JW3FR (closed symbols) and JW1,JW2,JW3 (open symbols) at design condition $\theta = \theta_C$, and Q_v = 1, 0.6, 0.37 $m^3.s^{-1}$, S = 10 mm

the influence of their RR, V_θ diminishes significantly almost part of blade span. Large negative V_θ appears near the hub region downstream of FR in JW3. It indicates the opposite rotating flow downstream of FR in CRS. The opposite rotating flow can also be observed both near the hub and tip region downstream of RR in JW2. One possible explication is that the potential effects from RR in JW3 propagate upstream and modify the flow field of its FR. This modification also exists downstream FR in JW2 both near the tip and hub region at partial flow rates, but not obviously for that of JW1.

In brief, the presence of RR is beneficial to eliminate the reverse flow downstream of the FR. But the potential effects of the RRs could largely reduce the work done by the FR near the hub and tip region, as well as create a swirled flow opposite to rotational direction of FR at both hub and tip region. This effects are more apparent as Q_v reduces from design flow rate to partial flow rates. In addition, one should notice that in Fig. 4.2, when $Q_v \in [0.6, 1]$ m^3.s^{-1}, the power consumption of the FR varies slightly with or without the influence of RR. However, as $Q_v < 0.6$ m^3.s^{-1}, the power consumption of the FR increases obviously with the presence of the RR compared to the isolated FR. In a word, $Q_v < 0.6$ m^3.s^{-1}, with the presence of RR, the power consumption of FR increases but the work done by the FR reduces. As we know, the power consumption (shaft power) is transferred to the work done by the blade row plus the loss without the consideration of the mechanical loss. It inferred that the loss increases largely in the FR by the potential effects of the RR as $Q_v < 0.6$ m^3.s^{-1}. This could be observed for all CRS (Figs. 4.2 and 4.8).

4.2.3 Velocity profiles downstream the RR in CRS at different flow rates

Figures 4.9 and 4.10 show the circumferential averaged velocity profiles downstream of FR(Z_p = 5 mm) and downstream the RR(Z_p = 50 mm) in CRS at different volume flow rates.

When the fluid passes through the RR, overall, as Q_v reduces to 0.6 m^3.s^{-1}, the axial velocities decrease at low blade span and thus increase at high span region. At design point, axial velocities V_z become slightly negative near the hub of the RR in JW1 and JW2, but quite noticeably negative at the hub of RR in JW3. Moreover, this negative region enlarges dramatically toward the midspan as flow rate reduces to 0.37 m^3.s^{-1} in all RRs, especially severely for RR of JW3. This reveals that as design distribution of load L_C enlarges, the reverse flow are decreased at outlet of RR at partial flow rate.

For tangential velocities in Fig. 4.10, as a whole, V_θ diminishes from inlet to outlet of RR for most part of blade span, as Q_v reduces for all CRS. At design flow rate, all the three CRS has non-zero V_θ at outlet of RR, which is positive at high span and negative at low blade span. This is contrary to our design consumption with $V_\theta = 0$ at outlet of RR. This swirled energy is considered to be lost. Among the three CRS, JW3 has largest V_θ at outlet of RR, therefore, it has largest discrepancy to the design point. When Q_v reduces to moderate flow rate, the ΔV_θ increases for all three RRs. As Q_v diminishes to very low flow rate, ΔV_θ increase less than at moderate flow rate at most of blade span. Moreover, a negative ΔV_θ appears below 40% blade span for RR of JW3 at Q_v = 0.37 m^3.s^{-1} in Fig. 4.10(c). It indicates the low blade span of RR in JW3 does not add energy to the fluid. On the contrary, the low blade span takes energy from fluid like a turbine.

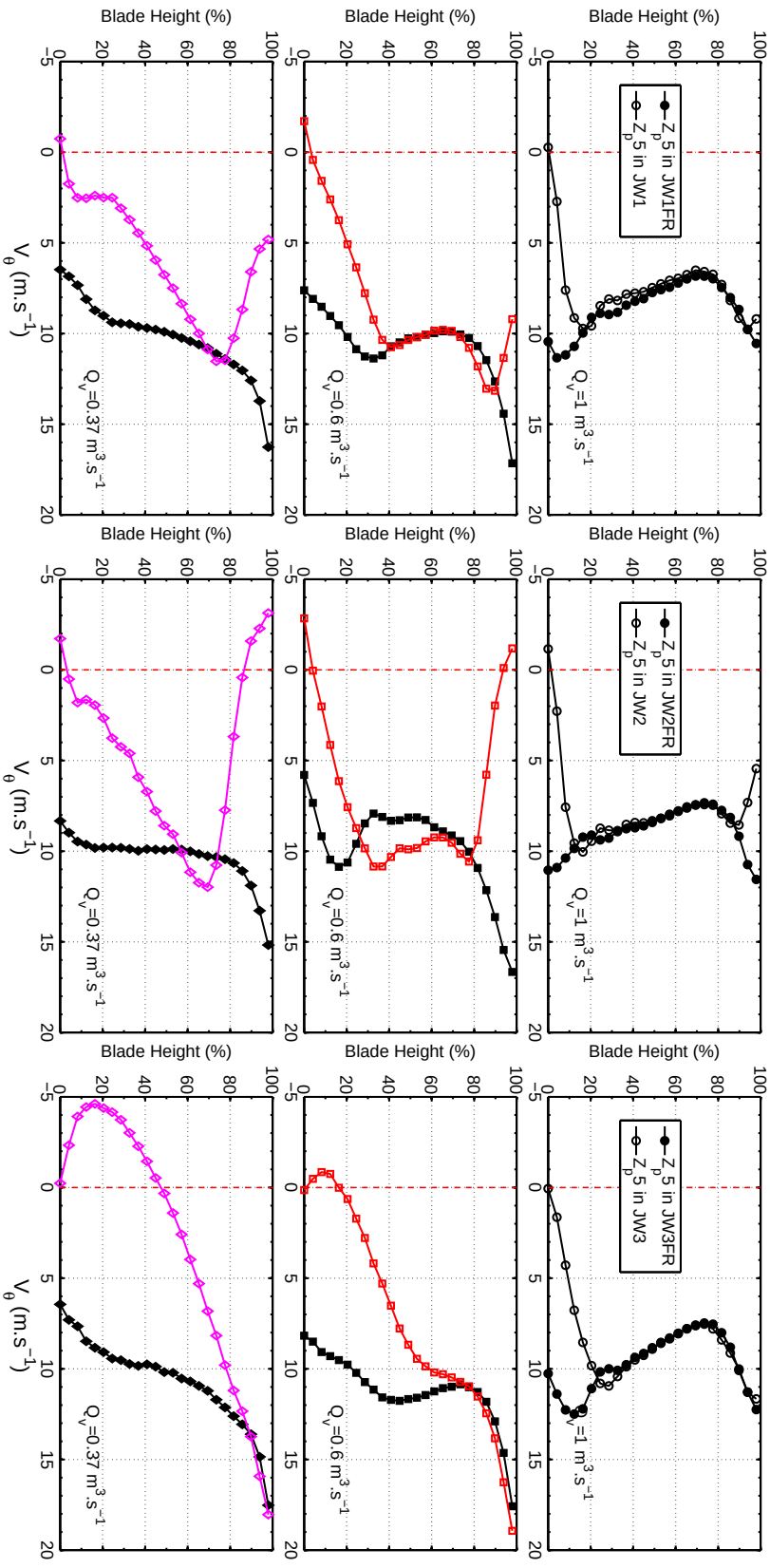

(a) JW1FR & JW1 *(b) JW2FR & JW2* *(c) JW3FR & JW3*

Figure 4.8: Radial distributions of circumferential averaged tangential velocities (V_θ) at Z_p = 5 mm, for JW1FR,JW2FR,JW3FR (closed symbols) and JW1, JW2, JW3 (open symbols) at design condition $\theta = \theta_C$, and Q_v = 1, 0.6, 0.37 $m^3.s^{-1}$, S = 10 mm

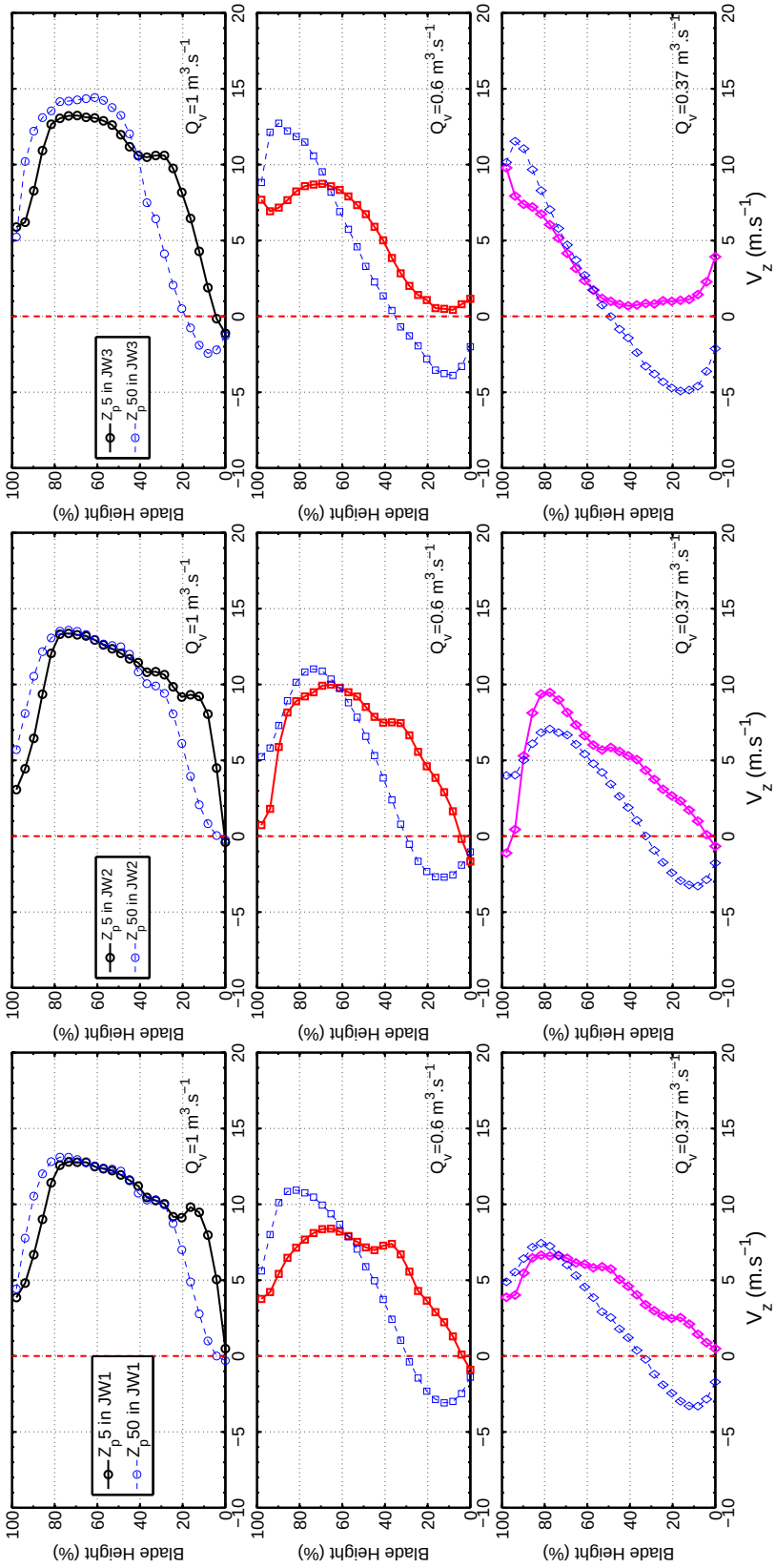

(a) JW1 *(b) JW2* *(c) JW3*

Figure 4.9: Radial distributions of circumferential averaged axial (V_z) velocities at Z_p = 5 mm (black, red and magenta lines) and Z_p = 50 mm (blue and thinner lines) for JW1, JW2, JW3 at design condition $\theta = \theta_C$, and Q_v = 1, 0.6, 0.37 $m^3.s^{-1}$, S = 10 mm

Therefore, at partial flow rate, downstream of RR, there are large reverse flow near the hub region and this reverse flow extends towards the midspan as the distribution of load L decreases. Moreover, the flow swirls with large magnitudes in the direction of RR, at large part of blade span, except for near the tip and hub region downstream RR in JW3. This indicates large energy loss at outlet of RR. And this reversed downstream of RR could possibly propagates upstream to modify the flow fields downstream of RR. Additionally, ΔV_θ increases dramatically owing to the enlarged incidence angle as Q_v reduces to moderate flow rate(except close to hub region). Then as Q_v reduces to very low flow rate, the load decreases at most part of blade for all RRs, even negative V_θ occurs near the hub region downstream RR in JW3.

4.2.4 Conclusion

The velocity fields obtained by the LDV measurements are investigated at design flow rate (Q_v = 1 m^3.s^{-1}), moderate partial flow rate (Q_v = 0.6 m^3.s^{-1}) and very low flow rate (Q_v = 0.37 m^3.s^{-1}) for all the configurations. The flow characteristics are mainly as follows:

- Downstream of FR, the presence of RR could eliminate the reversed flow at partial flow rates, owing to its aspiration effects. However, the potential effects of RR would significantly decrease the work done by FR near the tip and hub region as Q_v reduces. Moreover, V_θ at outlet FR decreases from positive to large negative downstream of FR in JW3 when coupled with its RR as Q_v decreases to very low flow rate. It represents an opposite rotating flow to the rotational direction of FR. This is caused by the potential effects of RR which propagated to the downstream of its FR.

- Downstream of RR, reverse flow aggravates at partial flow rates for the RR in JW3 which has low L_C. Meantime, large swirled flow in the rotational direction of RR exists which represents the large energy loss downstream of RR. This swirled reverse flow could possibly propagates upstream and modify the flow fields downstream of FR. JW3 with lower L_C exhibit poor adaptability to the high incidence angles at lower partial flow rate, which induces negative V_θ below 40% blade.

4.3 Analysis of the wall pressure fluctuations

The same measurements that have been reported in Chapter 3 and Fig. 3.16 have been done on JW2 and JW3. The wall pressure fluctuations are measured by a microphone situated at a distance 5 mm downstream of the FR (Z_p = 5 mm) and then 5 mm downstream of the RR (Z_p = 50 mm). The power spectral density (PSD) of these fluctuations for the CRS JW2 and JW3 working at their design conditions and with S = 10 mm are plotted in the Figs. 4.11 to 4.12. For each system, three flow rates have been studied: the design flow rate Q_v = 1 m^3.s^{-1}, a moderate partial flow rate Q_v = 0.6 m^3.s^{-1} and a very low partial flow rate Q_v = 0.37 m^3.s^{-1}.

One can notice the presence of several peaks in the spectra like those in JW1. Three types of peaks exist: those correspond to the blade passing frequency of the Front Rotor

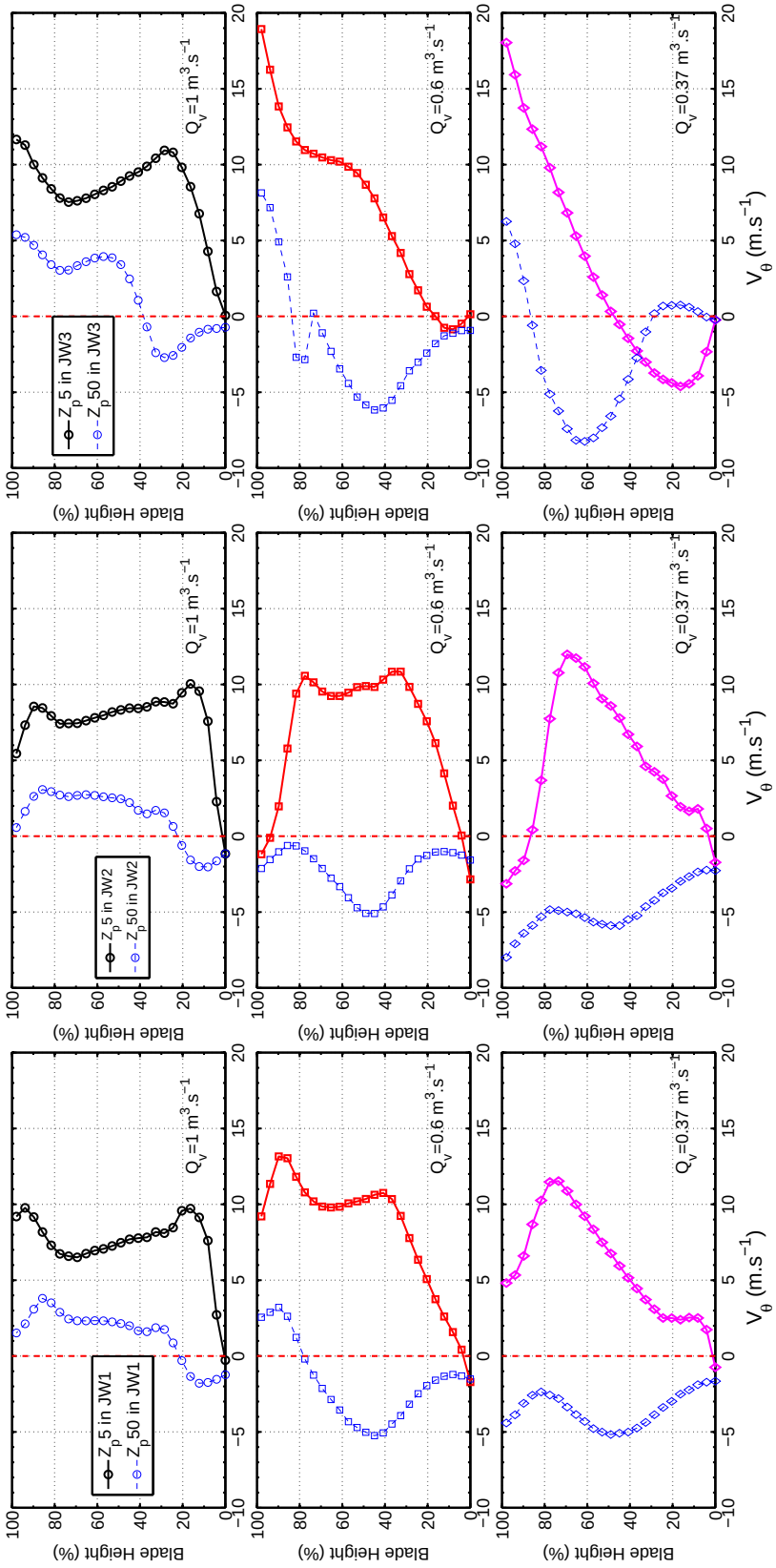

(a) JW1 *(b) JW2* *(c) JW3*

Figure 4.10: Radial distributions of circumferential averaged tangential (V_θ) velocities at $Z_p = 5$ mm (black, red and magenta lines) and $Z_p = 50$ mm (blue and thinner lines) for JW1, JW2, JW3 at design condition $\theta = \theta_C$, and $Q_v = 1$, 0.6, 0.37 $m^3.s^{-1}$, $S = 10$ mm

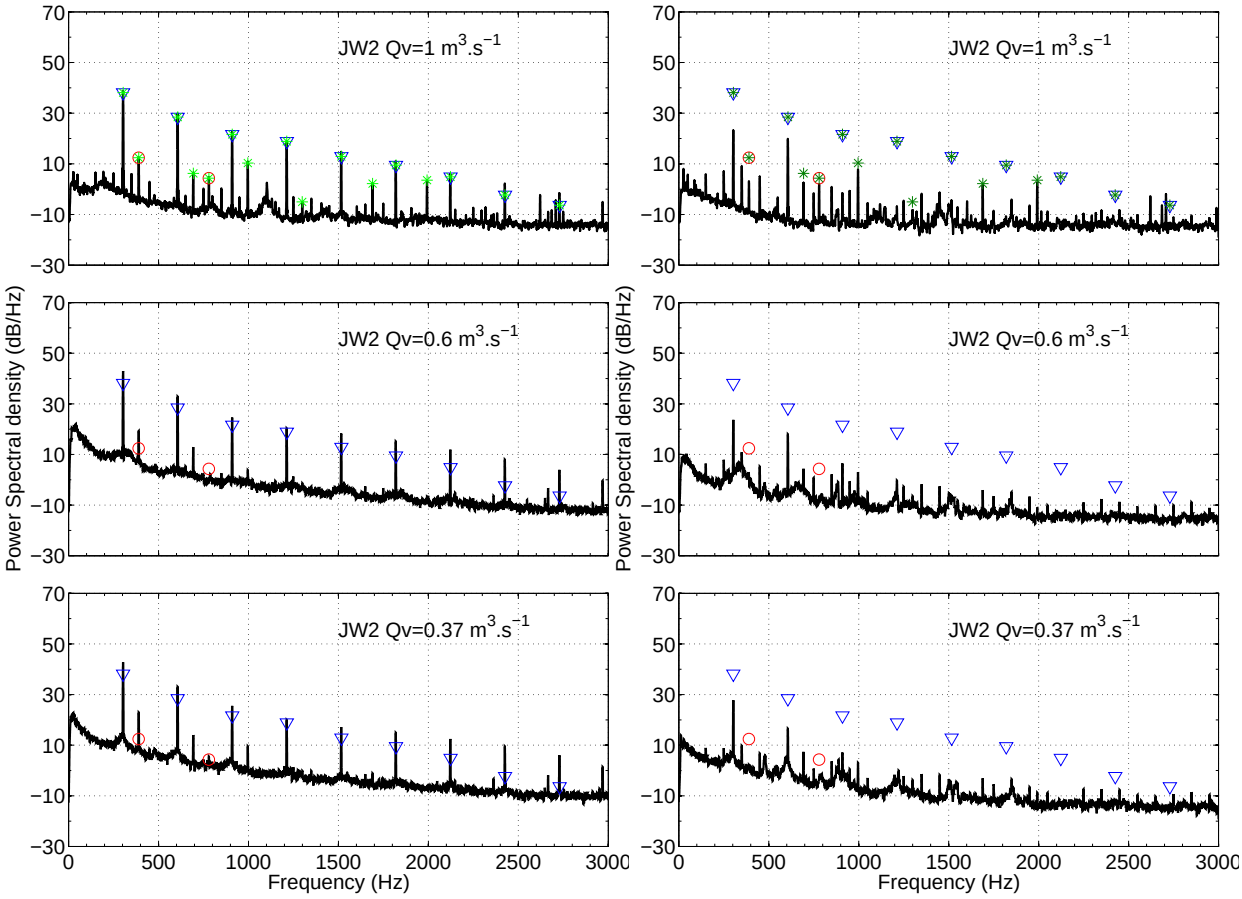

(a) at $Z_p = 5$ mm *(b) at $Z_p = 45$ mm*

Figure 4.11: PSD of the wall pressure fluctuations measured at $Z_p = 5$ and 45 mm, for JW2 at $N = 1800 - 2600$ rpm and $S = 10$mm, (a)$Q_v = 1$ $m^3.s^{-1}$; (b)$Q_v = 0.6$ $m^3.s^{-1}$, (c)$Q_v = 0.37$ $m^3.s^{-1}$. (○): $mf_{bpf,FR}$; (▽): $nf_{bpf,RR}$; and (∗): $mf_{bpf,FR} + nf_{bpf,RR}$ with $m \neq 0$ and $n \neq 0$.

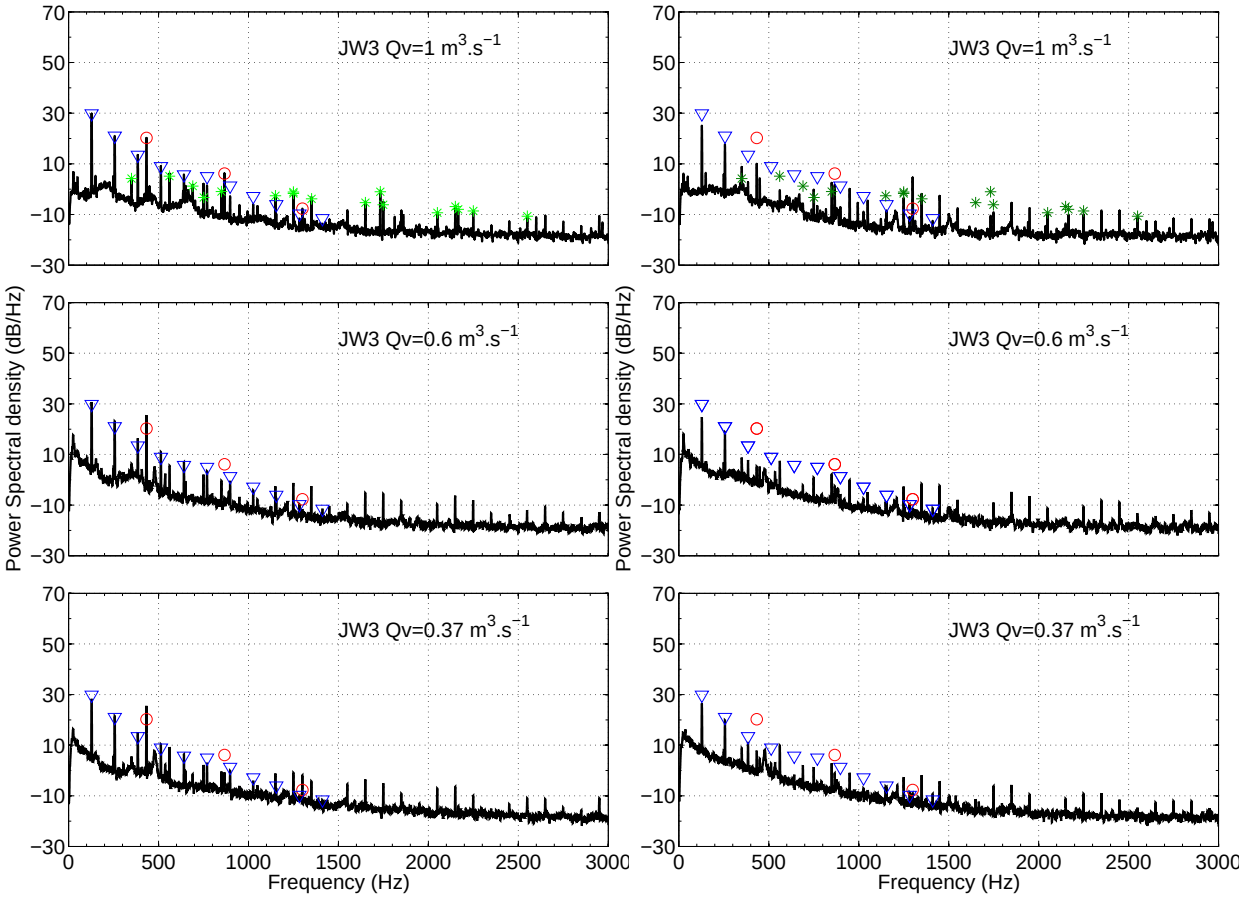

(a) at $Z_p = 5$ mm *(b) at $Z_p = 45$ mm*

Figure 4.12: PSD of the wall pressure fluctuations measured at $Z_p = 5$ and 45 mm, for JW3 at $N = 2600 - 1100$ rpm and $S = 10mm$, (a)$Q_v = 1\ m^3.s^{-1}$; (b)$Q_v = 0.6\ m^3.s^{-1}$, (c)$Q_v = 0.37\ m^3.s^{-1}$. (∘): $mf_{bpf,FR}$; (▽): $nf_{bpf,RR}$; and (∗): $mf_{bpf,FR} + nf_{bpf,RR}$ with $m \neq 0$ and $n \neq 0$.

($f_{bpf,FR}$) and its harmonics are marked with $\circ$, while the peaks corresponding to the Rear Rotor blade passing frequency ($f_{bpf,RR}$) are marked with $\triangledown$ and finally, the interactions frequencies corresponding to combinations of the Front and Rear Rotor blade passing frequencies are marked with $*$. For the purpose of emphasizing the changes in the amplitudes between design flow rate and partial flow rates as well as at different axial positions, the amplitudes of the symbols in the plots corresponding to partial flow rates are kept the same as in the design flow rate downstream of FR.

Comment features can be noticed for all CRS. Downstream FR (Figs. 4.11a and 4.12a), the amplitudes of the peaks corresponding to $f_{bpf,RR}$ and its harmonics are significantly higher than that of $f_{bpf,FR}$ at different axial positions. The influence of the Rear Rotor propagates upstream (potential effect) and interacts with than that of the Front Rotor (usually attributed to the wakes of the blades). Then, one can notice that the two rotors are in strong non-linear interaction at the design volume flow rate. However, for Q_v = 0.6 m^3.s^{-1}, the peaks corresponding to the interactions are dramatically attenuated, and in contrast, the amplitudes corresponding to both $f_{bpf,FR}$ and $f_{bpf,RR}$ are increased. Then downstream of RR (Figs. 4.11b and 4.12b), the peaks corresponding to $f_{bpf,FR}$ can still be noticed but quickly disappear as Q_v reduces. But the whole amplitudes are much lower than those of design flow rate downstream FR. It reveals that the influence of RR can propagate upstream and attenuate rapidly downstream.

In order to compare the three systems, the amplitude of the peaks corresponding to $f_{bpf,FR}$ and $f_{bpf,RR}$ downstream of FR are reported in Tab. 4.3 for the design volume flow rate. JW2 has the highest amplitude for $f_{bpf,RR}$ and the lowest for $f_{bpf,FR}$ among the three CRS. This is consistent with the ratio of rotational speeds. Finally, one can notice a correlation between the levels and the rotation rates of the rotors. The total level of the pressure fluctuations is thus obviously the lowest for JW3, and is almost similar for JW1 and JW2 when the sums of the two rotation rates are of the same order of magnitude.

	N_{CFR}/N_{CRR} (rpm)	PSD_{FR} (dB/Hz)	PSD_{RR} (dB/Hz)	Std(p') (dB)
JW1	2300/2200	17.4 ± 1	36.5 ± 1	40.9 ± 0.1
JW2	1800/2600	12.6 ± 1	38.5 ± 1	42.9 ± 0.1
JW3	2600/1100	20.2 ± 1	29.8 ± 1	35.1 ± 0.1

Table 4.3: The amplitude of the dominate frequency corresponded to $f_{bpf,FR}$ and $f_{bpf,RR}$ downstream of FR (Z_p = 5 mm), for JW1, JW2 and JW3, at Q_v = 1 $m^3.s^{-1}$. Std(p') represents the power of the total signal.

4.4 Influence of the axial distance S on the performances of CRS at $\theta = \theta_C$ and Q_v = 1 m^3.s^{-1}

The variations of performance with the axial distance S between the Front Rotor and the Rear Rotor at the design flow rate are plotted in Fig. 4.13 for the three CRS working on their design speed ratios $\theta = \theta_c$. The ΔP_s and η_s decrease monotonically with S for the three CRS, contrary to the results observed by Pundhir et Sharma [1] on a transonic case where an optimum in distance was found.

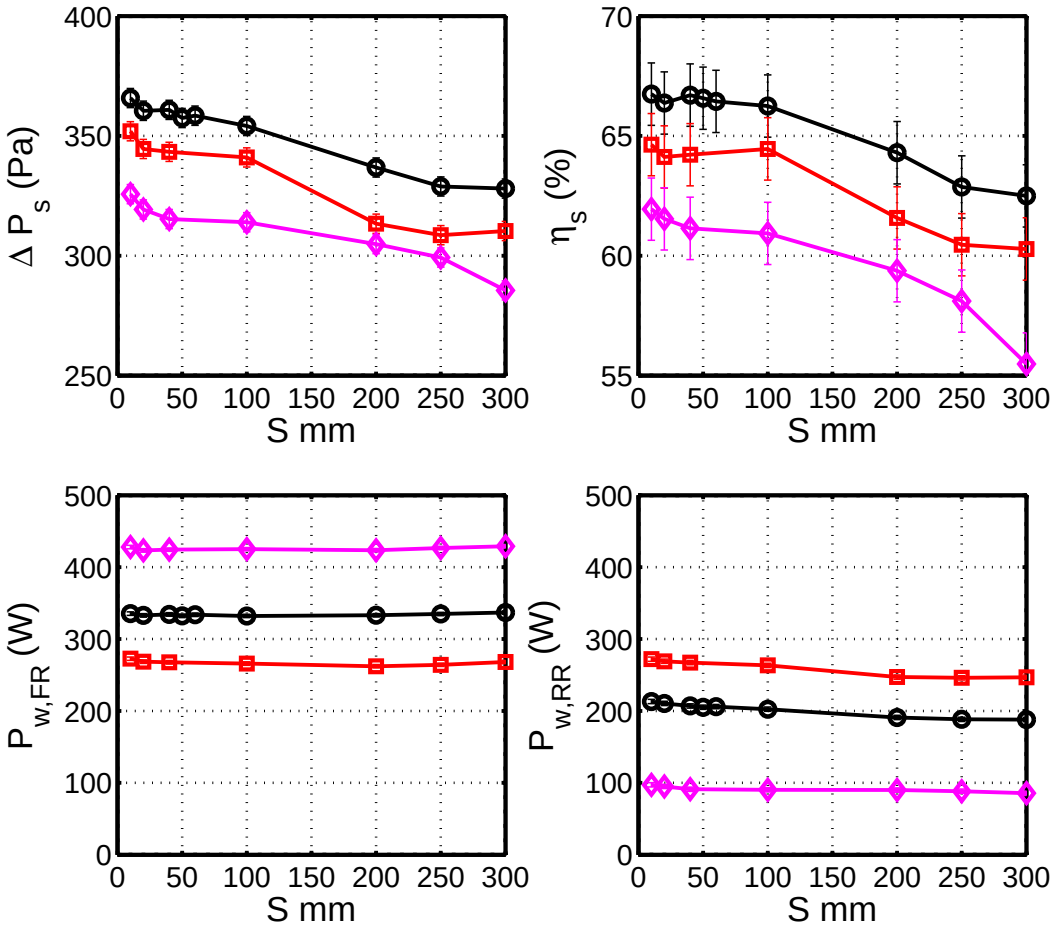

Figure 4.13: performance of JW1 (∘), JW2 (□) and JW3(◇) at $S = 10$, 20, 40, 100, 200, 250, 300 mm and Rront Rotor alone($S = 0$, filled symbols) at design point $Q_v = 1m^3.s^{-1}$, $\theta = \theta_c$, ΔP_s, $\mathcal{P}_{w,FR}$ and $\mathcal{P}_{w,RR}$ are rescaled by ρ_{ref}.

Further, the variations of the values are calculated from S = $[10, 100]$, $[100, 200]$, $[200, 300]$ mm, as shown in Tab. 4.4. For S increasing from 10 to 100 mm, the static pressure decreases by about 12 Pa and the static efficiency decreases slightly but still in the uncertainty range, for all CRS. The reason is that as the ΔP_s reduces, the power consumption for FR and RR diminishes as well. Thus, variations of η_s is not obvious. Wen S increases from 100 to 200 mm, for JW1 and JW2, the ΔP_s drops significantly. But the power consumption of FR varies slightly and that of RR falls relatively considerably. Thus, the power consumption of stage decreases not as fast as that of static pressure rise, therefore, the static efficiency deteriorates obviously by 2.0 and 2.9 percentages points for JW1 and JW2 respectively. For JW3, even if the static pressure rise reduces less than the other CRS, the power consumption for both FR and RR does not changes apparently. Nevertheless, the static efficiency for JW3 decreases by 1.5 percentage points. As S increases from 200 to 300mm, for JW1 and JW2, the ΔP_s and η_s decline relatively moderately. And the power consumption of stage increases because $\mathcal{P}_{w,FR}$ increase and $\mathcal{P}_{w,RR}$ varies slightly. However, for JW3, ΔP_s falls dramatically compared with the small distances. But power consumption of stage increases slightly because $\mathcal{P}_{w,FR}$ raises and $\mathcal{P}_{w,RR}$ reduces moderately. Thus, static efficiency of JW3 declines by 3.9 percentage points.

	S (mm)	JW1	JW2	JW3
ΔP_s (Pa)	10 to 100	−12	−11	−12
	100 to 200	−17	−28	−9
	200 to 300	−9	−3	−19
η_s (%)	10 to 100	−0.5	−0.1	−1.0
	100 to 200	−2.0	−2.9	−1.5
	200 to 300	−1.8	−1.3	−3.9
$\mathcal{P}_{w,FR}$ (W)	10 to 100	−3.2	−6.7	−3.0
	100 to 200	+1.0	−3.7	−1.5
	200 to 300	+3.7	+5.8	+5.6
$\mathcal{P}_{w,RR}$ (W)	10 to 100	−10.7	−8.7	−6.9
	100 to 200	−11.5	−16.1	−0.3
	200 to 300	−2.9	−0.4	−4.4

Table 4.4: Variations of ΔP_s, η_s, $\mathcal{P}_{w,FR}$ and $\mathcal{P}_{w,RR}$ with axial distances for the three CRS Q_v = 1 $m^3.s^{-1}$, at S = 10mm. + means the value increases; − means the value decreases

From another point of view, when the distance is smaller, the Rear Rotor recovers more swirl energy downstream of the Front Rotor. And less dynamic pressure drop is observed from FR to RR due to the friction loss and wake decay. But on the other hand, the power consumption of stage slightly increases. Nevertheless, in our case the relative increase in static pressure is greater than the relative increase in power consumption, which leads firstly, to a monotonic variation of the efficiency and secondly, to a stronger effect of the distance on the static pressure rise than on the efficiency.

4.5 Influence of speed ratio θ on the performances of CRS

Figure 4.14 gives the trend of the variation of the maximum static efficiency $\eta_{s,max}$ with the speed ratio for the three CRS. It should be noticed that the $\eta_{s,max}$ presented here are at decreased rotational speed of FR. Owing to the Reynolds effects on the low speed flow (seen in Fig. 3.30), the $\eta_{s,max}$ in Fig. 4.14 is slightly lower than $N_{FR} = N_{FR,C}$.

Favorably, all the CRS could maintain the $\eta_{s,max}$ beyond 60% as rotational speed varies in a large scale from 0.8 to 2 θ_C. This shows that a CRS does not only improve the efficiency to a high level, but is also robust at maintaining its high performance at various off-design conditions.

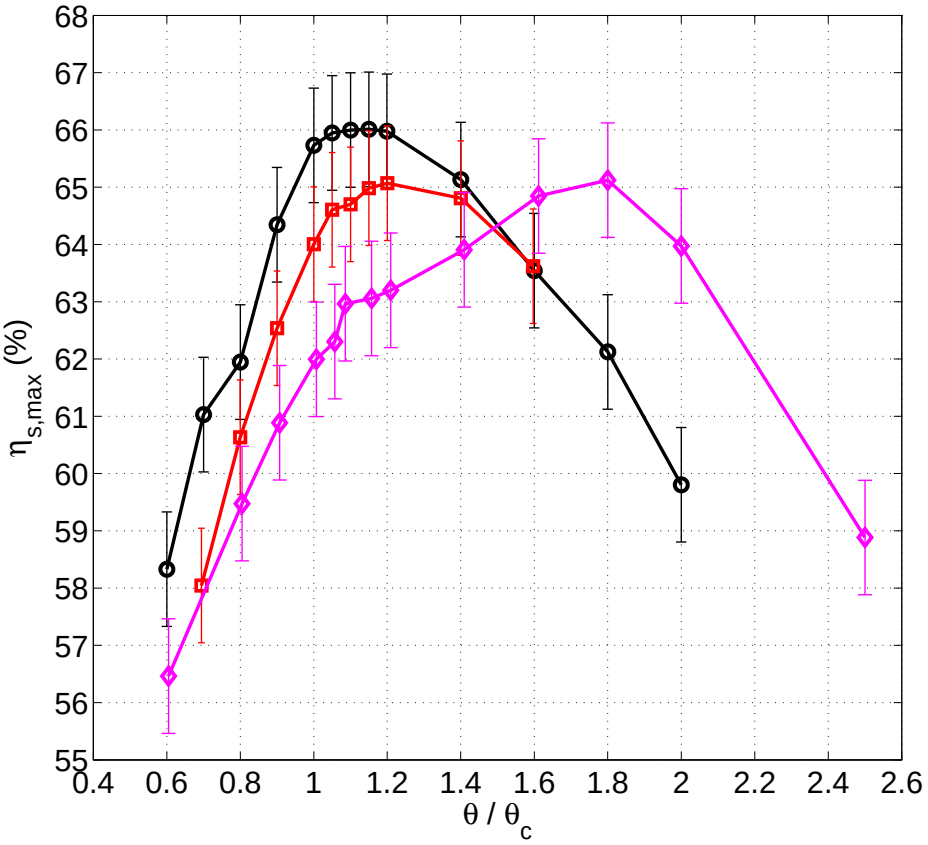

Figure 4.14: Maximum static efficiency vs. θ. *Stage JW1,* $N_{FR} = 1400$ *rpm,* $Re \approx 7.3{\times}10^4$ *(∘). JW2,* $N_{FR} = 1100$ *rpm,* $Re \approx 4.7 \times 10^4$ *(□). JW3,* $N_{FR} = 1600$ *rpm,* $Re \approx 7.4 \times 10^4$ *(◇).*

Additionally, it is obvious that $\eta_{s,max}$ increases significantly as θ is increased to θ_c, then continues to rise slightly as θ reaches $1.2\theta_c$, for all the three CRS. Nevertheless, the maximum efficiency drops down moderately as $\theta > 1.2\theta_c$ for JW1 and JW2, but on the contrary, for JW3 it continues to increase until $\theta = 1.8\theta_c$. This could own to the increased contribution of the Rear Rotor for this system. Additionally, it would be interesting to compare the flow features measured by LDV for JW3 at $\theta = \theta_C$ and $1.8\theta_C$.

4.6 Mix match of CRS

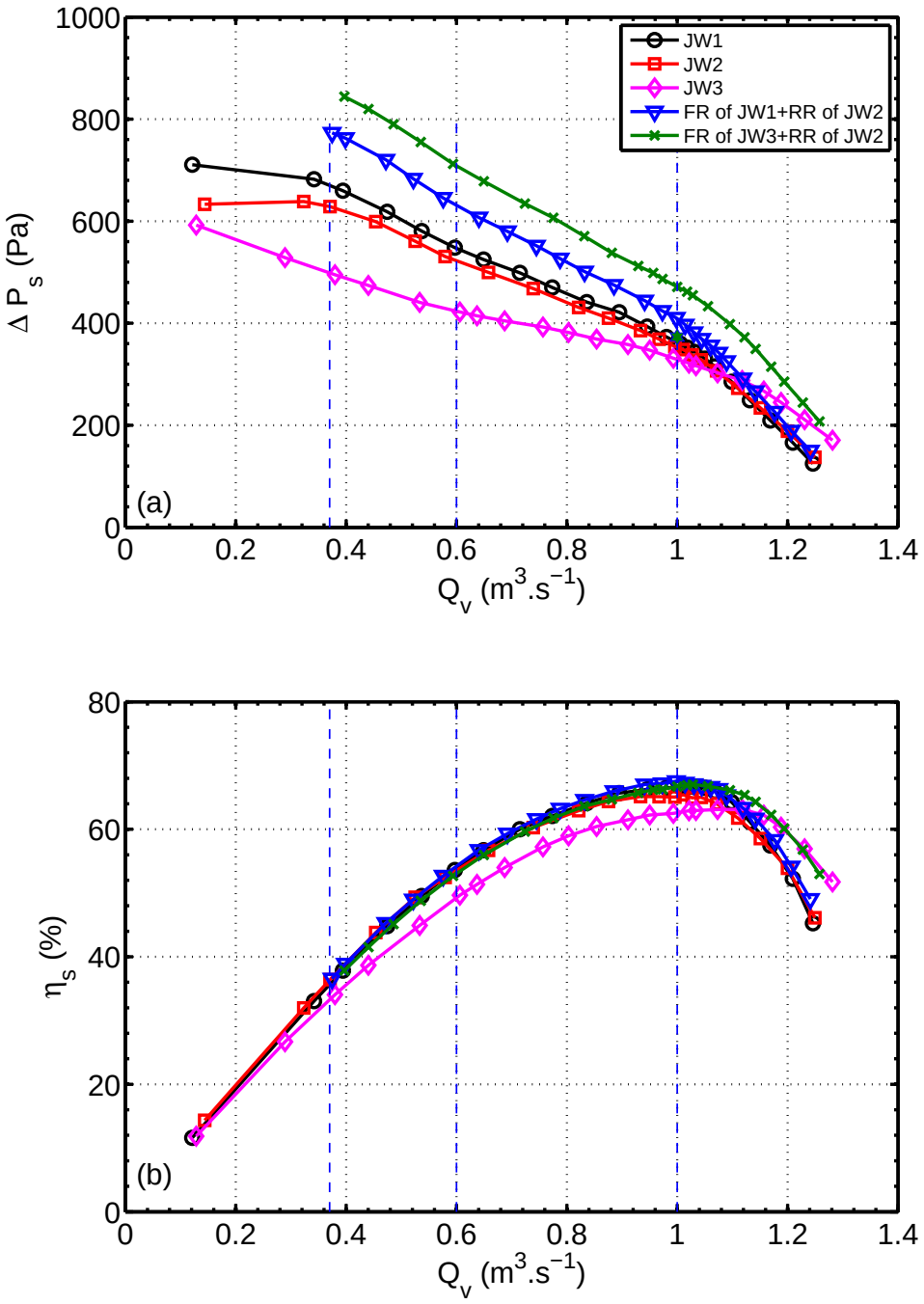

Figure 4.15: Overall performance of four systems: JW1(∘), JW2 (□) and JW3 (◇); FR of JW1+RR of JW2(▽ 2300 – 2600 rpm); FR of JW3+RR of JW2(× 2600 – 2600 rpm);design point,(✡) (a): Static pressure rise ΔP_s vs. volumetric flow rate Q_v. (b): Static efficiency η_s vs. volumetric flow rate Qv, at $S = 10$ mm.

The above analysis shows a higher speed ratio could increase the maximum efficiency,

theoretically, the mix match of high load of FR and RR could generate high performance. Additionally, as shown in Fig. 4.4, the circumferential averaged axial and tangential velocities have similar trends at outlet of all FRs. Thus, a mix match of the FR and RR between the CRS would be meaningful.

The three CRS are designed to achieve the same total pressure rise ΔP_t = 420 Pa, with the distribution of load 41%, 52% and 23%. It means that the total pressure rise of the combination FR of JW1+RR of JW2 should attain (59 + 52)% ×420 = 466 Pa (419 Pa for static pressure rise) without considering about additional loss due to the possible disadaptation. A combination of FR of JW3+RR of JW2 should achieve (77 + 52)% ×420 = 542 Pa (495 Pa for static pressure rise). Then the above inference is verified in the following parts.

The overall performance is presented in Fig. 4.15, for high load machine: FR of JW1 + RR of JW2 (2300 – 2600 rpm) and extremely high load machine: FR of JW3 + RR of JW2 (2600 – 2600 rpm), as well as the designed three CRS. First of all, it can be noticed that the new matching machines could provide much higher static pressure rise than designed CRS at almost of the operating range on keeping its high efficiency. Then, for the high load machine: FR of JW1 + RR of JW2 (2300 – 2600 rpm), the amelioration of ΔP_s and η_s is less at overflow flow rates. But for extremely high load machine: FR of JW3 + RR of JW2 (2600 – 2600 rpm), the improvement of performance is apparent at all operating range, especially high ΔP_s and η_s at overflow rates.

Then the performance at design flow rate for all configurations is listed in Tab. 4.5. It can be seen that with the mixed match of high load rotors, the ΔP_s could be improved to 409 and 471, for FR of JW1 + RR of JW2 (2300 – 2600 rpm) and FR of JW3 + RR of JW2 (2600 – 2600 rpm) respectively. They have −10 Pa (−2%) and −24 Pa (−5%) discrepancy to the predicted values. And the static efficiency could be largely improved as well. The highest static efficiency could be reached as 67.5% for the extremely high load combination FR of JW3 + RR of JW2 (2600 – 2600 rpm). Compared with the design JW3 which has lowest η_s by 62.6%, the higher load in RR could bring 4.9 percentage points gain. Therefore, the increase load in RR results in an improvement in the static pressure rise and efficiency. It indicates that the RR has a greater influence on the static pressure and efficiency than FR, which is consist with the results in Refs. [1][3].

CRS	N rpm	$\Delta P_{s,CRS}$ Pa	$\eta_{s,CRS}$ %
JW1	2300 – 2200	363 ± 4	66.6 ± 1.3
JW2	1800 – 2600	353 ± 4	65.2 ± 1.3
JW3	2600 – 1100	332 ± 4	62.6 ± 1.3
FR of JW1+RR of JW2	2300 – 2600	409 ± 4	67.5 ± 1.3
FR of JW3+RR of JW2	2600 – 2600	471 ± 4	66.7 ± 1.3

Table 4.5: Comparison performance at design point Q_v = 1 $m^3.s^{-1}$

Chapter 5

Conclusions ans perspective

5.1 Summary

This research continues the previous investigations on the performance and rotor-rotor interactions in the counter rotating subsonic axial flow fans. The purpose of this thesis is to attain three objectives. The first one is to provide an experimental basis for the parametric studies of CRS. It includes the design of new CRS configurations with different design parameters and evaluation of the uncertainty in the measurement methods. This has been presented in Chapter 2. The second objective is to validate the design methods in more details and provide suggestions for the optimisation of design and prediction methods. The third objective is to prepare a relatively comprehensive database for the parameter choice in the CRS design process. The main conclusions are outlined below.

5.1.1 Uncertainty evaluation of experimental methods

The study of the uncertainties showed that the experimental methods have satisfactory quality. For the global performance, the absolute uncertainties for static pressure rise ΔP_s and static efficiency of CRS are ±4 Pa (1%) and ±1.3 percentage points (2%) respectively. For LDV measurements, the uncertainty of circumferential averaged velocities is very sensitive to their magnitudes. Overall, the absolute uncertainty of averaged tangential velocities downstream RR are kept in the order of 0.05 m.s^{-1}. However, near the hub region where the magnitudes of velocities are really close to zero, the relative uncertainty could be in the order of 7 ~ 8%. For the measurements of wall pressure fluctuations, the absolute uncertainty are in the order of 1 dB/Hz and 0.1 dB for the amplitude of mains peaks in Power Spectrum Densities (PSD) and the power of total signal separately. And the positions of microphone on the block do have influence on the amplitudes of PSD, therefore, in the measurements of all experiments in this thesis, the microphone is always placed on the 'top' of the block.

5.1.2 Design of three new CRS

In order to verify the effects of the distribution of load $L_C = \frac{\Delta P_{t,RR}}{\Delta P_t}$, three CRS (JW1, JW2, JW3) are designed by varying the L_C at 41%, 52% and 23% respectively. Moreover, the Front Rotor (FR) of JW1 is designed to have large stagger angles to get a steep curve

of ΔP_s. JW2 is designed to have the highest L_C, which means more energy is transferred by the Rear Rotor (RR) among all the designed CRS. JW3 has the lowest L_C and with a highest and steepest characteristic of FR. Consequently, the Reynolds numbers of FRs in JW1 and JW3 are around 1.3×10^5 at midspan, which are much higher than those of FR in JW2 (by 8.0×10^4). Owing to the increased relative velocity by turning in opposite direction to FR, all RRs have much higher Reynolds numbers than those of FRs except the RR of JW3. Overall, the Re of almost all rotors are mainly in the order of $1 \sim 2 \times 10^5$, except near the hub region which is in the order of $4 \sim 6 \times 10^4$ for FRs and $8 \sim 9 \times 10^4$ for RRs. And the efficiency is quite dependent on the Reynolds number as reported for JW1 in Chapter 3.

5.1.3 Validation of design methods

The design methods are validated at the design flow rate for all configurations. The three CRS could well approach the same design point, with maximum −11.0% discrepancy for JW3. The static pressure curves are much steeper than those of the isolated FRs which indicates good work stability for CRS, regardless the characteristics of its FR. And all the CRS could work with minimum 62% for JW3 and maximum 66.6% static efficiency at design flow rate. It proves that CRS is a promising solution for high efficiency turbomachines. The work done by the Rotors measured by the torque meter and calculated based on the LDV measurements agrees well with the required values for CRS. It confirms that the estimation of the total pressure rise for FR and RR in CRS is in acceptable range.

The circumferential averaged axial (V_z) and tangential (V_θ) velocities are measured upstream, between and downstream the CRS at design flow rate, $\theta = \theta_C$, $S = 10$ mm for all CRS. The mains results are as below.

- The inlet of the CRS could be considered only in axial directions as expected, with only slight positive V_θ near the hub and tip region due to the aspiration effects together with the end wall and casing influences.

- Between the FR and RR of all CRS (5 mm downstream FR), MFT could well predict the tendency of radial profiles of V_z and V_θ for the isolated FRs, besides over-predicting the V_z near the tip region. This over prediction in V_z results in the under estimates of deviation angles downstream FR. It reveals that the loss model included in MFT could capture the main characteristics of flow fields downstream the isolated FR, but not sufficiently near the tip region where complex flow structures exist such as tip vortex interacting with the casing wall boundary layer. Moreover, the presence of RR has slight influence on the radial profiles of averaged velocities in most part of blade span. However, the averaged V_θ decreases significantly until zero near the hub region between the FR and RR, with the potential influence of RR. This decrease can even be observed at the tip region downstream of FR in JW2. These modifications increase dramatically the deviation angles near the hub region downstream of FR. Nevertheless, the power consumption of FRs keeps almost constant with or without FR at design flow rate.

- Since in the design process, the velocity fields outlet of FR are taken as the inlet conditions of the RR, the modifications of the velocity fields with the influence of

RR are not taken into accounts. Due to the unsuitable estimation of MFT near the tip region and potential effects of RR near the hub region, the incidence angle of RRs are not as expected at these regions. The results show that the incidence are mainly near zero at most blade span for RRs in JW1 and JW2 but positive near the tip region (maximum at 6°) and negative near the hub region (maximum about 5° in magnitudes). Consequently, at outlet of RR in JW1 and JW2, the tangential velocities are not completely recovered as required, with positive at most of blade span (in the order of 2 ~ 4 m.s^{-1}) and negative near the hub region (in the order of 1 ~ 2 m.s^{-1}). This part of energy is considered to be loss for a axial fan. Additionally, the deviation angles near the hub regions are much higher than near the tip region. It seems that the RRs are more sensitive to the negative angles near the hub region. This large deviation angles represents large loss resulting from the boundary separation. However, for RR of JW3, all the unsuitable estimation are much severe due to the potential effect of RR, the incidence angles are negative at most part of blade span except near the tip and hub region and the deflection angles increase dramatically below midspan. All the large increase in deviation angles reveal large separation of flow in RRs. This could be caused by the high stagger angle near the hub region of all RRs. On the other hand, it could infer that this big separation in RR could propagate upstream and modify the velocity fields downstream of RR. This could be one reason for the potential effects of RR. Therefore, one possible solution is to reduce the high stagger angles near the hub region of all RRs.

Aside from the unsuitable estimation near the hub and tip region, most part of the blade span of RR in three CRS can deflect the flow as required. These assumptions and prediction methods could be applied by the preliminary conception of subsonic counter rotating axial ducted fans. But the optimization could be suggested by modifying the loss model near the hub region of the FRs, as well as diminishing the stagger angle of all RRs.

5.1.4 Flow features at different flow rates

Radial profiles of the circumferential averaged V_z and V_θ are investigated at design flow rate Q_v = 1 m^3.s^{-1}, moderate partial flow rate Q_v = 0.6 m^3.s^{-1} and very low flow rate Q_v = 0.37 m^3.s^{-1}. These three points are where the slopes of ΔP_s curves change in the performance map. The results could be summarised as follows:

- For an isolated FR, during Q_v decreases to moderate partial flow rate, the reversed flow appears near the hub region and the load increase dramatically at almost all blade span besides near the hub region. Among all isolated FR, JW2FR has smallest reversed flow. As the Q_v continues to reduce, the reversed flow extends towards higher blade span and the increase of load is less than those of moderate flow rate. It reveal that at very low flow rate, the high incidence angle induces flow separation below midspan.

- When coupled to their RR, downstream of FR, the reversed flow are almost eliminated as Q_v reduces owing to the suction effects of RR. However, the load is largely

decreased at large part of blade span. Near the hub region downstream of the FR in JW3, the flow even turns in the direction of RR at partial flow rate. Similar opposite turning flow could be found both near the hub and tip region downstream FR in JW2 at partial flow rates, but in much smaller magnitudes of V_θ. When the flow passes trough RR, large reverse flow occurs near the hub at outlet of the RR and the flow swirls in the direction of RR with maximum magnitudes around 5 m.s^{-1} at partial flow rates. This indicates large loss at outlet of RR. All this reversed and contra swirling flow of RR could possibly propagate upstream to downstream of RR and much severe than at design flow rate. Additionally, at very low flow rate, when the flow goes through the RR in JW3, the V_θ increases from negative to positive below 40% of blade span, due to the opposite swirl flow at inlet of RR. This illustrates that at this part of blade the blade takes energy from the fluid instead of working on it. This would introduce large loss.

All the results show that the presence of RR decreases the adaptability of FR to the high incidence angle at design flow rate. This could be one of the reason that the slopes of static pressure curves change. Another reason could be the increased loss at outlet of RR.

5.1.5 Wall pressure fluctuation in CRS

The wall pressure fluctuations are measured at different axial positions of CRS. The results show that the Power Spectrum Density (PSD) of wall pressure fluctuations are characterised by three types of peaks which are corresponded to blade passing frequency of FR ($f_{bpf,FR}$) and RR ($f_{bpf,FR}$) including their harmonics and the interactions between them. The amplitudes of the peaks corresponding to $f_{bpf,FR}$ and its harmonics are relatively higher than those of $f_{bpf,RR}$ both downstream of FR and RR in CRS. Downstream of RR, the amplitudes of the peaks are much lower than those downstream of FR and peaks corresponding to FR are still visible. Furthermore, as Q_v reduces to partial flow rates, the peaks corresponding to interactions attenuate rapidly. It can infer that the fluctuations can propagate to far upstream without large attenuation but decay quickly downstream. Between the FR and RR, the wall pressure fluctuations are strengthened by the influence of both FR and RR and downstream FR the amplitudes are less influenced by the stage.

Additionally, downstream of FR, the amplitude of peak corresponding to $f_{bpf,RR}$ of JW2 is the highest and that of $f_{bpf,FR}$ is the lowest among all the peaks. This is correlated to the rotational speeds of the rotors. And the total level of the wall pressure fluctuations for JW3 is relatively lower than JW1 and JW2, owing to the much slower rotational speed of RR in JW3. It can infer that the RR has more influence on the total level of wall pressure fluctuations, which could be helpful for the control of related noise level.

5.1.6 Parameter study

A parameter study has been conducted to investigated the rotor-rotor interactions at various axial distances S and speed ratios θ for the three CRS. The main conclusions of this parameter study are the following:

Influence of axial distance S

The overall performance are investigated for JW1 working at $S \in [10, 300]$ mm ($[0.2, 5.5]L_{Chord}$), $\theta = \theta_C$. The results show the small axial distance is favorable because the ΔP_s and η_s deteriorate almost monotonically with the axial distance increases. Similar results can be obtained for JW2 and JW3. Precisely, when $S \in [10, 100]$ mm, the effects of static pressure drop could be canceled by the decrease of power consumption of FR and RR. Therefore, the static pressure diminishes slightly but still in the uncertainty range. When $S \in [100, 200]$ mm, the diminution in static pressure rise is much faster than that of power consumption, thus, the static pressure declines in the order of 2 percentage points. As $S \in [200, 300]$ mm, for JW1 and JW2, the decrease in static pressure drops relative slower but the power consumption of stage increases, thus the static efficiency reduces moderately. But for JW3, suddenly rapid drop in static pressure and increased power consumption cause 3.9 percentage points fall in static pressure.

In order to explain the effect of axial distance on the performance, the radial profiles of the circumferential averaged velocity fields are investigated for JW1 working on different S, at design flow rate. Three effects are found for the relative high loss in the JW1 at large axial distance:

- Increased loss in FR near the hub region. At the large distance, the averaged V_z is smaller and V_θ is higher than those of small S near the hub region, owing to less potential effects of RR. This causes the relatively larger deviations angles near the outlet hub of FR and loss increases in FR.

- Dynamic pressure deficit between FR and RR. When the distance is large, the tangential velocities attenuate significantly near both the hub and tip region, due to the wall friction loss and wake decay.

- Reduction of work done by RR. The velocity deficit induces large reduction in the incidence angle of RR near the hub region. Thus, the work done would be decreased significantly due to the smaller incidence angles near the tip region.

Influence of speed ratio θ

The speed ratio effects are firstly investigated on JW1 on keeping the FR rotating at designed speed $N_{FR,C}$ = 2300 rpm, at S = 10 mm, θ = $[0.86, 1.2]$ ($[0.9, 1.25]\theta_C$). The maximum static efficiency increases with the θ augments, even can reach as high as 68%. The static pressure grows significantly mainly owing to the significant increase of work done on the RR. This augmentation of work done attributes from the higher blade speed and larger ΔV_θ owing to increase in incidence angle by turning RR faster. At the same time, the increased incidence angle enlarges the separation in RR, when θ increases beyond $1.2\theta_C$, the attribution of static pressure augmentation on static efficiency is offset by the increased power consumption in RR, Thus, $\eta_{s,max}$ stops to raise.

In order to get higher θ and avoid exceeding the limits of maximum rotating speed of the motor, the N_{FR} of JW1 is decreased to 1400 rpm. The θ could be varied in $[0.6, 2]\theta_C$. However, the maximum efficiency also decreases by 2 percentage points with the reduced rotational speeds due to low Reynolds number effects. However, the tendency of $\eta_{s,max}$ as a function of θ/θ_C keeps almost the same for the both N_{FR}. The results of the reduced

N_{FR} show that $\eta_{s,max}$ raises first as θ enlarges then drop dramatically as θ is beyond $1.2\theta_C$ due to the large loss in RR. Similar results could be found for JW2 at reduced N_{FR}. However, for JW3, the $\eta_{s,max}$ increases to 65.1% as θ reaches 1.8θ then drops rapidly with θ augments. The possible reason could be the negative incidence angle at the inlet of RR in JW3 at $\theta = \theta_C$. Then the RR has more tolerance for the increased incidence angle owing to higher rotational speed of RR without large separation.

Thus, in the present research, the influence of θ on the performance of CRS depends on the incidence angle of RR at design θ_C, which is related to the stagger angles of RR.

Effects of distribution of load

Since the velocity fields at outlet of FR are quite similar for the three FRs, it could be meaningful to match the high load of FR and high load of RR to get better performance. In this concern, two new configurations are investigated. One is the high load machine formed by FR of JW1+RR of JW2, and the other is the extremely high load machine by FR of JW3+ RR of JW2. The new machines display improved global performance compared to the JW1, JW2 and JW3. They could attain the predicted value by only −2% and −5% for high load and extremely high load machine specifically. The maximum static efficiency of new configurations could reach a static efficiency at 67.5% for the extremely high load machine. Therefore, the increased load in RR could have a greater influence on the static pressure and efficiency than FR.

5.2 Recommendations for Future Work

The further work could be suggested as follows:

- All the FRs in three CRS in the thesis are designed by the "constant vortex method". It is suggested to design a new CRS by the "free vortex method", which could have a higher tangential velocity near the hub region. This could be beneficial concerning about the potential effects of RR which reduces the V_θ to zero near the hub region downstream of FR.

- Since the velocities presented in this thesis are the circumferential values, a measurement of velocities triggered with the rotational positions of two rotors could be helpful to investigate the blade to blade velocity fields.

- In the present work, the wall pressure fluctuations and flow fields are measured at design and partial flow rates. It could be also interesting to investigate the features at overflow rate, such as $Q_v = 1.2\ \mathrm{m^3.s^{-1}}$.

- It is suggested to study the flow features at $\theta = 1.8\theta_C$ for JW3 and compare them with those of $\theta = \theta_C$, in order to understand the mechanism of the higher performance at $\theta = 1.8\theta_C$.

- A specific investigation could be focused on the isolated RRs in the three CRS.

- The present experiments have provided a relatively comprehensive data base for the investigation of overall performance and parameters investigations of CRS. It could

be taken as a preliminary reference for the CFD validation which aims to model the flow and rotor rotor interactions in counter rotating subsonic axial ducted fans.

Bibliography

[1] D.S. Pundhir et P.B. Sharma : A study of aerodynamic performance of a contra-rotating axial compressor stage. *Defence Science Journal*, 42:191–199, 1992.

[2] Toru Shigemitsu, Junichiro Fukutomi et Takuya Agawa : Internal flow condition of high power contra-rotating small- sized axial fan. *International Journal of Fluid Machinery and Systems*, Vol.6, No.1:25–32, 2013.

[3] Chetan Mistry et AM Pradeep : Effect of variation in axial spacing and rotor speed combinations on the performance of a high aspect ratio contra-rotating axial fan stage. *Journal of Power and Energy*, 227(2):138–146, 2012.

[4] Linlin Cao, Satoshi Watanabe, Simpei Momosaki, Toshiki Imanishi et Akinori Furukawa : Low speed design of rear rotor in contra- rotating axial flow pump. *International Journal of Fluid Machinery and Systems*, Vol.6, No.2:105–112, 2013.

[5] Hussain Nouri : *étude expérimentale de l'écoulement et de l'interaction entre deux rotors contrarotatifs subsoniques.* Thèse de doctorat, Arts et Métiers Paristech, http://tel.archives-ouvertes.fr/tel-00795114, 2012.

[6] H. Nouri, A. Danlos, F. Ravelet, F. Bakir et C. Sarraf : Experimental study of the instationary flow between two ducted counter-rotating rotors. *J. Eng. Gas Turbines Power*, 135:022601, 2013.

[7] S. L. Dixon : *Fluid Mechanics and Thermodynamics of Turbomachinery.* Elsevier Inc. All, 2010.

[8] Erian A. Baskharone : *Principles of Turbomachinery in Air-Breathing Engines.* Cambridge University Press, Cambridge, 2006. ISBN 9780511616846.

[9] Tolga Köktürk : *Design and performance analysis of a reversible axial flow ran.* Thèse de doctorat, Middle East Technical University, 2005.

[10] Robert Rey : Aero-hydrodynamique interne des machines tome ||. Profiles, grilles d'aubes et machines axials.

[11] David Japikse et Nicholas C. Baines : *Introduction to Turbomachinery.* Concepts ETI, Inc. and Oxford University Press, 1997.

[12] Gröwoldt-Hesse Henning et Sohn AG : Stall and parallel operation. *In 6th International Conference- Tunnel Safety and Ventilation, Graz*, 2012.

[13] Bruno Eck : *Fans*. Pergamon Press, 1973.

[14] James E. Hatch, Charles C. Giaxnati et Robert J. Jackson : Application of radial-equilibrium condition to axial-flow turbomachine design including consideration of change of entropy with radius downstream of blade row. Rapport technique, Lewis Flight Propulsion Laboratory Cleveland, Ohio, 1954.

[15] Arthur J. Wennerstrom : *Design of highly loaded axial-flow fans and compressors*. Concepts ETI, Inc., 2000.

[16] Nicolas Courtiade : *Experimental analysis of the unsteady flow and instabilities in a high-speed multistage compressor*. Thèse de doctorat, Ecole Centrale de Lyon, 2012.

[17] A. J. Sanders, J. Papalia et S. Fleeter : Multi-blade row interactions in a transonic axial compressor part i: Stator particle image velocimetry (piv) investigation. *ASME*, Vol.124:10–18, 2002.

[18] Thomas Behr : *Control of Rotor Tip Leakage and Secondary Flow by Casing Air Injection in Unshrouded Axial Turbines*. Thèse de doctorat, Swiss Federal Institute of Technology Zurich, 2007.

[19] Jian Xu, Chunqing Tan, Haisheng Chen, Yangli Zhu et Dongyang Zhang : Influence of tip clearance on performance of a contra-rotating fan. *Journal of Thermal Science*, Vol.18, No.3:207–214, 2009.

[20] J. D. Denton : The 1993 igti scholar lecture: Loss mechanisms in turbomachines, 1993. ISSN 0889504X.

[21] Meinhard T. Schobeiri : *Turbomachinery Flow Physics and Dynamic Performance*. Springer, 2012.

[22] Rama S R Gorla : Turbomachinery design and theory. 2003.

[23] E. P. Lesley : Experiments with a counter-propeller. Rapport technique, National advisory committee for aeronautics, 1933.

[24] E. P. Lesley : Tandem air propellers. Rapport technique, National advisory committee for aeronautics, 1939.

[25] E. P. Lesley : Tandem air propellers-ii. Rapport technique, National advisory committee for aeronautics, 1941.

[26] Peter Schimming : Counter rotating fans- an aircraft propulsion for the future ? *J. of Thermal Science*, Vol.12, No.2, 2003.

[27] S. Dron : Toward acare 2020: Innovative engine architectures to achieve the environmantal goals? *In 26th International Congress of The Aeronautical Sciences*, pages ICAS 2008–4.2.2, 2008.

[28] T. Shigemitsu, T. Takano, A. Furukawa, K. Okuma et S. Watanabe : Pressure measurement on casing wall and blade rows interaction of contra-rotating axial flow pump. *J. of Thermal Science*, Vol.14:142–149, 2005.

[29] T. Shigemitsu, A. Furukawa, S. Watanabe, K. Okuma et J. Fukutomi : Experimental analysis of internal flow of contra-rotating axial flow pump. *In Proceedings of the 8th International Symposium on Experimental and Computational Aerothermodynamics of Internal Flows Lyon, July 2007*, 2007.

[30] T. Shigemitsu, J. Fukutomi et Y. Okabe : Performance and flow condition of small-sized axial fan and adoption of contra-rotating rotors. *Journal of Thermal Science*, 19:1–6, 2010.

[31] J. Fukutomi, T.Shigemitsu et T. Yasunobu : Performance and internal flow of sirocco fan using contra-rotating rotors. *Journal of Thermal Science*, Vol.17, No.1:35–41, 2008.

[32] L. Moroz, P. Pagur, Y. Govorushchenko et K. Grebennik : Comparison of counter-rotating and traditional axial aircraft low-pressure turbines integral and detailed performances. *In Int. Symp. on Heat Transfer in Gas Turbine Systems, Antalya, Turkey*, 2009.

[33] L. Cho, H. Choi, S. Lee et J. Cho : Numerical and experimental analyses for the aerodynamic design of high performance counter-rotating axial flow fans. *In Proc. ASME 2009 Fluids Engineering Division Summer Meeting, Colorado, USA*, pages FEDSM2009–78507, 2009.

[34] T. Shigemitsu, A. Furukawa, S. Watanabe, K. Okuma et J. Fukutomi : Internal flow measurement with ldv at design point of contra-rotating axial flow pump. *J. Fluid Sci. and Technology*, 4:723–734, 2009.

[35] S Momosaki, S Usami, S Watanabe et A Furukawa : Numerical simulation of internal flow in a contra-rotating axial flow pump. *In 25th IAHR Symposium on Hydraulic Machinery and Systems IOP IOP Conf. Series: Earth and Environmental Science 12 (2010) 012046*, 2010.

[36] L.-S. Cho, B.-J. Cha et J.-S. Cho : Experimental study on the three-dimensional unsteady flow characteristics of the counter-rotating axial flow fan. *Journal of Fluid Science and Technology*, Vol.4, No.1:200–209, 2009.

[37] Toru Shigemitsu, Junichiro Fukutomi et Hiroki Shimizu : Influence of blade row distance on performance and flow condition of contra-rotating small-sized axial fan toru. *International Journal of Fluid Machinery and Systems*, Vol.5, No.4:161–167, 2012.

[38] L L Cao, S Watanabe, T Imanishi, H Yoshimura et A Furukawa : Blade rows interaction in contra-rotating axial flow pump designed with different rotational speed concept. *In 6th International Conference on Pumps and Fans with Compressors andWind Turbines IOP Conf. Series: Materials Science and Engineering 52 (2013) 022004 doi:10.1088/1757-899X/52/2/022004*, 2013.

[39] R. Noguera, R. Rey, F. Massouh, F. Bakir et S. Kouidri : Design and analysis of axial pumps. *In Proc. ASME 1993 Fluids Engineering, Second Pumping Machinery Symposium, Washington USA*, pages 95–111, 1993.

[40] J. Vad : Forward blade sweep applied to low-speed axial fan rotors of controlled vortex design: An overview. *J. Eng. Gas Turbines Power*, 135:012601, 2012.

[41] C. Sarraf, H. Nouri, F. Ravelet et F. Bakir : Experimental study of blade thickness effects on the overall and local performances of a controlled vortex designed axial-flow fan. *Exp. Thermal and Fluid Science*, 35:684–693, 2011.

[42] Scott B. Reynolds, Steven E. Gorrell et Jordi Estevadeordal : Particle image velocimetry analysis on the effect of stator loading on transonic blade-row interactions. *Journal of Turbomachinery*, Vol.134:061012, 2012.

[43] J. Fernández Oro, K. Argüelles Díaz, C. Santolaria Morros et E Blanco Marigorta : Unsteady flow and wake transport in a low-speed axial fan with inlet guide vanes. *Journal of Fluids Engineering*, Vol.129:1015–1029, 2007.

[44] Meteociel.fr. http://www.meteociel.fr/temps-reel/obs_villes.php?code2=2.

[45] Knud Erik Meyer et William K George : Note on experimental fluid dynamics (efd) for course 41822 : Design of experiments and signal analysis . Rapport technique December, 2007.

[46] F. Bakir et S. Moreau : Efficient stator designed for automotive engine cooling fan systems. *In Proceedings of the ASME 2002 Fluids Engineering Division Summer Meeting*, pages FEDSM02–31318, 2002.

[47] S. C. Yen et F. T. Lin : Exit flow field and performance of axial flow fans. *J. Fluids Eng.*, 128:332–340, 2006.

[48] Michael Sturm et Thomas Carolus : Tonal fan noise of an isolated axial fan rotor due to inhomogeneous coherent structures at the intake. *In FAN 2012*, 2012.

[49] D. E. Van Zante, J. J. Adamczyk, A. J. Strazisar et T. H. Okiishi : Wake recovery performance benefit in a high-speed axial compressor. *Journal of Turbomachinery*, 124:275–284, 2002.

Appendix

Before conducting the research work on the three CRS, the author carried out the experiments on the existing CRS prototype "HSN" and a conventional Rotor Stator Stage (RSS), in which the stator is adapted to the Front Rotor (FR) of HSN. These studies provide an excellent opportunity to learn about the experimental methods, such as the pressure taps for measuring the static pressure rise of CRS, the Laser Doppler Velocimetry (LDV) for the instantaneous axial and tangential velocities at different axial positions, as well as the wall pressure fluctuation measurements. This is necessary for the following work. The experimental results show the difference between the CRS and RSS in overall performance and flow fields, which is given in detail in the following parts.

Appendix A

Experimental comparison between HSN and RSS

This article is published in the proceedings of the 10th European Turbomachinery Conference, Lappeenranta, Finlande (2013).

Experimental comparison between a counter-rotating axial-flow fan and a conventional rotor-stator stage

J. Wang - F. Ravelet - F. Bakir

DynFluid Lab., Arts et Metiers ParisTech, 151 boulevard de l'Hôpital, 75013 Paris, France,
florent.ravelet@ensam.eu

ABSTRACT

Based on the requirement of energy consumption level and weight and dimension restriction, compact axial machines are highly demanded in many industrial fields. The counter-rotating axial-flow fans could be a promising way to achieve these requirements. Because of the reduction of rotational speed and a better homogenization of the flow downstream of the rear rotor, these machines may have very good aerodynamic performances. However, they are rarely used in subsonic applications, mainly due to poor knowledge of the aerodynamics in the mixing area between the two rotors, where very complex structures are produced by the interaction of highly unsteady flows. The purpose of the present work is to compare the global performances (static pressure rise and static efficiency) and the wall pressure fluctuations downstream of the first rotor for three different stages operating at the same point: a single subsonic axial-flow fan, a conventional rotor-stator stage and a counter-rotating system that have been designed with in-house tools. The counter-rotating system allows large savings of energy with respect to the other two systems, for lower rotation rates and by adjusting the distance between the two rotors, a solution with comparable wall pressure fluctuations levels for the three systems is found.

NOMENCLATURE

Symbols

D	Pipe diameter
f	blade passing frequency
N	rotational rate (rpm)
P_{atm}	atmospheric pressure
P_s	static pressure
Q	Volumetric flow rate
s	axial distance
W	Power
z	axial coordinate
ΔP_s	static pressure rise
η_s	static efficiency
ϕ	volumetric flow rate coefficient
ω	angular velocity
Ψ_s	static head coefficient
ρ	density of the air
τ	torque
θ	ratio of angular velocities

Acronyms

CRS	counter-rotating system
FR	front rotor
RR	rear rotor
R1	front rotor alone
RSS	rotor-stator stage

INTRODUCTION

Nowadays, a revival of industrial interest for counter-rotating axial machines can be observed for various applications in subsonic regimes, as for instance fans and pumps, operating in ducted or free-flow configurations (Cho et al., 2009; Shigemitsu et al., 2009, 2010; Xu et al., 2009; Yoshihiko, 2003).

Counter-rotating axial-flow fans for electronic devices cooling application are for instance developed by SANYO DENKI (manufacturer of fans) with various diameters. According to Yoshihiko (2003), these products have the advantages of large air volume, high static pressure while lower noise and power consumption, compared to 2 conventional fans used in series. For the same type of industrial application, Shigemitsu et al. (2010) have shown with numerical studies that counter-rotating axial small-size fans provided higher pressure and efficiency than one single rotor. However, detailed experiments and analysis are still demanded to reveal the physical mechanisms that improve their efficiency compared to the conventional facilities.

The general idea of a counter-rotating system is that two rotors (front and rear) are rotating in opposite directions. The energy in the tangential velocity component of the flow after the first rotor is usually wasted in the wake (Dron, 2008). At the inlet of the rear rotor of a counter-rotating fan stage, this tangential velocity contributes to higher relative velocity, then it diffuses in the second rotor and is moreover converted to static pressure rise. Compared to a conventional rotor-stator stage, the rear rotor not only recovers the static head but also supplies energy to the fluid.

Given all the advantages indicated above, the counter-rotating system attracts attention of a large number of researchers. An original method to design such a system has been developped in the DynFluid Laboratory and has been validated on a first prototype: CRS (Nouri et al., 2013). In this experiment, the rotors operate in a duct of diameter $D = 380$ mm, the ratio $\theta = \frac{N_{RR}}{N_{FR}}$ of the rotation rates of the two rotors can be varied, and the axial distance s between the front rotor and the second rotor can be varied in a wide range (see Fig. 1).

The main results of this study are:

- the maximum of the peak static efficiency of CRS is $67 \pm 1\%$ whilst the peak static efficiency of the front rotor alone is $45 \pm 1\%$;
- at the design angular velocity ratio $\theta = 0.9$ the overall performances are not significantly

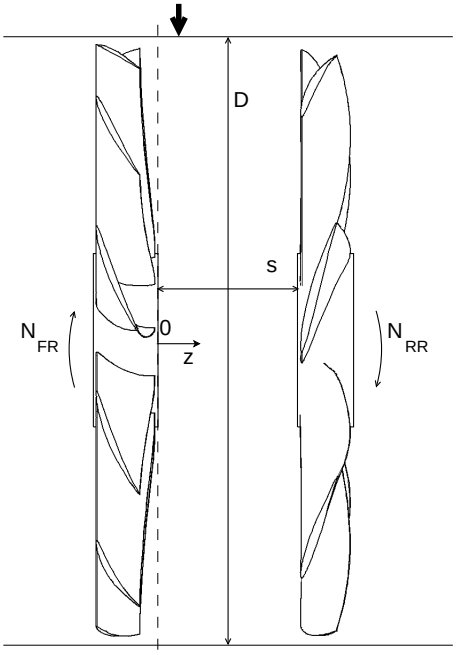

Figure 1: Sketch of the CRS arrangement that is considered in the present paper, showing the coordinate system and the main dimensions. The front rotor (FR) is on the left, and the rear rotor (RR) is on the right. The bold arrow stands for the microphone (position $z = 5$ mm).

affected by a variation of the axial distance in the range $s = \in [10; 50]$ mm, with s the distance between the trailing edge of the front rotor and the leading edge of the rear rotor;

- However, at $\theta = 0.9$, the pressure rise is decreased by 5% and the efficiency decreases from $65 \pm 1\%$ to $63 \pm 1\%$ when s is increased from 10 to 180 mm;
- at small axial distances ($s < 50$ mm), the analysis of the power spectral density for wall pressure fluctuations and of the radial profiles of the average velocity confirm that the rear rotor does significantly affect the flow field in the interaction area.

The main objective of the present study is to experimentally detail the differences between CRS, a conventional single rotor stage (R1) and a conventional rotor-stator stage (RSS). To achieve this target, a first series of experiments are carried out on a single axial-flow fan (R1). Then a stator is designed to fit with this rotor to form RSS and finally, the second counter-rotating rotor is used to form the counter-rotating stage (CRS). The experimental set-up is first briefly described. Then, the overall performances of the three systems are compared. In order to compare the levels and spectra of the wall pressure fluctuations, a seek for operating conditions of the three systems that lead to the same given output aerodynamic power is then performed. Finally, the effects of the axial distance s for RSS and CRS both on the global performances and on the pressure fluctuations levels and spectra are studied.

EXPERIMENTAL SET-UP AND MEASUREMENTS METHOD

The experimental investigations of the three configurations (R1, CRS and RSS) are performed on a normalized experimental test-bench: AERO^{2}FANS, built for this purpose in the DynFluid Laboratory. The design points of R1 and of CRS are respectively a total pressure rise of 260 Pa and 420 Pa at a nominal volumetric flow rate $Q = 1$ m^3.s^{-1} and for rotation rates $N_{FR} = 2000$ rpm and $\theta = 0.9$. More details about the test bench and those two configurations are given in the article of Nouri et al. (2013).

In the present paper, the static pressure rise is defined according to the ISO-5801 standard as the difference between the static pressure downstream of the studied machine and the total pressure at the inlet (atmospheric pressure): $\Delta P_s = P_{sRR2} - P_{atm}$. This value is obtained by averaging the results of four pressure taps placed downstream of a flow straightener, then corrected with the pressure drop of the circuit that is measured without the rotors. The static efficiency is defined as $\eta_s = \frac{\Delta P_s Q}{(\tau_{FR}\omega_{FR})+(\tau_{RR}\omega_{RR})}$. The torque τ is measured by the drivers of the DC brushless motors and has been calibrated against a rotating torquemeter. The casing wall pressure fluctuations are recorded by a 40BP pressure microphone, which has been calibrated by an acoustic calibrator. The sampling frequency for the signal of the wall pressure fluctuations is 6 kHz. The power spectral density and the total average power of the pressure fluctuations are expressed in dB.Hz^{-1} and dB with a pressure reference of 1 Pa. The axial distance between the two rotors s and the position of the microphone z are defined in Fig. 1.

RESULTS AND DISCUSSION

Comparison of the overall performances of R1, RSS and CRS

To compare the overall performance of the three configurations (R1, RSS, CRS), some working conditions are first set: the axial distance for RSS is $s = 15$ mm and for CRS it is $s = 10$ mm, which corresponds to 17% of the chord of FR at mid-span. In the following, the θ ratio of CRS is always set to $\theta = 1$ and the symbol N thus stands for the rotation rate of the rotor(s) for R1, RSS and CRS. The static head coefficient defined by $\Psi_s = \frac{\Delta P_s/\rho}{(N/60)^2 D^2}$ as a function of the volumetric flow coefficient defined by $\phi = \frac{Q}{(N/60)D^3}$ and the static efficiency η_s as a function of ϕ are plotted in Fig. 2. The

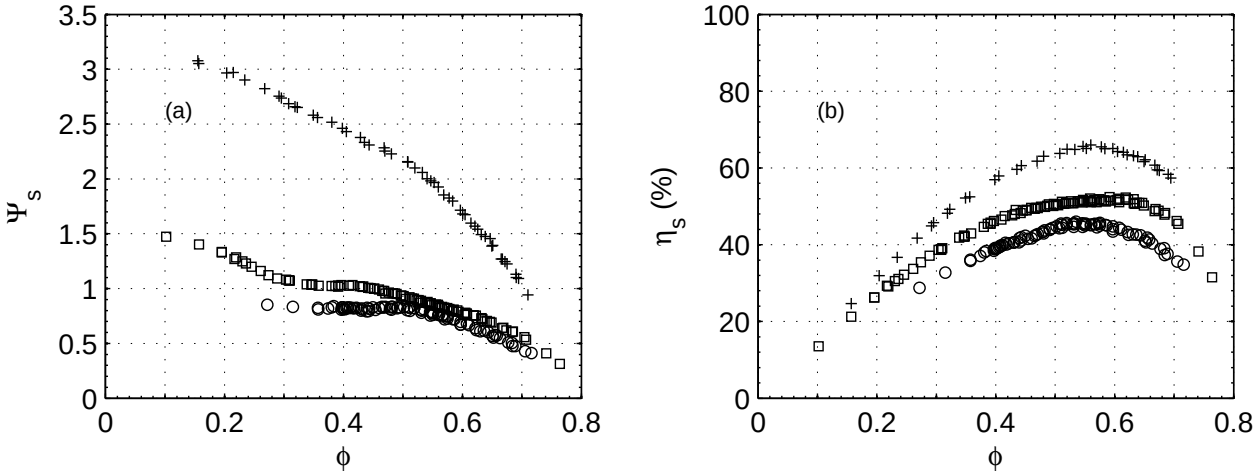

Figure 2: Dimensionless characteristics of the three systems: R1 (○), RSS at $s = 15$ mm (□) and CRS at $s = 10$ mm and $\theta = 1$ (+). (a): Static head coefficient Ψ_s *vs.* volumetric flow rate coefficient ϕ. (b): Static efficiency η_s *vs.* flow coefficient ϕ.

data reported in this figure have been obtained at various rotation rates: respectively $N = 2100$ and 2300 rpm for R1, $N = 2000$, 2100 and 2200 rpm for RSS, and $N = 1600$ and 1800 rpm for CRS. The Reynolds numbers based on the relative inlet velocity and on the chord at mid-span are all greater than 2.4×10^5 (Nouri et al., 2013).

The different curves fairly collapse for each system: the dimensionless coefficients do not depend on the Reynolds number, which is a classical result for developped turbulent flows (Tennekes and Lumley, 1972).

It can be moreover observed that the slope of the Ψ_s *vs.* ϕ curve is steeper for CRS than for R1 and RSS, as noticed by Shigemitsu et al. (2009): this feature can be explained close to the nominal volumetric flow rate with a theory based on the energy and angular momentum balances for perfect fluid (Euler's equation of turbomachinery). The present results moreover show that, contrary to what is observed for the single rotor R1 or the conventional rotor-stator stage RSS, the characteristic curve of CRS has a large negative slope even at very low volumetric flow rates which corresponds to a very good operating stability.

The maximum efficiency for R1 is $45 \pm 1\%$, while it is $51 \pm 1\%$ for RSS and $66 \pm 1\%$ for CRS. The gain in peak-efficiency brought by the use of the stator is approximately $+6$ percentage-points with respect to R1, which is a classical value according to Moreau and Bakir (2002). The gain in efficiency brought by the use of a counter-rotating rotor —roughly $+21$ percentage-points— is thus much higher.

Comparison of the systems when delivering the same given output aerodynamic power

Overall performances

In view of comparing both the global performances and the wall pressure fluctuations for the different systems R1, RSS and CRS in a dimensional point of view, three working conditions are now studied. The rotation rates of the three systems are adjusted such that the same aerodynamic output power is obtained. In other words, a seek for points such that $\Delta P_s Q = constant$ has been performed. The flow conditions and the corresponding operating conditions for each system are given in Tab. 1 for those three "crosspoints".

The crosspoint 1 corresponds to an operating point where CRS is working at a nominal flow

Cross points	Parameters	R1	RSS	CRS
Crosspoint 1	Q (m^3.s^{-1})		0.87	
	ΔP_s (Pa)		212	
	N (rpm)	2300	2100	1600
	η_s	40%	49%	66%
	W (W)	461	375	279
Crosspoint 2	Q (m^3.s^{-1})		0.95	
	ΔP_s (Pa)		177	
	N (rpm)	2100	2000	1600
	η_s	44%	51%	66%
	W (W)	380	328	256
Crosspoint 3	Q (m^3.s^{-1})		1.08	
	ΔP_s (Pa)		209	
	N (rpm)	2300	2200	1800
	η_s	45%	51%	61%
	W (W)	500	443	369

Table 1: Operating conditions of the three systems for the crosspoints 1, 2 and 3 ($\rho = 1.21$ kg.m^{-3}).

rate, the crosspoint 2 corresponds to RSS working at a nominal flow rate and the crosspoint 3 to R1 at a nominal point. It is obvious that to reach the same pressure rise at the same volumetric flow rate, CRS always requires much lower rotational velocity compared to R1 and RSS: in the worst case (crosspoint 3), the rotation rate of CRS is respectively 78% and 82% of that of R1 and RSS. In addition, the static efficiency of CRS is 16 percentage-points higher than that of R1 and 10 percentage-points higher than that of RSS in the worst case (crosspoint 3 corresponding to an overflow rate of 114% for CRS). Besides, at the three crosspoints, the mechanical power consumed by CRS is respectively 40%, 32% and 26% lower than that of R1. In another way, it could be concluded that CRS could provide higher pressure rise and air volumetric flow rate at a given power consumption, consequently allowing a decrease of the fan diameter and of the rotational speed.

Comparison of wall pressure fluctuations at crosspoint 1 and small axial distances

The figure 3 shows the power spectral density of the wall pressure fluctuations measured at the same operating point (crosspoint 1 in Tab. 1) for the three configurations and for the same s as in the previous paragraph. These power spectra are characterized by a broadband noise superimposed to a series of discrete frequency peaks. It is obvious that the spectrum for CRS presents much more peaks. These peaks can be classified into three categories: front rotor blade passing frequency f_{FR} and its harmonics ($\circ$), rear rotor blade passing frequency f_{RR} and its harmonics ($\square$) and the frequencies resulting from the interactions between the two aforementioned modes, that consist of linear combinations $mf_{FR} + nf_{RR}$ where $m, n \in \mathbb{Z}^*$. Results observed by Nouri et al. (2013) on the same facility at a different θ are in accordance with this theory for the CRS tonal noise. The additional peaks for CRS are due to the potential influence of the rear rotor on the front one, and to the influence of the front rotor on the rear rotor: both vortex shedding and viscous wakes impact the second rotor when the axial distance is small (Blandeau, 2011).

The tonal peaks corresponding to FR for CRS are lower than those for the R1 and RSS systems which is consistent with its lower rotation rate. However, the tonal peaks corresponding to RR are on the one hand larger than that of FR, which is consistent with the higher loading of RR's blades (Nouri et al., 2013) and in addition are even about twice as large as the FR peaks of R1 and RSS. Ultimately,

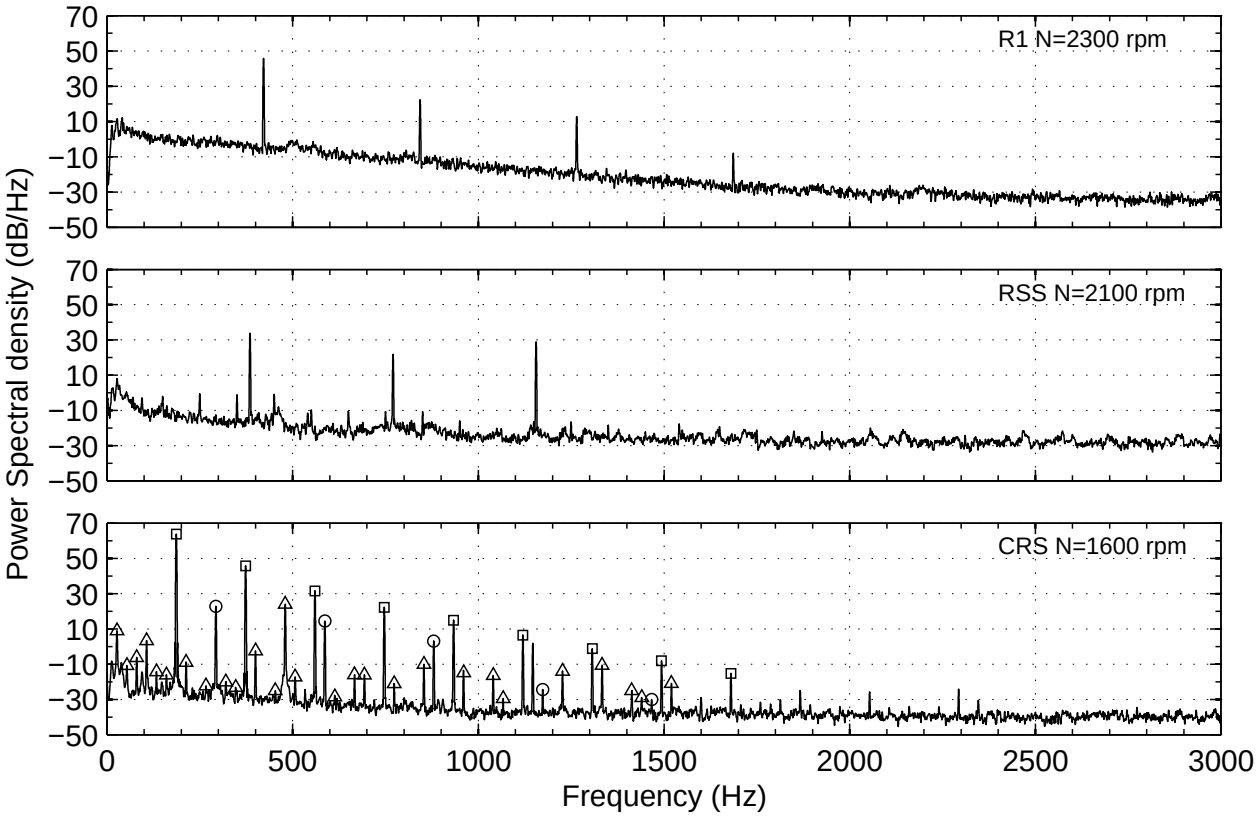

Figure 3: Power spectral density of the wall pressure fluctuations recorded at $z = +5$ mm downstream of FR under crosspoint 1 conditions (see Tab. 1). For CRS, the $\circ$ stand for the blade passing frequency of FR and its harmonics, the $\square$ stand for the blade passing frequency of RR and its harmonics, and the Δ stand for the interactions of these frequencies.

the total level of the wall pressure fluctuations, *i.e.* the average power, is respectively 26.9 ± 0.2 dB, 30.8 ± 0.2 dB and 37.4 ± 0.2 dB for RSS, R1 and CRS. As the wall pressure fluctuations may be in close relation to the acoustic sources (Joongnyon and Hyung, 2006), CRS at $s = 10$ mm may thus be much noisier than RSS for the same aerodynamic output power.

Influence of the axial distance s on RSS and CRS

The figure 4 presents the influence of the axial distance s on the performances of RSS and CRS. The performances of RSS for $s = 5$, 15 and 55 mm are plotted in Fig. 4(a-b) and that of CRS at $\theta = 1$ for $s = 10$ and 50 mm are plotted in Fig. 4(c-d). For both systems, the pressure rise is unaffected at nominal and overflow rates and slightly decreases with increasing s at partial flow rates. As explained by van Zante et al. (2002), viscous loss effects in the wake modify inlet angles for the second rotor and then less energy is recovered by the second —stationary or rotating— blade cascade for increased axial distance. Concerning the static efficiency, the small differences that can be observed are within the measurement uncertainty. This infers that the axial distance s does not have obvious influence on the global performances of RSS and CRS, in the studied range of axial distances that corresponds to $9\% \leq s \leq 95\%$ (in percentage of the chord of FR at mid-span).

The figure 5 presents the influence of the axial distance s on the wall pressure fluctuations downstream of FR for RSS and CRS. Concerning RSS, the increase of axial distance from $s = 15$ to $s = 55$ mm only leads to slight qualitative modifications of the spectrum with a low attenuation of the fourth harmonic. The total average power of the signal decreases from 28.6 ± 0.2 to 27.8 ± 0.2 dB. On

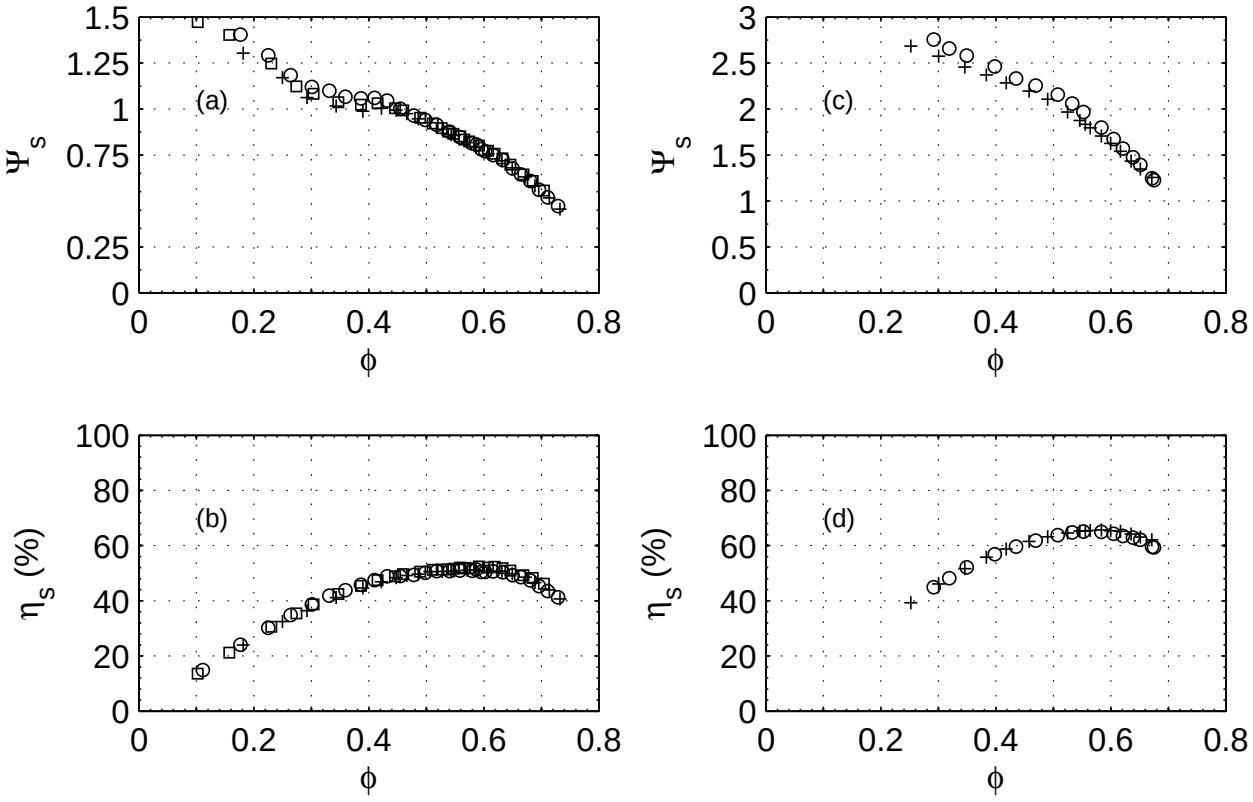

Figure 4: Influence of the axial distance on the performances. (a-b): RSS, Ψ_s and η_s *vs.* ϕ for ($\circ$): $s = 5$ mm, ($\square$): $s = 15$ mm and ($+$): $s = 55$ mm. (c-d): CRS, Ψ_s and η_s *vs.* ϕ for ($\circ$): $s = 10$ mm and ($+$): $s = 50$ mm.

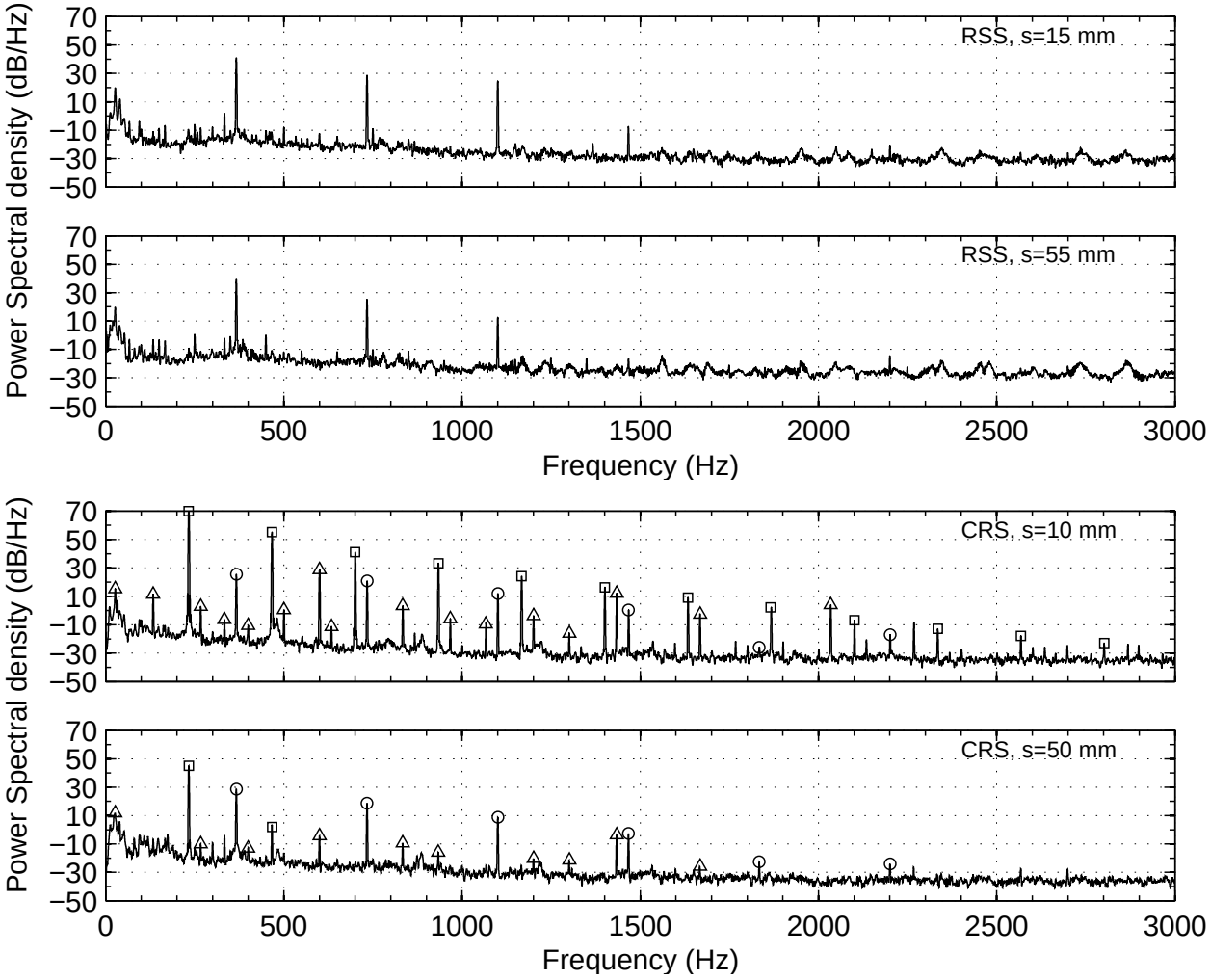

Figure 5: Power spectral density of the wall pressure fluctuations recorded at $z = +5$ mm downstream of FR for RSS and CRS rotating at $N = 2000$ rpm for various axial distances. The operating point is the nominal point of each case. The $\circ$ stand for the blade passing frequency of FR and its harmonics, the $\square$ stand for the blade passing frequency of RR and its harmonics, and the Δ stand for the interactions of these frequencies.

the opposite, one can observe a huge effect of the increase in axial distance on the spectral content for CRS. First of all, the peaks corresponding to the RR are strongly attenuated and only the fundamental (f_{RR}) and the second harmonic ($2f_{RR}$) are present for $s = 50$ mm while up to 10 harmonics are visible for $s = 10$ mm. Similarly, the interaction peaks are considerably weakened. On the other hand, the peaks corresponding to FR remain unchanged. Ultimately, the total average power is lowered from 42.0 ± 0.2 to 30.3 ± 0.2 dB. It can be concluded that increasing the axial distance would have more influence on CRS than on RSS in terms of wall pressure fluctuations and thus, the axial distance would be an efficient optimization parameter regarding the noise reduction of low-speed counter-rotating axial-flow fans.

CONCLUSIONS

Experimental investigations of the differences in terms of overall performances and wall pressure fluctuations between a single rotor, a conventional rotor-stator stage and a counter-rotating system have been performed. The results can be summarized as follows:

1. The characteristic curve of the counter-rotating system is significantly steeper than that of the single rotor and of the conventional rotor-stator stage and is still significantly negative at very low partial flow rates. This improves the operating stability compared to the conventional configurations.

2. At a given power consumption, the counter-rotating system could produce a much larger pressure rise and efficiency, with a lower rotation rate. The gains in efficiency and in rotation rate with respect to the rotor-stator stage are at least of the order of $+10$ percentage-points and -20% respectively.

3. The study of the wall pressure fluctuations for a small axial distance between the two rotors shows that for the same output aerodynamic power, though CRS is rotating more slowly, it may still be much noisier than R1 and RSS.

4. A slight increase in the axial distance could nonetheless be a very efficient way to cope with this problem, as the overall performances are hardly affected but the average power of wall pressure fluctuations is strongly reduced.

The future works that are now undertaken are first, to design different counter-rotating systems that all have the same design point and differ in the repartition of the load between the two rotors, and on the radial distribution of the Euler work on the first rotor, and also to build a small-scale CRS in order to study its far-field acoustic radiation under anechoic conditions.

References

V. Blandeau. *Aerodynamic Broadband Noise from Contra-Rotating Open Rotors*. PhD thesis, University of southampton, 2011.

L.-S. Cho, B.-J. Cha and J.-S. Cho. Experimental study on the three-dimensional unsteady flow characteristics of the counter-rotating axial flow fan. *Journal of Fluid Science and Technology*, 4: 200–209, 2009.

S. Dron. Toward acare 2020: Innovative engine architectures to achieve the environmantal goals? In *26th International Congress of The Aeronautical Sciences*, pages ICAS 2008–4.2.2, 2008.

K. Joongnyon and J.S. Hyung. Wall pressure fluctuations and flow-induced noise in a turbulent boundary layer over a bump. *J. Fluid Mech.*, 558:79–102, 2006.

S. Moreau and F. Bakir. Efficient stator designed for automotive engine cooling fan systems. In *ASME 2002 Fluids Engineering Division Summer Meeting*, pages FEDSM02–31318, 2002.

H. Nouri, A. Danlos, F. Ravelet, F. Bakir, and C. Sarraf. Experimental study of the instationary flow between two ducted counter-rotating rotors. *Journal of Engineering for Gas Turbines and Power*, 135:022601, 2013.

D.S. Pundhir and P.B. Sharma. A study of aerodynamic performance of a contra-rotating axial compressor stage. *Defence Science Journal*, 42:191–199, 1992.

T. Shigemitsu, A. Furukawa, S. Watanabe, K. Okuma, and J. Fukutomi. Internal flow measurement with ldv at design point of contra-rotating axial flow pump. *Journal of Fluid Science and Technology*, 4:723–734, 2009.

T. Shigemitsu, J. Fukutomi, and Y. Okabe. Performance and flow condition of small-sized axial fan and adoption of contra-rotating rotors. *Journal of Thermal Science*, 19:1–6, 2010.

H. Tennekes and J. L. Lumley. *A First Course in Turbulence*. MIT Press, Cambridge, 1972.

J. Xu, C. Tan, H. Chen, Y. Zhu and D. Zhang. Influence of tip clearance on performance of a contra-rotating fan. *Journal of Thermal Science*, 18:207–214, 2009.

A. Yoshihiko. Cooling system technology that changes the conventional trend. Technical report, SANYO DENKI, 2003.

D. E. van Zante, J. J. Adamczyk, A. J. Strazisar, and T. H. Okiishi. Wake recovery performance benefit in a high-speed axial compressor. *Journal of Turbomachinery*, 124:275–284, 2002.

Appendix B

Flow fields comparison between CRS and RSS by LDV

The previous studies show that cross-points with the same aerodynamic power could be found for the R1, RSS and CRS on varying the rotational speeds. These points could be plotted in the performance map, as shown in Fig. B.1.

As can be seen in Fig. B.1, Crosspoint 1 corresponds to an operating point where CRS is working at a nominal flow rate. In the present chapter, the instantaneous velocities are first measured by LDV at the same axial position for R1, RSS and CRS at Crosspoint 1. An the velocity fields at Q_v = 1 $m^3.s^{-1}$ are then presented.

B.1 Velocity field downstream FR measured by LDA at crosspoint1

Figures B.2 and B.3 show circumferential averaged velocity profiles 5 mm downstream of Front Rotor in three configurations: R1, RSS and CRS. The vertical axis is normalized radial position, calculated by the radius divided by the blade height. It should be pointed out that all the rotors in three configurations have small hub radius (55 mm) compared with JW1, JW2 and JW3 (65 mm).

At crosspoint1, CRS has much lower RMS of velocity field at most part of blade passage (above 20% of the blade height). Besides, negative axial velocities appear at low blade span of all three configurations, and the locations are below 15%, 23% and 5% of blade span for R1, RSS and CRS, respectively.

For R1 alone, the tangential velocities are the highest among the three configurations. With the presence of a stator, the load diminishes significantly below 50% blade span. Then by replacing the stator with a rear rotor, the V_θ reduces largely above 40% blade span and increases in the lower span.

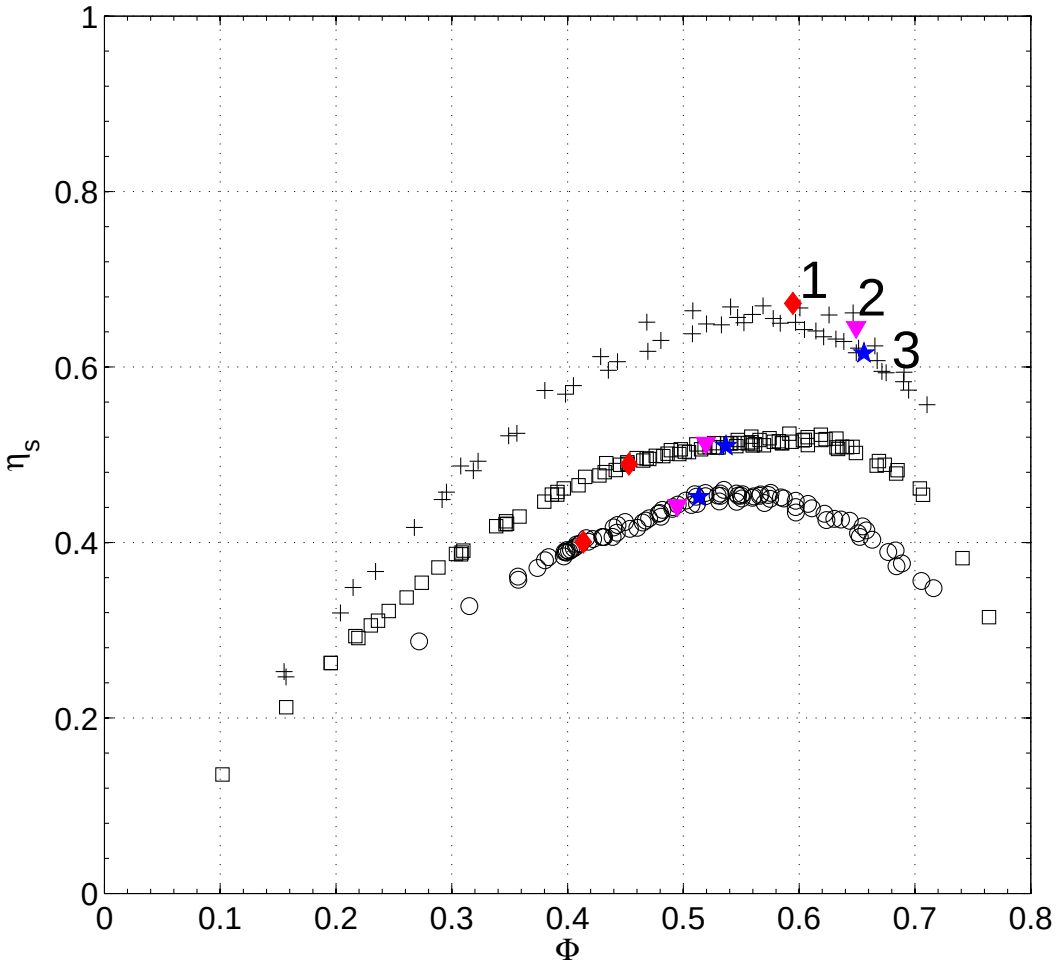

Figure B.1: Static efficiency η_s vs. *flow coefficient* ϕ, *for the three systems: R1 (∘), RSS at* s = 15 *mm (□) and CRS at* s = 10 *mm and* θ = 1 *(+). Crosspoint 1(◆), Crosspoint 2(▼),Crosspoint 3(★)*

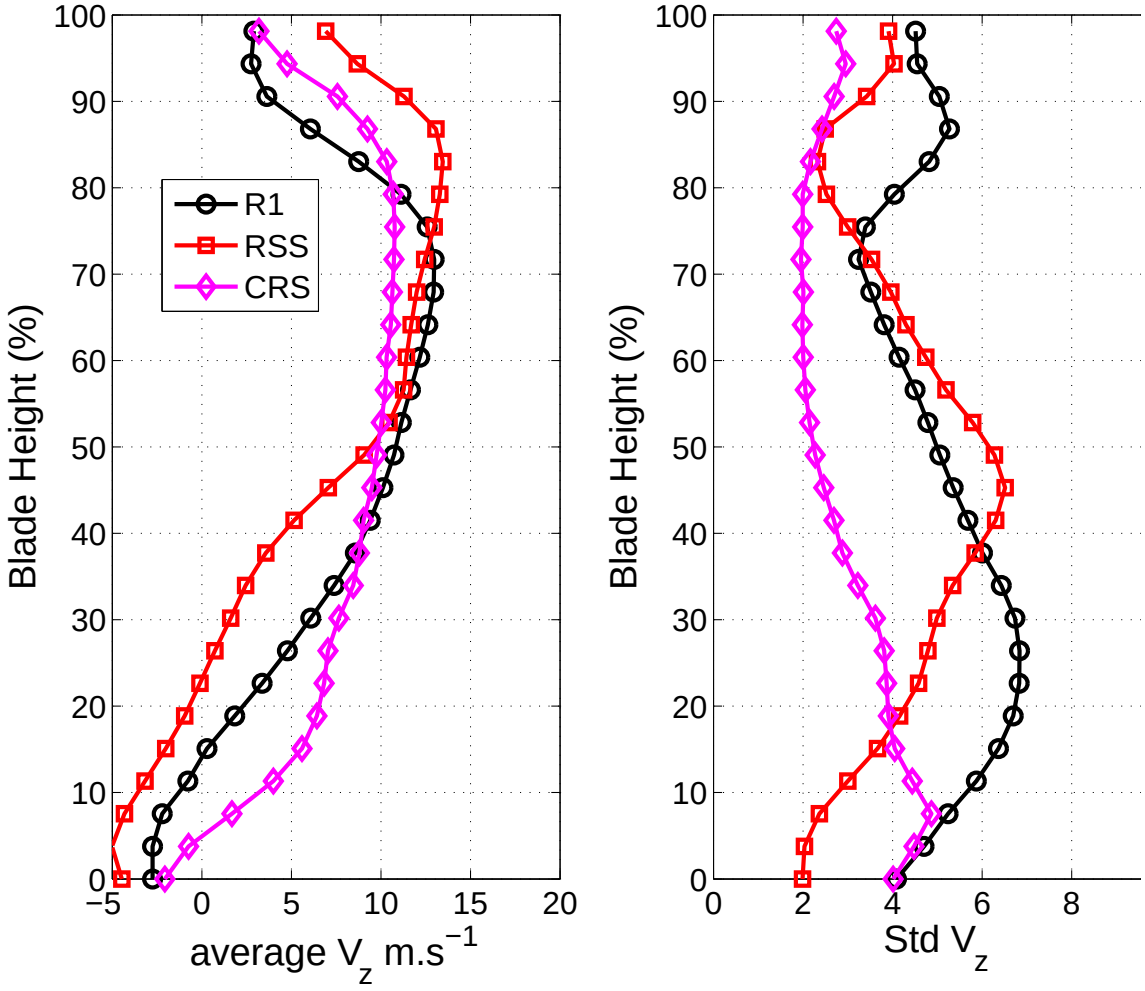

Figure B.2: Circumferential averaged axial velocities and their STD for different configuration:
$R1(\circ), N = 2300rpm$
$RSS, S = 15mm(\square)\ N = 2100rpm$
$CRS, S = 10mm(\diamond)\ N = 1600 - 1600rpm$
at about $Qv = 0.87\ m^3.s^{-1},\ Z_p = 5mm$

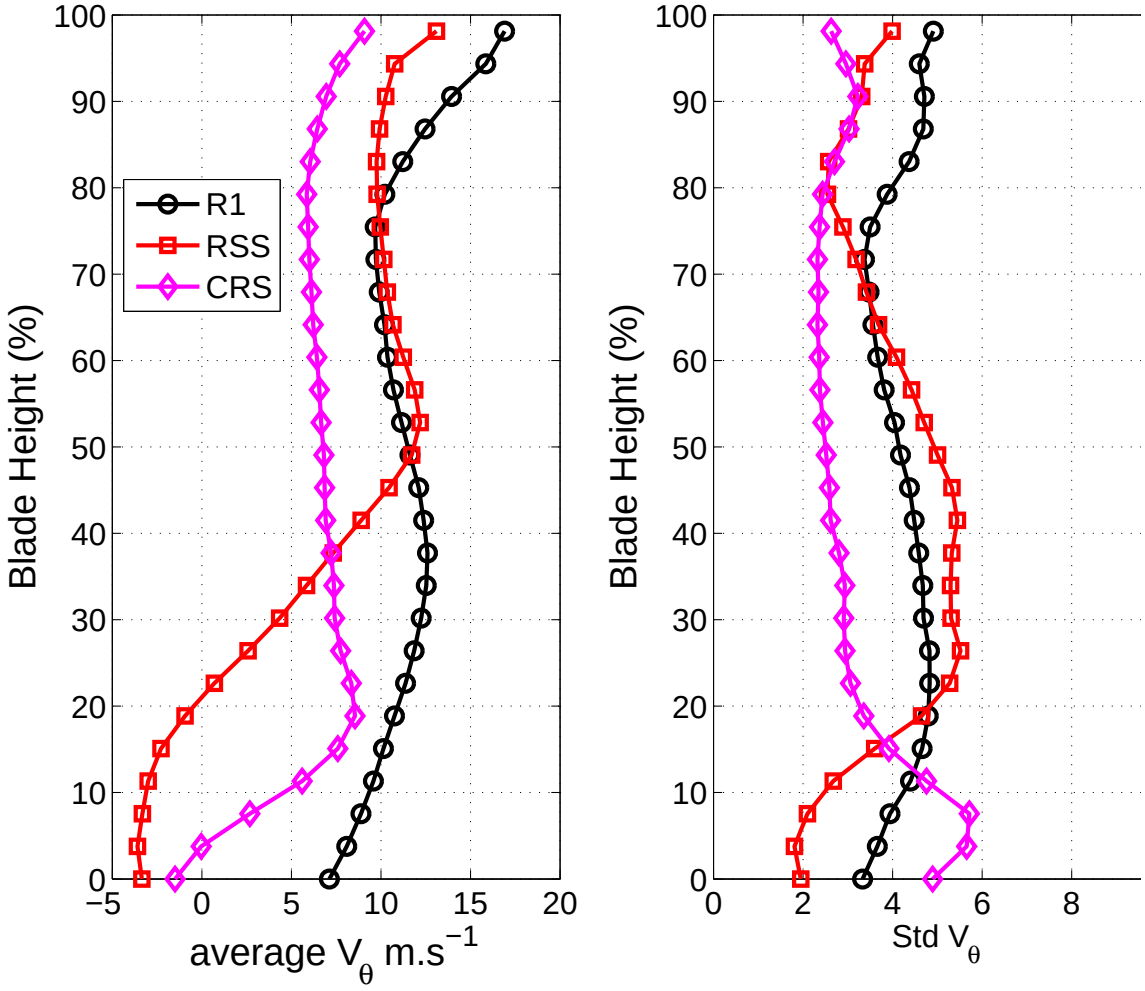

Figure B.3: Circumferential averaged tangential velocities and their STD for different configuration:
$R1(\circ), N = 2300rpm$
$RSS, S = 15mm(\square),\ N = 2100rpm$
$CRS, S = 10mm(\diamond), N = 1600 - 1600rpm$
at $Qv = 0.87\ m^3.s^{-1},\ Z_p = 5mm$

B.2 Velocity field downstream FR measured by LDA at $Q_v = 1$ m^3.s^{-1}

Then at design flow rate, the circumferential averaged velocities downstream the front rotor are presented in Fig. B.4 and B.5, in R1, RSS and CRS working at their design conditions.

Figure B.4 shows the averaged axial velocities are always positive at all blade span. With the presence of rotor, the V_z reduces significantly below 40% blade span, even to negative below 20% span. Then with the presence of Rear rotor, the deterioration in low blade span is largely improved.

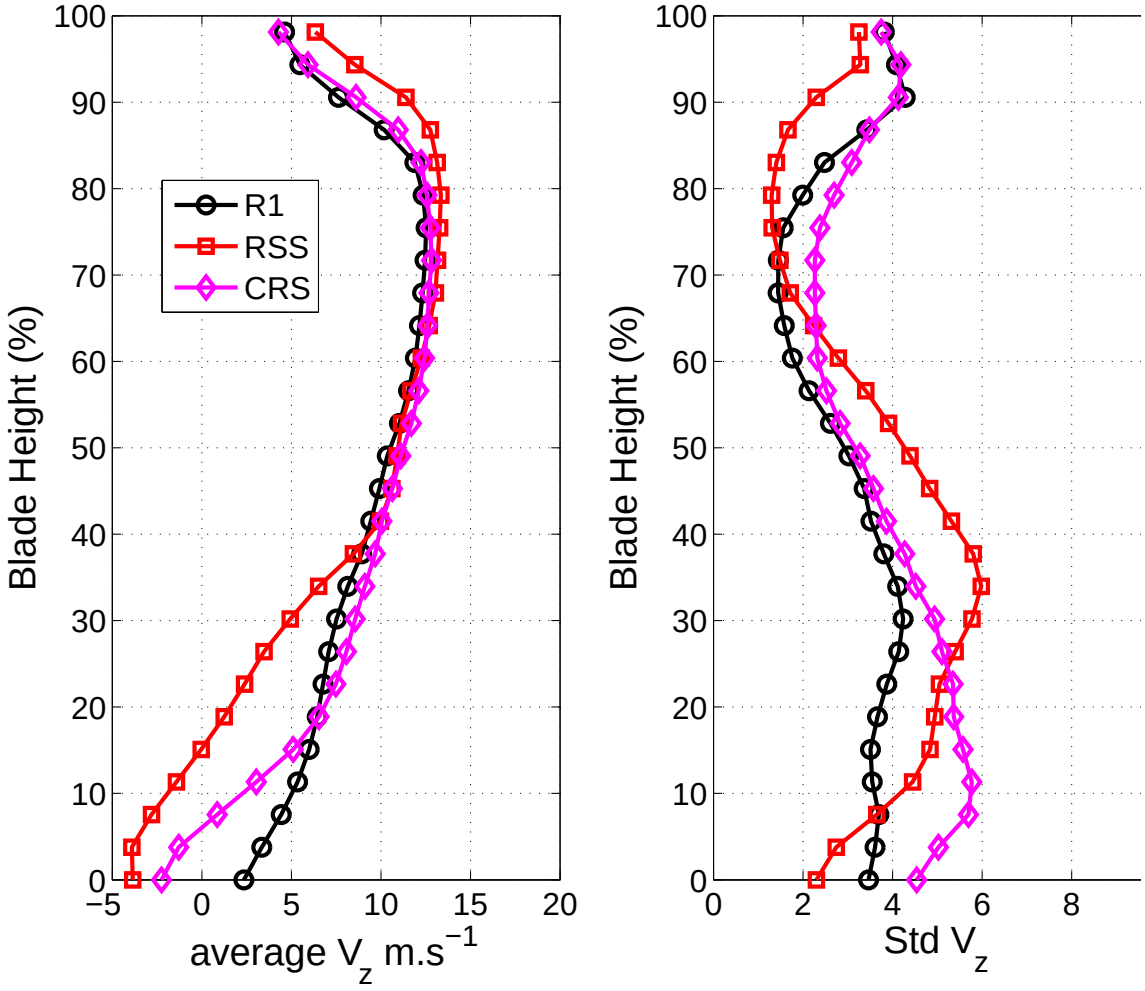

Figure B.4: Circumferential averaged axial velocities and their STD for different configuration:
R1(∘),N = 2000rpm
RSS, S = 15mm(□) N = 2000rpm
CRS, S = 10mm(◇) N = 2000 − 1800rpm
at about Qv = 1 m³.s⁻¹, Z_p = 5mm

Figure B.4 shows the averaged tangential velocities remains almost constant above midspan downstream of Front Rotor for R1, RSS and CRS. Below midspan, the presence of stator decrease the V_θ dramatically and even to negative close to the hub region. But the rear rotor only diminishes the V_θ below 20%.

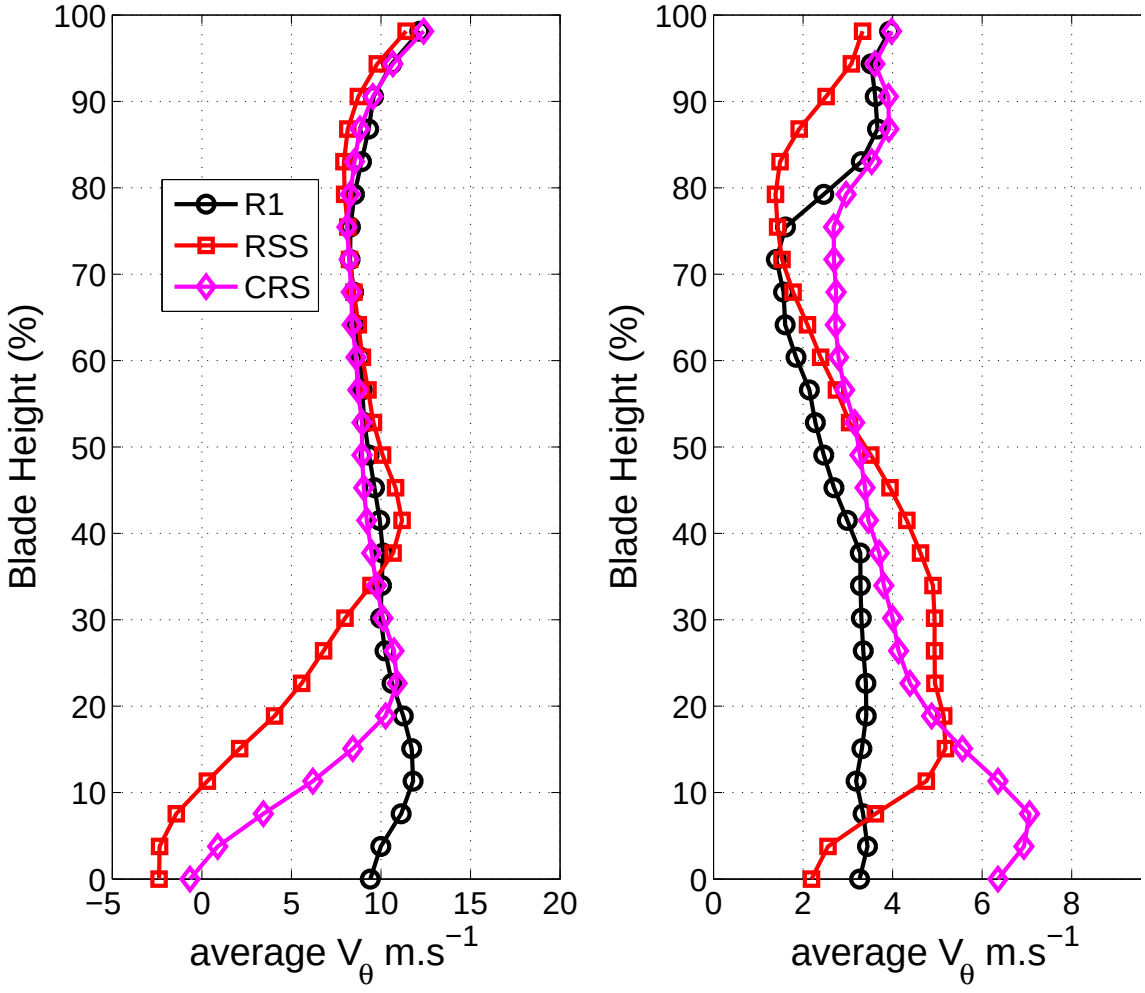

Figure B.5: Circumferential averaged tangential velocities and their STD for different configuration:
R1(∘),N = 2000rpm
RSS, S = 15mm(□) N = 2000rpm
CRS, S = 10mm(◇) N = 2000 – 1800rpm
at about Qv = 1 $m^3.s^{-1}$, Z_p = 5mm

Appendix C

Résumé de Thèse

Étude expérimentale des ventilateurs axiaux à double rotors contrarotatifs

C.1 Introduction

Les turbomachines sont des éléments incontournables dans de nombreuses industries et le besoin de meilleurs performances et de réduction de volume de ces machines est une recherche permanente. C'est pourquoi les rotors contra rotatifs sont étudiés de plus près. En effet, le remplacement de l'habituel stator par un deuxième rotor tournant dans le sens inverse du premier rotor permet de diminuer d'une part la vitesse de rotation et d'autre part de mieux homogénéiser l'écoulement de sortie. Néanmoins, le comportement complexe d'un étage contra rotatif n'est pas encore totalement maîtrisé, notamment au niveau de l'interaction entre les écoulements instationnaires provenant des deux rotors.

Au laboratoire Dynfluid (Arts et métiers ParisTech), un étage contrarotatif subsonique a été conçu par une méthode novatrice en utilisant un code interne au laboratoire (MFT). Un prototype a été créé et testé sur un banc d'essai normalisé selon la norme ISO-5801 (AERO2FANS) [5, 6]. Les résultats ont montré une augmentation nette des performances et du rendement par rapport au cas d'un rotor seul ou d'un étage rotor-stator. De plus, ces résultats restent valables pour de grande variation de paramètres qui ont été testés, à savoir la distance entre les deux rotors et le rapport de vitesse des deux rotors. Néanmoins, un paramètre important a été choisi arbitrairement : la répartition de la charge entre les deux rotors L_C. Un des objectifs principaux de cette thèse sera d'appréhender l'impact de ce paramètre sur le comportement global d'un étage contra rotatif en étudiant trois systèmes contra rotatifs (CRS) possédant des distributions de charge différentes.

La thèse est composée de trois parties. D'abord, après un rappel théorique et une étude bibliographique sur les rotors conta rotatifs, une description du banc d'essai et de la conception des trois CRS sera faite. Dans une deuxième partie, une analyse complète sera réalisée sur le premier CRS conçu (JW1). Dans la dernière partie, une comparaison des trois CRS sera faite.

C.2 Théorie des ventilateur et étude Bibliographique

Les machines à rotors contrarotatifs (appelées CRS pour Counter Rotating Stage) sont composées de deux rotors tournant chacun dans un sens différent. Cela signifie que le classique stator des machines dites « rotor stator » est remplacé par un deuxième stator (appelé RR pour Rear Rotor) en aval du premier rotor (appelé pour FR pour Front Rotor). De plus, ce deuxième rotor RR a la particularité de tourner dans le sens opposé du rotor FR. La figure C.1 montre que la vitesse relative en entrée du RR ($W_{1,RR}$) est clairement augmentée grâce à cette contra rotation des deux rotors. Ensuite comme dans le FR, le flux d'air traverse le RR et fournit une augmentation significative de l'élévation de la pression statique. Comparé à un étage rotor-stator (appelé RSS pour Rotor Stator Stage), le RR convertit non seulement la pression dynamique en aval du FR en pression statique, mais aussi donne de l'énergie au flux d'air.

Par contre, dans les machines RSS classiques, on sait que le jeu radial et des interactions rotors stators créent des pertes. Pour les machines contrarotatives, les phénomènes 3D sont exacerbés par les interactions rotors rotors.

Ensuite, la littérature confirme à partir d'essais qu'une machine contrarotative à faible vitesse (pompe, turbine, compresseur, petits ventilateurs) a une meilleur performance qu'une machine classique type RSS. Mais il a aussi été constaté que les paramètres S

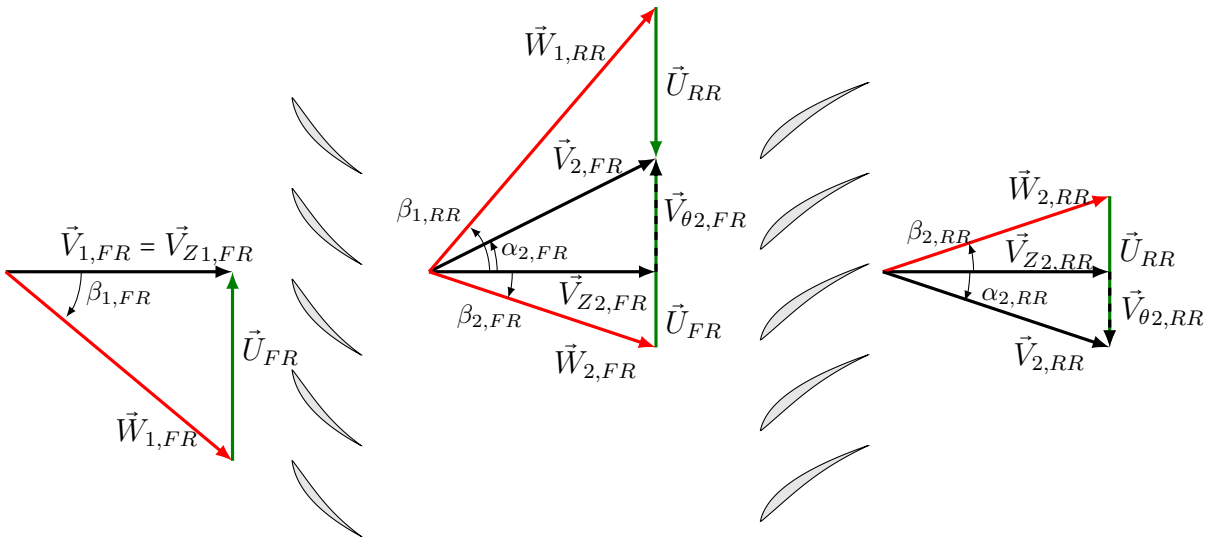

Figure C.1: Velocity triangles in a Counter Rotating compressor/fan [5], $\alpha_{2,RR} \neq 0°$.

et θ représentant respectivement la distance et le rapport de vitesse des deux rotors jouaient au premier ordre sur la performance globale de l'étage. Malheureusement, selon la configuration l'optimum de ces paramètres peut beaucoup varier. Pour une pompe CRS, un RR à faible vitesse est conseillé pour éviter les cavitations [4, 29]. Néanmoins, un RR avec une vitesse élevée peut améliorer l'élévation de pression statique de l'étage grâce un effet d'aspiration accru en entrée de RR [1, 3]. Au niveau de la distance S entre le deux rotors, il a été montré que plus la distance augmentait plus le rendement d'un compresseur était détérioré [1]. Au contraire pour un petit ventilateur il existe un optimum pour la distance S pour optimiser le rendement et les fluctuations de pression [37].

L'étude de l'étage contrarotatif HSN au laboratoire Dynfluid [5] a quand à lui montré peu d'influence de la distance S si S est inférieur à deux fois la corde de FR. Quand au paramètre θ, il peut être optimisé.

Pour résumer, trop peu d'études ont été menées sur les paramètres influents sur la performance d'un CRS pour pouvoir complètement appréhender le comportement global de ces machines. On peut noter qu'il est surprenant que très peu d'études aient été faites en considérant que le flux d'air sortant de FR et celui rentrant de RR était identique pour concevoir le rotor RR. De plus, dans l'état actuel de nos connaissances bibliographiques, aucune étude n'a regardé l'impact de la distribution de charge entre FR et RR, ce qui semble être un paramètre important. Cette thèse a donc pour but d'investiguer trois machines CRS ayant des distributions de charge différentes mais avec le même point de fonctionnement.

C.3 Configuration Expérimentale et incertitude de mesure

Cette partie porte sur quatre points: tout d'abord, le dispositif expérimental utilisé sera brièvement présenté; ensuite les grandeurs pertinentes pour la comparaison des comportements des étages CRS seront détaillées. La troisième partie sera constituée d'une présentation des designs des trois CRS. Enfin les incertitudes expérimentales seront déterminées.

C.3.1 Banc d'essai

Le banc d'essai se nomme AERO2FANS. Il a été construit selon la norme ISO-5801 au laboratoire Dynfluid (Arts et métiers ParisTech). Une représentation schématique du banc est visible sur la Figure 2.1. Tout d'abord, l'air rentre dans un tube de diamètre D = 380 mm, il est ensuite homogénéisé après avoir passé un nid d'abeille en amont de l'étage CRS. En sortie de l'étage CRS, l'air traverse un redresseur d'écoulement en forme d'étoile pour supprimer la composante tangentiel du flux d'air ; puis la pression statique est mesurée à l'aide de quatre capteurs. Après le coude de retour, le débit du flux d'air est mesuré à l'aide d'un diaphragme (norme ISO-5167). Enfin à l'aide d'un ventilateur de refoulement et un diaphragme à iris, l'air sort du banc.

C.3.2 Grandeurs Pertinentes

Trois caractéristiques ont été choisies pour évaluer au mieux l'efficacité d'un CRS : la performance globale de l'étage, le champ de vitesse et la fluctuation de la pression pariétale.

Performances Globales

Au sujet de la performance globale, elle peut être évaluée à travers deux paramètres qui sont l'élévation de pression statique ΔP_s et le rendement statique η_s. L'élévation de pression statique correspond à la différence entre la pression atmosphérique à l'entrée du banc et la pression statique mesurée par les quatre capteurs après l'étage CRS et le redresseur.

$$\Delta P_s = P_{s,CRS} - P_{atm} \tag{C.1}$$

Le rendement statique dépend du débit mesuré à l'aide du diaphragme:

$$\eta_s = \frac{\Delta P_s Q_v}{(\tau_{FR}\omega_{FR}) + (\tau_{RR}\omega_{RR})} \tag{C.2}$$

τ représente le couple de l'arbre (du rotor avant ou arrière) et ω la vitesse angulaire (du rotor avant ou arrière).

Champ de Vitesse

La vitesse instantanée est déterminée en amont de FR, entre FR et RR et en aval de RR. Le champ de vitesse en un point est déterminée par un système de Vélocimétrie Laser Doppler (LDV pour Laser Doppler Velocimetry) pour la composante axiale et tangentielle

de la vitesse du flux d'air. La composante circonférentielle moyenne du champ de vitesse est déterminée en moyennant les vitesses obtenues par LDV en un même point.

Fluctuation de la pression pariétale

La fluctuation de la pression pariétale est mesurée par un microphone placé entre le FR et le RR. Le signal obtenu est converti en densité spectrale de puissance et en énergie totale moyenne par transformée de Fourier.

C.3.3 Design des CRS

L'objectif est de concevoir trois CRS qui ont le même point de fonctionnement mais une distribution de charge différente. Le point de fonctionnement est décrit ci-dessous:

D (mm)	R_{tip} (mm)	R_{hub} (mm)	ΔP_{tC} (Pa)	Q_{vC} ($m^3.s^{-1}$)
380	187.5	65	420	1

Table C.1: Design point for air at $\rho_a = 1.21\ kg.m^{-3}$.

ΔP_{tC} est la pression totale entre l'amont et l'aval du CRS.

En considérant que le flux d'air dans le CRS est purement axial, l'élévation de pression statique théorique pour nos trois CRS à concevoir est donc de :

$$\Delta P_{sC} = \Delta P_{tC} - \frac{1}{2}\rho_a(\frac{Q_{vC}}{\pi D^2/4})^2 \approx 373\ Pa. \tag{C.3}$$

Ensuite, la distribution de charge se définit comme le rapport entre l'élévation de pression totale due à RR et l'élévation de pression totale globale du CRS :

$$L_C = \frac{\Delta P_{t,RR}}{\Delta P_t} \tag{C.4}$$

Au final, les trois CRS conçus, JW1, JW2 et JW3 ont une répartition de charge L_C différente en ce point de fonctionnement. Leurs caractéristiques sont décrits ci-dessous et dans le tableau C.2 :

JW1. Cet étage ressemble à l'étage HSN (Ref. [6]), excepté son angle de calage des pales qui est plus grand. Cela permet d'avoir une courbe d'élévation de pression statique en fonction du débit plus raide.

JW2. Cet étage a un L_C assez haut (52%). Cela signifie que le rotor arrière transfère plus d'énergie que le rotor avant. De plus, l'angle de calage des pales du FR est faible et le RR tourne $1,44$ fois plus vite que le FR. Au final, son élévation de pression statique en fonction du débit est faible (voir Figure C.2)

JW3. Cet étage a un L_C assez bas (23%). En conséquence, son RR tourne beaucoup plus vite que son FR et l'évolution de pression statique est plus importante (voir Figure C.2).

	N_{FR}/N_{RR} (rpm)	θ_C	L_C %	Z_{FR}/Z_{RR}	γ_{FR}
JW1	2300/2200	0.96	41	10/7	large
JW2	1800/2600	1.44	52	13/7	small
JW3	2600/1100	0.42	23	10/7	large
HSN	2000/1800	0.9	38	11/7	small

Table C.2: Design parameters of the three CRS JW1, JW2 JW3 and Initial CRS HSN.

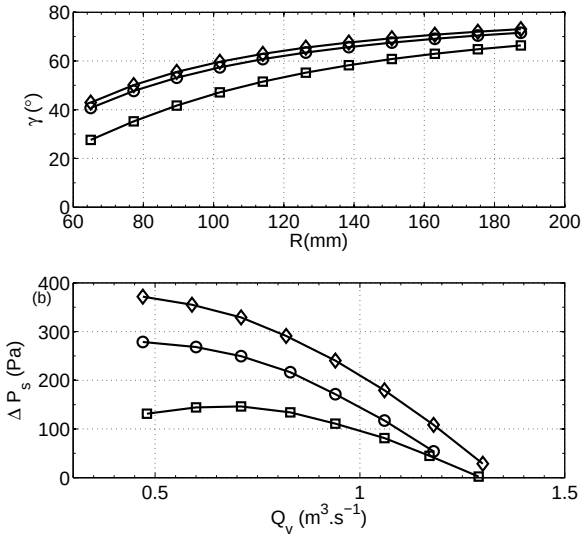

Figure C.2: Conception by MFT [39], Front Rotor of JW1 (∘); JW2 (□) and JW3(◇). (a): radial profile of the stagger angle and (b): static pressure rise calculated by a semi-empirical model [39].

C.3.4 Incertitude expérimentales

Pour pouvoir interpréter d'une façon complète des résultats expérimentaux, il est essentiel de déterminer au préalable les incertitudes expérimentales. Cela permet de différentier lors d'une comparaison entre deux CRS les vraies tendances physiques et les incertitudes expérimentales.

Deux types d'incertitudes existent lors d'essais expérimentaux. Le premier type provient de l'incertitude des mesures. Cela se traduit par un écart entre la valeur affichée par le capteur et la valeur réelle. Cet écart est un pourcentage d'erreur maximum qui dépend de la précision du capteur. Le deuxième type d'incertitude provient des différences constatées lorsque l'on réalise plusieurs fois la même mesure (mesure du champ de vitesse par LDV par exemple). Ces écarts sont traduits par la détermination d'un écart type par rapport à la valeur moyenne déterminée.

Au final, les incertitudes des grandeurs mesurées directement par essais et des grandeurs dérivées des grandeurs mesurées sont présentées dans les tableaux C.3 et C.4.

Quantities	mean value	absolute uncertainty e	relative uncertainty ϵ (%)
Pa (Pa)	100880	100	0.1
T_{Seche} (K)	290	0.4	0.1
ΔP_q (Pa)	299.0	1.2	0.4
ΔP_v (Pa)	288.8	1.0	0.3
$C1$ (%)	63.0	0.2	0.3
$C2$ (%)	46.5	0.2	0.4

Table C.3: Mean values and uncertainties for quantities measured directly, according to the 10 *repeated experiments in Fig. 2.6.*

Quantities	mean value	absolute uncertainty e	relative uncertainty ϵ (%)
ρ_a (kg.m^{-3})	1.21	0.004	0.3
Q_v (m^3.s^{-1})	0.994	0.004	0.4
ΔP_s (Pa)	358.5	4.0	1.0
$\mathcal{P}_{w,FR}$ (W)	269.2	2.4	0.9
$\mathcal{P}_{w,RR}$ (W)	273.1	3	1.1
$\mathcal{P}_{w,t}$ (W)	542.3	5.4	1.0
η_s (%)	65.7	1.3	2

Table C.4: Mean values and uncertainties for derived quantities, the values of ΔP_s and $\mathcal{P}_w$ are after correcting by ρ_{ref}

C.4 Résultat du JW1

Cette partie décrit les analyses faites à partir des résultats expérimentaux menés sur JW1. Dans un premier temps, la validation de la méthode de design de la machine sera faite en vérifiant les performances et les caractéristiques du flux d'air au point de fonctionnement. Ensuite, le champ de vitesse mesuré par LDV sera analysé à divers débits. Après les fluctuations de pressions pariétales seront présentées et enfin les influences de la distance et du ratio de vitesse des deux rotos seront étudiées.

C.4.1 Validation de la méthode de design

Les résultats expérimentaux montrent que l'élévation de pression statique du FR seul (nommé par la suite JW1FR) de la machine JW1 est bien corrélée avec la prédiction faite avec la méthode de design de la machine (écart à $-2,7\%$ pour JW1) (Voir le tableau 3.1). De plus, la courbe de pression statique en fonction du débit est plus raide pour JW1 que pour JW1FR et la pente de cette courbe est négative sur un très large domaine de débit autour du point de conception pour JW1 (voir la figure C.3). Cela démontre une très bonne stabilité opérationnelle de la machine CRS. Ensuite, le rendement statique de JW1 atteint au maximum $66,6\%$ au point de fonctionnement, ce qui est bien plus important comparé à une machine rotor-stator classique. Au final il apparaît qu'un CRS est une très bonne solution pour toute industrie cherchant une turbomachine à très haute efficacité statique.

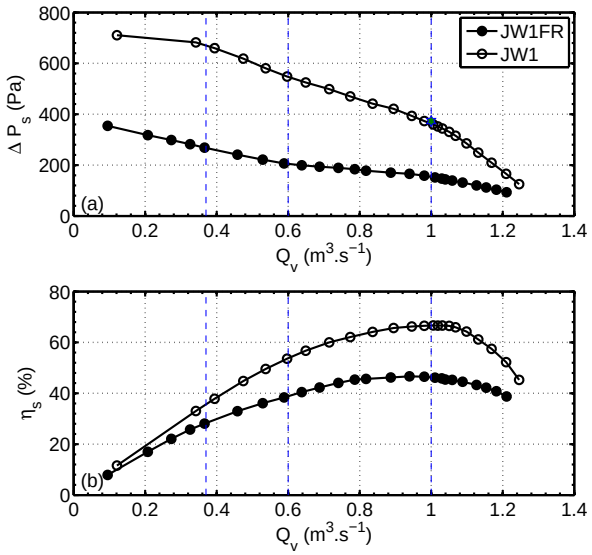

Figure C.3: Overall performance of the JW1FR (•), JW1 (∘) and the design point (✶) (a): Static pressure rise ΔP_s vs. volumetric flow rate Q_v (ΔP_s is corrected by ρ_{ref}). (b): Static efficiency η_s vs. volumetric flow rate Q_v, at $S = 10$ mm.

Au niveau des champs de vitesse moyen au point de fonctionnement, plusieurs commentaires peuvent être faits :

- En amont du CRS, comme attendu, le champ de vitesse de l'air est quasiment purement axial. Une petite vitesse tangentielle est mesurée près du moyeu et du

bout de pale, due à l'effet d'aspiration du FR et aussi due à l'effet de la paroi et du carter (voir Figure 3.3).

- Entre le FR et le RR (5mm après FR), la méthode MFT prédit correctement la tendance du profil radial de la vitesse axiale (V_z) et tangentielle (θ) pour le rotor FR seul (figure C.4 et C.5). De plus, on peut constater que la méthode MFT surestime la vitesse axiale en bout de pale. Cela a pour conséquence la sous estimation de l'angle de déviation en sortie du FR par la méthode MFT. Cela signifie donc que le modèle de pertes inclus dans la méthode MFT appréhende correctement le comportement du flux d'air en sortie du rotor FR seul, mais il ne simule pas correctement les phénomènes complexes présents en bout de pales (couche limite du carter, turbulence). Ensuite, pour la machine JW1, on s'aperçoit que le rotor RR a une influence faible sur le profil radial de vitesse moyenne axiale. Au niveau de la vitesse tangentielle, on a une bonne corrélation entre la prédiction MFT et la mesure expérimentale sauf proche du moyeu où la vitesse tangentielle mesurée est quasi nulle. Cela fait significativement augmenter les angles de déviations proches du moyeu en sortie de FR. Néanmoins, l'énergie consommée par le FR reste constante avec ou sans RR au point de fonctionnement. Au finale pour un design préliminaire d'un CRS, la méthode MFT qui considère que le champ de vitesse en sortie de FR peut être considéré égal au champ de vitesse en entrée du corrèle d'une façon satisfaisante à la réalité expérimentale sauf proche du moyeu et du carter où des phénomènes complexes ne sont pas modélisés suffisamment dans MFT.

- En sortie du RR, la vitesse tangentielle mesurée n'est pas complètement nulle alors que théoriquement elle devrait l'être. On remarque qu'expérimentalement le flux d'air tourne dans le sens de FR sauf proche du moyeu où il tourne dans le sens de RR (voir figure C.6). Le fait que la vitesse tangentielle ne soit pas nulle explique que l'élévation de la pression statique mesurée soit légèrement inférieure à la valeur prévue.

C.4.2 Champ de vitesse du JW1 pour des débits différents

Les champs de vitesse de la machine JW1FR et JW1 sont mesurés dans cette partie à des débits autres qu'au point de conception, où la pente de la courbe de la pression statique en fonction du débit change. Les résultats sont présentés sur les figures C.7 et C.8. On peut observer que :

- Quand le débit diminue de 1 à $0,6$ $m^3.s^{-1}$, la vitesse axiale du flux sortant de JW1FR diminue beaucoup et il apparaît même un flux d'air inverse proche du moyeu. La vitesse tangentielle au contraire augmente significativement tout le long de la pale sauf proche du moyeu. Cela signifie une augmentation de la charge le long de la pale par rapport au point de fonctionnement, ce qui s'explique dans les triangles de vitesse. Avec la présence du RR, la vitesse axiale augmente, devient même positive et le flux inverse disparaît. Par contre, la charge diminue sur la portion correspondant aux 40% inférieurs de la pale, par rapport au point de fonctionnement. Cela provient de l'interaction entre le RR et le moyeu du FR et la couche limite du carter.

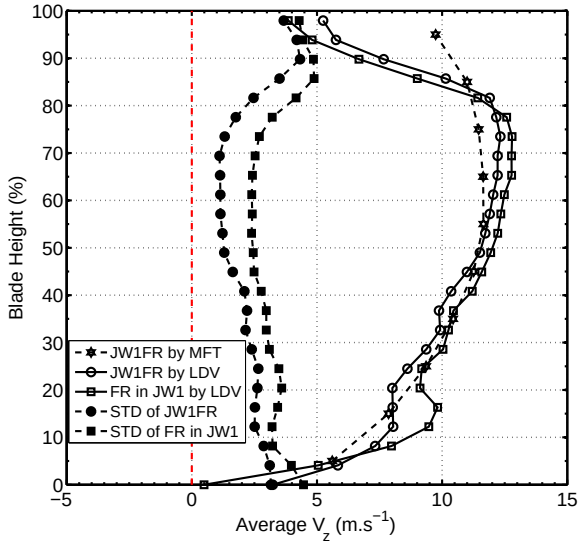

Figure C.4: Averaged axial velocity V_z near the outlet of the FR (Position $Z_p = 5mm$) at design point $Q_v = 1m^3.s^{-1}$, $\theta = \theta_C$, in: JW1FR analyzed by MFT(☆); JW1FR measured by LDV(∘) and their STD(•); JW1 measured by LDV(□) and their STD(■)

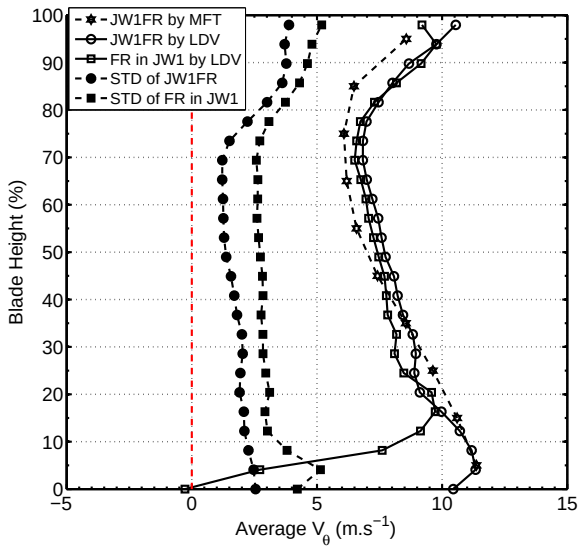

Figure C.5: Averaged axial velocity V_θ near the outlet of the Front Rotor (Position $Z_p = 5mm$) at the design point $Q_v = 1m^3.s^{-1}$, $\theta = \theta_C$, In: JW1FR analyzed by MFT(☆); JW1FR measured by LDV (∘) and their STD(•); JW1 measured by LDV(□) and their STD(■)

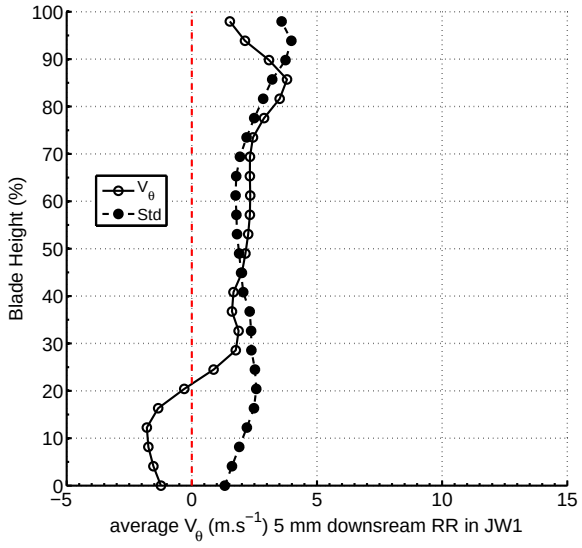

Figure C.6: Averaged tangential velocity V_θ ($\circ$) by LDV and its STD ($\bullet$) at the outlet of stage JW1 (Position $Z_p = 50mm$) at design point $Q_v = 1m^3.s^{-1}$, $\theta = \theta_C$

- Quand le débit diminue de 1 à $0,37$ m^3.s^{-1}, la vitesse axiale du flux sortant de JWFR1 a un flux inverse sur une hauteur de pale plus grande et la charge augmente sur quasiment toute la pale en comparaison avec le point de fonctionnement. En présence du RR, le flux inverse a quasiment disparu grâce à l'effet d'aspiration du RR. Par contre, la charge diminue significativement sur 50% de la hauteur de pale et en bout de pale. Ailleurs la charge a quand à elle considérablement augmenté.
- En sortie de RR, pour un point en dehors de celui de fonctionnement, un large flux inverse apparaît au moyeu et de plus le RR corrige trop la vitesse tangentielle ce qui est une perte.

C.4.3 Fluctuations de pressions pariétale

Les fluctuations de pressions pariétales sont mesurées à l'aide d'un microphone en sortie du FR ou du RR au point de fonctionnement et à un débit de $0,6$ m^3.s^{-1} et $0,37$ m^3.s^{-1}. La densité spectrale d'énergie des fluctuations de pressions pariétales pour $\theta = \theta_C$ et $S = 10$ mm sont montrés sur la figure C.9.

Les résultats montrent que la densité spectrale d'énergie des fluctuations de pressions pariétales est caractérisée par trois types de pics correspondant à la fréquence de passage des pales de FR ($f_{bpf,FR}$), de RR ($f_{bpf,RR}$), et enfin de leurs interactions. Les amplitudes des pics correspondant à $f_{bpf,RR}$ et ses harmoniques sont relativement supérieurs à celles de $f_{bpf,FR}$ en sortie de FR et RR. Aussi les pics sont d'amplitudes bien supérieures en sortie de FR par rapport à la sortie de RR. Ensuite si on fait baisser le débit, les pics correspondant aux interactions s'atténuent fortement. On peut dire au final que les fluctuations peuvent se propager loin en amont de l'étage sans grande atténuation mais en aval elles s'atténuent très rapidement. De plus, entre FR et RR, les fluctuations de pressions pariétales sont renforcées par l'influence des deux rotors FR et RR et en sortie de FR les amplitudes sont moins influencées par l'étage.

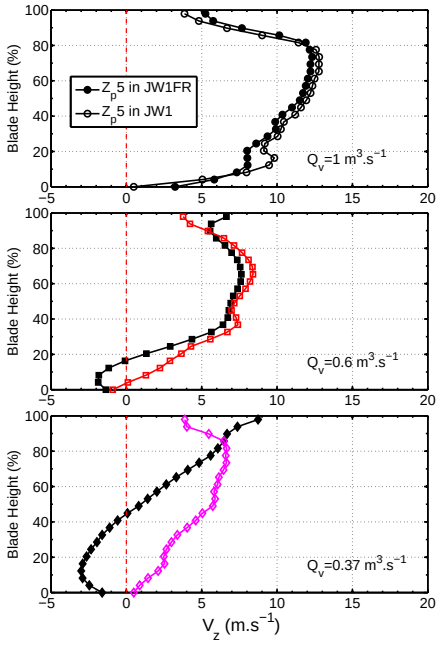

(a) Averaged axial velocities V_z

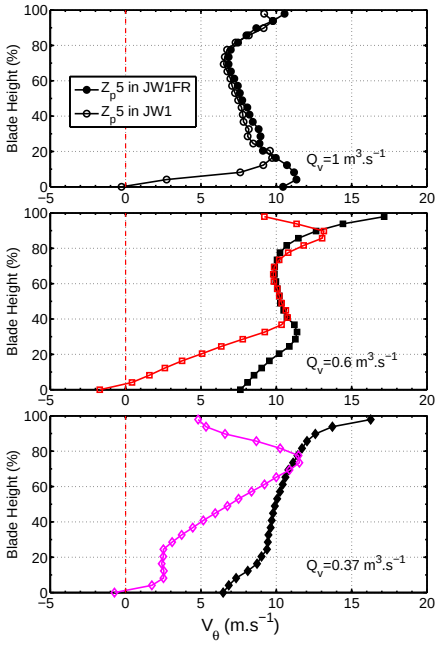

(b) Averaged tangential V_θ

Figure C.7: Radial distributions of circumferential averaged axial (V_z) and circumferential (V_θ) velocities at Z_p = 5 mm, for JW1FR(closed symbols) and JW1(open symbols) at Q_v = 1, 0.6, 0.37 $m^3.s^{-1}$, S = 10 mm

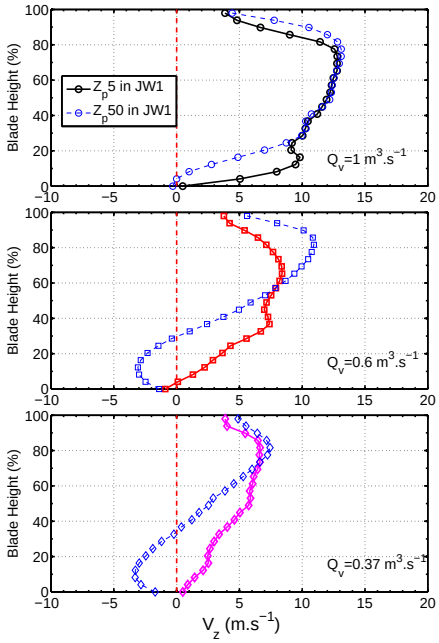

(a) Averaged axial velocities V_z

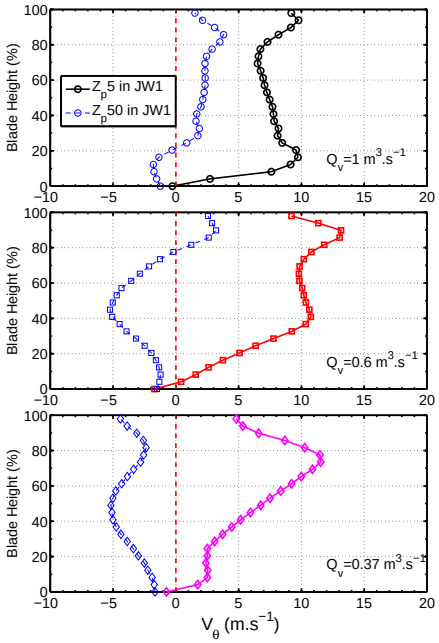

(b) Averaged tangential velocities V_θ

Figure C.8: Radial distributions of circumferential averaged axial (V_z) and circumferential (V_θ) velocities at Z_p = 5 mm, and Z_p = 50 mm(blue and thinner lines) for JW1 at Q_v = 1, 0.6, 0.37 $m^3.s^{-1}$, S = 10 mm

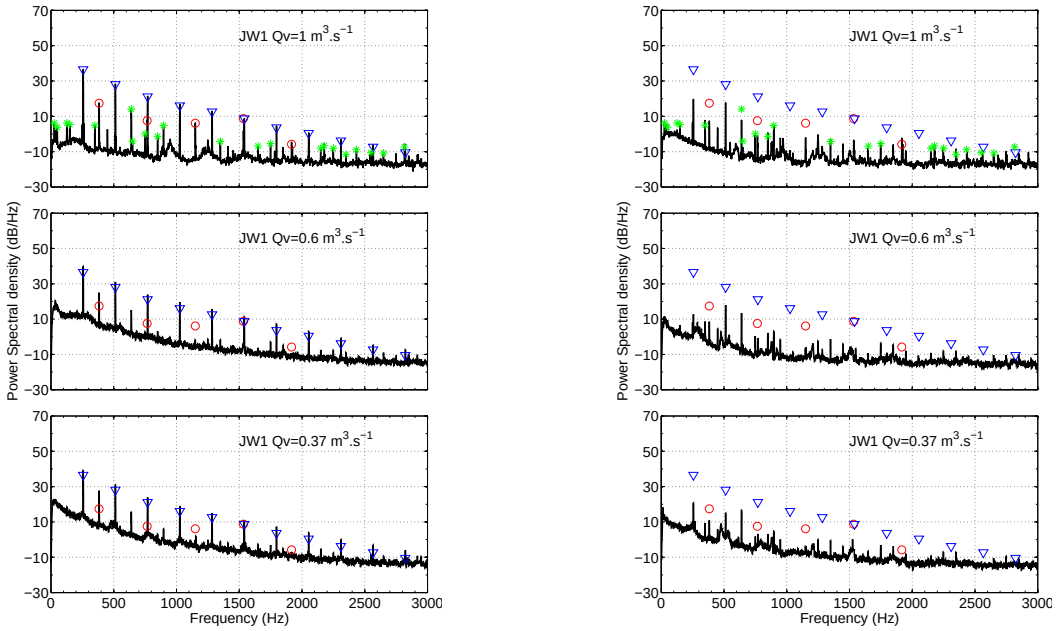

(a) at $Z_p = 5$ mm *(b) at $Z_p = 45$ mm*

Figure C.9: PSD of the wall pressure fluctuations measured at $Z_p = 5$ and 45 mm, for JW1 at $N = 2300 - 2200$ rpm and $S = 10$mm, $Q_v = 1$, 0.6 and 0.37 $m^3.s^{-1}$. (○): $mf_{bpf,FR}$; (▽): $nf_{bpf,RR}$; and (⋆): $mf_{bpf,FR} + nf_{bpf,RR}$ with $m \neq 0$ and $n \neq 0$.

C.4.4 L'influence de distance axiale S

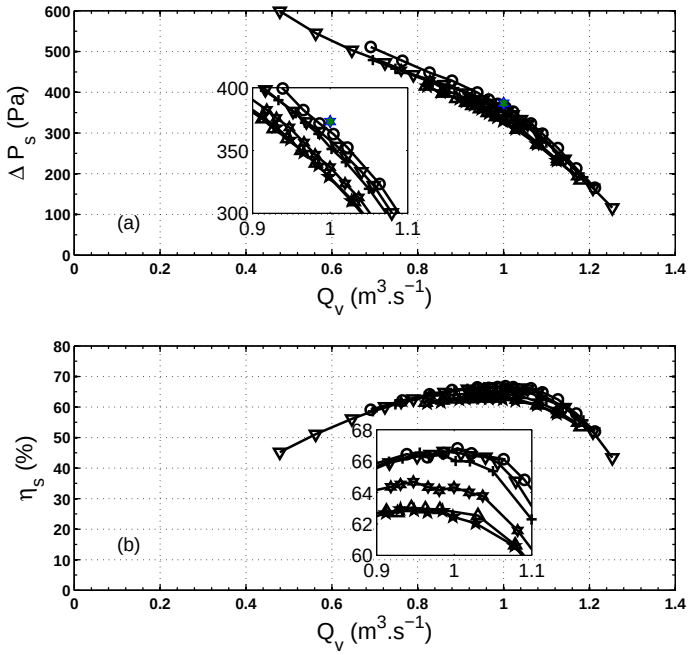

Figure C.10: Performance $S = 10 - 300$ mm: $s = 10$(○),50(▽), 100(+),200 (✡), 250(△), 300 mm(★); the design point (✶), ΔP_s rescaled by ρ_{ref}.

Une série d'expériences a été menée en faisant varier la distance entre les deux rotors S sur JW1 au moyen de Blocs PMMA entre FR et RR [5]. La performance globale de l'étage est présentée en figure C.10 en fonction du débit Q_v pour $\theta = \theta_C$. S varie de 10 à 300 mm correspondant à un intervalle de 20% à 550% de la longueur de la corde L_{chord} au milieu de pale de FR.

On remarque qu'une petite distance S est bénéfique pour la performance de JW1. De plus, le rendement reste autour de 66% quand S varie de 10 à 100 mm. Durant cette évolution de la distance S de 10 à 100 mm, l'élévation de pression statique diminue modérément. Néanmoins, le rendement statique varie légèrement. Cela s'explique par la baisse de la consommation d'énergie totale de l'étage, et surtout de RR. Ensuite quand S augmente au dessus de 100 mm, une baisse significative de l'élévation de pression statique a plus d'influence que la baisse continue de la puissance totale. C'est pourquoi le rendement statique descend à $62,5\%$ à $S = 300$ mm.

Pour comprendre précisément les raisons de la baisse de l'élévation de la pression statique quand S évolue, une mesure des champs de vitesses au point de fonctionnement de JW1 entre FR et RR pour $S = 10, 20, 40 et 200$ mm a été menée par LDV. D'abord, le champ de vitesse à 5 mm en sortie de FR et à 5 mm en entrée de RR a été étudié pour valider l'influence de la distance S (voir figure C.11). En entrée de RR, la vitesse axial diminue significativement au pied de la pale. De plus, la vitesse tangentielle diminue beaucoup aux extrémités de la pale et au pied du pale. La raison peut être la perte par frottement et la diminution sillage entre FR et RR. Ce déficit de vitesse tangentielle provoque la baisse de la part tangentielle de la pression dynamique entre FR et RR.

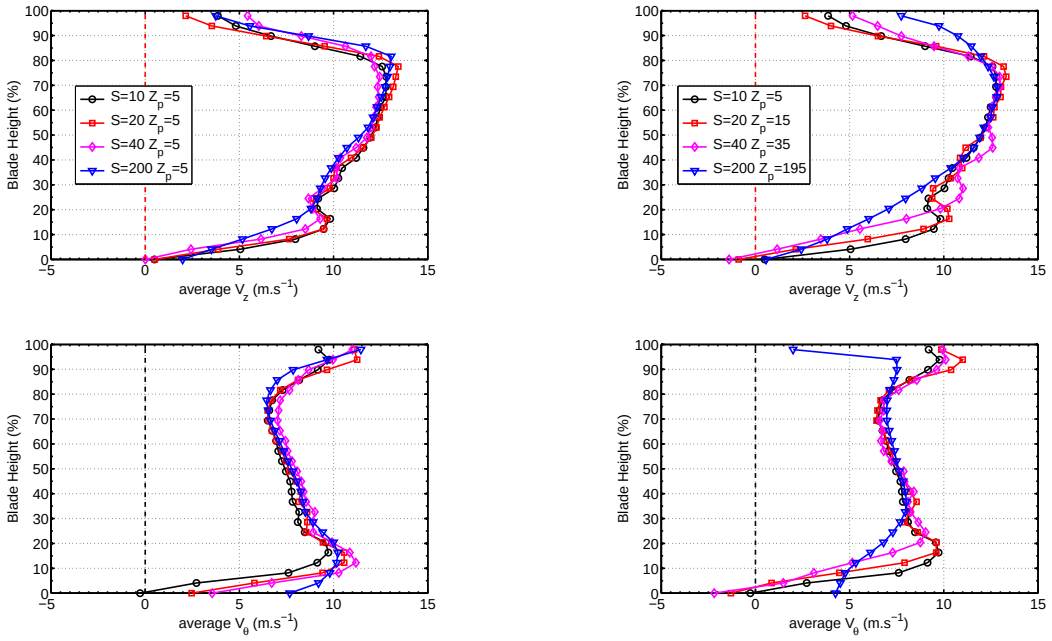

(a) Downstream FR in JW1 *(b) Upstream of RR in JW1*

Figure C.11: Circumferential averaged velocity fields between FR and RR in JW1 at various S at design point $Q_v = 1m^3.s^{-1}$, $\theta = \theta_C$. (a) downstream of FR $Z_p = 5$ mm, $S = 10$, 20, 40, 200 mm; (b) upstream of RR at $Z_p = 5(S = 10)$, $Z_p = 15(S = 20)$,$Z_p = 35(S = 40)$ and $Z_p = 195(S = 200)$ mm

Dans un second temps, l'angle d'écoulement est calculé à partir des mesures par LDV à la sortie de FR et à l'entrée de RR (figure 3.21). On note que la distance S a peu d'influence sur l'angle d'écoulement sur une très large partie de la hauteur de pale à la sortie du FR. Par contre, en dessous de 20% de hauteur de pale, l'angle de déviation du FR augmente de 6 à 10 pour S variant de 10 à 200 mm. Cela signifie que la déviation du flux est importante en bord de fuite de la pale créant de fortes pertes. D'un autre côté, quand S augmente à 200 mm, l'angle d'incidence de RR diminue beaucoup dans la région en bout de pale. Cela fait diminuer la charge et la déviation du flux d'air dans cette région.

Au final, trois explications peuvent expliquer la baisse de la pression statique pour une distance S importante. La première cause provient du FR. Quand la distance S est importante, l'angle de déviation de l'écoulement en sortie de FR augmente substantiellement et donc l'écoulement suit moins bien la pale. La seconde cause provient de la différence de vitesse aux extrémités et pied de la pale entre le FR et le RR due aux frottements et au sillage. Ce déficit de vitesse tangentielle provoque la baisse de la part tangentielle de la pression dynamique entre FR et RR. La dernière cause provient de la diminution de charge en haut de pale de RR. Quand S augmente, l'air est transféré au bout de pale tandis que la vitesse tangentielle est faible aux extrémités de la pale. Cela a pour conséquence un angle d'incidence diminuant beaucoup en haut de pale et augmentant proche du moyeu. Or d'après l'équation d'Euler, il y a moins de travail en haut de pale quand la distance axiale est grande.

C.4.5 L'influence de rapport de vitesse θ

Le second paramètre important est le rapport de vitesse entre les deux rotors θ. La machine JW1 est conçue pour un $\theta_C = 0.96$ et une vitesse de rotation de FR de $N_{FR,C} = 2300$ rpm. Dans un premier temps, N_{FR} est fixé à $N_{FR,C}$ et $\theta \in [0.86, 1.2]([0.9, 1.25]\theta_C)$ avec $S = 10$ mm. Les performances globales sont présentées figure C.12. On montre que le rendement statique maximum peut atteindre 68% quand θ augmente de $0.9\theta_C$ jusqu'à $1.25\theta_C$. Cela a déjà été observé dans le prototype "HSN", qui atteint $\eta_{s,max} = 66.5\%$ quand θ augmente [6]. Ensuite les champs de vitesse sont mesurés pour $\theta = 0.86(0.9\theta_C), 0.96(1.0\theta_C), 1.1(1.15\theta_C)$ en sortie de FR et en sortie de RR à $Q_v = 1$ m^3.s^{-1} et $S = 10$ mm (voir figure C.13).

A la sortie du FR (figure C.13(a)), l'augmentation de θ a peu d'influence sur la charge de FR sur une grande longueur de pale, sauf aux extrémités et au pieds où la charge diminue. En conséquence la déviation de l'angle d'écoulement augmente proche du moyeu, créant des pertes dans le FR. A l'entrée du RR, une augmentation de la vitesse de rotation de RR augmente l'incidence de l'angle d'une valeur négative à positive sur la grand partie de la longueur de pale augmentant la charge de RR (voir figure 3.26). A la sortie de RR (figure C.13(b)), un flux inverse apparaît près du moyeu pour $\theta = 1.15\theta_C$. De plus, l'augmentation de la vitesse de rotation de RR créée plus d'énergie tangentielle au dessus du milieu de la pale, mais tourne le flux dans la position tangentielle opposée. De plus, une forte augmentation de l'angle d'incidence est visible en bas de hauteur de pale (figure 3.27). Cela provient de l'augmentation de la diffusion de RR créant une separation de couche limite plus importante. En dépit de la grande déviation de l'ange d'écoulement à la sortie de RR pour des valeurs de θ grande, plus de charge est créée

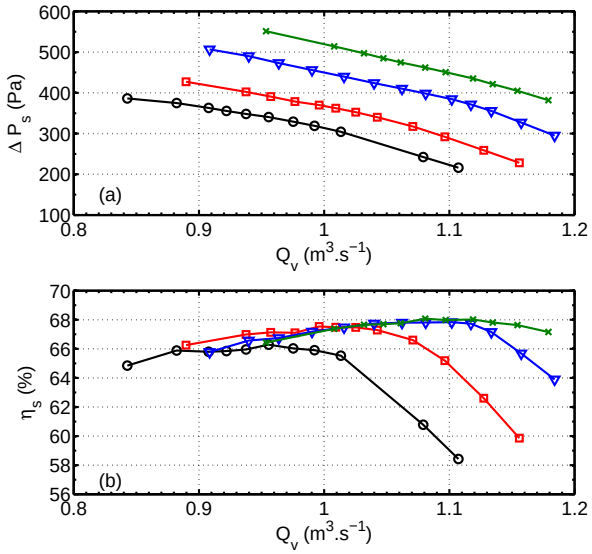

Figure C.12: Overall performance of stage JW1 at Q_v = 1 $m^3.s^{-1}$, S = 10 mm, N_{FR} = 2300 rpm, $\theta = [0.86\ (0.9\theta_C\ \circ), 0.96\ (1.0\theta_C\ \square), 1.1\ (1.15\theta_C \triangledown), 1.2\ (1.25\theta_C \times)]$, $\theta_C = 0.96$.

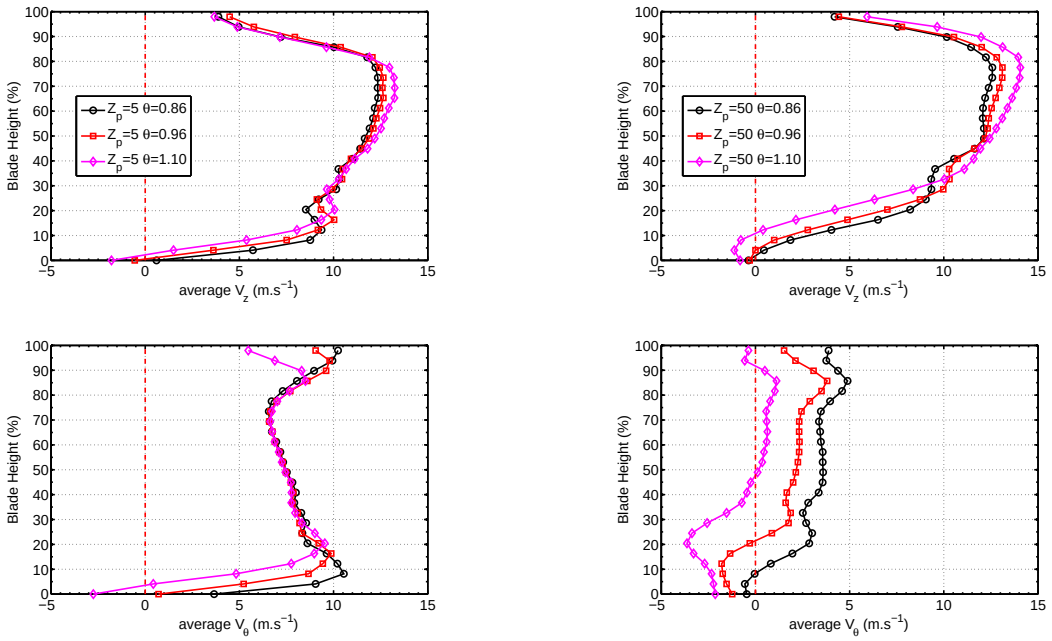

(a) Downstream FR in JW1 *(b) Downstream of RR in JW1*

Figure C.13: Circumferential averaged velocities profiles in JW1 , for θ = $0.86(0.9\theta_C)$,$0.96(\theta_C)$, $1.1(1.15\theta_C)$ at design point Q_v = $1m^3.s^{-1}$, S = 10 mm (a) downstream of the FR at Z_p = 5 mm; (a) downstream of the RR at Z_p = 50 mm

par RR par l'augmentation de la vitesse de pale U et la rotation de l'air V_θ à travers RR. Donc, l'élévation de pression statique augmente significativement quand θ augmente. L'augmentation de l'élévation de la pression statique est plus rapide que l'augmentation de la consommation d'énergie de l'étage, donc le rendement est amélioré.

Enfin, pour avoir des θ encore plus grands, la rotation de FR est diminué à 1400 rpm, à cause de la limitation de la rotation des moteurs. La réduction de N_{FR} introduit aussi une perte de rendement statique d'environ 2% à cause de l'effet d'un nombre de Reynolds bas (voir figure C.14). C'est pourquoi seule la tendance de la rendement maximum est analysée. Les résultats montrent que η_{smax} augmentent d'abord avec θ mais diminue rapidement quand θ atteint $1.2\theta_C$.

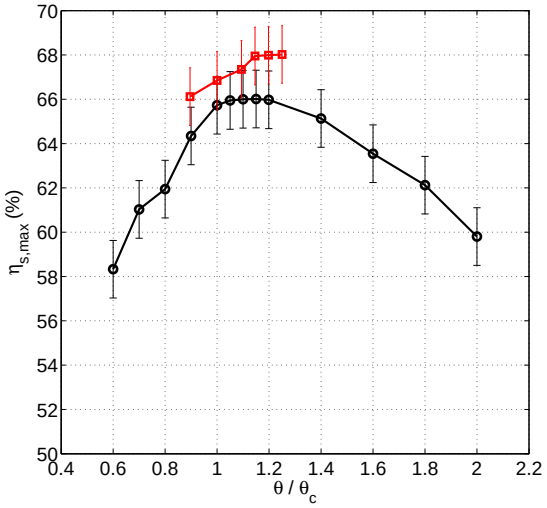

Figure C.14: Maximum static efficiency vs. θ. *Stage JW1, at* N_{FR} = 1400 *rpm* (∘), N_{FR} = 2300 *rpm* (□), S = 10 *mm.*

C.5 Résultat des trois systèmes

Dans cette partie, les résultats des trois machines JW1, JW2 et JW3 sont présentés. On rappelle que ces trois machines ont été conçues pour avoir le même point de fonctionnement mais une répartition de charge différente (41%, 52% et 23% pour respectivement JW1, JW2 et JW3). Tout d'abord les performances globales de ces trois machines seront comparées au point de fonctionnement. Ensuite le champ de vitesse et les fluctuations de pression pariétale des trois machines seront analysés. Enfin les influences de la distance et du rapport de vitesse entre les deux rotors seront aussi comparées entre les trois machines.

C.5.1 Performance global pour les CRS

Les trois machines, qui ont été conçues pour avoir le même point de fonctionnement mais une répartition de charge différente, ont une élévation de pression statique conforme à l'attendu, excepté pour JW3 où une différence de −11% apparait (voir figure C.15). La courbe de pression statique pour les trois machines ont des pentes plus raides que la courbe d'une machine FR seule pour des grandes plages de débit. Cela montre que la présence du deuxième rotor RR stabilise grandement la machine même pour des débits faibles. De plus, les trois machines ont un fort rendement maximum (62% au minimum pour JW3 qui a la répartition de charge la plus faible). Dans un second temps, la distribution de puissance consommée (définie par la formule $L_{power} = \frac{\mathcal{P}_{w,RR}}{\mathcal{P}_{w,FR}+\mathcal{P}_{w,RR}}$) est déterminée en fonction du débit (voir figure 4.3). Au point de fonctionnement, L_{power} est similaire aux valeurs de répartition de charge de conception L_C. Pour JW1 et JW2, quand le débit diminue tout en étant inférieur au point de conception, L_{power} augmente jusqu'à un débit de Q_v = 0.6 $m^3.s^{-1}$ puis diminue. Quand le débit augmente tout en étant supérieur au point de conception, L_{power} s'écroule rapidement. Pour JW3, L_{power} varie faiblement (moins de 20%) pour une large plage de débit mais s'effondre quand $Q_v > 1.2$ $m^3.s^{-1}$. Ces tendances peuvent refléter les changements de répartition de la charge, car la puissance consommée est reliée à la pression totale en considérant que le processus est isentropique et sans prendre en compte la perte mécanique.

C.5.2 Champs de vitesse au débit du conception pour les CRS

La figure C.16 montre que globalement les champs de vitesses prédits par la méthode MFT sont bien corrélés avec les mesures LDV. Cela montre que la méthode MFT est une bonne première approche pour estimer le champ de vitesse en sortie de FR. Par contre, la méthode MFT sous estime la vitesse axiale (V_z) pour tous les FR sur une grande partie de la hauteur de pale mais surestime cette vitesse en bout de pale. Pour la vitesse moyenne tangentielle (V_θ), la présence du rotor RR fait diminuer V_θ modérément proche du carter et fortement proche du moyeu. Cette forte diminution proche du moyeu peut provoquer un angle d'incidence inadapté au moyeu du RR et créer des pertes.

A partir des résultats LDV en sortie de FR et RR, l'angle d'incidence et de déviation du RR peuvent être déterminés (figure4.5). Ces résultats montrent que sur la plupart de la hauteur de pale du RR dans JW1 et JW2, les angle sont proche de 0. Cela signifie que le fluide longe correctement la pale. Par contre quand on est proche du moyeu, l'écoulement suit moins bien la pale à cause des décollements qui créent des pertes. De

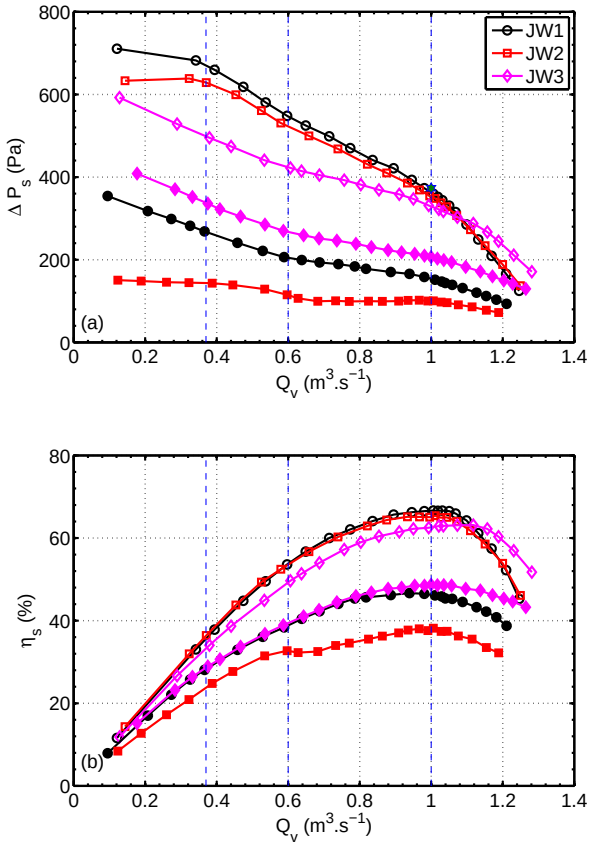

Figure C.15: Overall performance of three systems: JW1(∘), JW2 (□) and JW3 (◇); JW1FR (•), JW2FR (■) and JW3FR (⧫), design point,(✡) (a): Static pressure rise ΔP_s (Rescaled by ρ_{ref}) vs. *volume flow rate Q_v. (b): Static efficiency η_s* vs. *volume flow rate Qv, at $S = 10$ mm.*

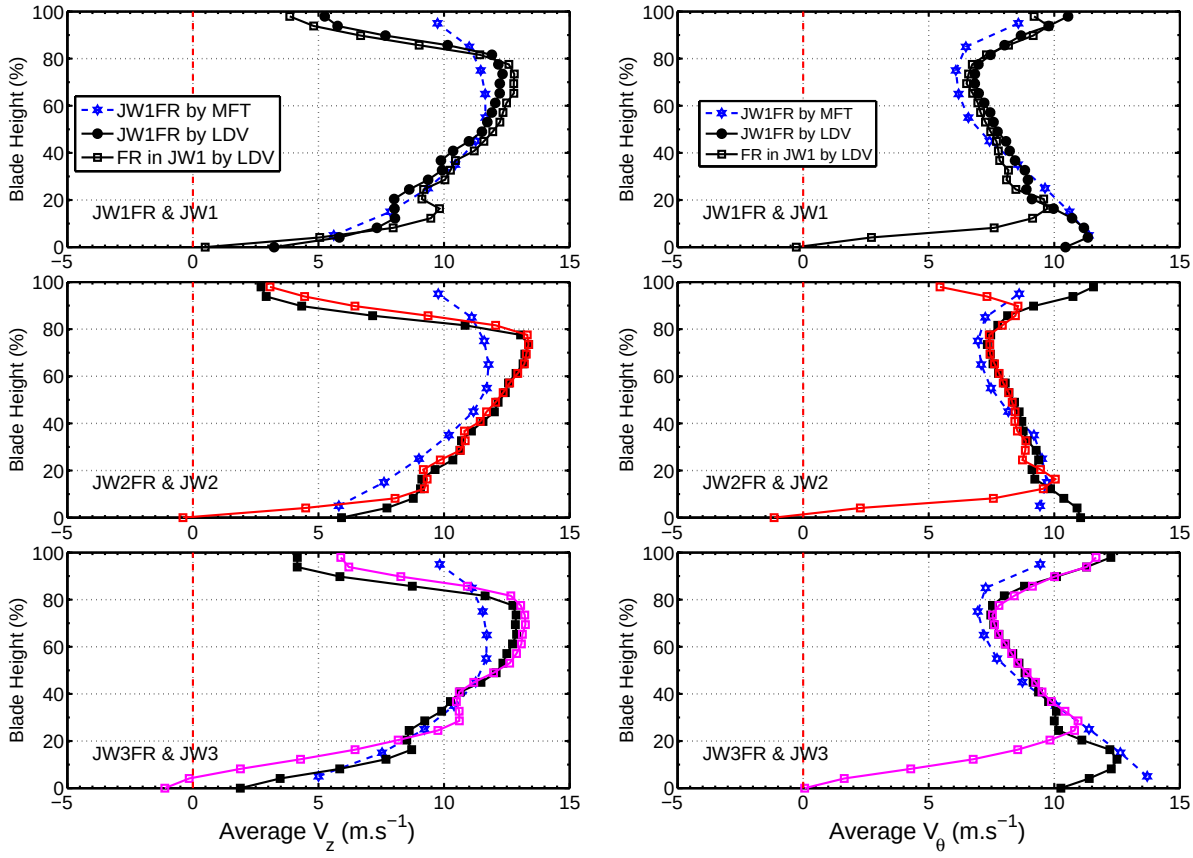

(a) Axial velocities V_z *(b) Tangential velocities V_θ*

Figure C.16: Averaged axial V_z and tangential V_θ velocities near the outlet of the FR (Position Z_p = 5mm) at design point Q_v = $1m^3.s^{-1}$, θ = θ_C, in: FR alone analyzed by MFT(☆); FR alone measured by LDV(closed symbols); in CRS measured by LDV(open symbols)

plus, l'incidence est positive au carter et négative au moyeu, or la pale de RR semble plus sensible à une incidence négative créant plus de décollement. Pour le RR de JW3 avec une répartition de charge faible a une faible incidence négative sur la plupart de la hauteur de pale introduisant de fortes pertes sur toute cette hauteur. Au final, une des solutions possibles à ce problème de perte pour les trois machines est de diminuer l'angle de calage de RR en pied de pale pour JW1 et JW2 et de diminuer l'angle de calage de RR sur la plupart de la hauteur de pale pour JW3.

C.5.3 Champs de vitesse au débits différents pour les CRS

Les vitesses moyennes axiale et tangentielle sont étudiées au point de fonctionnement Q_v = 1, à Q_v = 0.6 et à 0.37 $m^3.s^{-1}$ (figure 4.7 et 4.8). Ces trois points correspondent à un changement de pente de la courbe d'élévation de pression statique en fonction du débit. Les résultats sont indiqués ci-dessous :

- Pour un FR seul, quand le débit diminue, un flux inverse apparaît proche du moyeu et la charge diminue beaucoup sur toute la hauteur de pale au dessus de la région proche du moyeu. Si on regarde les trois FR seuls, JW2FR a le flux inverse le plus petit. On s'aperçoit que plus le débit diminue, plus la région où le flux est inversé est grande.

- Pour un étage CRS complet, en sortie de FR, le flux inverse est quasiment éliminé grâce au phénomène d'aspiration de RR. Néanmoins, la charge diminue fortement sur une grande hauteur de pale. En pied de pale, le flux de sortie de FR pour JW3 le flux tourne même dans le sens de RR pour un débit faible. Un résultat similaire est trouvé pour JW2 proche du moyeu et du carter mais avec des amplitudes de V_θ plus petites. Quand le flux d'air passe RR, de fort flux inverses apparaissent proche du moyeu et le flux tourne dans le sens de RR avec une amplitude maximum de 5 $m.s^{-1}$ pour des débits faibles. Cela montre de larges pertes en sortie de RR. Tous ces flux inversés et tournant dans dans le sens du RR peuvent se propager en amont de RR jusqu'à en aval du FR.

Tous ces résultats montrent que la présence de RR fait diminuer l'adaptabilité de FR aux hautes incidences au point de fonctionnement. Cela peut expliquer les changement des pentes dans les courbe de ΔP_s. Une autre raison peut être l'augmentation des pertes en sortie de RR.

C.5.4 Comparaison des fluctuations de pressions pariétale

Un comportement similaire est observé entre JW1 qui est déjà étudié précédemment, et JW2 et JW3. De plus, en sortie de FR, l'amplitude des pics correspondant à $f_{bpf,RR}$ de JW2 est la plus haute et l'amplitude de $f_{bpf,FR}$ est la plus basse parmi tous les pics (voir figure C.5). Cela est lié à la vitesse des rotors. Aussi, on note que niveau de fluctuation de pression pariétale pour JW3 est légèrement plus basse que pour JW1 et JW2 du fait de la rotation plus faible du RR de JW3. On peut donc dire que le RR a plus d'influence sur le niveau total de fluctuation de pression pariétale, ce qui peut être utile pour le contrôle du niveau de bruit.

	N_{CFR}/N_{CRR} (rpm)	PSD_{FR} (dB/Hz)	PSD_{RR} (dB/Hz)	Std(p') (dB)
JW1	2300/2200	17.4 ± 1	36.5 ± 1	40.9 ± 0.1
JW2	1800/2600	12.6 ± 1	38.5 ± 1	42.9 ± 0.1
JW3	2600/1100	20.2 ± 1	29.8 ± 1	35.1 ± 0.1

Table C.5: The amplitude of the dominate frequency corresponded to $f_{bpf,FR}$ and $f_{bpf,RR}$ downstream of FR (Z_p = 5 mm), for JW1, JW2 and JW3, at Q_v = 1 $m^3.s^{-1}$. Std(p') represents the power of the total signal.

C.5.5 L'influence de S sur les CRS

La performance globale des trois machines a été étudiée pour S variant de 10 à 300 mm ($[0.2, 5.5]L_{Chord}$) à $\theta = \theta_C$ pour les trois CRS. Les résultats montrent qu'une petite distance est favorable car l'augmentation de pression et le rendement statique diminuent d'une façon monotone quand la distance augmente (voir figure C.17). Plus précisément, pour S entre 10 et 100 mm, l'effet de la baisse de l'élévation de la pression statique peut être contré par la diminution de la puissance consommée par FR et RR. C'est pourquoi sur cette fourchette de valeur de S la pression statique diminue très légèrement dans des pourcentages comparables aux incertitudes de mesure. Pour S variant de 100 à 200 mm, la diminution de la pression statique est beaucoup plus rapide que la baisse de la puissance consommée par RR et FR, c'est pourquoi la pression statique perd 2% points de pourcentage. Pour S variant de 200 à 300 mm, pour JW1 et JW2, la baisse de la pression statique ralentit légèrement et comme la puissance consommée augmente, le rendement diminue faiblement. Pour JW3 par contre, la soudaine baisse de la pression statique combinée à l'augmentation de la puissance consommée fait chuter lourdement le rendement statique de $3,9$ points de pourcentage.

C.5.6 L'influence de θ sur les CRS

Les résultats de la réduction de N_{FR} du JW1 montrent que le rendement statique maximum augmente dans un premier temps quand θ augmente aussi. Dans un deuxième temps, le rendement diminue fortement à partir de $1.2\theta_C$ à cause des grosses pertes dans RR. Des résultats similaires sont présents pour JW2 pour un N_{FR} réduit (voir figure C.18). Pour JW3, le rendement atteint 65.1% quand θ vaut $1.8\theta_C$ puis s'effondre quand θ continue à augmenter. Cela peut provenir de l'incidence négative en entrée de RR pour JW3 à $\theta = \theta_C$. De plus, le RR du JW3 a plus de tolérance face à de fortes incidences du flux d'air grâce une plus grande vitesse de rotation de RR sans décollement.

Au final, dans cette thèse, l'influence de θ sur la performance du CRS dépend de l'angle d'incidence du RR au point de fonctionnement, ce qui est relié à l'angle de calage du RR.

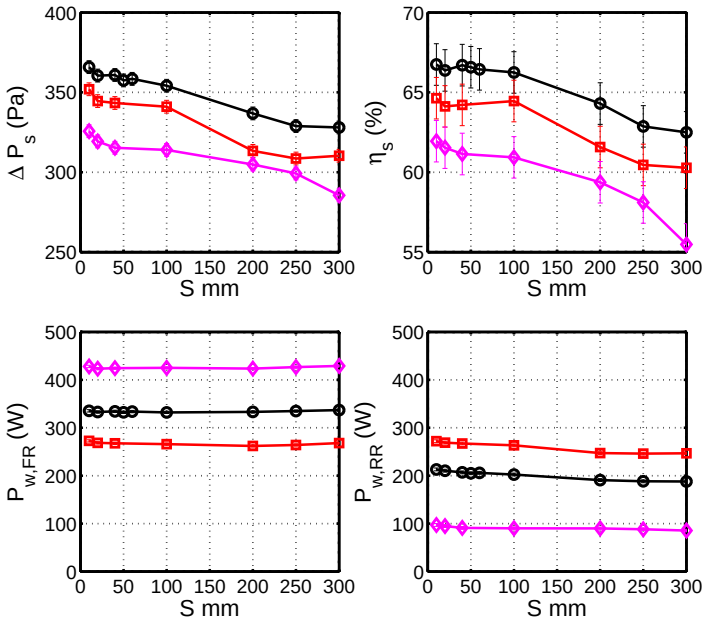

Figure C.17: performance of JW1 (∘), JW2 (□) and JW3(◇) at $S = 10, 20, 40, 100, 200, 250, 300$ *mm and Rront Rotor alone(*$S = 0$*, filled symbols) at design point* $Q_v = 1m^3.s^{-1}$, $\theta = \theta_c$, ΔP_s, $\mathcal{P}_{w,FR}$ *and* $\mathcal{P}_{w,RR}$ *are rescaled by* ρ_{ref}.

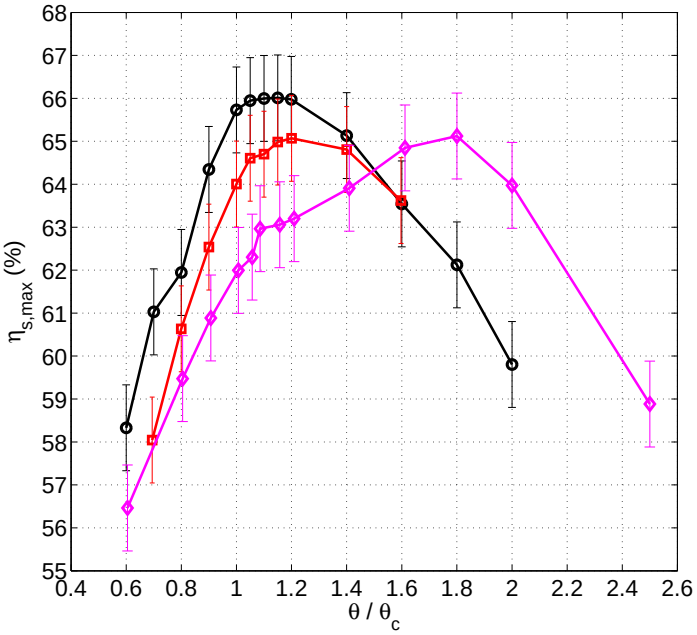

Figure C.18: Maximum static efficiency vs. θ. *Stage JW1,* $N_{FR} = 1400$ *rpm,* $Re \approx 7.3{\times}10^4$ *(∘). JW2,* $N_{FR} = 1100$ *rpm,* $Re \approx 4.7 \times 10^4$ *(□). JW3,* $N_{FR} = 1600$ *rpm,* $Re \approx 7.4 \times 10^4$ *(◇).*

C.6 Conclusion

Cette thèse est le prolongement de précédentes investigations sur la performance et les interactions rotors-rotors sur les machines CRS. La thèse avait trois objectifs. Le premier était de fournir une base expérimentale pour les paramètres étudiés des CRS. Cela inclue la conception de nouveaux CRS avec différents paramètres et la détermination des incertitudes des mesures lors des expérimentations. Cette détermination des incertitudes a montré une bonne qualité de la mesure expérimentale. Par exemple, l'incertitude de l'élévation de la pression statique est de 1% (soit ±4 Pa) et 2% pour le rendement statique (soit ±1.3 point de pourcentage). Les détails sont dans le chapitre 2.

Le second objectif de cette thèse était de valider la méthode de conception en détails et de fournir des optimisations pour le design et la méthode de prédiction. Dans le but de valider les effets de la distribution de charge $L_C = \frac{\Delta P_{t,RR}}{\Delta P_t}$; trois machines CRS (JW1, JW2 et JW3) ont été conçues avec un L_C de 41%, 52% et 23% respectivement. De plus, le nombre de Reynolds pour les trois machines restent autour d'une valeur de $1 \sim 2 \times 10^5$. Au final, la méthode de conception a été validé au point de fonctionnement pour les trois machines. Ces dernières atteignent le même point de fonctionnement, avec un biais maximum de −11% pour JW3. Les courbes de pression statique des trois machines sont plus raides que les courbes obtenues pour un rotor seul indiquant une bonne stabilité des machines CRS indépendamment du FR. Au niveau du rendement statique, au point de fonctionnement, il peut atteindre 62% pour JW3 et 66, 6% pour JW1 et JW2. Cela montre que les machines contra rotatives sont une solution très prometteuse pour obtenir des rendements très hauts. La charge du rotor mesurée à l'aide d'un couple-mètre ou bien calculée par les mesures LDV est cohérente avec la valeur de conception. Cela confirme que l'estimation de l'élévation de la pression statique pour FR et RR est bonne. Ensuite, les vitesse axiales et tangentielles moyennes sont mesurées en amont, au milieu et en aval du CRS au point de fonctionnement pour $\theta = \theta_C$ et $S = 10$ mm pour les trois machines. Excepté en pied de pale et en bout de pale où des phénomènes complexes apparaissent, le flux d'air suit la pale de RR sur quasiment toute la hauteur de pale comme l'avait prédit la méthode MFT. Au final, la méthode MFT peut être appliquée pour une conception préliminaire d'un CRS subsonique. Mais une optimisation peut être suggérée en modifiant le modèle de perte près du moyeu de la pale et en diminuant l'angle de calage de tous les RRs. En effet, la vitesse pour des débits faibles montrent que la présence du RR fait diminuer l'adaptabilité du FR aux hautes incidences au point de fonctionnement. Cela pourrait expliquer la baisse de la pente des courbes de pression statique. Une autre raison peut être l'augmentation des pertes en sortie de RR.

Le troisième objectif de cette thèse est de faire une base de donnée préliminaire des paramètres influents pour la conception d'un CRS. La performance globale est investigué pour JW1 pour S variant de 10 à 300 mm ($[0.2, 5.5]L_{Chord}$) et $\theta = \theta_C$. Les résultats montrent qu'une distance axiale faible est favorable car l'augmentation de pression et le rendement statique se détériorent à mesure que S augmente. Néanmoins, les résultats avec un N_{FR} réduit montrent que $\eta_{s,max}$ augmentent en même temps que θ puis diminue fortement à partir de $1.2\theta_C$ à cause des fortes pertes dans RR pour JW1 et JW2. De plus, pour JW3, $\eta_{s,max}$ augmente jusqu'à $65, 1\%$ quand θ augmente jusqu'à $1.8\theta_C$ puis diminue quand θ continue d'augmenter. Cela peut s'expliquer par une incidence négative en entrée de RR pour JW3 au point de fonctionnement. De plus, le RR a plus de tolérance face

à de fortes incidences du flux d'air grâce une plus grande vitesse de rotation de RR sans décollement.

Experimental study of two counter rotating axial flow fans

ABSTRACT : The counter rotating subsonic axial flow fans could be a good solution for applications where the highly improved static pressure and efficiency are required without the increase of rotational speed and fan diameter. However, the mechanisms of high performance CRS and the influence of parameters are not well understood nowadays. This thesis is an experimental investigation of the performance and parameter studies of two counter rotating axial flow ducted fans. The design and measurement methods are based on the previous research work in Laboratory Dynfluid (Arts et Métiers ParisTech). Three Counter Rotating Stages (CRS) (named JW1, JW2 and JW3) are developed and tested on a normalized test bench (AERO2FANS). These systems have the same design point and differ by the distribution of loading as well as the ratio of angular velocity between the Front Rotor (FR) and Rear Rotor (RR). The first part of results focuses on the JW1. The overall performance is obtained by the experimental results of the static pressure rise and static efficiency, as well as the wall pressure fluctuations recorded by a microphone on the casing wall. The parameter study is conducted to investigate the effects of the axial distance and the ratio of angular velocity between the FR and RR on the global performance and flow fields measured by Laser Doppler Velocimetry (LDV). The last part of the work is devoted to analyzing the differences of the three CRS with different distribution of work, in terms of the global performance and flow features.

Keywords : Counter rotating rotors, Axial fan, Turbomachine, Performance, Parameters influences, Rotors interaction, Wall pressure fluctuations, LDV

Etude expérimentale des ventilateurs axiaux à double rotors contrarotatifs

RESUME : Les machines axiales à rotors contrarotatifs subsoniques sont une bonne solution pour les industries où de fortes élévations de pressions et d'efficacités sont nécessaires sans augmenter le diamètre ou la vitesse de rotation des rotors. Néanmoins, le comportement des CRS et les paramètres impactant ses performances ne sont pas encore totalement compris. Cette thèse mène une investigation expérimentale sur la performance et les paramètres influents sur un étage contrarotatif. La technique de design et les méthodes de mesure sont repris sur une thèse précédente réalisée au laboratoire Dynfluid (Arts et métiers ParisTech). Trois étages contrarotatifs ont été fabriqués (JW1, JW2 et JW3) et testés sur le banc d'essai normalisé AERO2FANS. Ces machines ont été conçues pour avoir le même point de fonctionnement mais avec une répartition de charge différente. Les résultats expérimentaux se concentrent dans un premier temps sur JW1. Les grandeurs physiques regardées sont l'efficacité globale et l'élévation de pression statique pour juger de la performance globale de la machine. La fluctuation de pression pariétale et le champ de vitesse sont aussi mesurés. L'impact du changement de rapport de vitesse ou la distance entre les deux rotors sur la machine JW1 a été étudiée grâce aux grandeurs physiques décrits précédemment. Enfin dans une dernière partie, les trois machines sont comparées toujours grâce aux grandeurs physiques définies précédemment.

Mots clés : Rotors contrarotatifs, Ventilateur axial, Turbomachine, Performance, Influence des paramètres, Interaction rotors, Mesure de fluctuations pression pariétale, LDV

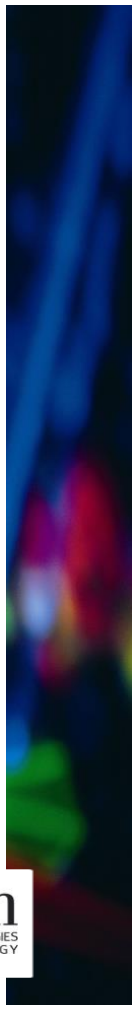

ARTS ET MÉTIERS ParisTech

ParisTech INSTITUT DES SCIENCES ET TECHNOLOGIES PARIS INSTITUTE OF TECHNOLOGY